

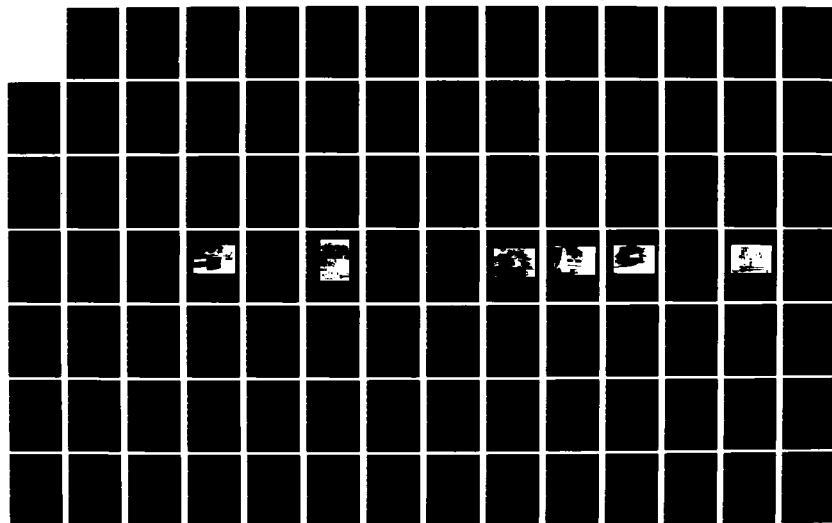
AD-A124 740

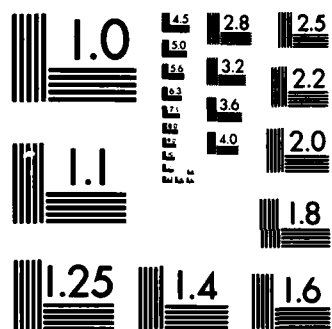
A FINITE ELEMENT ANALYSIS OF THE CREEP RESPONSE OF
LUMBAR INTERVERTEBRAL (U) AIR FORCE INST OF TECH
WRIGHT-PATTERSON AFB OH SCHOOL OF ENGI... W J ROTHWELL
DEC 82 AFIT/GAE/AA/82D-24 F/G 6/19

1/2

UNCLASSIFIED

NL





MICROCOPY RESOLUTION TEST CHART
NATIONAL BUREAU OF STANDARDS-1963-A

AD A322740



A FINITE ELEMENT ANALYSIS OF THE CREEP
RESPONSE OF LUMBAR INTERVERTIBRAL
JOINTS IN THE RHESUS MONKEY

THESIS

AFIT/GAE/AA/82D-24

William J. Rothwell, Jr
Capt USAF

DTIC
ELECTE
FEB 23 1983

DTIC FILE COPY

DEPARTMENT OF THE AIR FORCE
AIR UNIVERSITY (ATC)
AIR FORCE INSTITUTE OF TECHNOLOGY

Wright-Patterson Air Force Base, Ohio

This document is approved for public release and distribution.

8124740
AFIT/GAE/AA/82D-24

A FINITE ELEMENT ANALYSIS OF THE CREEP
RESPONSE OF LUMBAR INTERVERTEBRAL
JOINTS IN THE FÆSUS MONKEY

THESIS

AFIT/GAE/AA/82D-24

William J. Rothwell, Jr.
Capt USAF

Approved for public release; distribution unlimited

A FINITE ELEMENT ANALYSIS OF THE CREEP
RESPONSE OF LUMBAR INTERVERTEBRAL
JOINTS IN THE RHESUS MONKEY

THESIS

Presented to the Faculty of the School of Engineering
of the Air Force Institute of Technology

Air University

in Partial Fulfillment of the
Requirements for the Degree of

Master of Science

by

William J. Rothwell, Jr.

Capt

USAF

Graduate Aeronautical Engineering

December 1982

Accession For	
NTIS GRA&I	<input checked="" type="checkbox"/>
DTIC TAB	<input type="checkbox"/>
Unannounced	<input type="checkbox"/>
Justification	
By	
Distribution	
Availability Codes	
Avail and/or	
Dist. Special	
A	



Preface

I wish to thank Dr. Anthony N. Palazotto, my thesis advisor, for his timely advice and encouragement throughout this research effort. I am also indebted to Dr. Peter J. Torvik and Major Michael M. Wallace for their constructive review of the draft copy. Thanks also to Cheryl Nicol for her flawless typed copies from impossible manuscript. Finally, I am forever grateful to my wife, Claudette, without whose love and support this study would have been impossible.

Contents

	<u>Page</u>
Preface	ii
List of Figures	v
List of Tables	xi
List of Symbols	xii
Abstract	xv
I. Introduction	1
1.1 Purpose	1
1.2 Anatomy	1
1.3 Background	5
1.4 Assumptions	7
1.5 Approach and Presentation	8
II. Theory	10
2.1 Linear Viscoelasticity	10
2.2 Finite Element Method	17
2.2.1 General Concepts	17
2.2.2 Analysis	20
III. Centrum Analysis	25
3.1 Experimentation	25
3.1.1 Equipment	25
3.1.2 Procedure	29
3.1.3 Results	36
3.2 Analysis	40
3.2.1 Development of Model	40
3.2.2 Solution Technique	42
3.3 Results	42
3.3.1 Flexible Case	42
3.3.2 Stiff Case	96

Contents

	<u>Page</u>
IV. Joint Analysis	111
4.1 Finite Element Model	111
4.2 Film Data	113
4.3 Results	115
V. Conclusions and Recommendations	133
Bibliography	135
Appendix A: Stiffness Matrix and Nodal Force Vector for Axisymmetric Problems	138
Appendix B: Experimental Data	142
Appendix C: Example of Calibration Procedure	161
Appendix D: Method for Predicting q_1	162
VITA	165

List of Figures

<u>Figure</u>		<u>Page</u>
1.2-A	Rhesus Monkey Spine	3
1.2-B	Sagittal View of Intervertebral Joint	4
1.2-C	Superior View of Intervertebral Joint	4
1.2-D	Portion of Intervertebral Disk	4
2.1-A	Elastic Model	11
2.1-B	Maxwell Fluid Model	11
2.1-C	Kelvin Solid Model	13
2.1-D	Three-Parameter Kelvin Solid Model	13
2.1-E	Typical Creep Curve	15
2.1-F	Significance of the q_1 Material Parameter	16
2.2-A	Triangular Element	18
2.2-B	Flow Chart of Solution Technique	23
3.1-A	Experimental Apparatus	26
3.1-B	Block Diagram of Experimental Apparatus . . .	27
3.1-C	Test Chamber	28
3.1-D	Dental Acrylic Mounting Device, Initial Configuration	31
3.1-E	Dental Acrylic Mounting Device, Final Configuration	32
3.1-F	Calibration Cylinders	33
3.1-G	Configuration of Specimen for Testing	35
3.1-H	Average Experimental Displacements Relative to Midplane, 15 Pound Load	37

<u>Figure</u>		<u>Page</u>
3.1-I	Average Experimental Displacements Relative to Midplane, 30 Pound Load	38
3.2-A	Centrum Mesh	43
3.3-A	Finite Element Solution, 15 Pound Load, Flexible Case	44
3.3-B	Finite Element Solution, 30 Pound Load, Flexible Case	45
3.3-C	Relative Locations of Centrum Planes and Elements Used in the Stress Analysis . .	47
3.3-D	Symbols Used for Quick Reference to Stress Plots	49
3.3-E	σ_z Distribution in Boundary Plane, Homogeneous Case	51
3.3-F	σ_z Distribution in Boundary Plane, Higher Load Case	52
3.3-G	σ_z Distribution in Boundary Plane, Inhomogeneous Case	53
3.3-H	σ_r Distribution in Boundary Plane, Homogeneous Case	54
3.3-I	σ_r Distribution in Boundary Plane, Higher Load Case	55
3.3-J	σ_r Distribution in Boundary Plane, Inhomogeneous Case	56
3.3-K	σ_θ Distribution in Boundary Plane, Homogeneous Case	57
3.3-L	σ_θ Distribution in Boundary Plane, Higher Load Case	58
3.3-M	σ_θ Distribution in Boundary Plane, Inhomogeneous Case	59
3.3-N	σ_{rz} Distribution in Boundary Plane, Homogeneous Case	60
3.3-O	σ_{rz} Distribution in Boundary Plane, Higher Load Case	61

<u>Figure</u>		<u>Page</u>
3.3-P	σ_{rz} Distribution in Boundary Plane, Inhomogeneous Case	62
3.3-Q	σ_z Versus Time in Boundary Element, Homogeneous and Higher Load Cases	64
3.3-R	σ_z Versus Time in Boundary Element, Homogeneous and Inhomogeneous Cases	65
3.3-S	σ_r Versus Time in Boundary Element, Homogeneous and Higher Load Cases	66
3.3-T	σ_r Versus Time in Boundary Element, Homogeneous and Inhomogeneous Cases	67
3.3-U	σ_θ Versus Time in Boundary Element, Homogeneous and Higher Load Cases	68
3.3-V	σ_θ Versus Time in Boundary Element, Homogeneous and Inhomogeneous Cases	69
3.3-W	σ_{rz} Versus Time in Boundary Element, Homogeneous and Higher Load Cases	70
3.3-X	σ_{rz} Versus Time in Boundary Element, Homogeneous and Inhomogeneous Cases	71
3.3-Y	σ_z Distribution in Midplane, Homogeneous Case	72
3.3-Z	σ_z Distribution in Midplane, Higher Load Case	73
3.3-AA	σ_z Distribution in Midplane, Inhomogeneous Case	74
3.3-AB	σ_r Distribution in Midplane, Homogeneous Case	75
3.3-AC	σ_r Distribution in Midplane, Higher Load Case	76
3.3-AD	σ_r Distribution in Midplane, Inhomogeneous Case	77
3.3-AE	σ_θ Distribution in Midplane, Homogeneous Case	79

<u>Figure</u>		<u>Page</u>
3.3-AF	σ_{θ} Distribution in Midplane, Higher Load Case	80
3.3-AG	σ_{θ} Distribution in Midplane, Inhomogeneous Case	81
3.3-AH	σ_{rz} Distribution in Midplane, Homogeneous Case	82
3.3-AI	σ_{rz} Distribution in Midplane, Higher Load Case	83
3.3-AJ	σ_{rz} Distribution in Midplane, Inhomogeneous Case	84
3.3-AK	Comparison of Deformed to Undeformed Shape	85
3.3-AL	σ_z Versus Time in Midplane Element, Homogeneous and Higher Load Cases	87
3.3-AM	σ_z Versus Time in Midplane Element, Homogeneous and Inhomogeneous Cases	88
3.3-AN	σ_r Versus Time in Midplane Element, Homogeneous and Higher Load Cases	89
3.3-AO	σ_r Versus Time in Midplane Element, Homogeneous and Inhomogeneous Cases	90
3.3-AP	σ_{θ} Versus Time in Midplane Element, Homogeneous and Higher Load Cases	91
3.3-AQ	σ_{θ} Versus Time in Midplane Element, Homogeneous and Inhomogeneous Cases	92
3.3-AR	σ_{rz} Versus Time in Midplane Element, Homogeneous and Higher Load Cases	93
3.3-AS	σ_{rz} Versus Time in Midplane Element, Homogeneous and Inhomogeneous Cases	94
3.3-AT	Comparison of Deformed Shapes for the Homogeneous and Higher Load Cases After 1100 Sec	95
3.3-AU	Finite Element Solution, Stiff Case	97

<u>Figure</u>		<u>Page</u>
3.3-AV	σ_r Distribution in Boundary Plane, Stiff Case	98
3.3-AW	σ_r Distribution in Midplane, Stiff Case . . .	99
3.3-AX	σ_z Distribution in Boundary Plane, Stiff Case	100
3.3-AY	σ_z Distribution in Midplane, Stiff Case	101
3.3-AZ	σ_θ Distribution in Boundary Plane, Stiff Case	102
3.3-BA	σ_θ Distribution in Midplane, Stiff Case	103
3.3-BB	σ_{rz} Distribution in Boundary Plane, Stiff Case	104
3.3-BC	σ_{rz} Distribution in Midplane, Stiff Case	105
3.3-BD	σ_r Versus Time in Boundary and Midplane Elements, Stiff Case	107
3.3-BE	σ_z Versus Time in Boundary and Midplane Elements, Stiff Case	108
3.3-BF	σ_θ Versus Time in Boundary and Midplane Elements, Stiff Case	109
3.3-BG	σ_{rz} Versus Time in Boundary and Midplane Elements, Stiff Case	110
4.1-A	Joint Mesh	112
4.3-A	Finite Element Solution, Joint Analysis . . .	122
4.3-B	Planes Chosen for Stress Profiles, Joint Analysis	123
4.3-C	σ_r Distribution in Disk Plane	124
4.3-D	σ_z Distribution in Disk Plane	125
4.3-E	σ_θ Distribution in Disk Plane	126

<u>Figure</u>		<u>Page</u>
4.3-F	σ_{rz} Distribution in Disk Plane	127
4.3-G	σ_r Distribution in Centrum Plane	129
4.3-H	σ_z Distribution in Centrum Plane	130
4.3-I	σ_θ Distribution in Centrum Plane	131
4.3-J	σ_{rz} Distribution in Centrum Plane	132
A.2-A	Triangular Element with Surface Traction	140
B-1	External Measurement Code, Centrum Tests	147
B-2	Test Curve, Specimen KAZ 3(L1)	149
B-3	Test Curve, Specimen KAZ 3(L2)	150
B-4	Test Curve, Specimen KAZ 6(L1)	151
B-5	Test Curve, Specimen KAZ 6(L2)	152
B-6	Test Curve, Specimen KAZ 7(L1)	153
B-7	Test Curve, Specimen KAZ 7(L2)	154
B-8	Test Curve, Specimen KAZ 10(L1)	155
B-9	Test Curve, Specimen KAZ 10(L1)	156
B-10	Test Curve, Specimen KAZ 30(L1)	157
B-11	Test Curve, Specimen KAZ 30(L2)	158
B-12	Test Curve, Specimen RHESUS 17(L1)	159
B-13	Test Curve, Specimen RHESUS 17(L2)	160
D-1	Approximate Slope of the Displacement- Time Curve After Elastic Deformation	163

List of Tables

<u>Table</u>		<u>Page</u>
3-1	Constants of Curve-fit Equation Representing Model Displacements	39
4.2-A	Film Measurement Data, Test R/1	116
4.2-B	Film Measurement Data, Test R/4	117
4.2-C	Film Measurement Data, Test R/9	118
4.2-D	Average Film Measurement Data	119
4.3-A	Comparison of Disk Radial Displacement from Film Measurements and Analytical Results	121
B-1	Calibration Data	143
B-2A	Extracted Data, 15 Pound Tests	144
B-2B	Extracted Data, 30 Pound Tests	145
B-3	Specimen External Measurements	146
B-4	Specimen Internal Measurements	148

List of Symbols

A	Area of triangular finite element
a	Approximate slope of displacement-time curve after elastic deformation
a_i	Constants in displacement polynomials ($i = 1, 2, 3$)
[B]	Matrix relating nodal degrees-of-freedom to elemental strains
b_i	Constants in shape functions, N_i ($i = 1, 2, 3$)
c_i	Constants in shape functions, N_i ($i = 1, 2, 3$)
C_i	Constants in experimental curve-fit equation ($i = 1, 2, 3$)
cm	Centimeters
[D]	Elastic material property matrix
DC	Direct Current
E	Young's Modulus
F_i	i th component of surface traction $F(r, z)$ ($i = r, z$)
in	Inches
[K]	Global or structural stiffness matrix
[k]	Element stiffness matrix
K_p	Kiloponds (1 Kilopond = 9.8 Newtons)
L	Length of a side of a triangular element
lb	Pounds
L_i	Area coordinate ($i = 1, 2, 3$)
L_0	Average axial length after initial elastic deformation
mm	Millimeters
{P}	Global vector of applied nodal forces

$\{p\}$	Element vector of applied nodal forces
p_{ij}	Element nodal force component at node i ($i = 1,2,3$) in the j direction ($j = r,z$)
$\{Q\}$	Vector of nodal residual forces due to initial strains
q_0	Material parameter related to creep stiffness
q_1	Material parameter related to initial creep rate
r	Radial variable
\bar{r}	Radial coordinate of element centroid
r_i	Radial coordinate of i th node ($i = 1,2,3$)
s	Hydrostatic (volumetric) stress; also, a variable along an edge of an element
TMAX	Maximum simulated time in computer program algorithm
t	Time
Δt	Small time increment
t_0	Initial time
t_1	Initial time plus small timestep
$\{u\}$	Vector of nodal degrees-of-freedom
u_i	Nodal degree-of-freedom in the r direction ($i = 1,2,3$)
u_z	Axial (z) displacement
u_{z0}	Axial displacement immediately after initial elastic deformation
u_{z1}	Axial displacement at $t=t_1$
\dot{u}_0	Initial axial displacement rate
V	Volume
v_i	Nodal degree-of-freedom in the z direction ($i = 1,2,3$)

z	Axial variable
\bar{z}	Axial coordinate of element centroid
z_i	z coordinate of i th node ($i = 1, 2, 3$)
ϵ	Total strain
$\{\epsilon\}$	Vector of total strain
ϵ_c	Viscoelastic (Creep) strain
$\{\epsilon_c\}$	Vector of total accumulated creep strains
$\{\Delta\epsilon_c\}$	Vector of accumulated creep strains over a time increment Δt
ϵ_E	Elastic strain
$\{\epsilon_0\}$	Vector of initial strains
λ	Constant in experimental curve-fit equation
η	Dashpot or fluidity constant
σ	Stress
$\{\sigma\}$	Vector of stresses
σ_{AVG}	Average stress
σ_D	Stress in dashpot of rheological model
σ_{ij}	Stress component ($i, j = x, y, z$ or r, θ, z)
σ'_{ii}	Deviatoric stress ($i = x, y, z$ or r, θ, z)
σ_s	Stress in spring of rheological model
ν	Poisson's ratio
ν_c	Poisson's ratio for viscoelastic (creep) strain
$[]$	Matrix
$\{ \}$	Vector
$\{ \}^T$	Vector transpose
(\cdot)	Differentiation with respect to time

Abstract

This study consisted of two phases. During the first phase, Lumbar intervertebral centra from healthy, adolescent Rhesus Monkeys (*Macaca Mulatta*) were subjected to axial compression loads of 15 and 30 pounds for a period of eight hours and displacement-time data was gathered. An axisymmetric finite element model was used to analytically determine material parameters describing the observed creep for each applied load. A Three-parameter Kelvin Solid was used to represent the elastic and viscoelastic response. Parameters were found by adjusting them until the analytical displacement-time response matched the experimental response. The parameters determined characterized the initial elastic stiffness, initial creep rate, and creep stiffness.

Analytical stress profiles in two horizontal planes through the vertebral centrum indicated a predominance of stress in Cortical bone and the transition of stress from the Trabecular bone to the Cortical bone as creep proceeded. According to the model, the Centrum behaved as though the Cortex was acting like a thin shell constraining the outward flow of a viscoelastic Trabecular bone region.

During the second phase, viscoelastic constants determined for the Trabecular bone region were incorporated into an overall model of the intervertebral joint minus the Articular Facet Joint and associated spinous processes.

Viscoelastic constants were then found for the disk. However, they proved to be unreasonably high, describing a very stiff, creep-resistant disk. It was determined that the rheological model used, two Three-Parameter Kelvin Solids in series, was inadequate to allow one to determine unique values of these parameters in the disk.

Final results indicate that an accurate model of the intervertebral joint must incorporate a viscoelastic Centrum. Creep behavior can no longer be attributed solely to the disk.

A FINITE ELEMENT ANALYSIS OF THE
CREEP RESPONSE OF LUMBAR INTER-
VERTEBRAL JOINTS IN THE RHESUS MONKEY

I. Introduction

1.1 Purpose

The behavior and mechanical properties of intervertebral joints are of interest to researchers in several areas. Among these are the effects of sustained loading, vibration, and ejection forces, as might be experienced by aircrews in high-performance aircraft, as well as problems associated with disc degeneration.

Intervertebral joints have long been known to creep under load. Previously, the disk has been treated as the sole medium of the creep (viscoelastic) behavior. This study was undertaken to discover material constants which may account for such behavior experienced by the bony portion of the joint external to the disk region. These values were then incorporated into a model of the joint in order to determine viscoelastic constants for the disk. In both phases, stress redistributions resulting from creep behavior were analyzed for the various internal regions. The results of this study will be used to further refine a biodynamic model of the spine.

1.2 Anatomy

A thorough understanding of this thesis requires a brief description of applicable anatomy. The spine will first be discussed followed by a more detailed description of the intervertebral joint.

The Rhesus Monkey spine is a complex structure composed of a number of mobile vertebrae. It is divided into 4 regions, as indicated in Fig. 1.2-A. The concern of this study was with joints in the Lumbar region, specifically at the L1-L2 level (indicating the top lumbar joint).

Each joint consists of two vertebral bodies superior and inferior to a disk (Fig. 1.2-B); two associated ligaments joining the vertebral bodies with the disk, one running vertically along the posterior edge, and one running vertically along the anterior edge of the joint; and an Articular Facet Joint.

The vertebral body consists of a centrum and a set of processes (Fig. 1.2-C) which provide attachment points for muscles and ligaments. The spinous processes are attached to the centrum by two pedicles and extend rearward. Posterior spinous processes from adjacent vertebral bodies form the Articular Facet Joint near the edges of the pedicles. Two lateral processes, one on each side of the centrum, extend to the sides.

The centrum consists of spongy Trabeculae or Trabecular

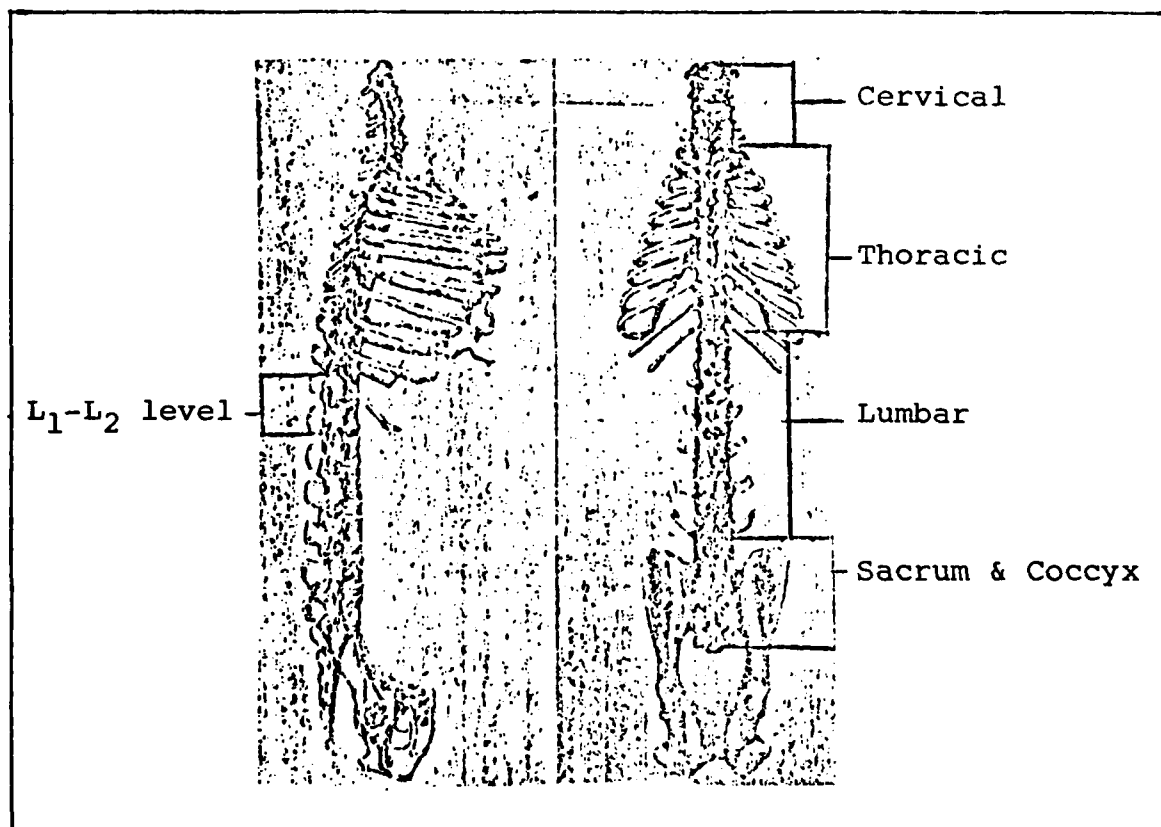


Fig. 1.2-A (Ref 17). Rhesus Monkey Spine

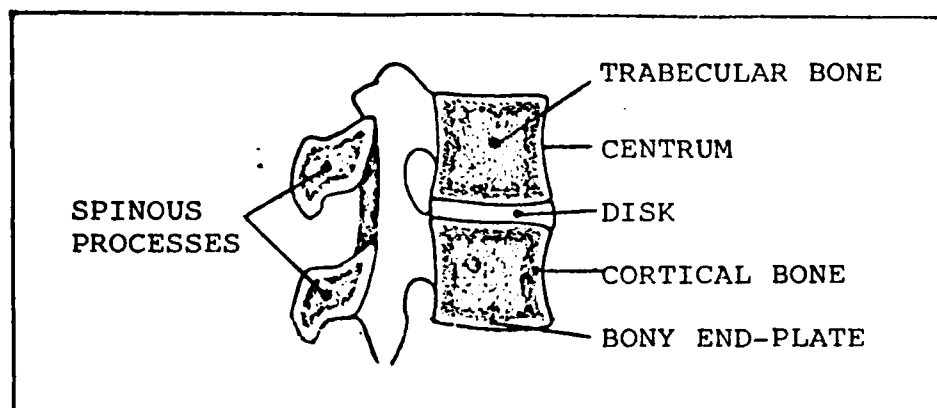


Fig. 1.2-B (Ref 29). Sagittal View of Intervertebral Joint

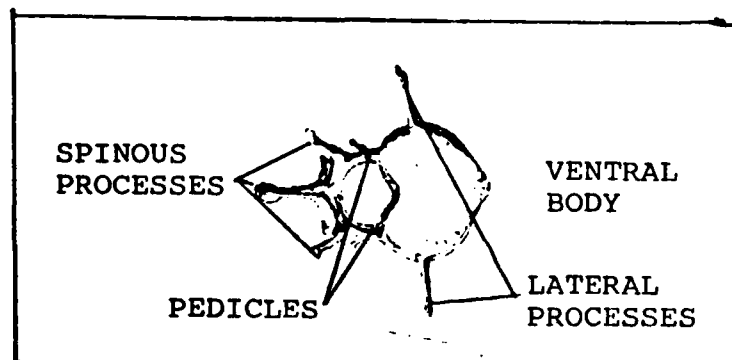


Fig. 1.2-C (Ref 15). Superior View of Intervertebral Joint

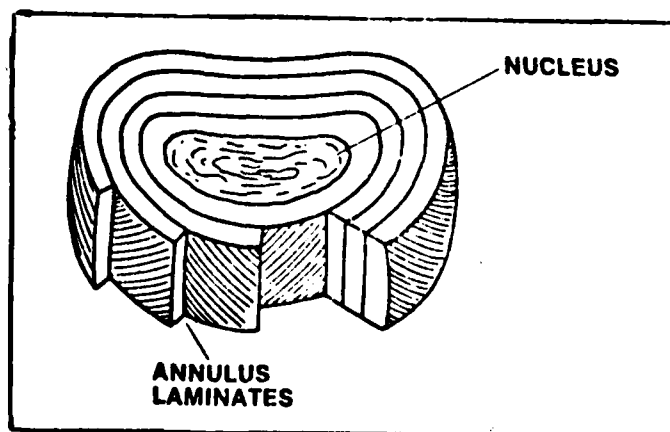


Fig. 1.2-D (Ref 29). Portion of Intervertebral Disk

bone (Fig. 1.2-B) encased circumferentially in a thin layer of denser Cortical bone (Cortex). The upper and lower surfaces are composed of still denser bone (relative to the Trabeculae and Cortex) called the Bony End-plate, which serves as a transition region between the centrum and the disk.

The disk is made up of solid and fluid material in three regions. In the center of the disk is a region known as the Nucleus Pulposus (Fig. 1.2-D) comprised of a loose network of fine fibrous strands in a muco-protein gel. Surrounding this region is the Annulus Fibrosus, composed of layers of collagen fibers imbedded in muco-protein gel. These fibers are arranged in a helicoid manner, and fiber directions are fairly uniform within each laminate. In the human case, fiber principal directions alternate between adjacent laminae at a fairly constant angle with respect to the disk midplane (White et al, Ref 29). The orientation of these fibers as well as the number of laminates is not known for the Rhesus Monkey.

Not shown in the figure is the cartilagenous end-plate, which is comprised of a hyaline cartilage structure. It serves as a boundary region between a disk and its adjacent vertebral body.

1.3 Background

Many studies have been performed in order to gain an

understanding of the elastic and viscoelastic response of intervertebral joints. Brown (1957), Nachemson (1960), Hirsch (1965), and Rolander (1966) all conducted experiments on the basic load-deflection behavior of the unit. Kulak, et al (1976) showed that the human disk behaved like a medium-length thick-walled tube subjected to internal pressure (Ref 18). Lin, et al (1978) concluded that human joints exhibit a nearly linear stress-strain relationship (Ref 20).

Evans (1957) experimentally examined the relative contributions of human Trabecular and Cortical bone in supporting axial loads and concluded that the latter contributed more. Bell et al (1967), however, noted that the Cortex was too thin to transfer the load. Rockoff, et al (1969) determined that Cortical bone contributes 45 to 70% of peak strength of human lumbar vertebrae (Ref 23).

Virgin (1951) examined the viscoelastic response of human disks and determined that stress redistributions were related to a fluid seepage phenomena occurring among internal regions of the joint (Ref 28). Fung (1960) showed that stress in some biological materials could be separated into an elastic and a viscoelastic part (Ref 6). Kazarian, et al (1978) showed that the creep response could be modelled by a three-parameter Kelvin Solid (Ref 17). Burns (1980) developed a method for determining values describing that model (Ref 4).

Lin et al used a three-dimensional model of the joint in axial compression to show that posterior elements could

be ignored in such an analysis (Ref 20). Tencer, et al (1982) confirmed that same conclusion for all possible loading configurations except posterior shear and axial torque (Ref 27).

Belytschko, et al (1974, Ref 3) and Spilker (1980, Ref 24) independently employed axisymmetric finite element models to study the elastic response of human disks. Hinrichsen (1980) applied a similar approach to determine the creep response of the human disk modelled as a three-parameter Kelvin Solid (Ref 13). Allen (1981) used results from Galante (1967, Ref 10), Lin, et al (1978, Ref 19), and Kulak, et al (1976, Ref 18) to develop an inhomogeneous model of the human disk incorporating an orthotropic Annulus Fibrosis (Ref 2). Furlong (1981) examined the effects of degenerated disks on the viscoelastic response of Rhesus Monkey joints. He assumed that the creep response of the joint could be modelled by a homogeneous, creeping disk (Ref 8).

1.4 Assumptions

In this study, a disk and the adjoining vertebral centrum will be considered an "intervertebral unit". This unit is treated from observation as axisymmetric about a vertical centroidal axis, as was done by Furlong (Ref 8). The vertebral centrum is also assumed to have symmetry about a horizontal midplane. Finally, the unit is considered to have symmetry about the horizontal midplane of the disk. These assumptions will permit a simplified analysis requiring a

minimum of computer resources.

Any observed creep is considered a quasi-static phenomena wherein inertia effects may be ignored. The magnitude of deformations are assumed small enough that linear elastic response may be assumed (Ref 15). Resultant internal stresses are considered small enough that yielding does not occur; hence, any plastic deformation will be ignored. The disk is treated as nearly incompressible, as expressed by other authors (Refs 2, 3, 13, and 8). Biological seepage among regions is ignored. To permit analysis, each region is considered homogeneous and isotropic. Since the relative stiffnesses are unknown, the Bony end-plate and Cortical bone are initially assumed to have identical material properties; later, the former region will be assumed stiffer than the latter. Both regions are considered elastic. Since the anatomical nature of the annulus fibrosus is also not precisely known, the disk will be treated in a "smeared-out" manner as one homogeneous unit. Any viscoelastic behavior is attributed to both the Trabecular bone and the disk and is considered linear for the magnitude of deformations experienced.

1.5 Approach and Presentation

This thesis consisted of two phases. During the first phase, vertebral centra were subjected to axial compressive loads of 15 and 30 pounds. Data were gathered concerning

axial displacement versus time. Loads were chosen to provide a measurable creep response, and not necessarily to represent realistic anatomical loads. Finite element techniques were used to model the centrum and determine material constants which characterized the average experimental response for each load value.

During the second phase, the viscoelastic constants derived in the first phase were incorporated into a finite element model of the intervertebral joint minus the articular facet joint and associated ligaments. Viscoelastic constants were then determined for the disk.

Starting with a brief explanation of classical viscoelastic theory, the following chapters describe some fundamental concepts necessary for an understanding of this thesis. A detailed discussion of each phase of analysis follows.

II. Theory

2.1 Linear Viscoelasticity

The theory of viscoelasticity accounts for accumulating strains in some materials when subjected to a constant load over a period of time. It also accounts for the relaxation of stresses experienced by those same materials when subjected to a constant strain over a period of time.

From a one-dimensional viewpoint, Hooke's Law relates the stress and elastic strain experienced by a material having a Young's Modulus, E . Such a response may be modelled by a linear spring having a "stiffness" of E (Fig. 2.1-A). Any strain produced by the application of stress would occur instantaneously. The value of that strain would not change unless the value of the stress changed.

Such is not the case in materials which exhibit viscoelastic or creep behavior: strain may change, even at constant stress values. The behavior of viscoelastic materials may be modelled by various combinations of the linear spring and dashpot, which represents the time-dependent material response. The simplest such model is the Maxwell Fluid (Fig. 2.1-B) wherein the rheological elements are connected in series. The total strain ϵ is the sum of the elastic ϵ_E and creep ϵ_C strains:

$$\epsilon = \epsilon_E + \epsilon_C \quad (2-1)$$

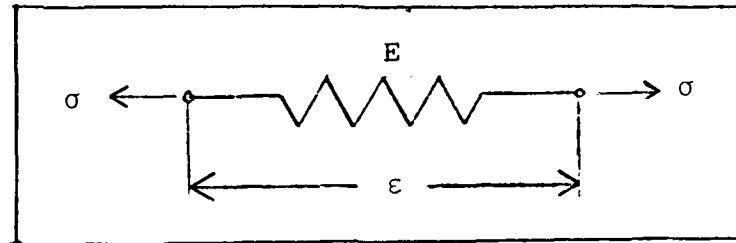


Fig. 2.1-A. Elastic Model

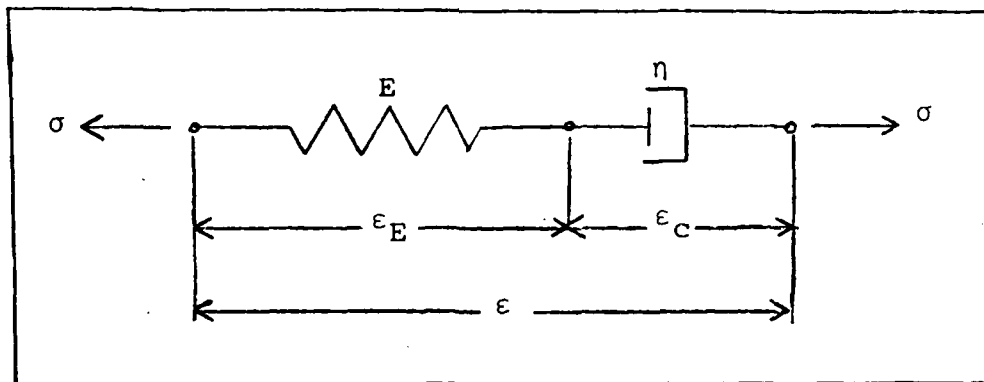


Fig. 2.1-B. Maxwell Fluid Model

The application of stress would cause an instantaneous elastic strain ϵ_E of the spring followed in time by an accumulation of creep strain ϵ_C , which is related to stress by

$$\sigma = \eta \dot{\epsilon}_C \quad (2-2)$$

where η is the dashpot or fluidity constant. In theory, this creep strain would be infinite; hence, this model represents a "fluid" quite nicely.

A more realistic model for a solid material is represented by the Kelvin Solid (Fig. 2.1-C), in which the two elements are connected in parallel. In this model

$$\epsilon = \epsilon_E = \epsilon_C \quad (2-3)$$

so that

$$\sigma = \sigma_S + \sigma_D \quad (2-4)$$

or

$$\sigma = E\epsilon + \eta \dot{\epsilon} \quad (2-5)$$

The application of stress would cause strain only after a period of time, as the dashpot gradually permits strain to occur; such strain would proceed until the stiffness of the parallel spring will no longer permit further deformation. Obviously, even this model is somewhat unrealistic in that it does not permit any elastic (instantaneous) strain.

In order to permit both elastic and viscoelastic deformation, the Three-Parameter Kelvin Solid (Fig. 2.1-D) is used. It will be incorporated into this thesis. In this

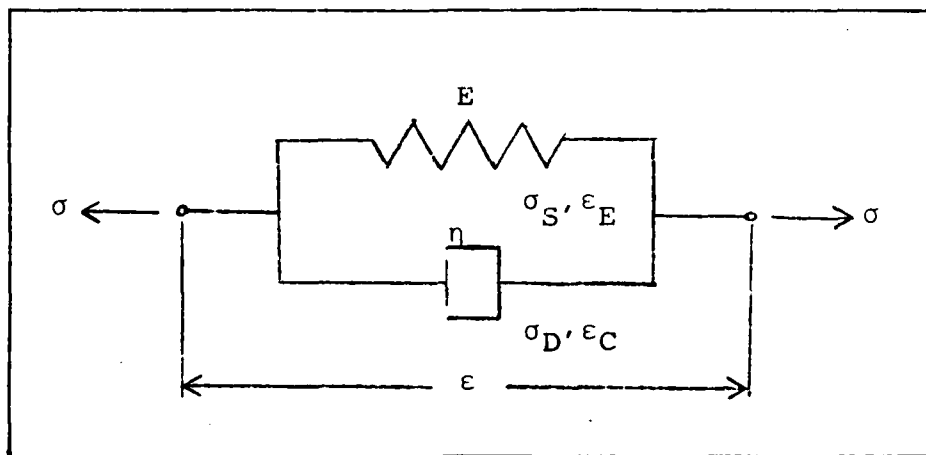


Fig. 2.1-C. Kelvin Solid Model

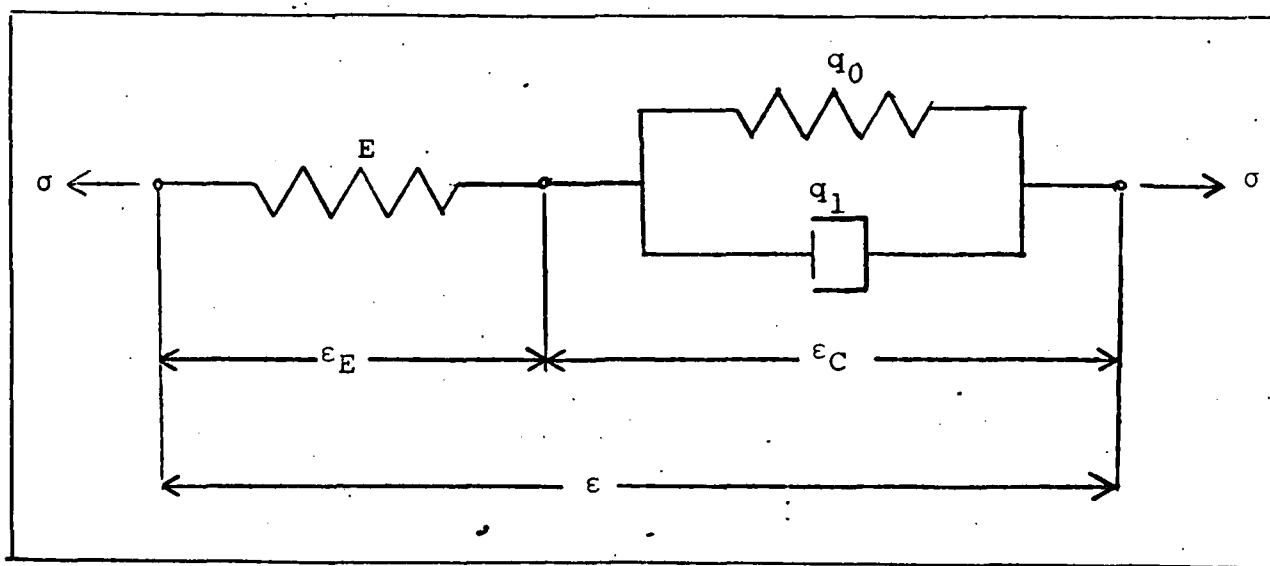


Fig. 2.1-D. Three-Parameter Kelvin Solid Model

model

$$\epsilon = \epsilon_E + \epsilon_C \quad (2-5a)$$

so that

$$\sigma = E\epsilon_E = q_0\epsilon_C + q_1\dot{\epsilon}_C \quad (2-6)$$

Instantaneous elastic deformation is performed by the series spring of stiffness E . Creep strain rate $\dot{\epsilon}_C$ is limited by the dashpot having a constant q_1 . Ultimate strain is limited by the parallel spring of stiffness q_0 . Figure 2.1-E shows a typical creep curve for such a model. Rearranging Eq (2-6) results in

$$d\epsilon_C = \frac{dt}{q_1} (\sigma - q_0\epsilon_C) \quad (2-7)$$

which shows that incremental creep strain $d\epsilon_C$ depends on total accumulated creep strain ϵ_C for any incremental time step dt . Rearranging Eq (2-7) again results in

$$\frac{d\epsilon_C}{dt} = \frac{\sigma}{q_1} - \frac{q_0}{q_1} \epsilon_C \quad (2-8)$$

which indicates that q_1 is the fluidity constant for the dashpot. This parameter is also the slope of the σ versus $\dot{\epsilon}$ curve, as seen in Fig. 2.1-F.

Application of such a model to a multidimensional state of stress is limited by its inability to accurately describe the complex constitutive relation between stresses and

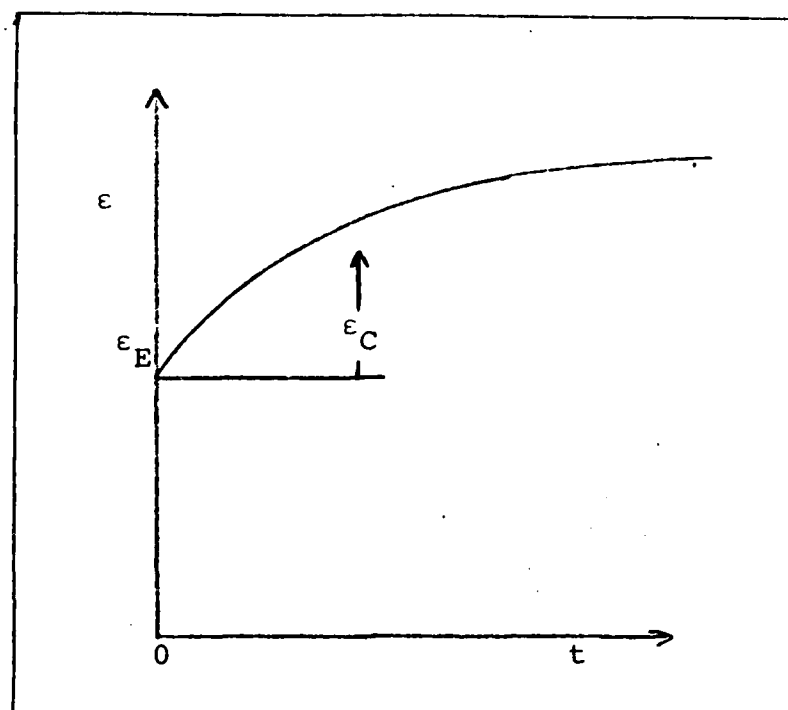


Fig. 2.1-E. Typical Creep Curve

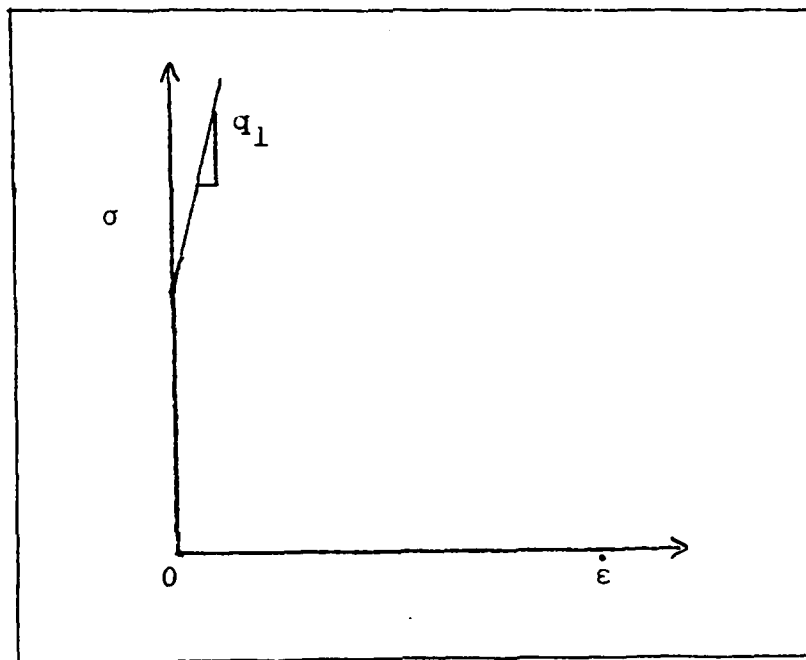


Fig. 2.1-F. Significance of the q_1 Material Parameter

strains. However, finite element techniques, discussed next, will allow development of a relationship similar to Eq (2-7).

2.2 Finite Element Method

2.2.1 General Concepts. The complexity of many problems in mechanics will not permit exact closed-form solutions. In such cases, techniques have been used to obtain exact force-displacement solutions at a finite number of points and approximate solutions at other points in the body. The Finite Element Method is one such technique.

This method presumes that the body of interest can be subdivided into elements within which actual displacement functions may be approximated by simple polynomials. Figure 2.2-A shows one such element. Other one-, two-, and three dimensional elements have also been used successfully. Each element has a set of node points and each node is permitted certain rotational and/or translational degrees of freedom. In the case of the triangular element shown, each node has two orthogonal translational degrees of freedom.

Element displacements may be written as a polynomial function of these nodal degrees of freedom. The choice of displacement function within each element must satisfy three requirements. First, displacements must be continuous between elements. Second, any rigid body motion of the element must not produce strain within the element. Finally, as the size of the element is reduced to zero, the strain within it

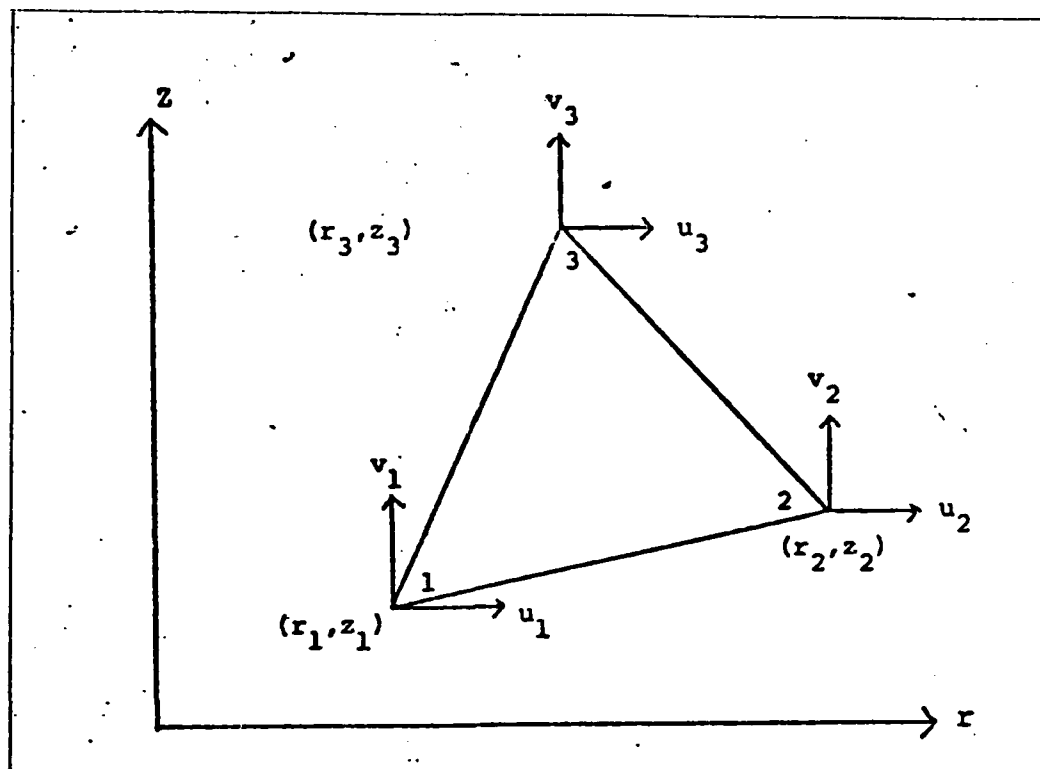


Fig. 2.2-A (Ref 2). Triangular Element

must approach a constant value.

Element displacements are characterized by the total set of nodal degrees of freedom $\{u\}$. In the case of the element shown

$$\{u\} = \{u_1 \ v_1 \ u_2 \ v_2 \ u_3 \ v_3\}^T \quad (2-9)$$

In this element, the displacement polynomials are written as

$$u = a_1 + a_2 r + a_3 z \quad (2-10a)$$

$$v = a_4 + a_5 r + a_6 z \quad (2-10b)$$

where the a_i are constants to be determined.

For the element shown, the nodal displacements thus become

$$\begin{Bmatrix} u_1 \\ u_2 \\ u_3 \end{Bmatrix} = \begin{bmatrix} 1 & r_1 & z_1 \\ 1 & r_2 & z_2 \\ 1 & r_3 & z_3 \end{bmatrix} \begin{Bmatrix} a_1 \\ a_2 \\ a_3 \end{Bmatrix} \quad (2-11a)$$

and

$$\begin{Bmatrix} v_1 \\ v_2 \\ v_3 \end{Bmatrix} = \begin{bmatrix} 1 & r_1 & z_1 \\ 1 & r_2 & z_2 \\ 1 & r_3 & z_3 \end{bmatrix} \begin{Bmatrix} a_4 \\ a_5 \\ a_6 \end{Bmatrix} \quad (2-11b)$$

Solving Eq 2-3a and Eq 2-3b for the constants a_i and substituting them into Eq 2-2a and Eq 2-2b, respectively, yields an expression for internal displacements in terms of nodal displacements:

$$u = N_1 u_1 + N_2 u_2 + N_3 u_3 \quad (2-12a)$$

$$v = N_1 v_1 + N_2 v_2 + N_3 v_3 \quad (2-12b)$$

where

$$N_i = \frac{1}{2A} (a_i + b_i r + c_i z) \quad (2-13)$$

$$a_i = r_j z_m - r_m z_j \quad (2-14)$$

$$b_i = z_j - z_m \quad (2-15)$$

$$c_i = r_m - r_j \quad (2-16)$$

and the area of the triangle is

$$A = \frac{1}{2} \det \begin{bmatrix} 1 & r_1 & z_1 \\ 1 & r_2 & z_2 \\ 1 & r_3 & z_3 \end{bmatrix} \quad (2-17)$$

The indices i , j , and m are permuted cyclically in the order given and are assigned integer values from 1 to 3. The problem therefore is to compute a vector of nodal displacements after which interval displacements may be computed.

2.2.2 Analysis. Problems of a three-dimensional nature in elasticity can be simplified by expressing the stress tensor as the sum of a hydrostatic (volumetric) and a deviatoric stress tensor, respectively:

$$\begin{bmatrix} \sigma_x & \sigma_{xy} & \sigma_{xz} \\ \sigma_{yx} & \sigma_y & \sigma_{yz} \\ \sigma_{zx} & \sigma_{zy} & \sigma_z \end{bmatrix} = \begin{bmatrix} s & 0 & 0 \\ 0 & s & 0 \\ 0 & 0 & s \end{bmatrix} + \begin{bmatrix} \sigma'_x & \sigma_{xy} & \sigma_{xz} \\ \sigma_{yx} & \sigma'_y & \sigma_{yz} \\ \sigma_{zx} & \sigma_{zy} & \sigma'_z \end{bmatrix} \quad (2-18)$$

In this relationship, s is the hydrostatic stress given by

$$s = (\sigma_x + \sigma_y + \sigma_z)/3 \quad (2-19)$$

and

$$\begin{aligned} \sigma_x &= s + \sigma'_x \\ \sigma_y &= s + \sigma'_y \\ \sigma_z &= s + \sigma'_z \end{aligned} \quad (2-20)$$

Hydrostatic and deviatoric strain tensors are related to the total strain tensor in the same manner.

The viscoelastic analysis used in this thesis (Ref 6) will assume that the total strain at any time can be expressed as the sum of hydrostatic elastic strain and deviatoric elastic/viscoelastic strain. The total solution will thus be obtained by superimposing an elastic and a viscoelastic solution.

The elastic solution is obtained by solving

$$[K]\{u\} = \{P\} + \{Q\} \quad (2-21)$$

for $\{u\}$, the nodal degrees of freedom, where $[K]$ is the elastic stiffness matrix, $\{P\}$ is the vector of applied nodal forces, and $\{Q\}$ is the vector of nodal residual forces due to initial strains. Appendix A describes the derivation of $[K]$ and $\{P\}$ for an axisymmetric problem.

For the elastic/viscoelastic solution, the constitutive relationship for the Three-Parameter Kelvin Solid is integrated over time (Ref 13) to give

$$\{\Delta \epsilon_c\} = \frac{\Delta t}{q_1} \left[\frac{2}{3} [A] \{\sigma\} - q_0 \{\epsilon_c\} \right] \quad (2-22)$$

where $\{\Delta \epsilon_c\}$ is a vector of creep strains accumulated over a small time increment Δt , $\{\epsilon_c\}$ is the vector of total creep strains, and $[A]$ is given by

$$[A] = \begin{bmatrix} 1 & -v_c & -v_c & 0 \\ & 1 & -v_c & 0 \\ & & 1 & 0 \\ \text{Sym} & & & 2(1+v_c) \end{bmatrix} \quad (2-23)$$

Since the creep strain is assumed incompressible, v_c , the Poisson's Ratio for the creep strain is 0.5.

Figure 2.2-B illustrates the flow chart used in the elastic/viscoelastic analysis. The quantity $\{\Delta \epsilon_c\}$ may be considered an incremental initial strain $\{\epsilon_0\}$. Since the initial strains enter into the governing equation (2-21) in the residual force term $\{Q\}$, Eq (2-21) must be solved at each timestep for $\{u\}$. Strains $\{c\}$ may then be obtained from nodal displacements $\{u\}$ by

$$\{\epsilon\} = [B] \{u\} \quad (2-24)$$

where

$$[B] = \frac{1}{2A} \begin{bmatrix} 0 & c_i & 0 & c_j & 0 & c_k \\ b_i & 0 & b_j & 0 & b_k & 0 \\ d_i & 0 & d_j & 0 & d_k & 0 \\ c_i & b_i & c_j & b_j & c_k & b_k \end{bmatrix} \quad (2-25)$$

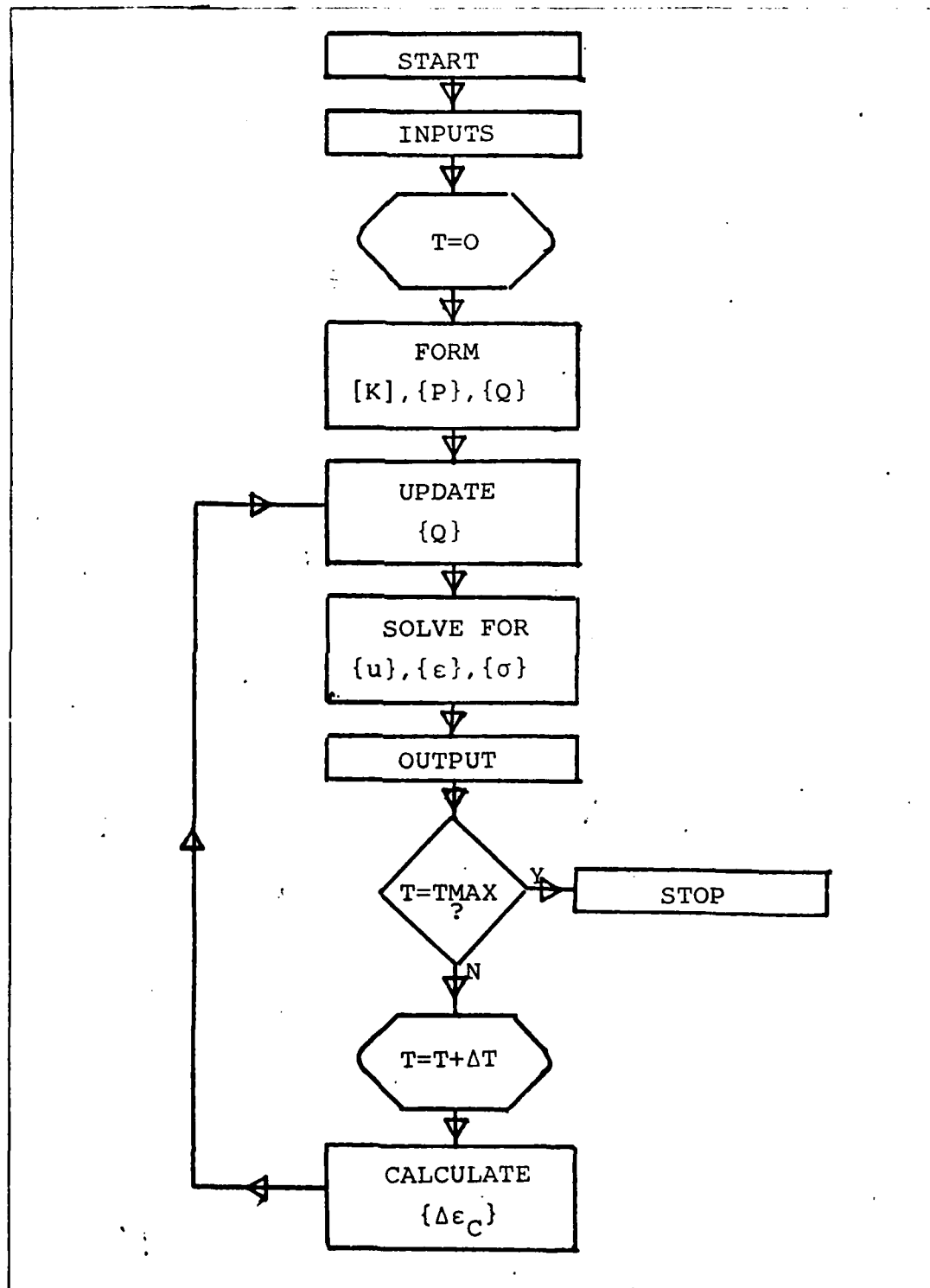


Fig. 2.2-B (Ref 13). Flow Chart of Solution Technique

and

$$d_i = \frac{a_i}{r} + b_i + c_i \frac{z}{r} \quad (2-26)$$

As before, i , j , and k are permuted cyclically over the integers 1 to 3, inclusive.

Stresses $\{\sigma\}$ are related to the strains $\{\epsilon\}$ by the usual constitutive relationship

$$\{\sigma\} = [D] [\{\epsilon\} - \{\epsilon_c\}] \quad (2-27)$$

where $[D]$ is the elastic material property matrix for an axisymmetric body given by

$$[D] = \frac{E(1-\nu)}{(1+\nu)(1-2\nu)} \begin{bmatrix} 1 & \frac{\nu}{1-\nu} & \frac{\nu}{1-\nu} & 0 \\ & 1 & \frac{\nu}{1-\nu} & 0 \\ & & 1 & 0 \\ \text{Sym} & & & \frac{1-2\nu}{2(1-\nu)} \end{bmatrix} \quad (2-28)$$

Finally, since

$$\{\epsilon\} = \{\epsilon_E\} + \{\epsilon_c\} \quad (2-29)$$

$\{\epsilon_c\}$ follows directly. These values of $\{\sigma\}$ and $\{\epsilon_c\}$ are then substituted into Eq (2-22), time is incremented, and the cycle repeats itself until a maximum time is reached (Ref 13).

III. Centrum Analysis

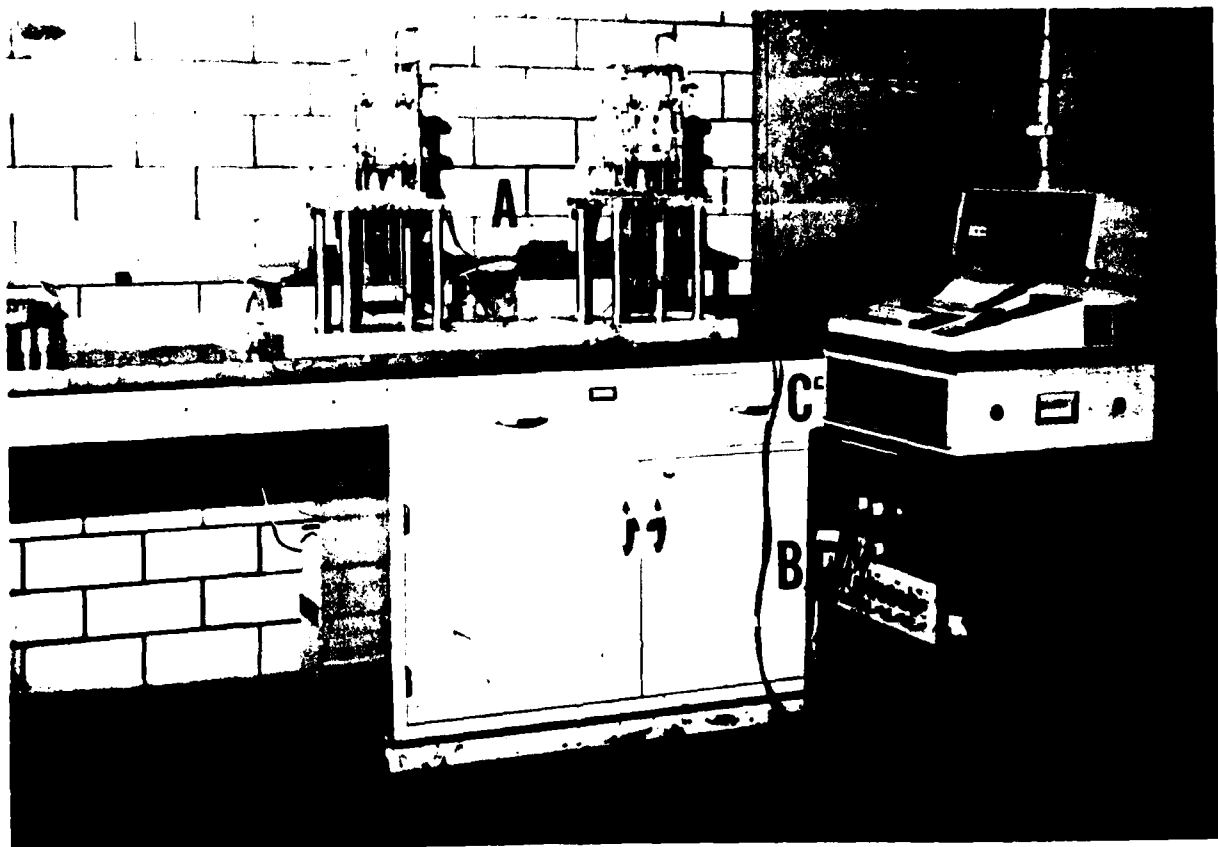
The first phase of this study involved obtaining material constants describing the creep response of the Vertebral Centrum. These viscoelastic characteristics were assumed to be attributable exclusively to the Trabecular region.

During this phase, axial compression tests were performed on Vertebral Centra from the L1-L2 level of the spine of the Rhesus Monkey (*Macaca Mulatta*). Six specimens (three L1-L2 pairs) were loaded with 15 pounds (67 Newtons) and six were loaded with 30 pounds (133 Newtons). The duration of loading in both cases was 8 hours. A 16-hour relaxation period followed.

3.1 Experimentation

3.1.1 Equipment. Figure 3.1-A shows the experimental apparatus. Figure 3.1-B shows a related block diagram. Each test chamber was connected to a humidifier. Data from each test chamber was passed first to one of a set of four Dana DC amplifiers, then to an Analog-to-Digital Converter unit, and finally to a Texas Instruments Silent 700 ASR Electronic Data Terminal.

Each test chamber (Fig. 3.1-C), incorporated a DC-DC Linear Variable Displacement Transducer (LVDT), and each test cell was partially enclosed during testing. The front of the unit is shown open for viewing in this figure. To



- A - Test Chambers and Humidifiers
- B - Dana DC Amplifiers
- C - Analog-to-Digital Converter Unit
- D - Texas Instruments Silent 700 ASR Electronic Data Terminal

Fig. 3.1-A. Experimental Apparatus

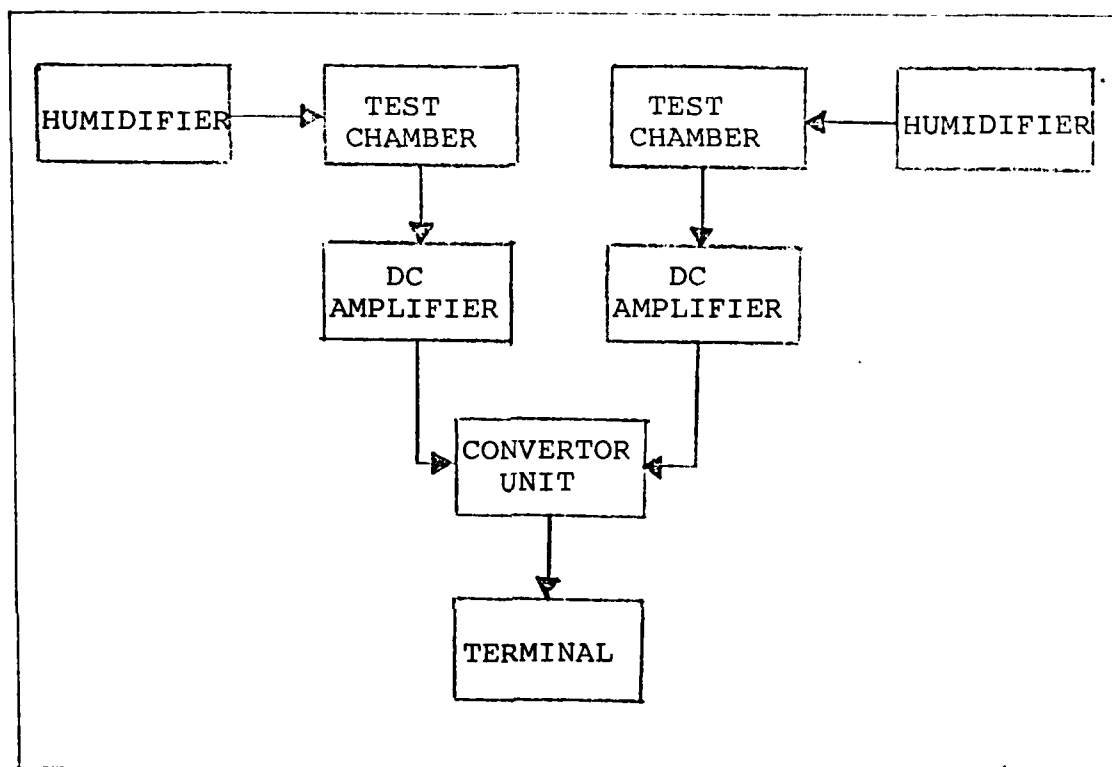
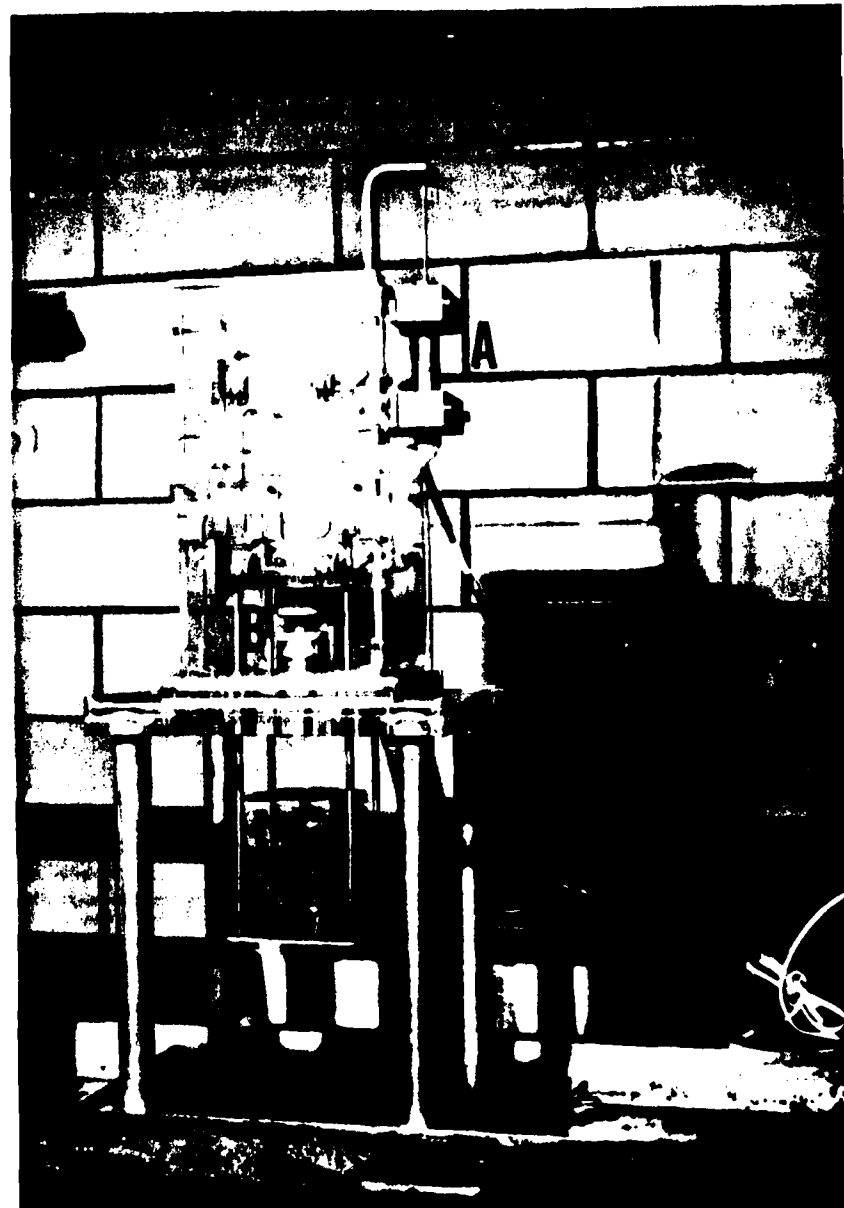


Fig. 3.1-B. Block Diagram of
Experimental Apparatus



- (A) Linear Variable Displacement Transducer (LVDT)
- (B) Test Specimen
- (C) Test Chamber

Figure 1. Test Chamber

preserve the specimens during testing, 100% humid air was provided by the commercial cool-mist humidifier.

Voltage from the LVDT was amplified at a gain of 500 by an amplifier. Sampling interval was adjustable and amplified signals were digitized, that is, converted to raw displacement, by the convertor unit. Raw displacements were then displayed and recorded on cassette tape by the data terminal. Four data streams were available and selectable at the convertor unit. Only two data streams were used, however. In this manner, two tests could be run simultaneously.

3.1.2 Procedure. Spines from adolescent Rhesus Monkeys (*Macaca Mulatta*) were radiographed to determine unacceptable abnormalities. An L1-L2 unit was excised from a selected spine using a scalpel by cutting through the end disks and by disarticulating the facet joints. Each unit was then separated into an L1 and an L2 segment by cutting through the center disk midplane using the scalpel. All soft tissue and musculature were removed as well as the cartilagenous endplate. Processes were removed by cutting through the pedicles flush with the centrum using a low-speed diamond saw. The prepared specimen was then frozen in a normal saline solution to preserve it for testing.

Prior to testing, the specimen was thawed and then the superior and inferior surfaces were photographed at a magnification power of two. These photographs were used to determine the surface areas, as will be discussed in the following

section. Then, the end surfaces of the specimen was potted in dental acrylic using a special mounting device. The purpose of the acrylic was to provide a smooth, flat surface upon which the load could be evenly distributed. Figure 3.1-D shows a specimen just after being placed in one end of the device. Figure 3.1-E shows the final configuration with the specimen in the center. The potted specimen was removed once the acrylic hardened.

Before testing could begin, the LVDT was zeroed and the chamber displacement calibrated. Two cylinders were used for this task (Fig. 3.1-F); one cylinder was $1/8$ inch longer than the other. With the longer cylinder in place in the test cell, the LVDT attachment bolts were loosened and the LVDT moved vertically until zero was displayed on a selected data stream at the terminal. The bolts were then retightened.

Once zeroing was completed, the longer cylinder was then removed and the shorter cylinder placed in the cell. The new output was recorded after which that cylinder was replaced by the first cylinder and a third reading taken. In this manner, outputs were compared to determine a value representing a displacement of $1/8$ inch as follows. The readings from the longer cylinder (the one measured twice) were averaged and the result subtracted from the reading using the shorter cylinder (the one measured only once). This measured difference thus represented $1/8$ (0.1250) inch. All test data was first adjusted for zero and then multiplied by a factor based on this difference:

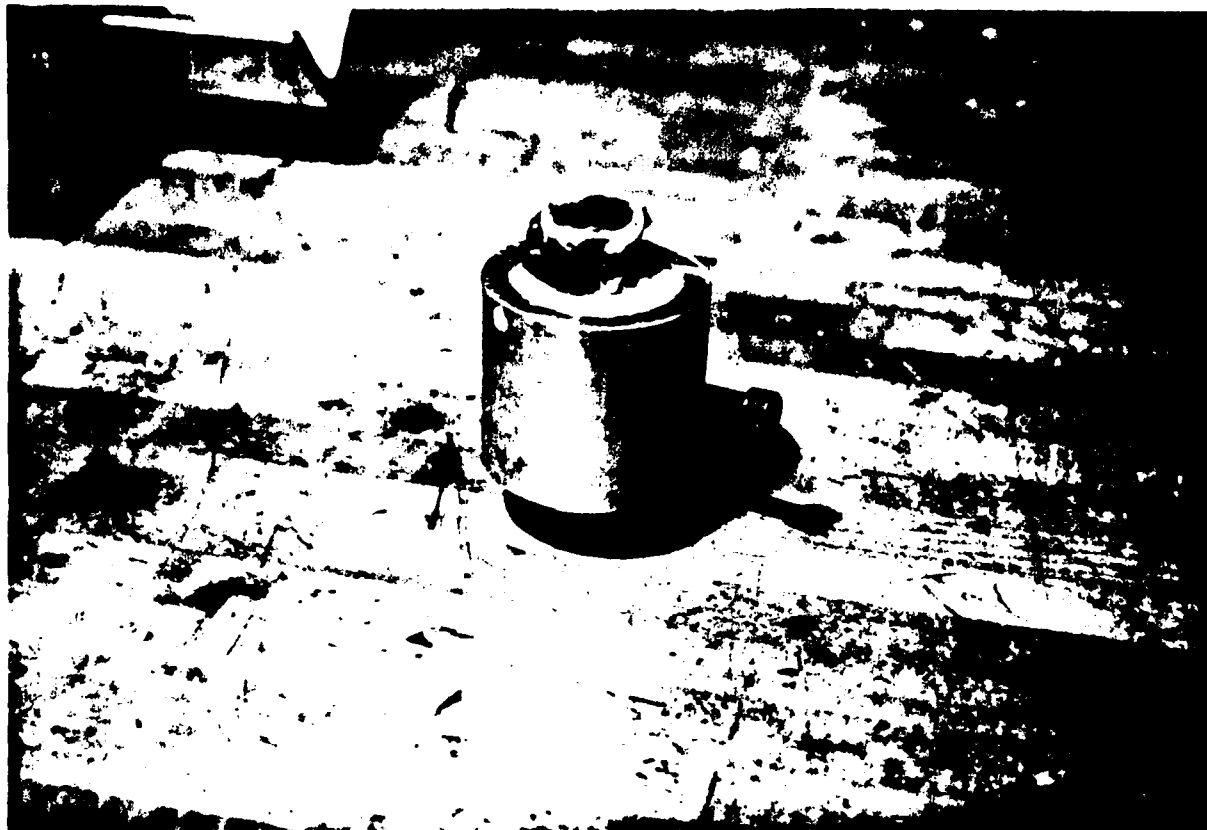
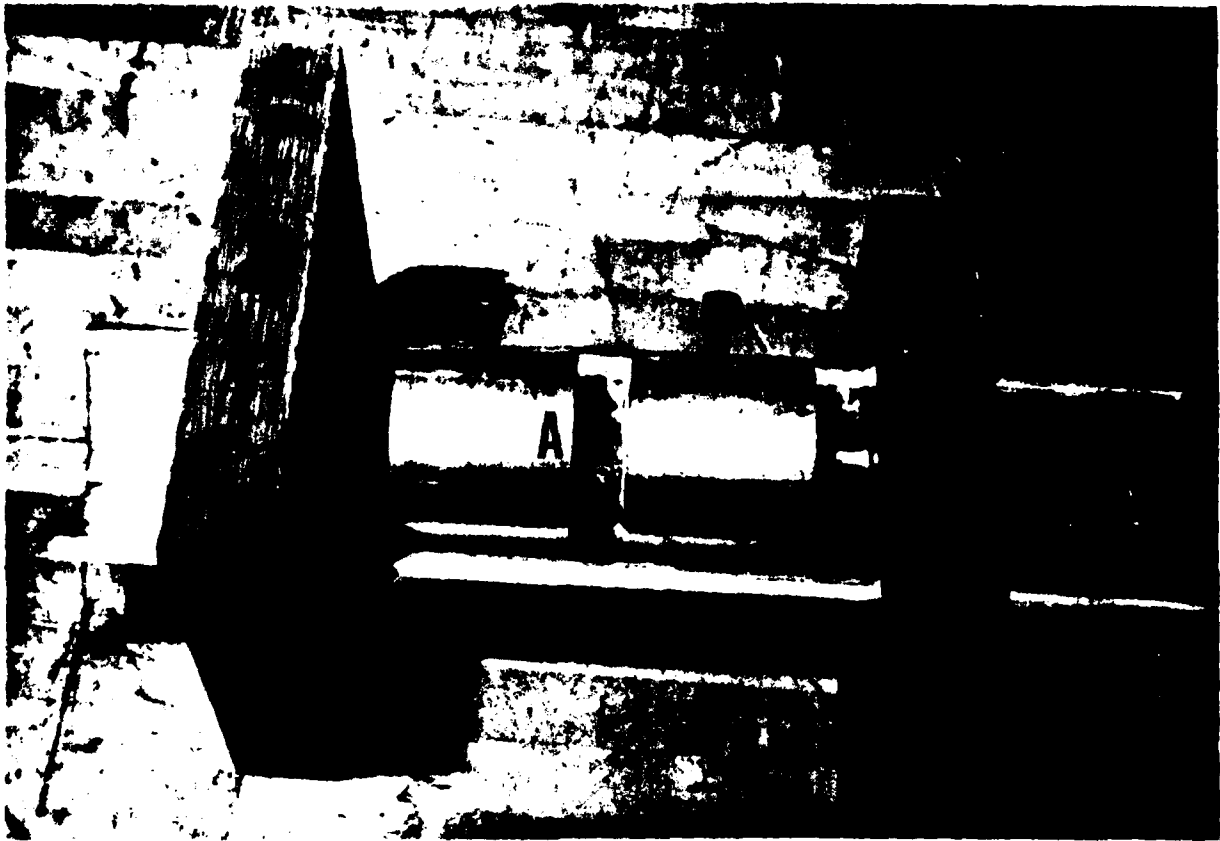


Fig. 3.1-D. Dental Acrylic Mounting Device,
Initial Configuration



A - Test Specimen

Fig. 3.1-E. Dental Acrylic Mounting Device,
Final Configuration

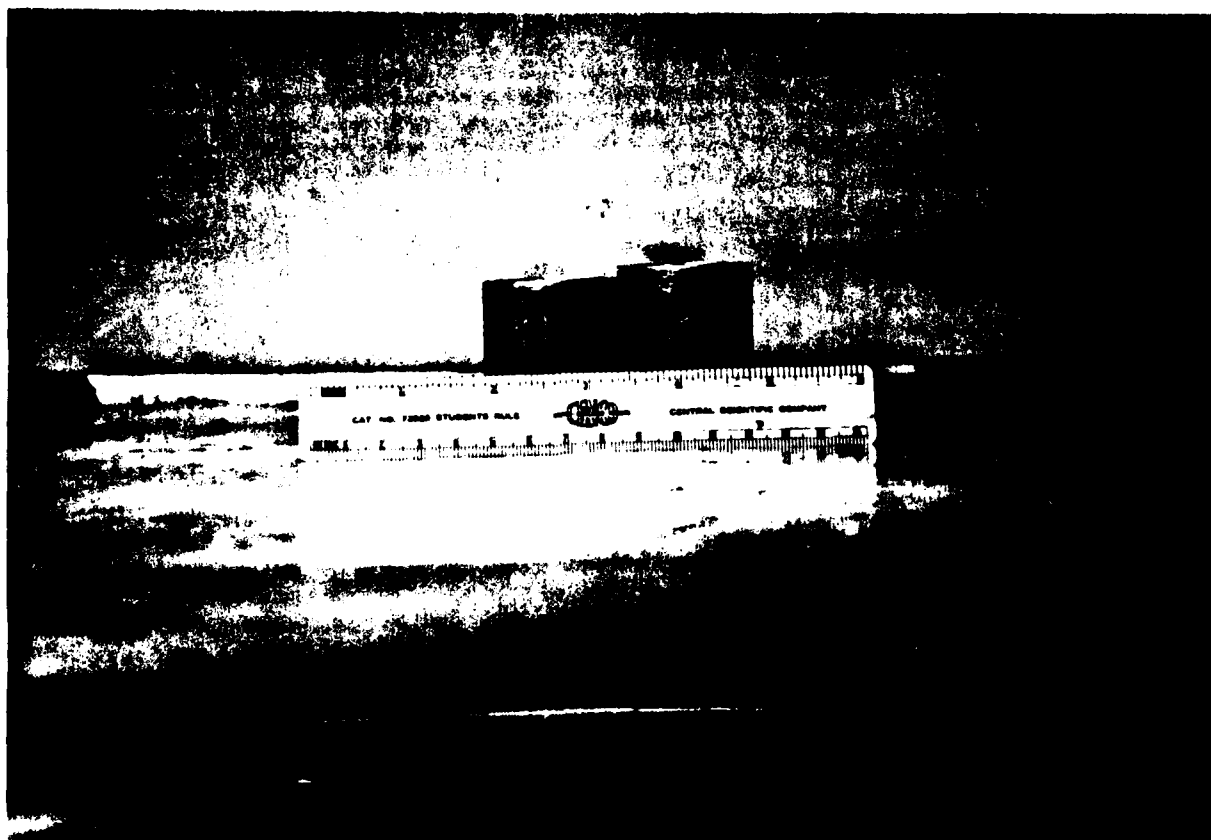


Fig. 3.1-F. Calibration Cylinders

$$\text{Calibration Factor} = \frac{0.1250}{|\text{Measured Difference}| 10^{-4}} \quad (3-1)$$

The factor 10^{-4} was required in Eq (3-1) to convert this measured difference to an actual displacement. The absolute value is required to convert negative differences to absolute differences. Appendix C presents an example of this calibration procedure.

Once calibration was completed, the specimen was mounted in the loading chamber (Fig. 3.1-G) and the test commenced. The recorder on the terminal was started, and the load was added. Sampling times were approximately once every second for the first ten minutes, once every ten seconds for the following ten minutes, and then once every minute for the remainder of the test.

After eight hours, the load was removed and the above sampling sequence repeated. After another sixteen hours, the test was concluded and the specimen removed. Recorded data was then passed to the computer and a displacement-time plot generated for the test using an existing plotting program.

Vernier Calipers were used to measure the specimen laterally and longitudinally, after which the specimen was cut sagittally (front to rear) using a low-speed saw and a 1 mm slice removed. This slice was mounted in a dissecting microscope. The Cortex and Bony end-plate were then measured

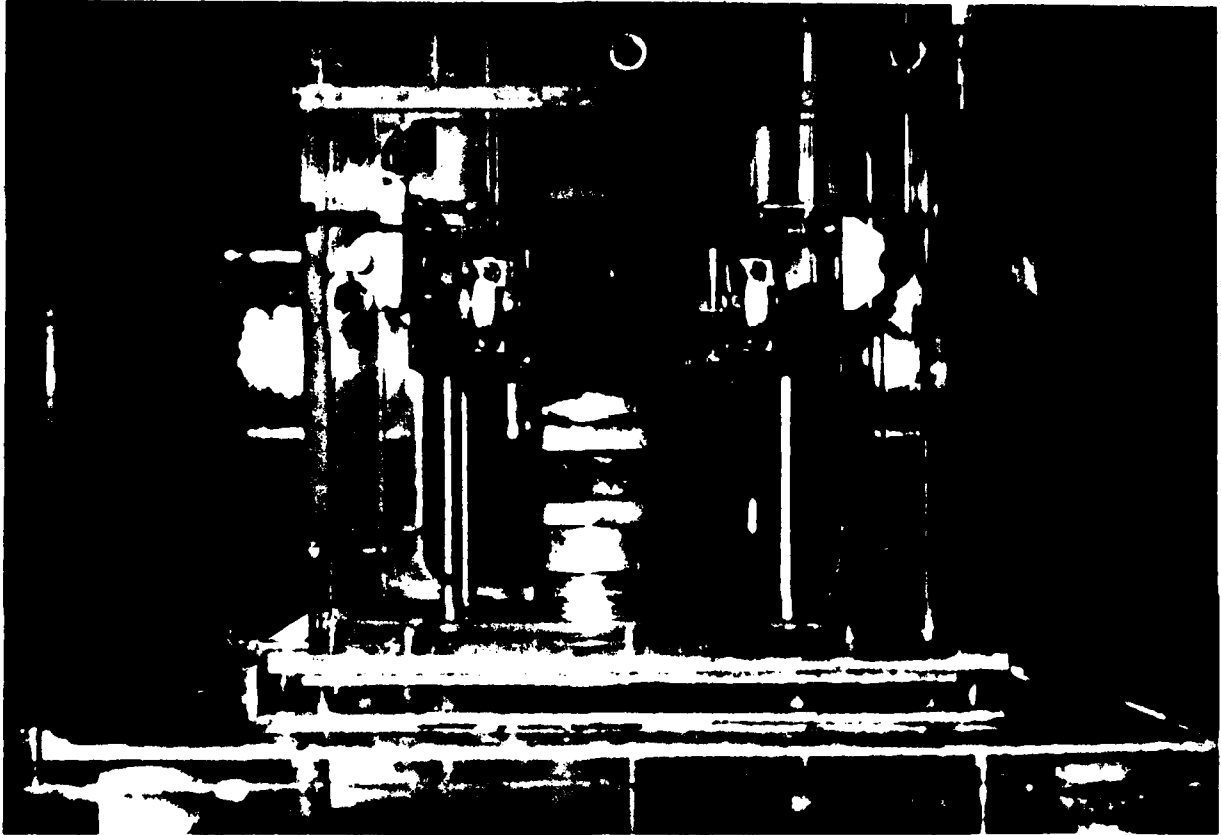


Fig. 3.1-G. Configuration of Specimen
for Testing

using a transparent graduated reticle.

3.1.3 Results. Appendix B contains the experimental results for each test. Displacement-time curves varied from test to test, especially between vertebrae from different animals. These variations were due to differences in size, condition, and preparation of the specimens.

Discrete time values were selected from the first 10,000 seconds of the loading period and formed a basis for two average experimental data sets, one for each load (15 and 30 pounds). Only the first 10,000 seconds were chosen in order to preserve computational resources during the analytical phase when these displacement-time values were matched. For each test, displacements were extracted corresponding to these times. Then, for all tests having a given load, either 15 or 30 pounds, these values were averaged at each time to produce a set of average experimental displacement-time values. Two such sets were thus produced, one for the 15 pound load and one for the 30 pound load. Finally, each average experimental displacement was divided by two. This was done in order that these displacement sets could be compared to the respective analytically-generated sets of the finite element mesh used, which assumed midplane symmetry and hence only displaced half of what the full-size centrum would displace.

Figure 3.1-H illustrates these displacements for the 15 pound load case and Fig. 3.1-I shows the set for the 30 pound case. The function

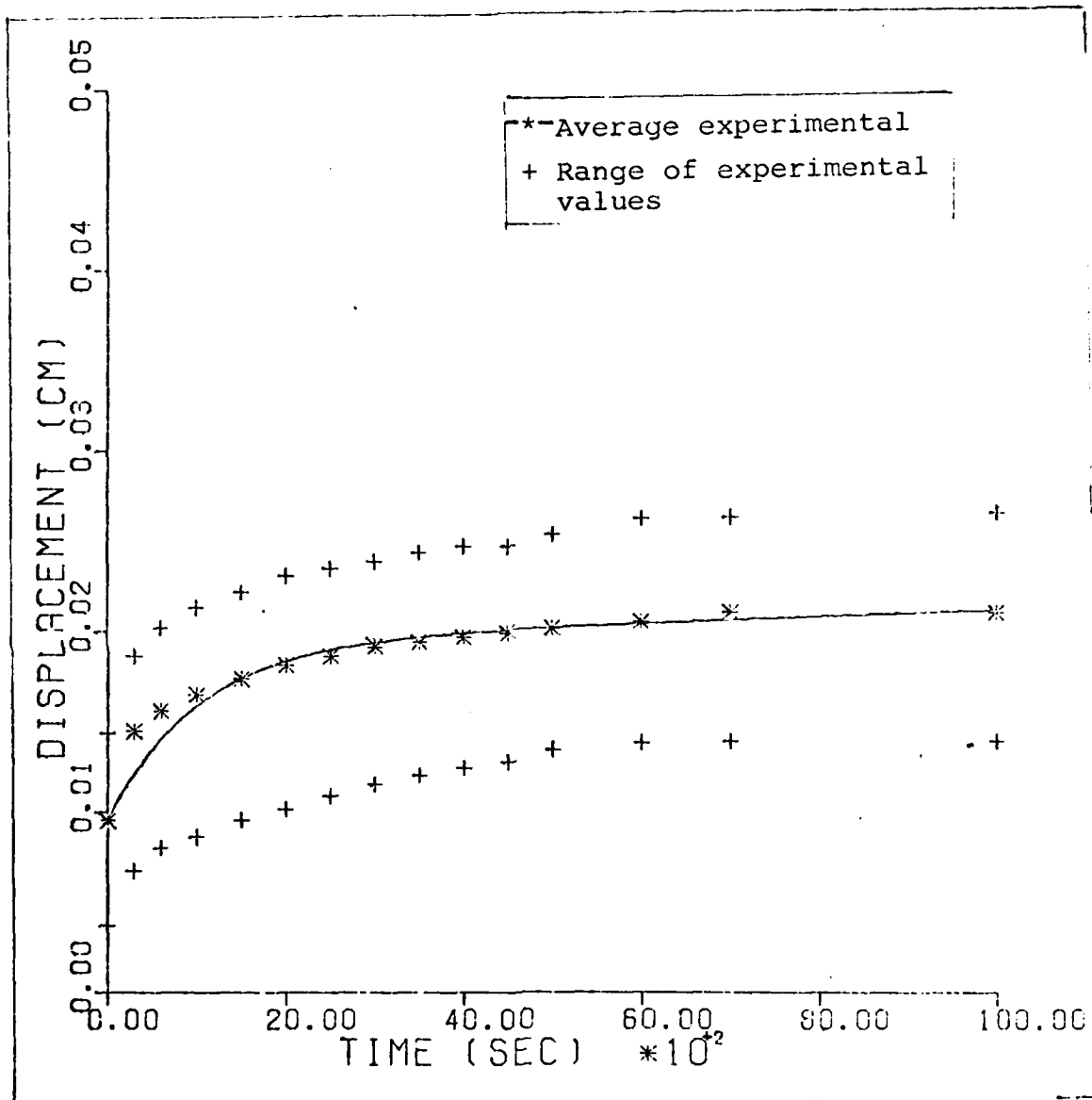


Fig. 3.1-H. Average Experimental Displacements
Relative to Midplane, 15 Pound Load

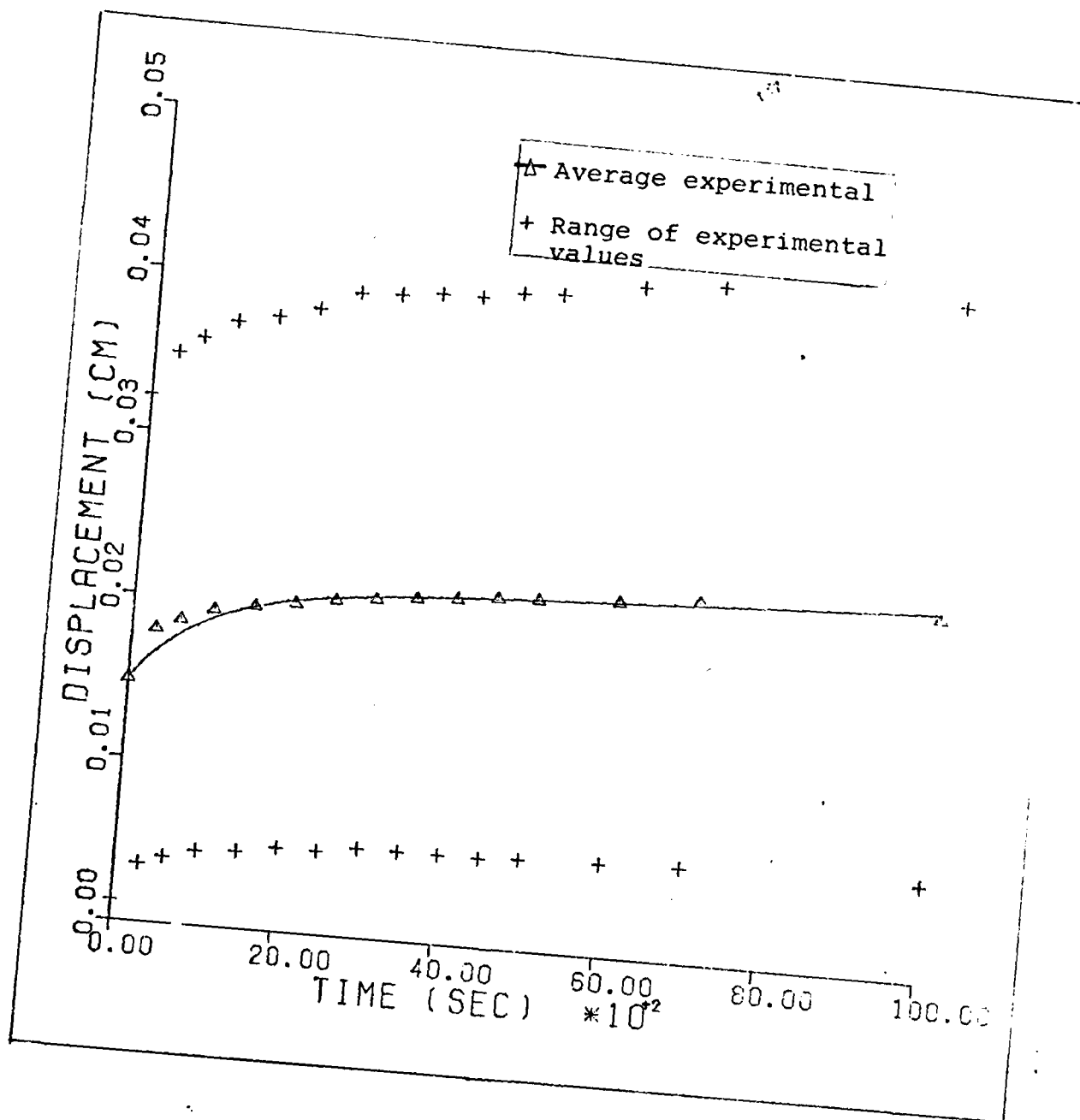


Fig. 3.1-I. Average Experimental Displacements
Relative to Midplane, 30 Pound Load

$$u(t) = C_1 + C_2 t - C_3 e^{-\lambda t} \quad (3-2)$$

where u represents axial displacement in Cm and t represents time in seconds, was determined to provide the best equation representing a curve through these points. The constants C_1 , C_2 , C_3 , and λ for each load case are listed in Table 3-1.

TABLE 3-1
Constants of Curve-fit Equation
Representing Model Displacements

Constant	Load (lb)	
	15	30
C_1	1.935×10^{-2}	2.040×10^{-2}
C_2	1.900×10^{-7}	2.140×10^{-7}
C_3	9.800×10^{-3}	5.600×10^{-3}
λ	9.854×10^{-4}	1.115×10^{-3}

Figures 3.1-H and 3.1-I show that most of the creep occurred in the first 2000 seconds of the loading period for both loads. The initial slope of the creep curve for the 15 pound load case was higher than in the 30 pound load case, indicating a higher initial creep rate. However, as time progressed past about 4000 seconds, the slopes were approximately equal. This fact would indicate that the creep rate

depended on load only initially. Also, initial elastic response for the 30 pound case was less than twice that for the 15 pound case, as it would be if the elastic stiffness was independent of load. Apparently, then, the initial elastic response was a non-linear phenomena with load as was the creep response. Finally, the final displacement at 10,000 seconds relative to the initial elastic displacement was higher in the 15 pound load case, also indicating that the stiffness for the creep deformation depended on load.

3.2 Analysis

3.2.1 Development of Model. In developing the finite element mesh, two factors were considered. First, the external shape and dimensions were required to accurately reflect the test specimens. In order to assure that this requirement was met, average dimensions were used. The photographs of the superior and inferior surfaces were used as a basis for establishing an end-surface average radius: these areas were averaged and the radius computed for a circle of equivalent area. The point of maximum waisting (where the centrum was slenderest) occurred at the midplane. The midplane radius was determined such that the ratio of the computed end-surface average radius to this radius equaled the ratio of corresponding average values obtained from the caliper measurements. Finally, measured heights were averaged to obtain a height for the model.

Internal measurements for the Cortical and Bony end-plate were averaged in the respective cases. Each region was modelled with a uniform thickness.

The second consideration was that realistic regional material properties be used. Properties for the Cortical and Bony end-plate were determined using a process developed by Furlong (Ref 8), who formed the proportionality:

$$\frac{E_{\text{Human Centrum}}}{E_{\text{Rhesus Centrum}}} = \frac{E_{\text{Human Cortex}}}{E_{\text{Rhesus Cortex}}} = \frac{E_{\text{Human Trabeculae}}}{E_{\text{Rhesus Trabeculae}}} \quad (3-3)$$

This was done because the modulus of elasticity, E , for the Rhesus Monkey Cortical is not known. The centrum values for the human were obtained from Belytschko, et al (Ref 3) and for the Rhesus Monkey from Kazarian and Graves (Ref 15).

A broad range of values were listed for the Rhesus Monkey modulus of elasticity (Ref 15). Hence, it was determined that two values of the modulus would be used representing a lower and upper bound, and that viscoelastic constants would be determined in both cases. The values determined were 3,400 Kp/Sq cm and 22,000 Kp/Sq cm, respectively, for the Cortex modulus of elasticity. Since the Bony end-plate and Cortex were assumed homogeneous, the Bony end-plate was assigned an identical modulus in each case. Poisson's ratio was 0.25 for both regions.

Figure 3.2-A illustrates the mesh used and its relationship to the actual Intervertebral Joint. Internal regions are also shown.

3.2.2 Solution Technique. An existing finite element program developed by Hinnerichs (Ref 12) was used to determine the material values for this analysis as well as the follow-on analysis of the entire joint. Values of E , q_0 , and q_1 were adjusted between computer runs so that the average end-surface displacement-time response of the finite element model matched the average experimental data.

3.3 Results

As was discussed in the previous section, two values of the modulus of elasticity were used for the Cortex and Bony end-plate. These cases will be referred to as the "flexible" and "stiff" cases, and correspond to the low- and high-modulus values used.

It was experimentally observed that the Trabecular region reacted viscoelastically as a function of load. Thus, for the flexible case, finite element solutions were obtained to match two load levels, 15 and 30 pounds. Since the overall analysis can be observed at a given load, it was assumed sufficient to study the stiff case considering only the 15 pound load.

3.3.1 Flexible Case. Figure 3.3-A shows the solution for the applied 15 pound load, and Fig. 3.3-B shows the solution for the 30 pound load case. Viscoelastic constants

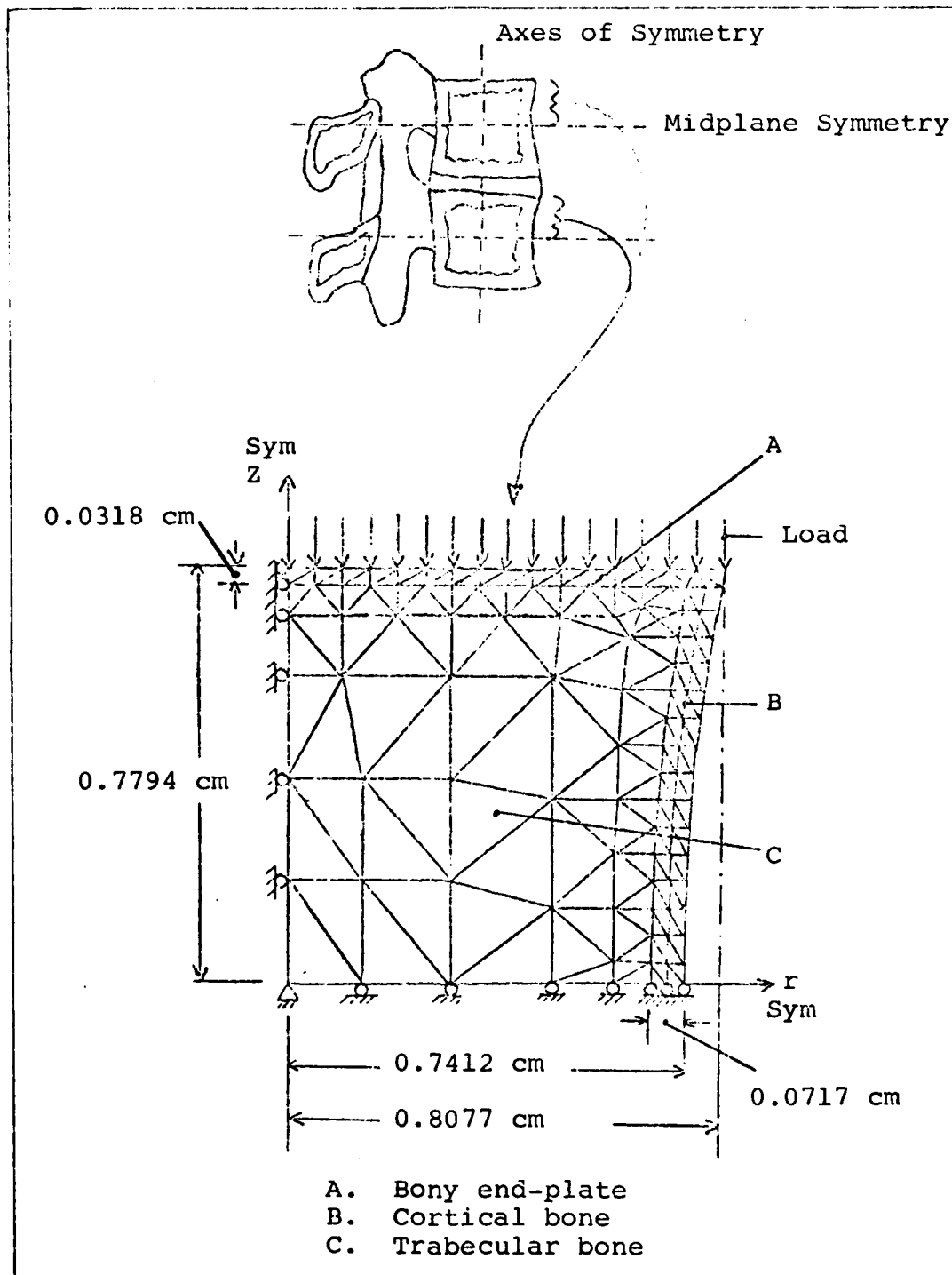


Fig. 3.2-A. Centrum Mesh

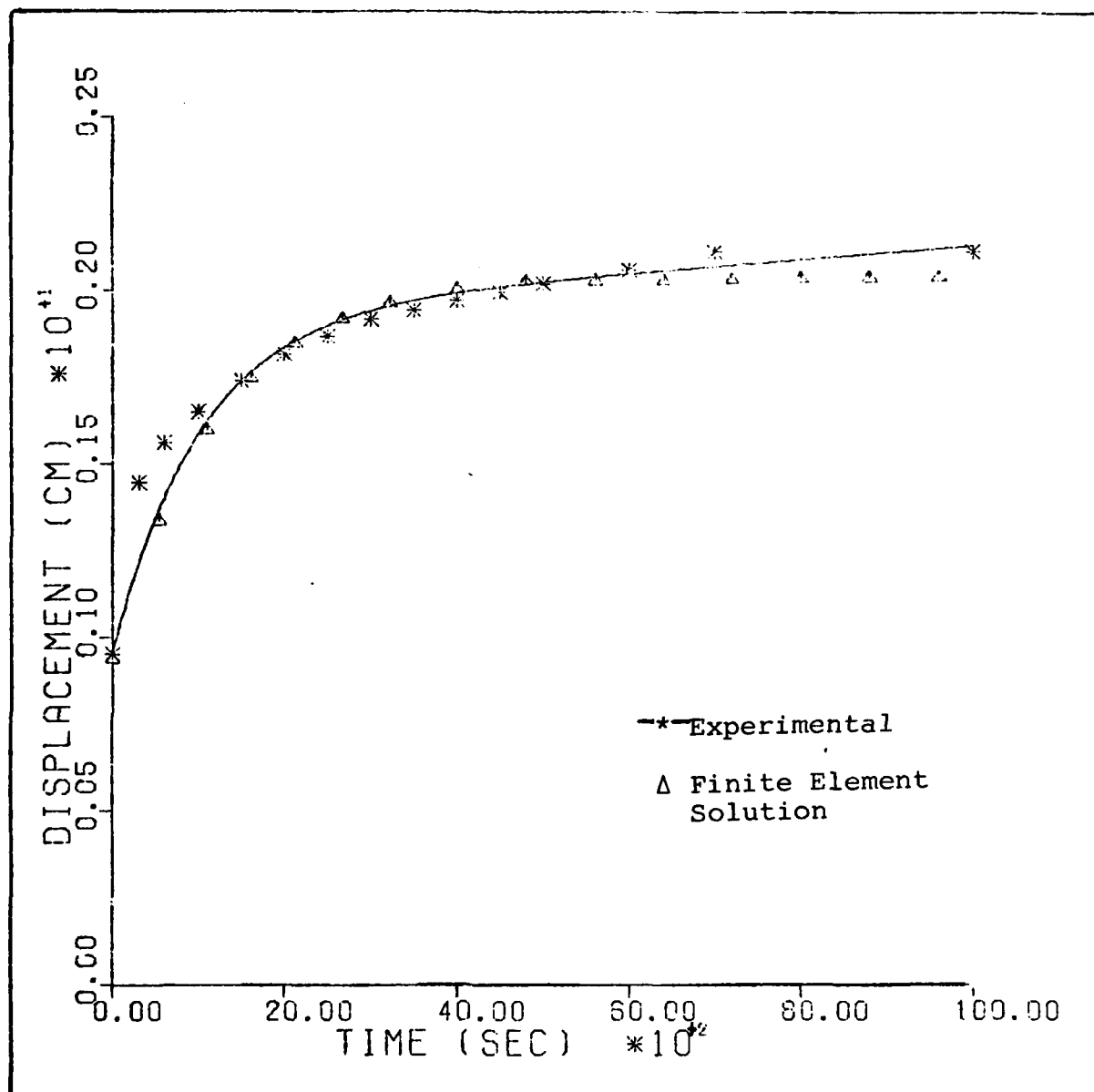


Fig. 3.3-A. Finite Element Solution, 15 Pound Load, Flexible Case

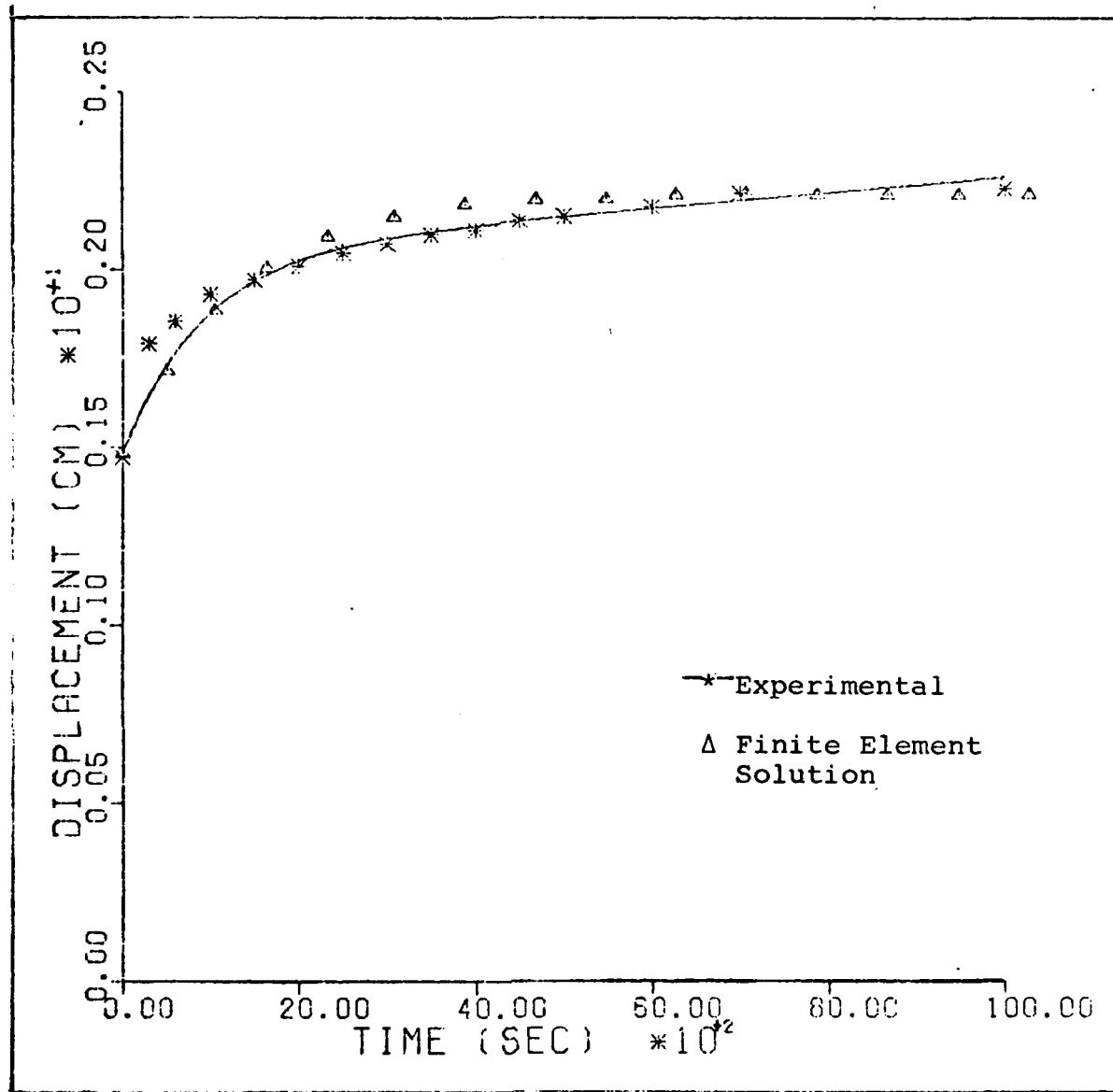


Fig. 3.3-B. Finite Element Solution, 30 Pound Load, Flexible Case

which produced a model-experimental curve agreement for the 5 pound case were $E = 160 \text{ Kp/Sq cm}$, $q_0 = 39 \text{ Kp/Sq cm}$, and $q_1 = 77,400 \text{ Kp/Sq cm-sec}$. The values for the 30 pound case were $E = 218 \text{ Kp/Sq cm}$, $q_0 = 176 \text{ Kp/Sq cm}$, and $q_1 = 281,400 \text{ Kp/Sq cm-sec}$.

Two planes (Fig. 3.3-C) were chosen for analysis purposes in order to study the radial variation of stresses as well as the effects of creep on the manner in which stresses were redistributed radially. These planes were selected for a better appreciation of the effects on stress patterns brought about by the proximity of the Bony end-plate. The two elements were chosen to gain an even greater understanding of these effects, as well as others to be discussed in the following paragraphs. For these elements, stress components were studied as they varied with time. It was determined that a combined analysis of stress in a given plane as well as stress in a given element in that plane would provide the greatest insight into the nature of the stress distribution in the Centrum. Hereafter, the top plane and element in Fig. 3.3-C will be referred to as the "boundary" set; the lower plane and element will be referred to as the "midplane" set.

The original finite element model assumed identical properties for the Bony end-plate and Cortex. However, the former region is known to be stiffer, although precisely how much stiffer is not known. The results using the

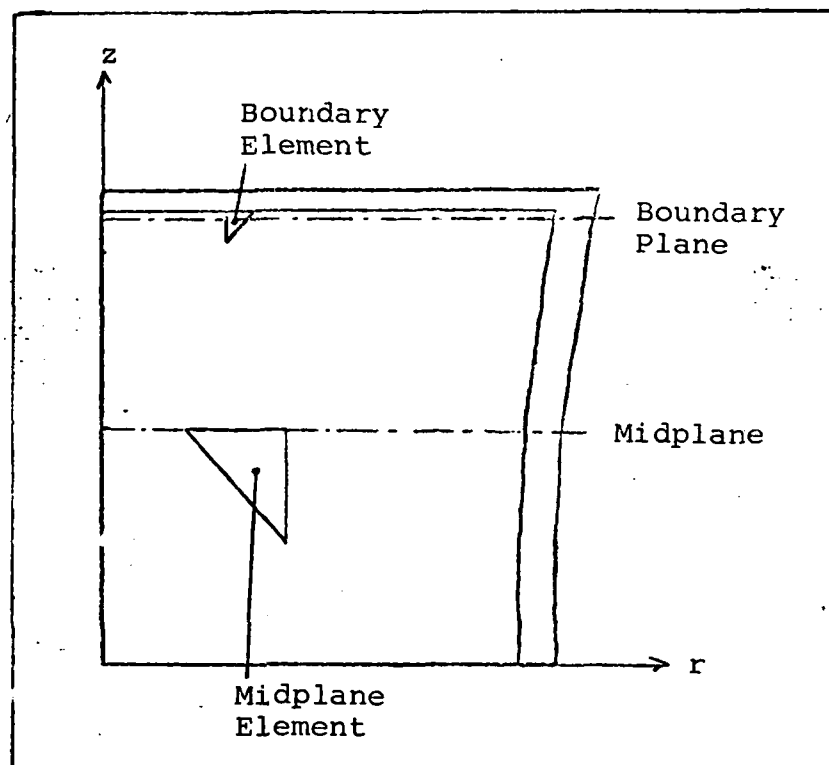


Fig. 3.3-C. Relative Locations of Centrum Planes and Elements Used in the Stress Analysis

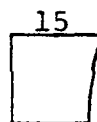
homogeneous assumption for these two regions was therefore compared to the results for an assumption of inhomogeneity, wherein the Bony end-plate was assigned a modulus of elasticity double that of the Cortex. Thus, the effect of increasing the Bony end-plate stiffness (relative to the Cortical) on creep deformation, stress distributions, and stress redistributions could be analyzed in order to determine if a more precise stiffness relationship between the two regions is required to adequately model the Centrum. Two cases were therefore analyzed for the applied 15 pound load, a "homogeneous" and an "inhomogeneous", depending on whether the Bony end-plate was equally stiff or twice as stiff, respectively, as the Cortex. The analysis incorporating the 30 pound load will hereafter be referred to as the "higher load" case and will assume that the Bony end-plate and Cortex are homogeneous only.

In each case, stresses were plotted as a function of radius and time for the two planes. Two time values were selected, 0+ and 1100 seconds, to represent stresses existing immediately after the initial elastic deformation and after some creep deformation has occurred, respectively. To aid in locating and comparing these plots, symbols are used (Fig. 3.3-D). These will be annotated in the upper right-hand corner of the page having a given plot for a particular case. Plots are grouped by stress component for comparison

I. CASES

A. Flexible

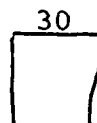
1. Homogeneous



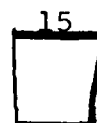
2. Inhomogeneous



3. Higher Load



B. Stiff



II. PLANES/ELEMENTS

Plane Location

Boundary

Midplane

Plane



Element



Fig. 3.3-D. Symbols Used for Quick Reference to Stress Plots

purposes among the three cases.

Figures 3.3-E through 3.3-P show these plots in the boundary plane. Generally, stress patterns varied little among the cases. The highest stress was typically in the Cortex. (Note: the Cortex position is represented in each plot by the single point having the largest radius; all other radii are points in the Trabecular region). The effect of creep was to transfer stress from the Trabecular region to the Cortex. Axial stress (Figs 3.3-E through 3.3-G) increased most notably in the Cortex. Radial stress (Figs 3.3-H through 3.3-J) increased in compression throughout. Hoop stress (Figs 3.3-K through 3.3-M) increased in compression in the Trabeculae but transitioned from compression to tension in the Cortex. Shear stress (Figs 3.3-N through 3.3-P) decreased in the Trabeculae while increasing in the Cortex. These trends suggest that, in the boundary plane, the Centrum is behaving like a thin-walled cylinder in which the Cortex is a shell constraining the Trabecular.

The effect of increasing the load on the stress in this plane was most noticeable in the hoop stress component (Fig. 3.3-L). The maximum tension reached in the Cortex (at 1100 seconds) was actually less than in the homogeneous case, even though the stress at 0+ seconds was greater in the higher load case. Since the creep rate was shown to be less in this case, the stress redistribution was also less.

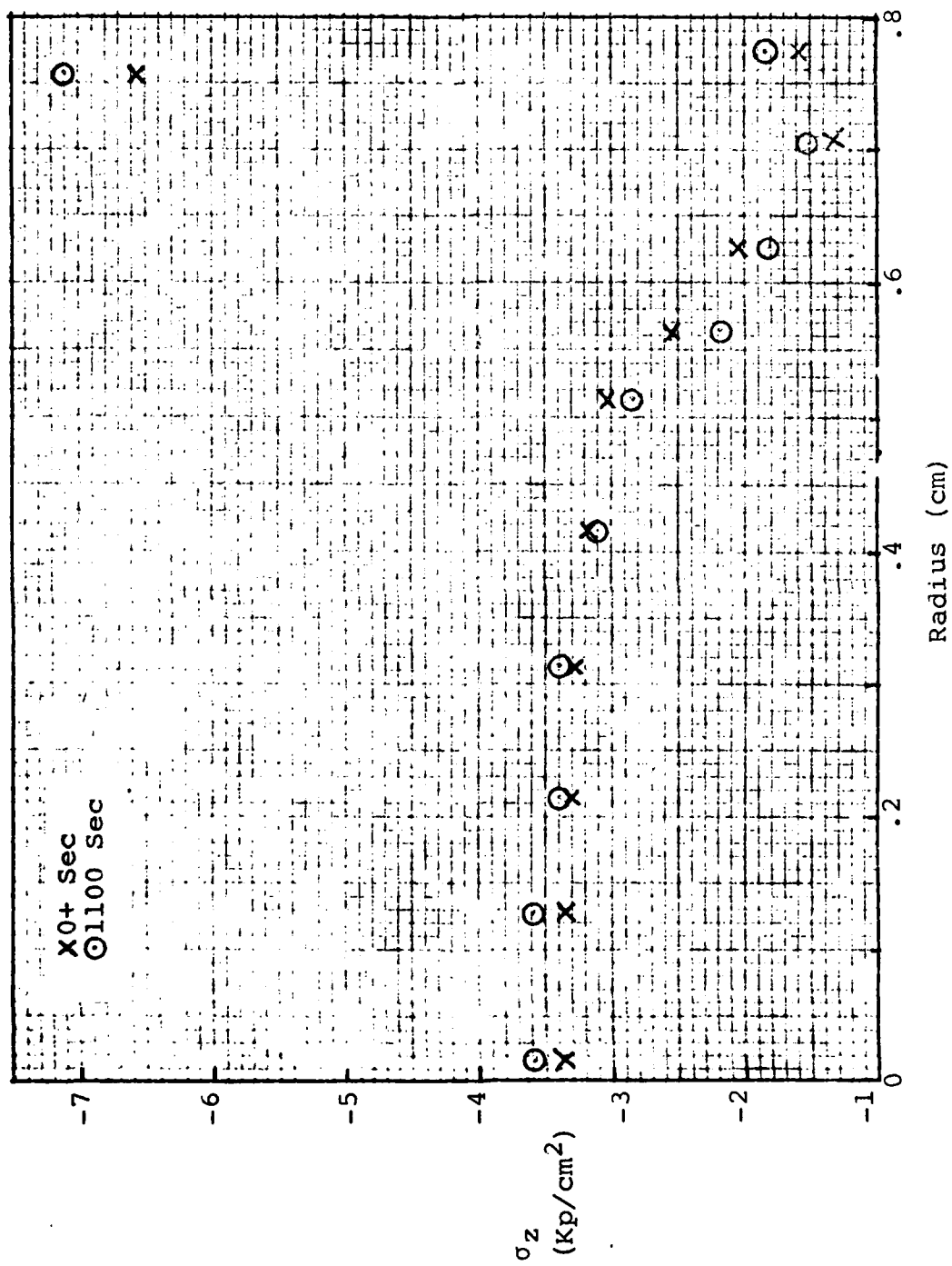


Fig. 3.3-E. σ_z Distribution in Boundary Plane, Homogeneous Case

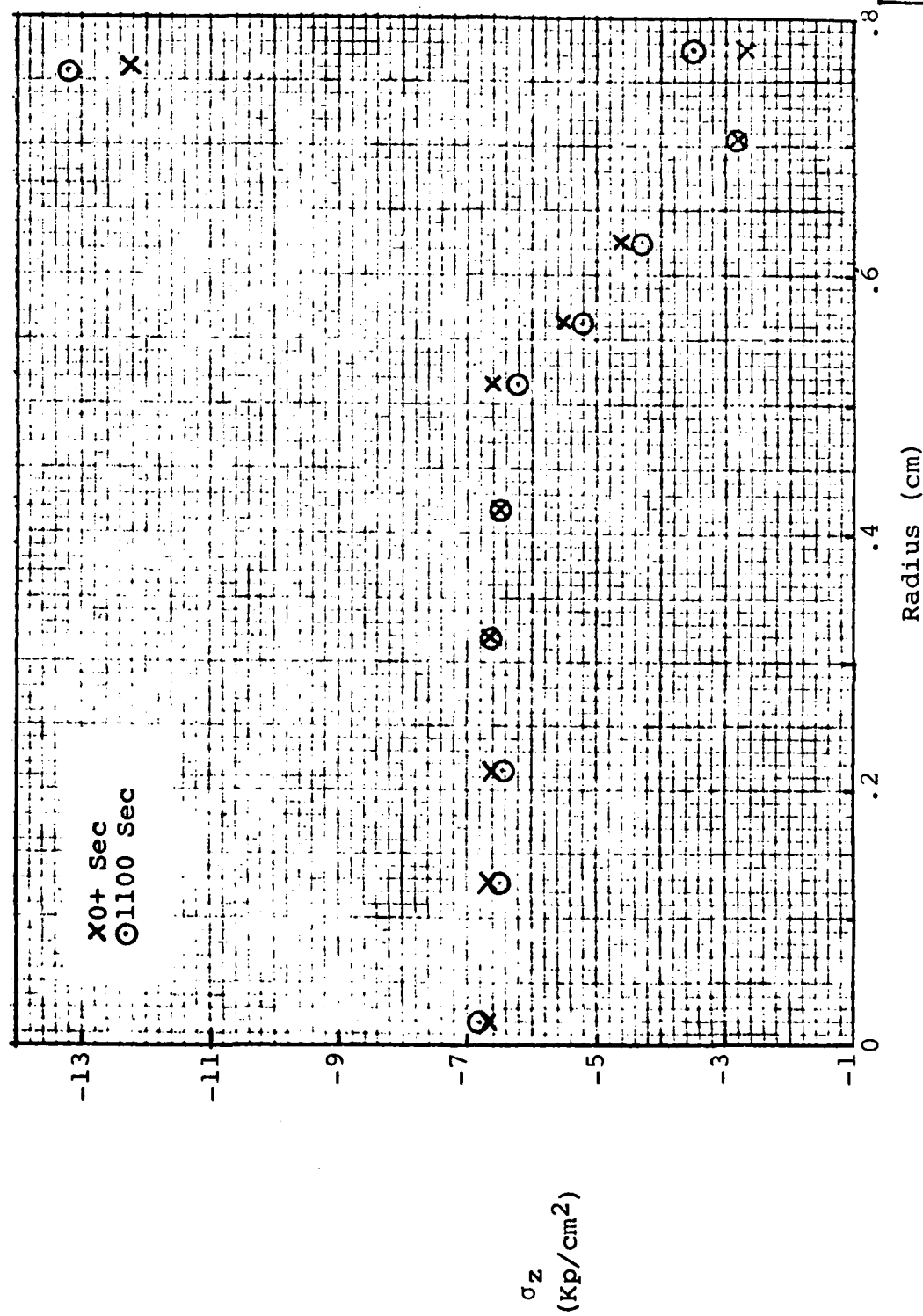


Fig. 3.3-F. σ_z Distribution in Boundary Plane, Higher Load Case

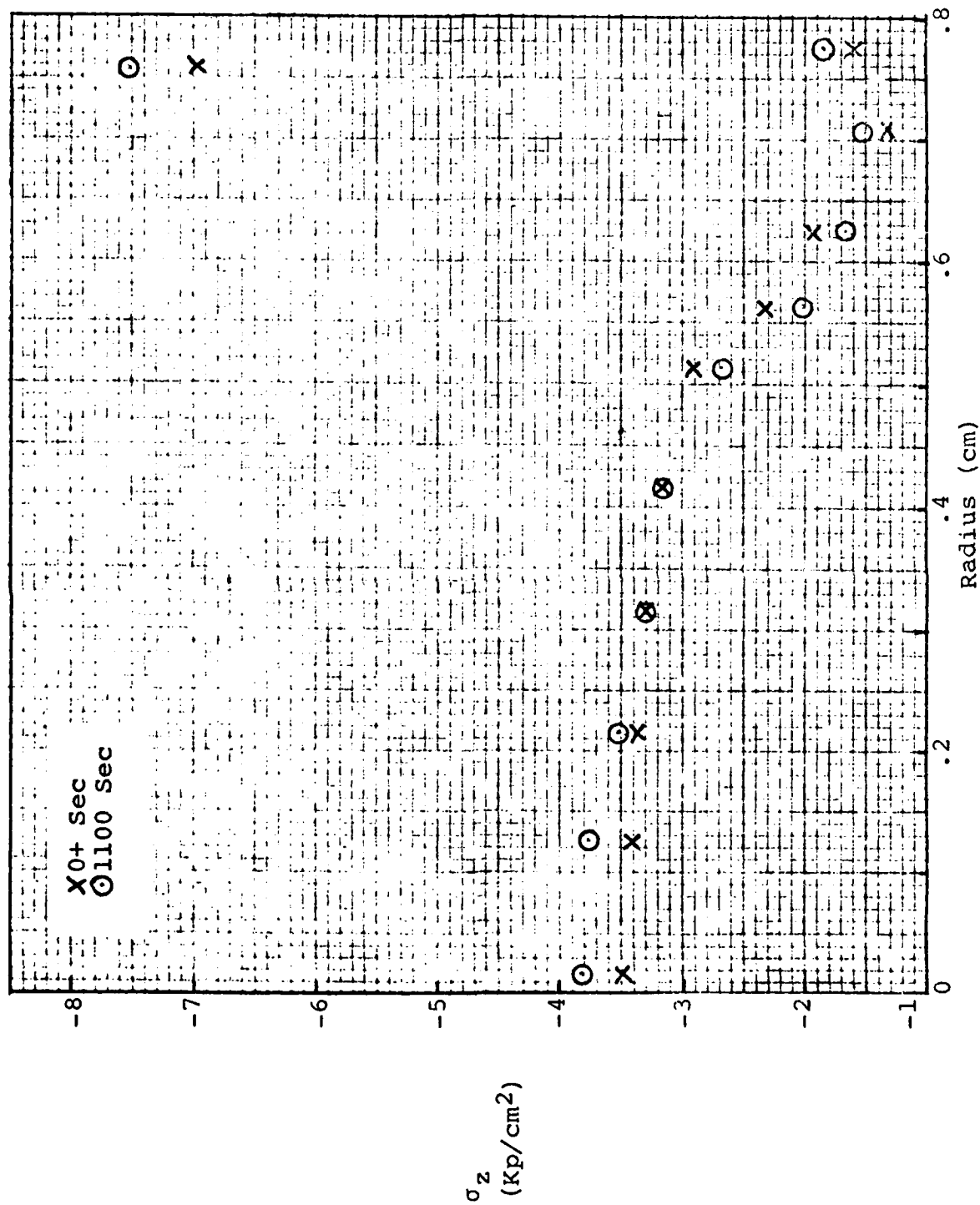


Fig. 3.3-G. σ_z Distribution in Boundary Plane, Inhomogeneous Case

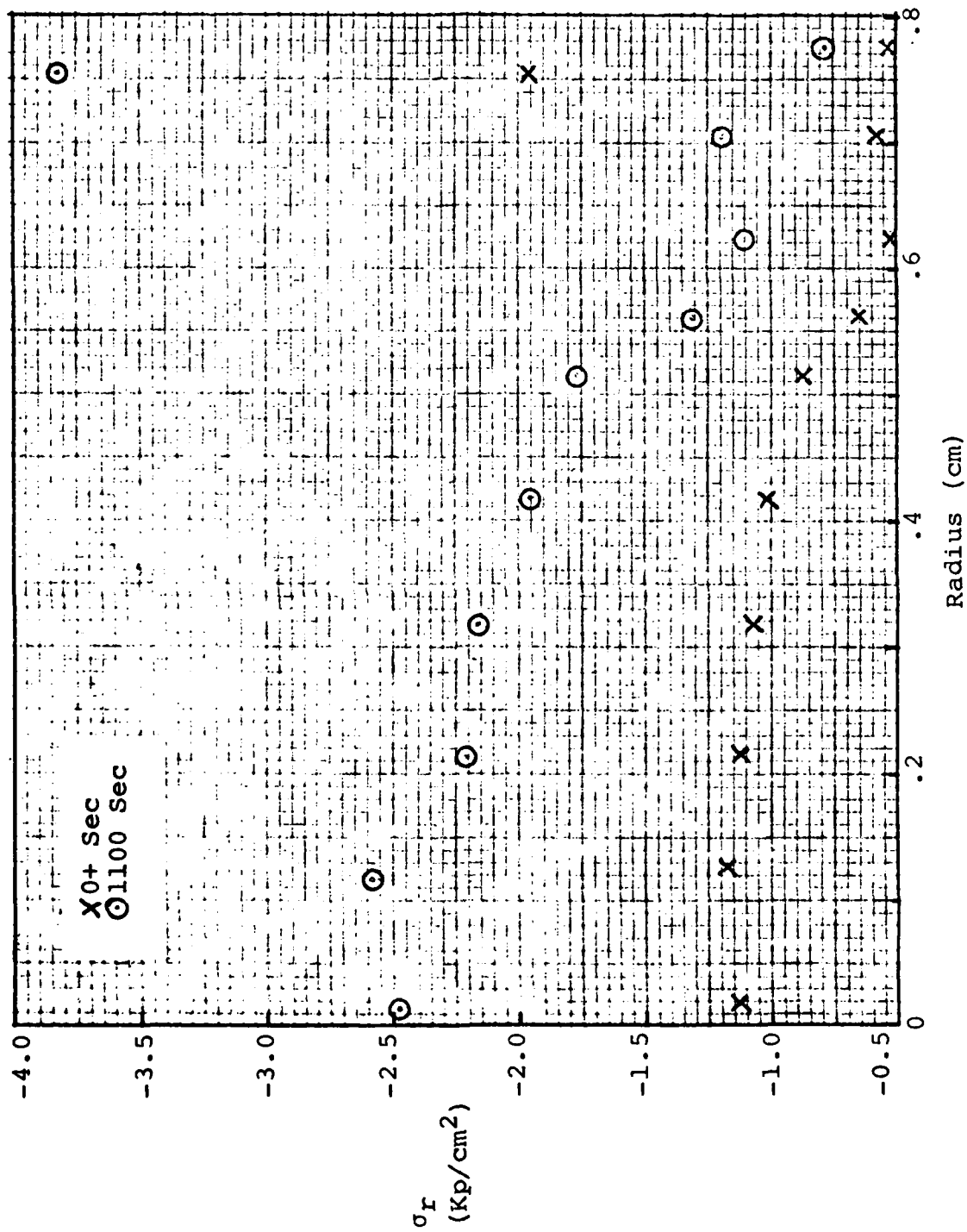


Fig. 3.3-H. σ_r Distribution in Boundary Plane, Homogeneous Case

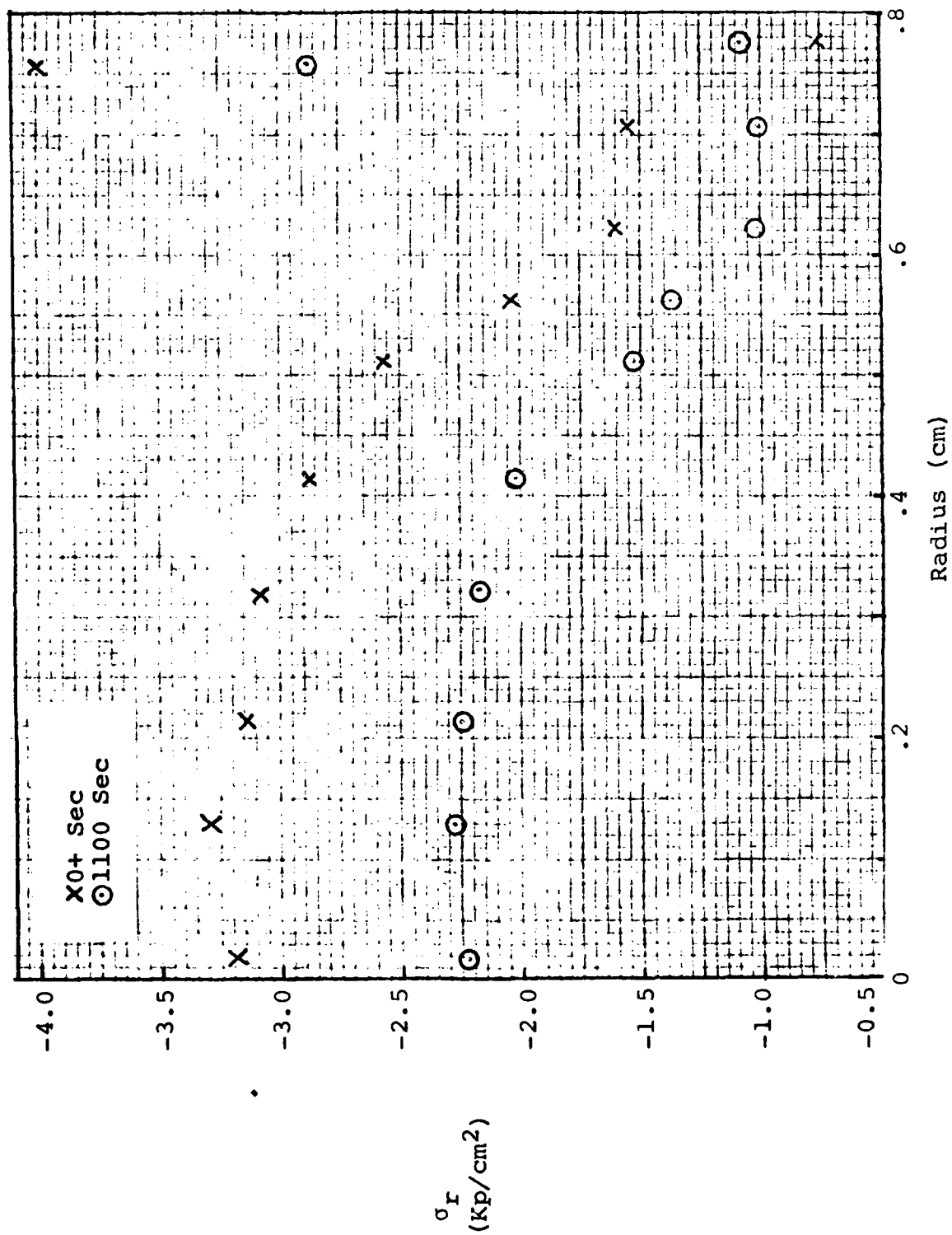


Fig. 3.3-I. σ_r Distribution in Boundary Plane, Higher Load Case

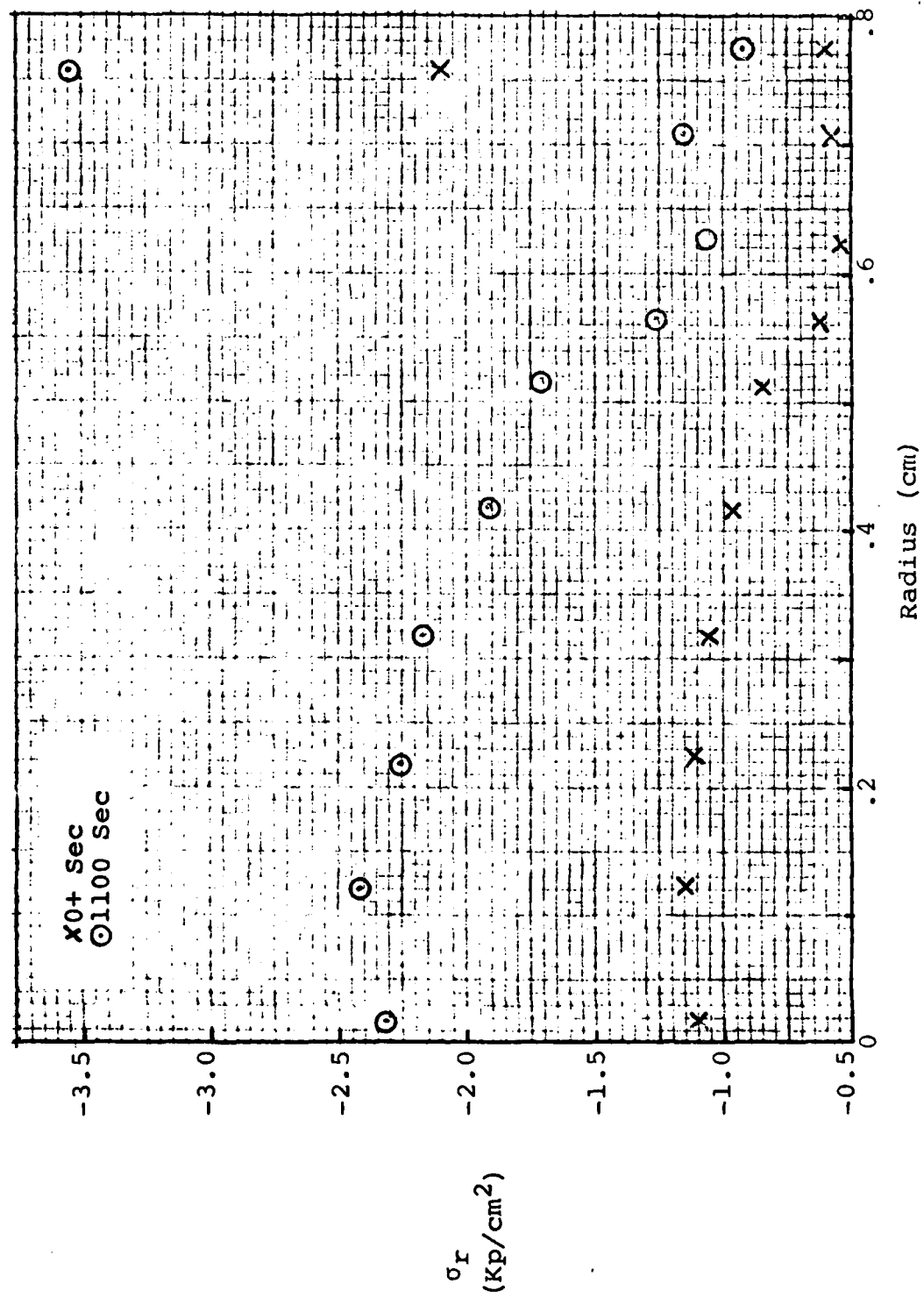
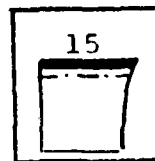


Fig. 3.3-J. σ_r Distribution in Boundary Plane, Inhomogeneous Case



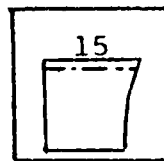
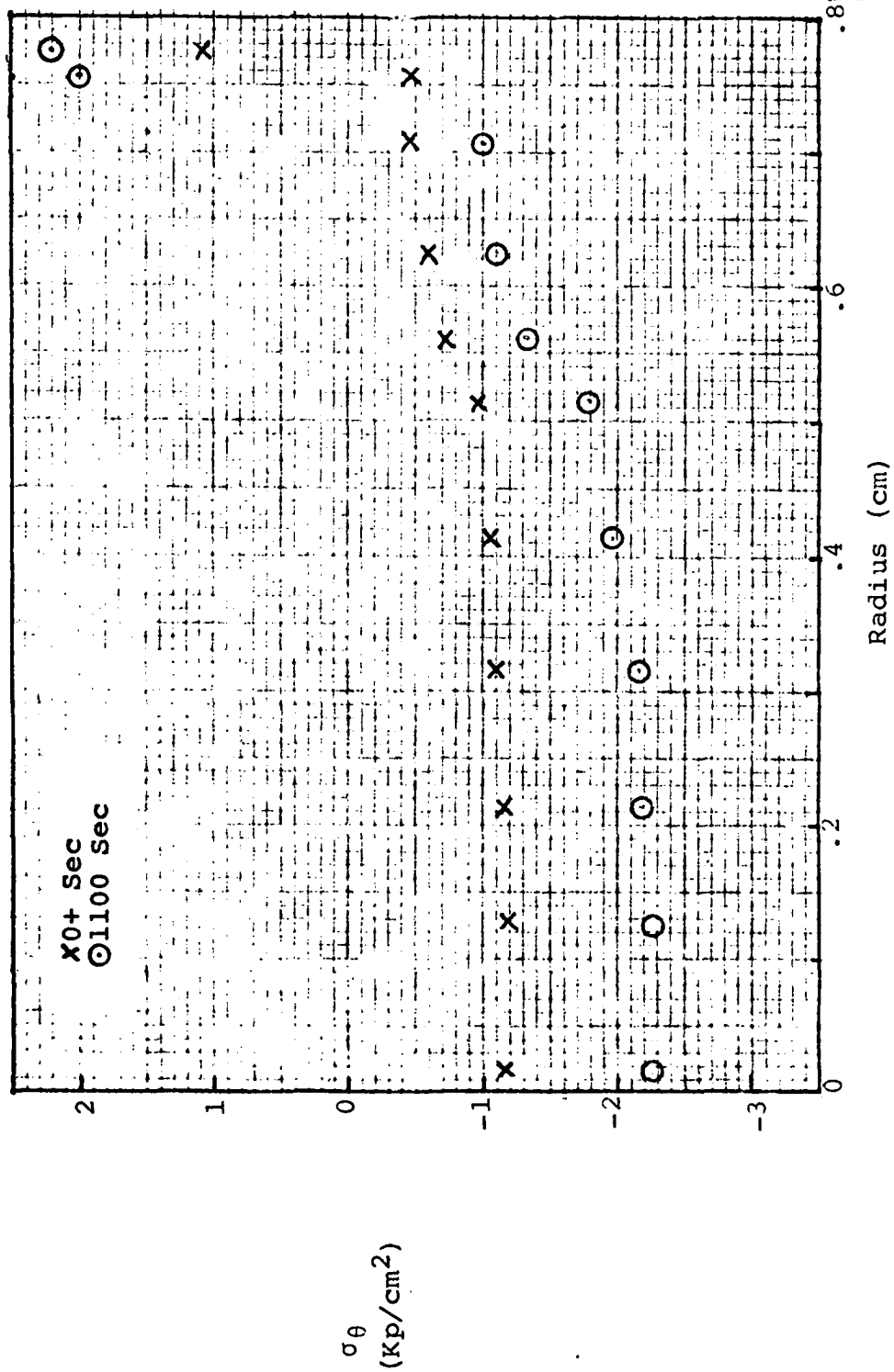


Fig. 3.3-K. σ_θ Distribution in Boundary Plane, Homogeneous Case

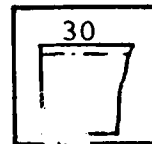
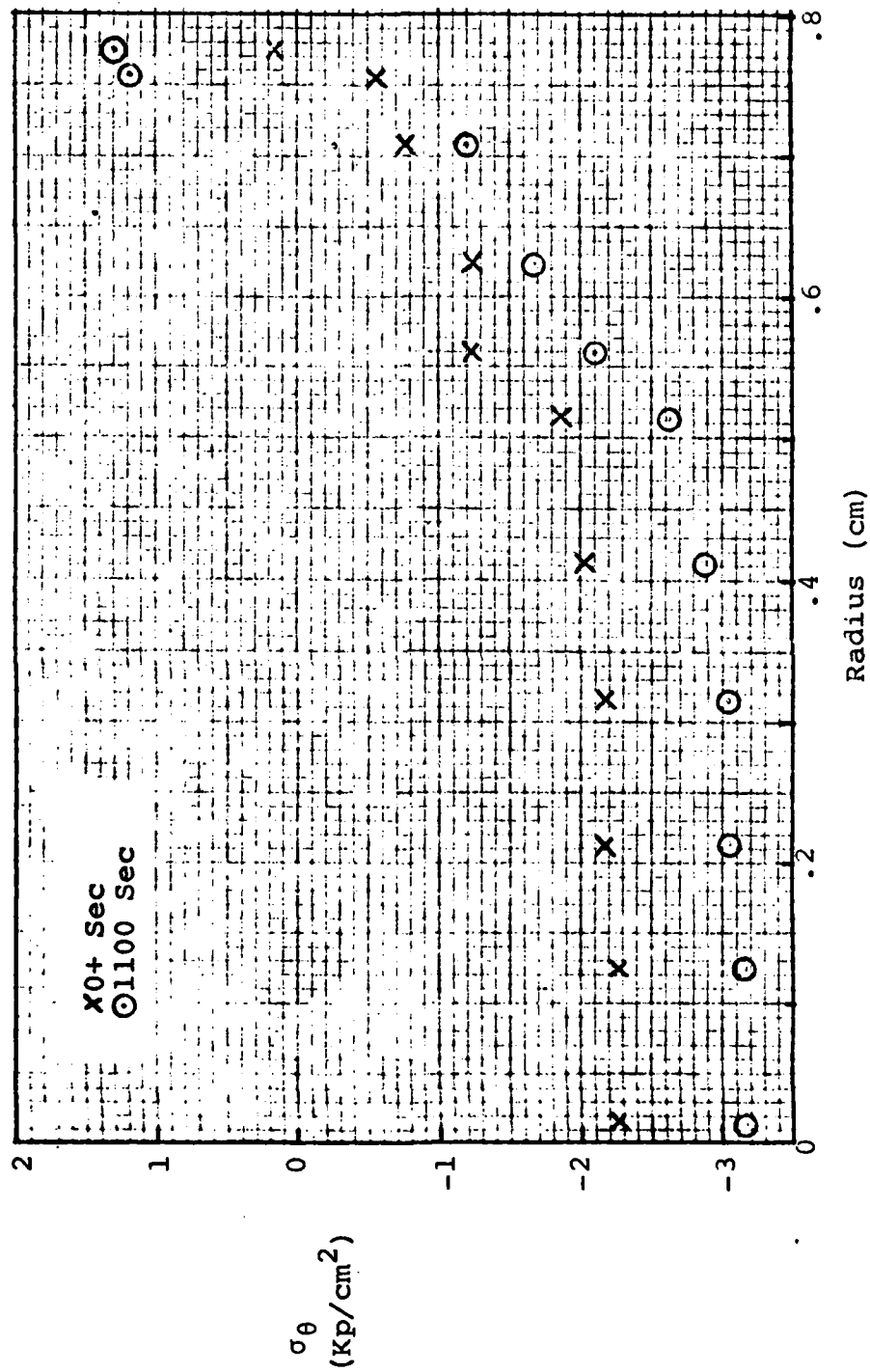


Fig. 3.3-L. σ_θ Distribution in Boundary Plane, Higher Load Case

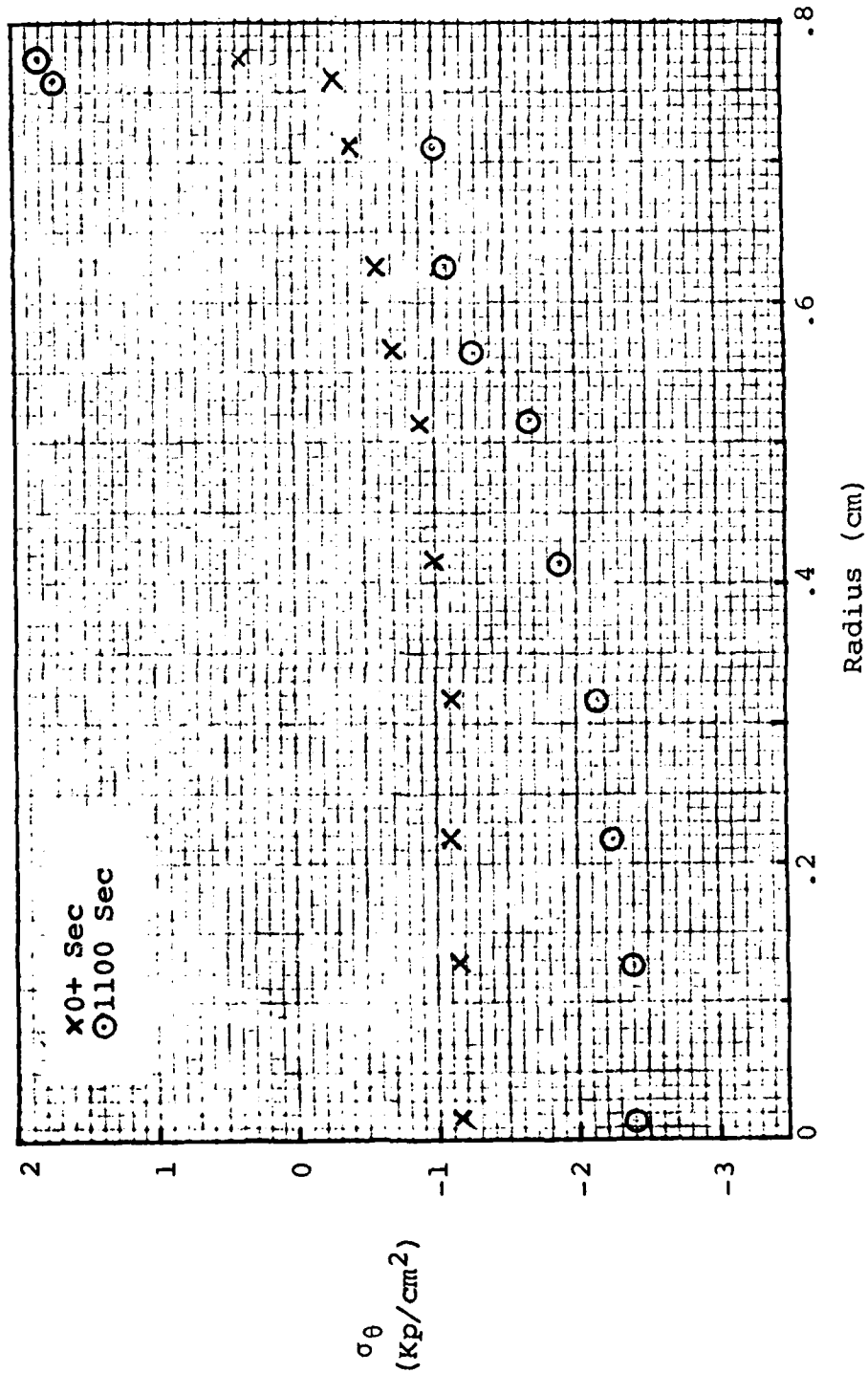


Fig. 3.3-M. σ_θ Distribution in Boundary Plane, Inhomogeneous Case

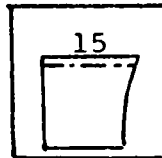
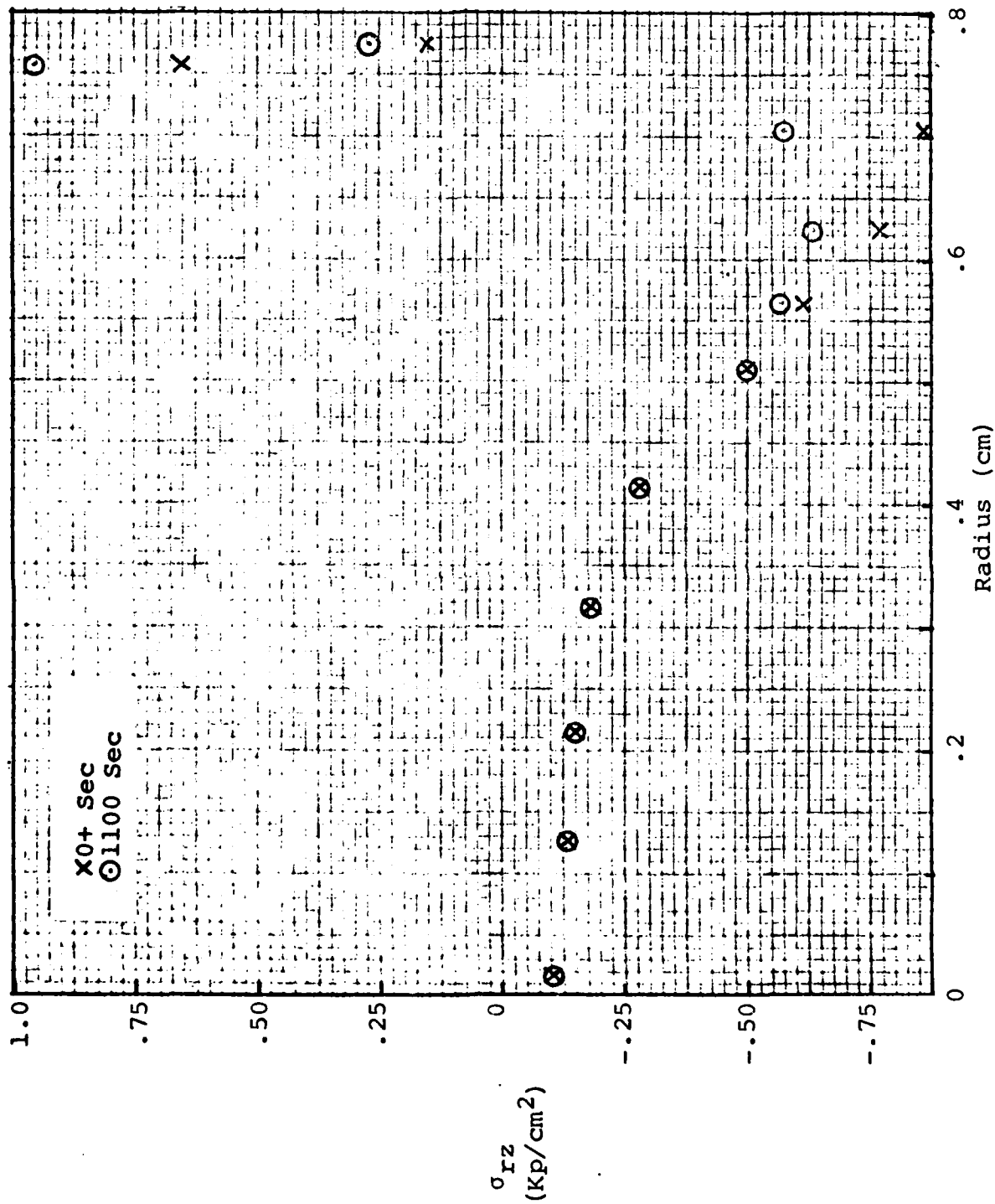


Fig. 3.3-N. σ_{rz} Distribution in Boundary Plane, Homogeneous Case

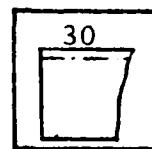
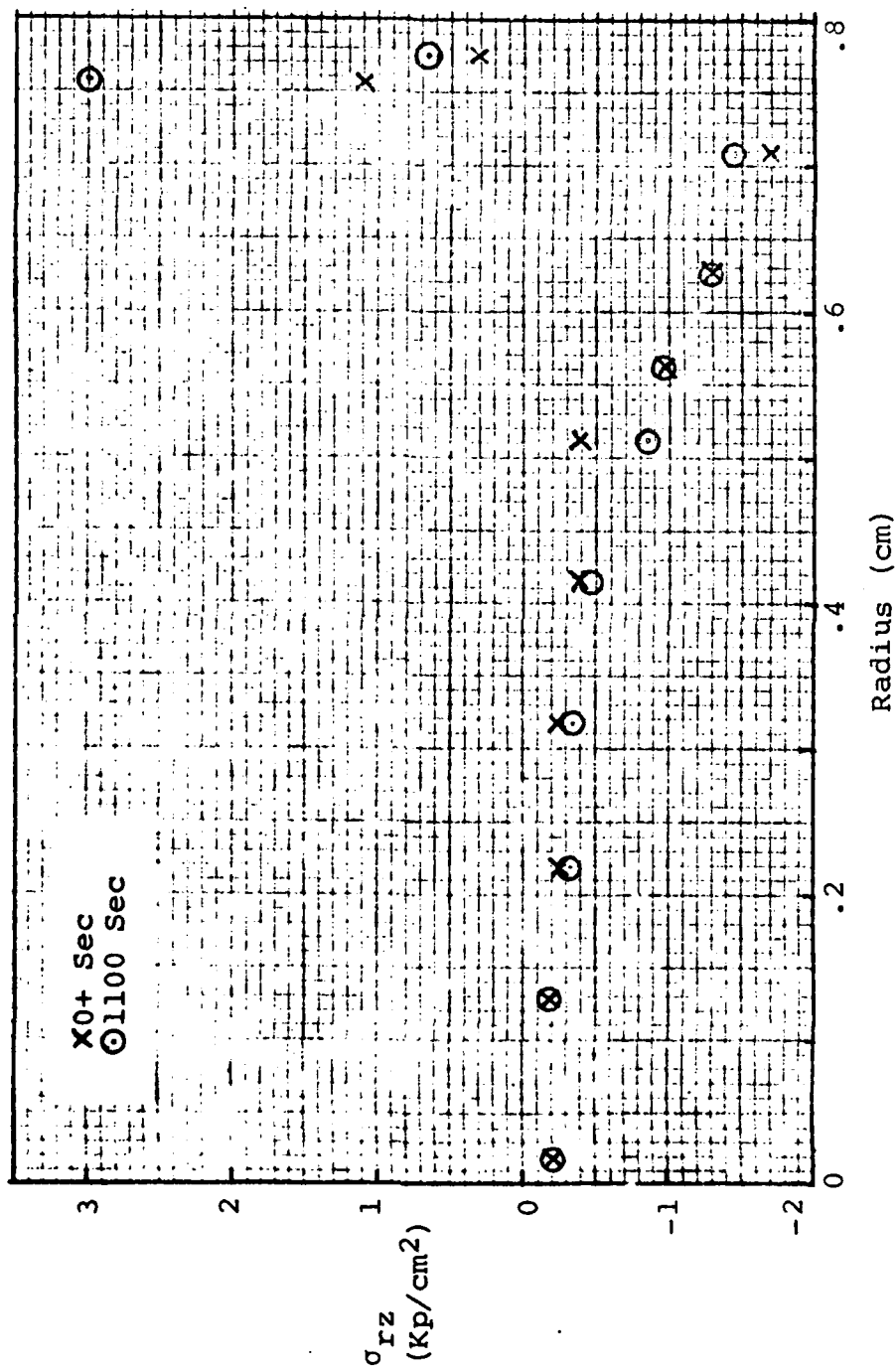


Fig. 3.3-0. σ_{rz} Distribution in Boundary Plane, Higher Load Case

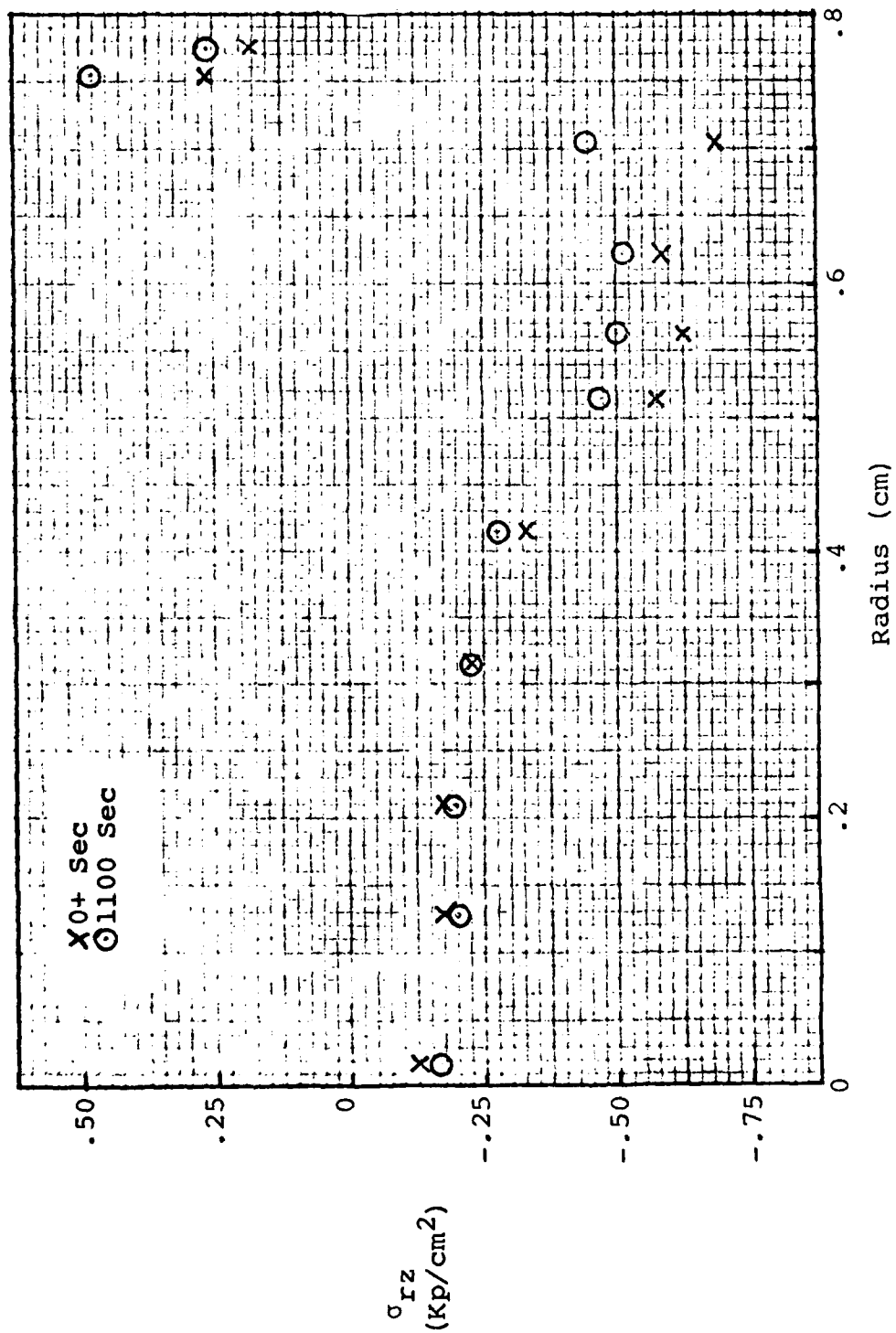
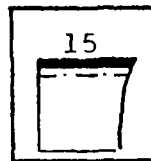


Fig. 3.3-P. σ_{rz} Distribution in Boundary Plane, Inhomogeneous Case



Comparing the inhomogeneous with the homogeneous case shows much less effect on the stress in this plane. For the inhomogeneous case, all Cortex stress components were slightly higher than the values in the homogeneous case, except for the shear stress. Apparently, the stiffer Bony end-plate had a role in transferring relatively more stress to the Cortex as it deformed.

Figures 3.3-Q through 3.3-X show the effects of homogeneity and load on the time variation of stresses in the boundary element. The manner in which each stress component varied with time was generally the same in all three cases. The greatest effect was caused by the higher load of 30 pounds, which nearly doubled each stress component at each time value as compared to the homogeneous case.

Again, the inhomogeneous case differed much less than the higher load case in terms of its effect on these time response characteristics. Generally, the stiffer Bony end-plate caused slightly higher stresses in the element, paralleling the results for the entire boundary plane.

Stresses in the midplane also generally followed a consistent pattern. Axial stress (Fig. 3.3-Y through 3.3-AA) generally followed the radial variation pattern determined in the boundary plane, but the variation of radial stress (Figs 3.3-AB through 3.3-AD) was exactly opposite the trend in the boundary plane: the lowest stress was in the Cortex.

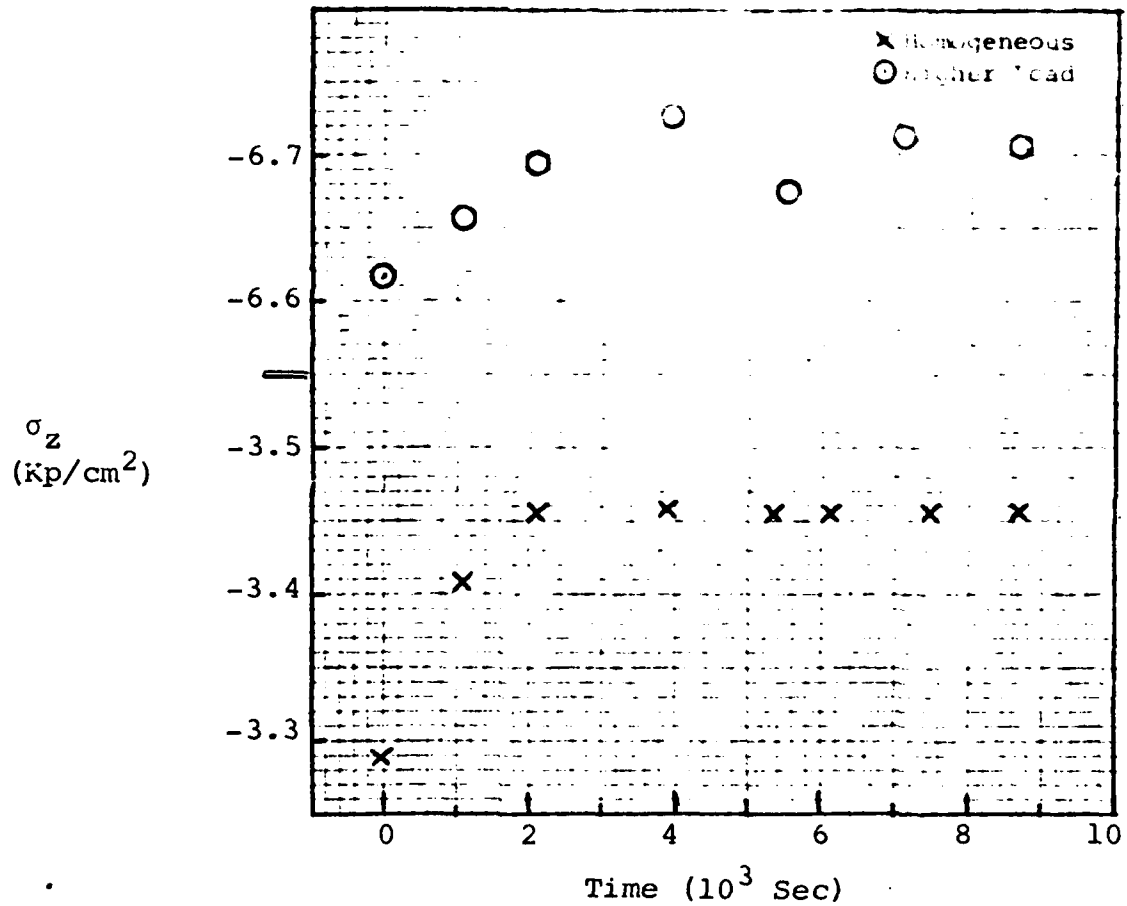
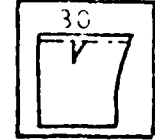
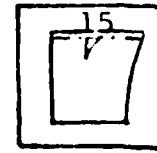


Fig. 3.3-Q. σ_z Versus Time in Boundary Element, Homogeneous and Higher Load Cases

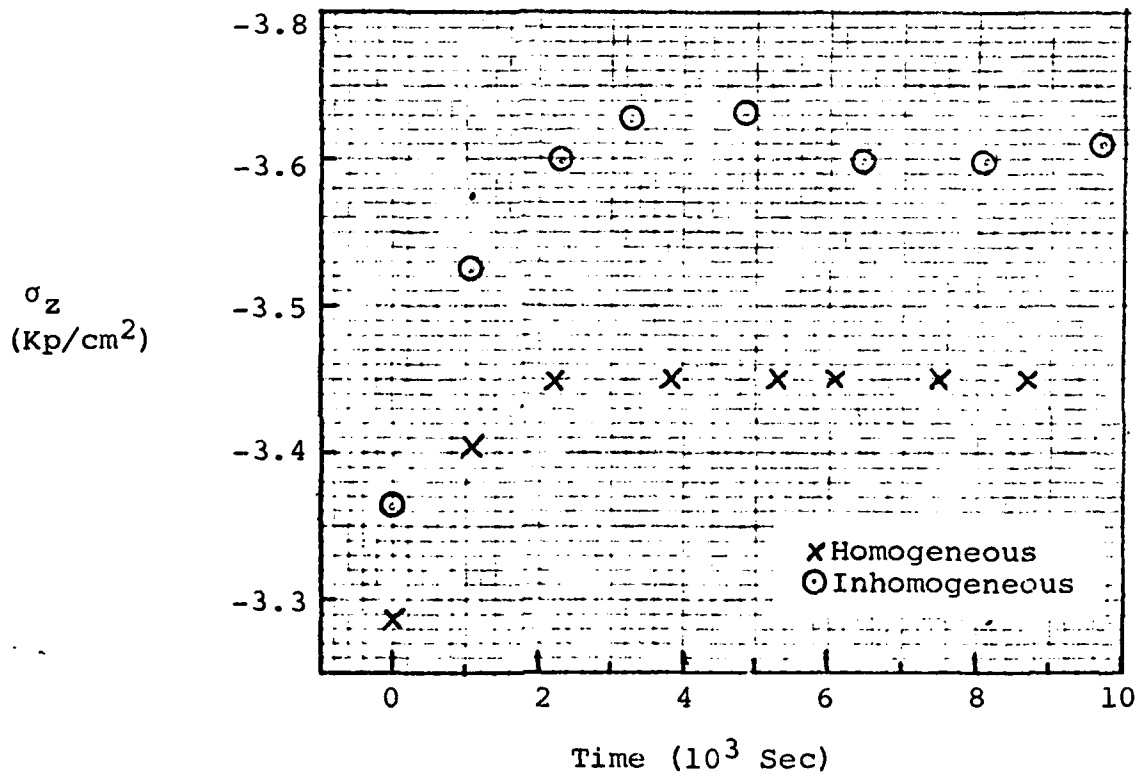
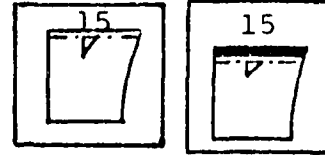


Fig. 3.3-R. σ_z Versus Time in Boundary Element, Homogeneous and Inhomogeneous Cases

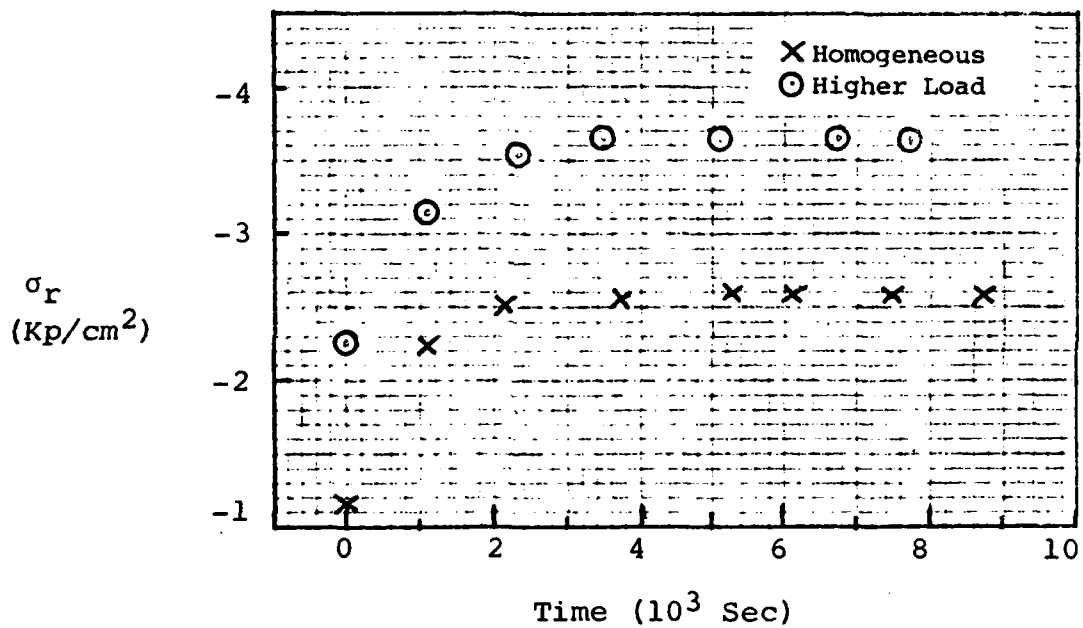
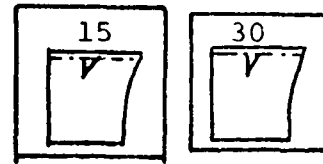
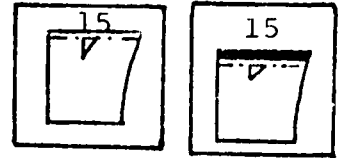


Fig. 3.3-S. σ_r Versus Time in Boundary Element, Homogeneous and Higher Load Cases



σ_r
(Kp/cm²)

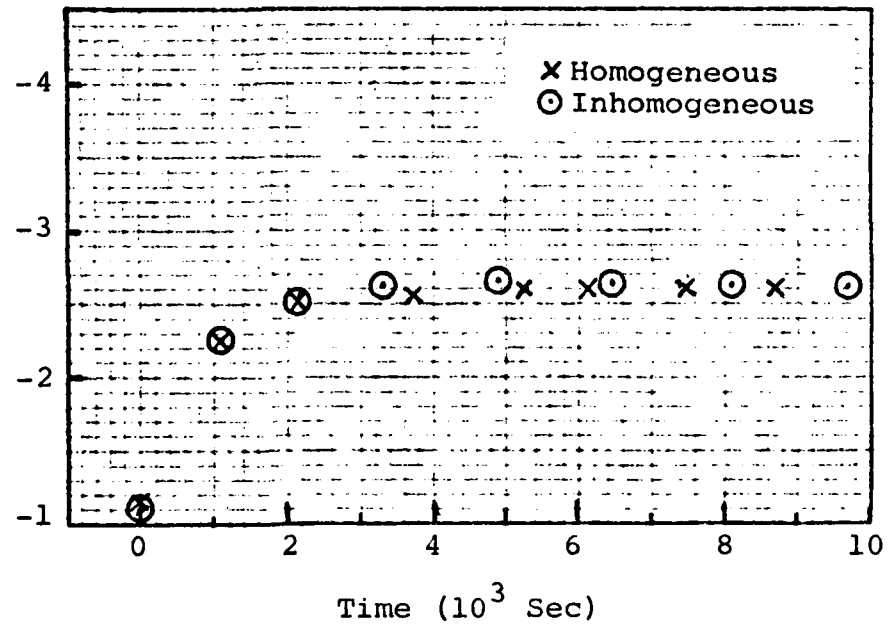


Fig. 3.3-T. σ_r Versus Time in Boundary Element,
Homogeneous and Inhomogeneous Cases

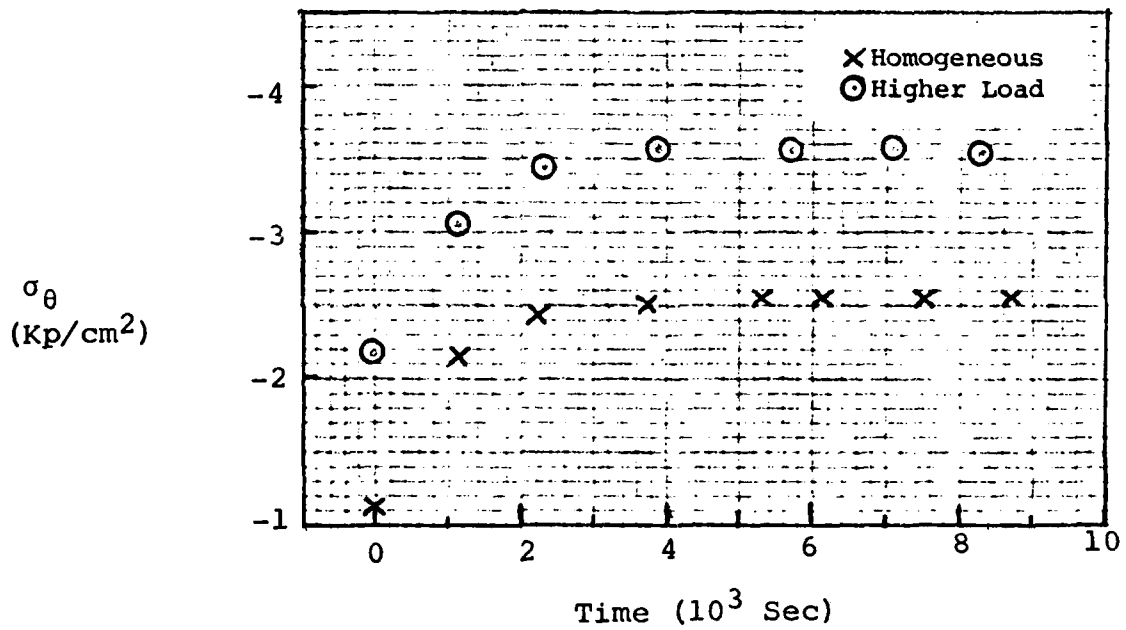
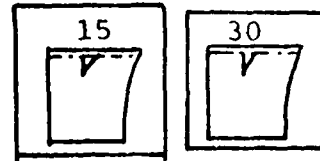
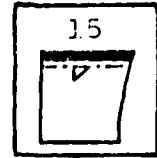
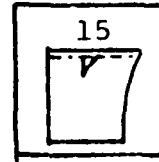


Fig. 3.3-U. σ_{θ} Versus Time in Boundary Element, Homogeneous and Higher Load Cases



σ_{θ}
(Kp/cm²)

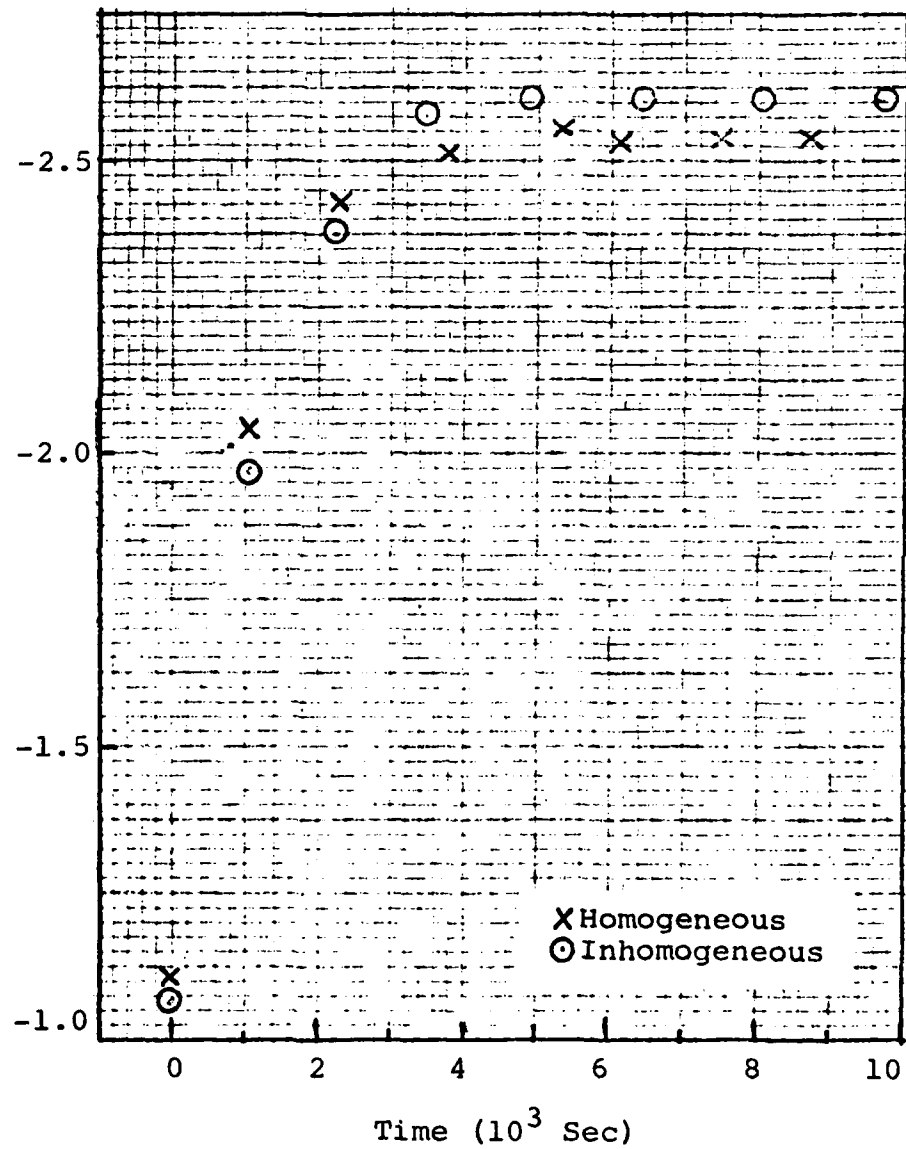


Fig. 3.3-V. σ_{θ} Versus Time in Boundary Element, Homogeneous and Inhomogeneous Cases

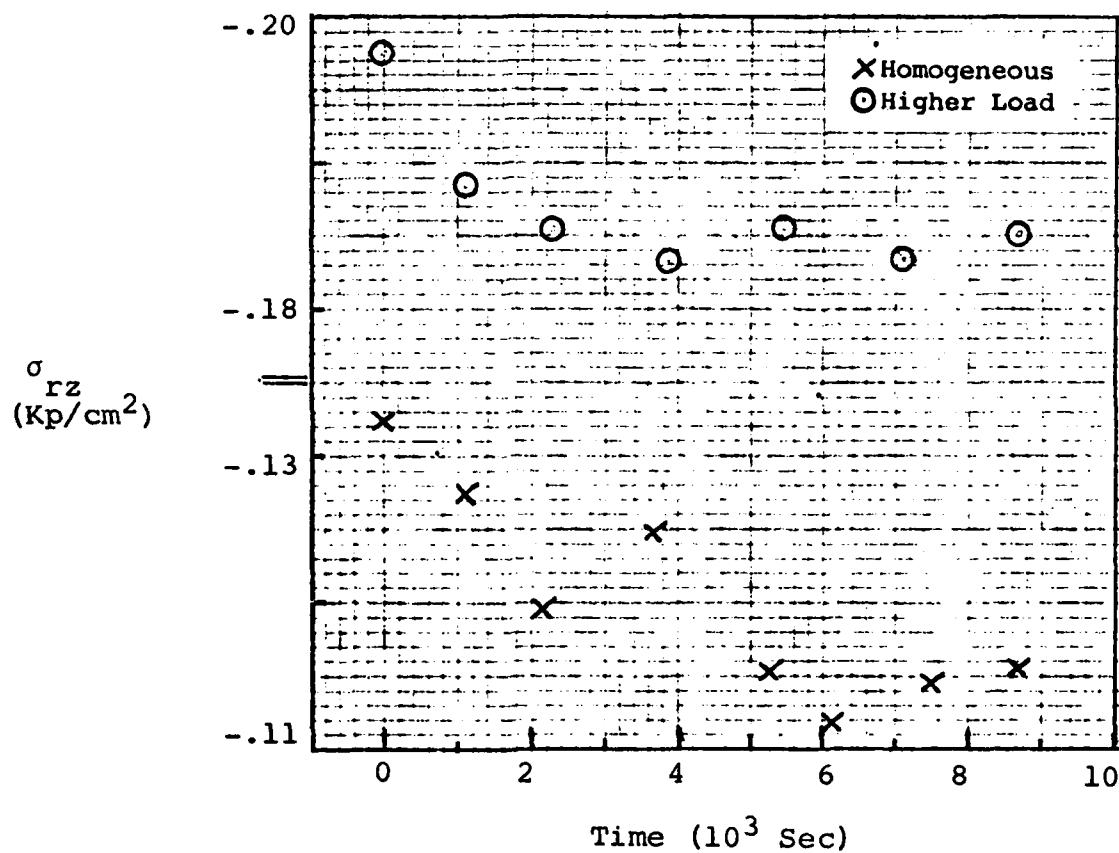
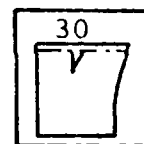
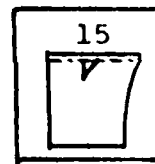


Fig. 3.3-W. σ_{rz} Versus Time in Boundary Element, Homogeneous and Higher Load Cases

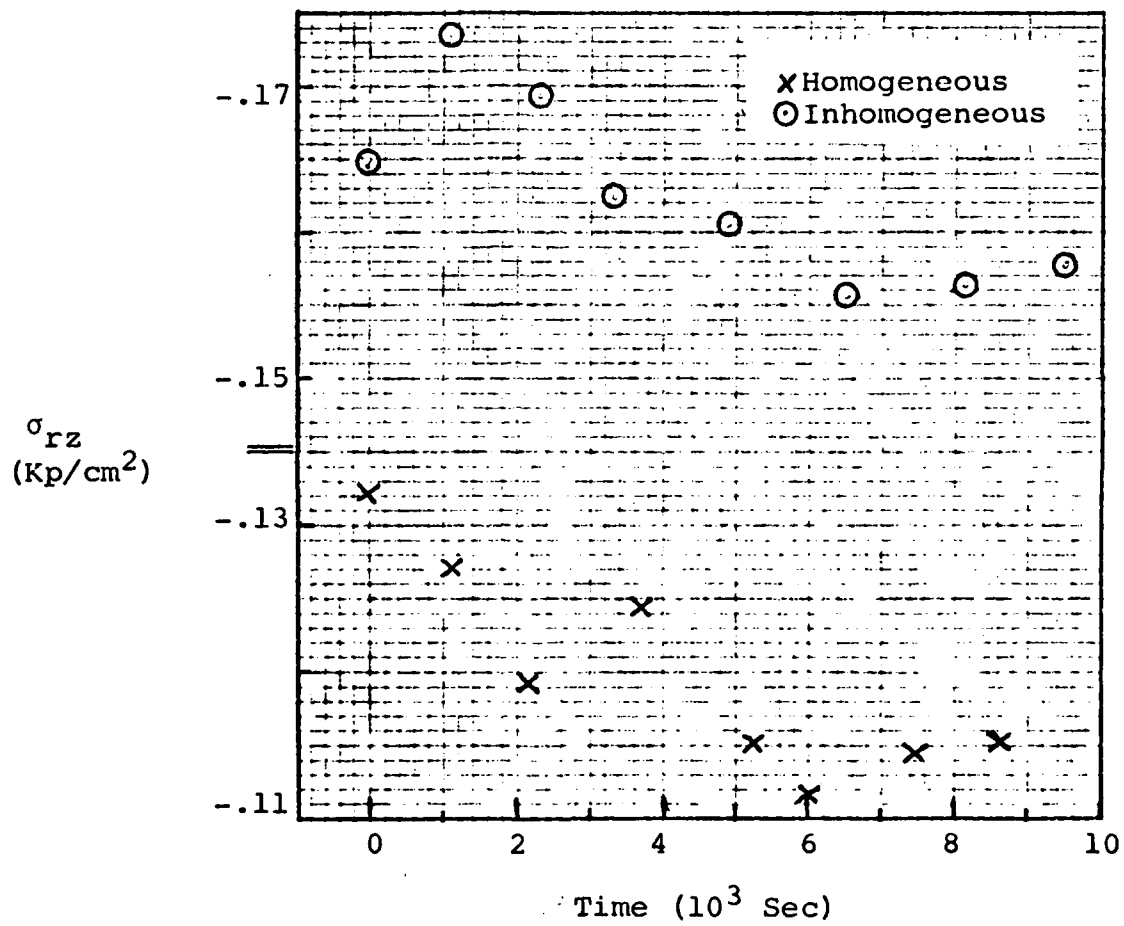
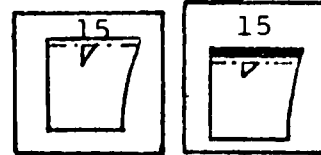


Fig. 3.3-X. σ_{rz} Versus Time in Boundary Element, Homogeneous and Inhomogeneous Cases

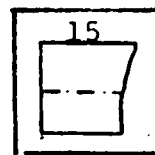
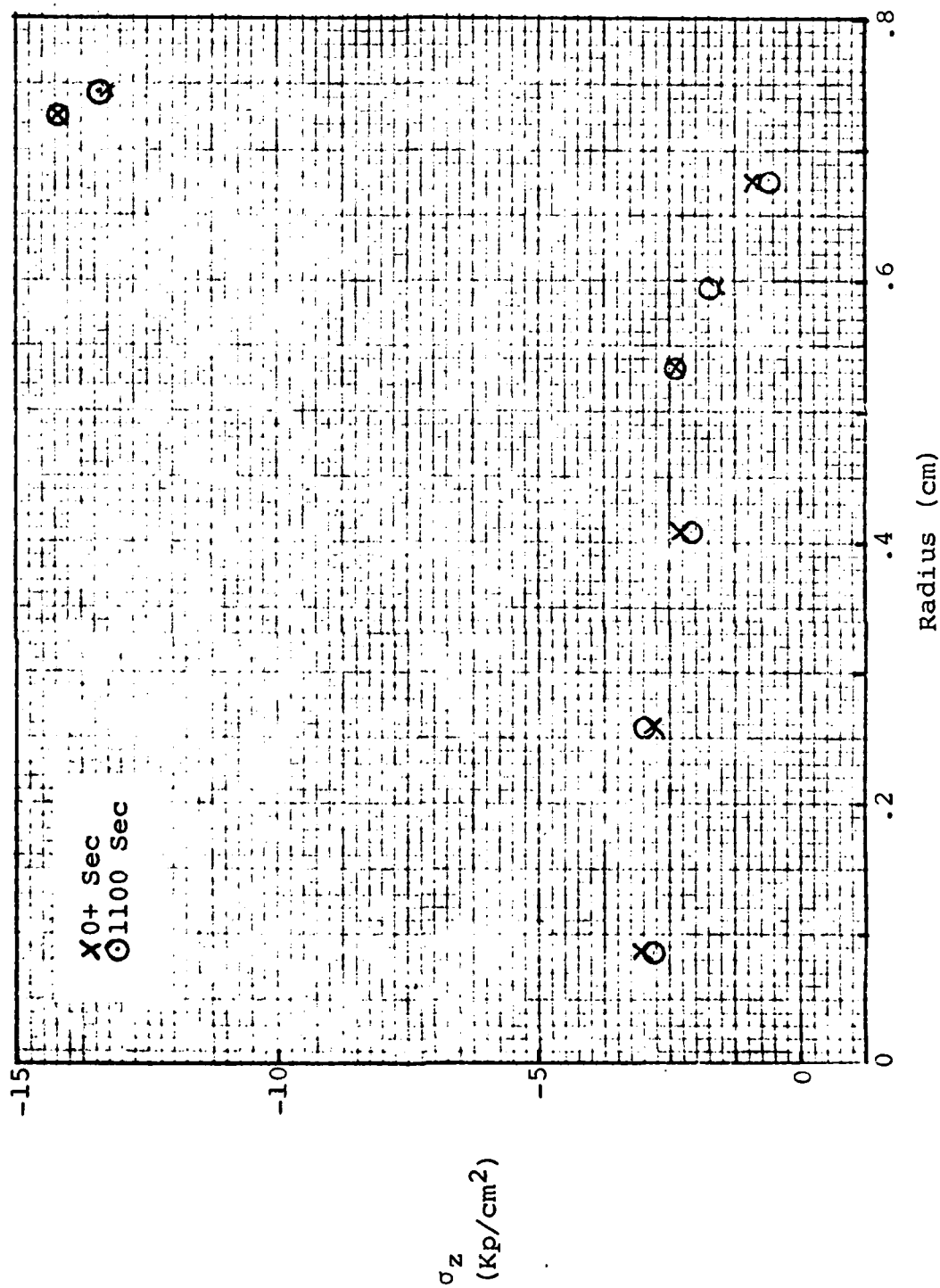


Fig. 3.3-Y. σ_z Distribution in Midplane, Homogeneous Case

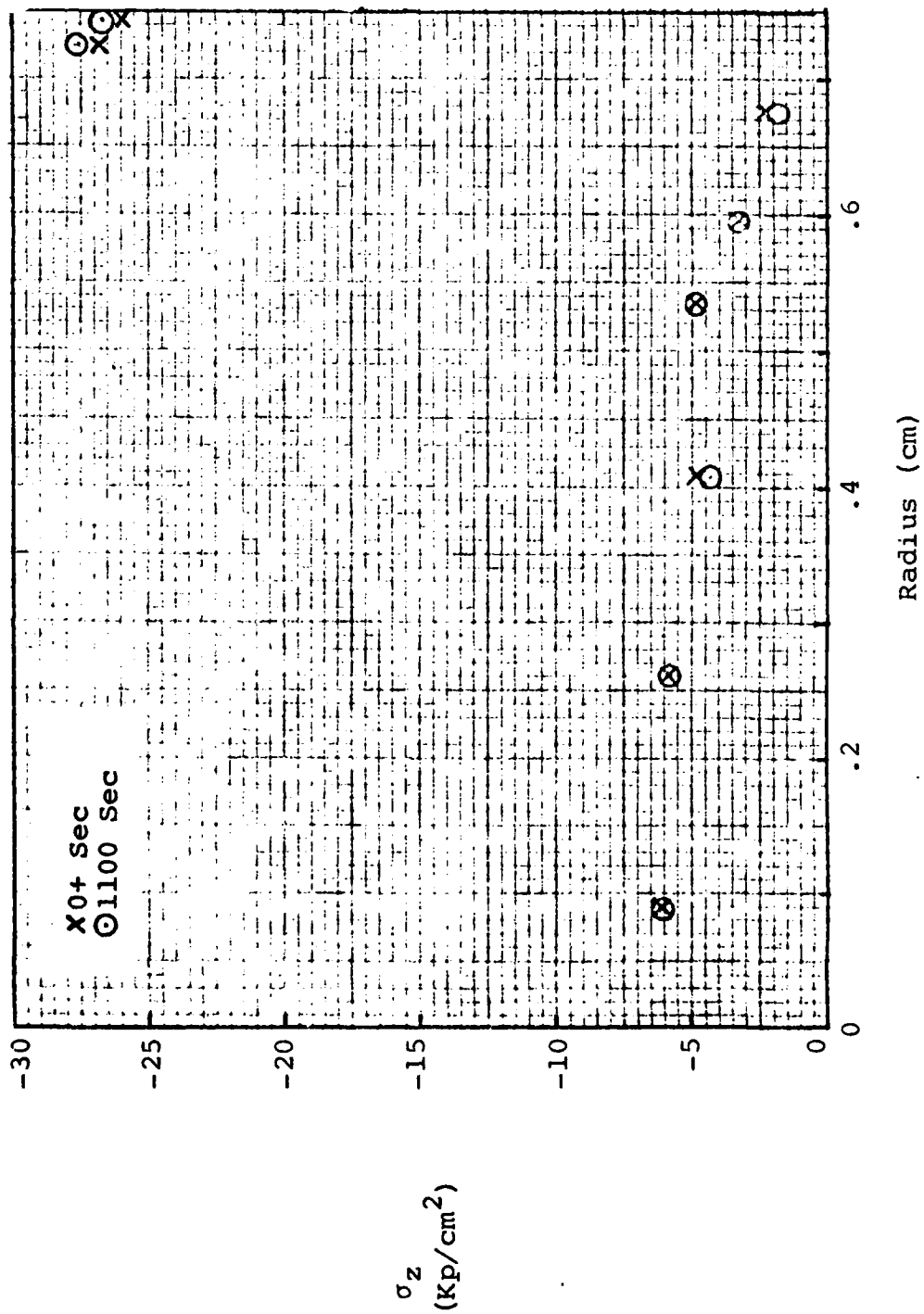
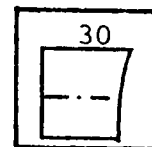


Fig. 3.3-Z. σ_z Distribution in Midplane, Higher Load Case



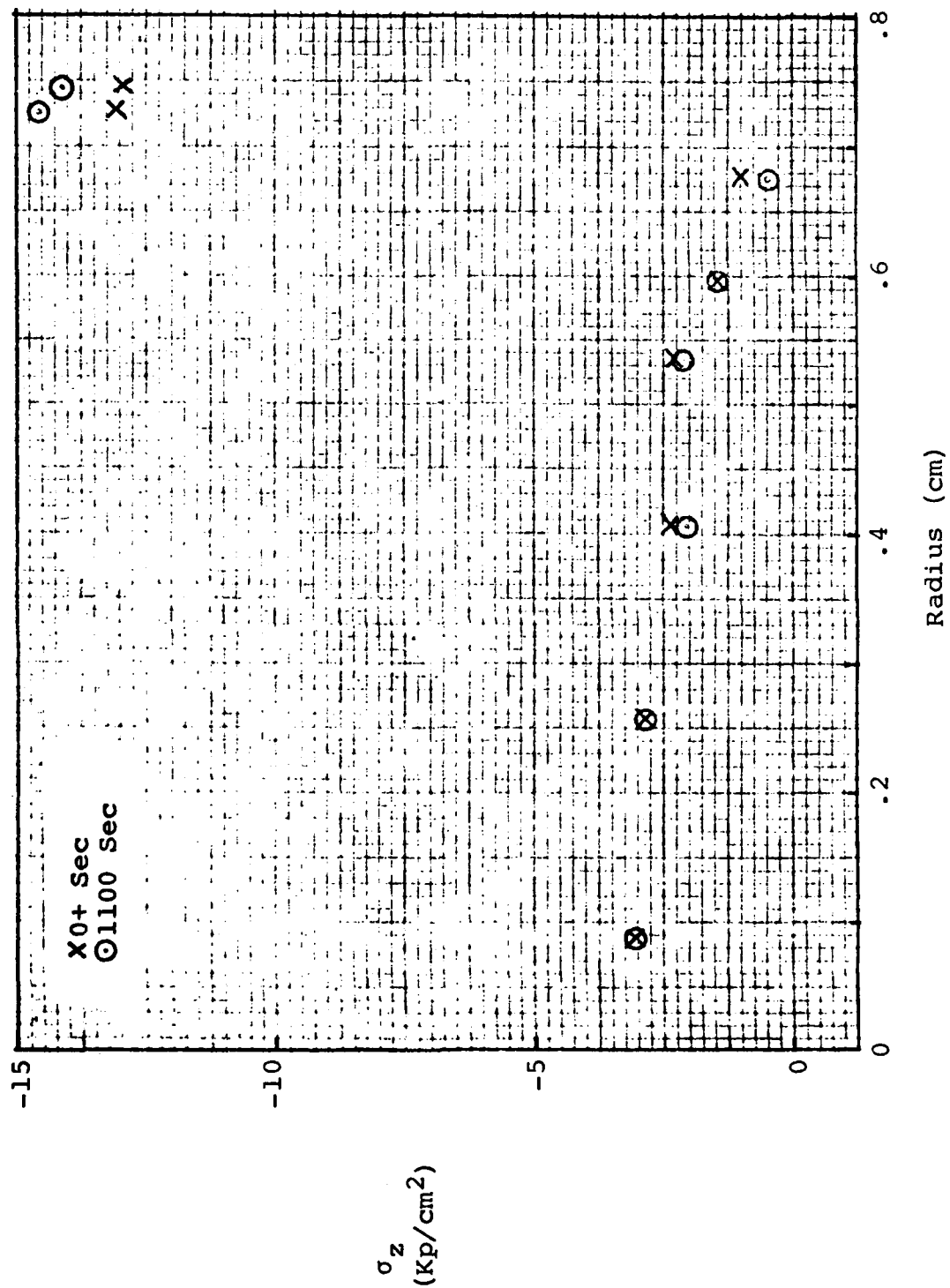


Fig. 3.3-AA. σ_z Distribution in Midplane, Inhomogeneous Case

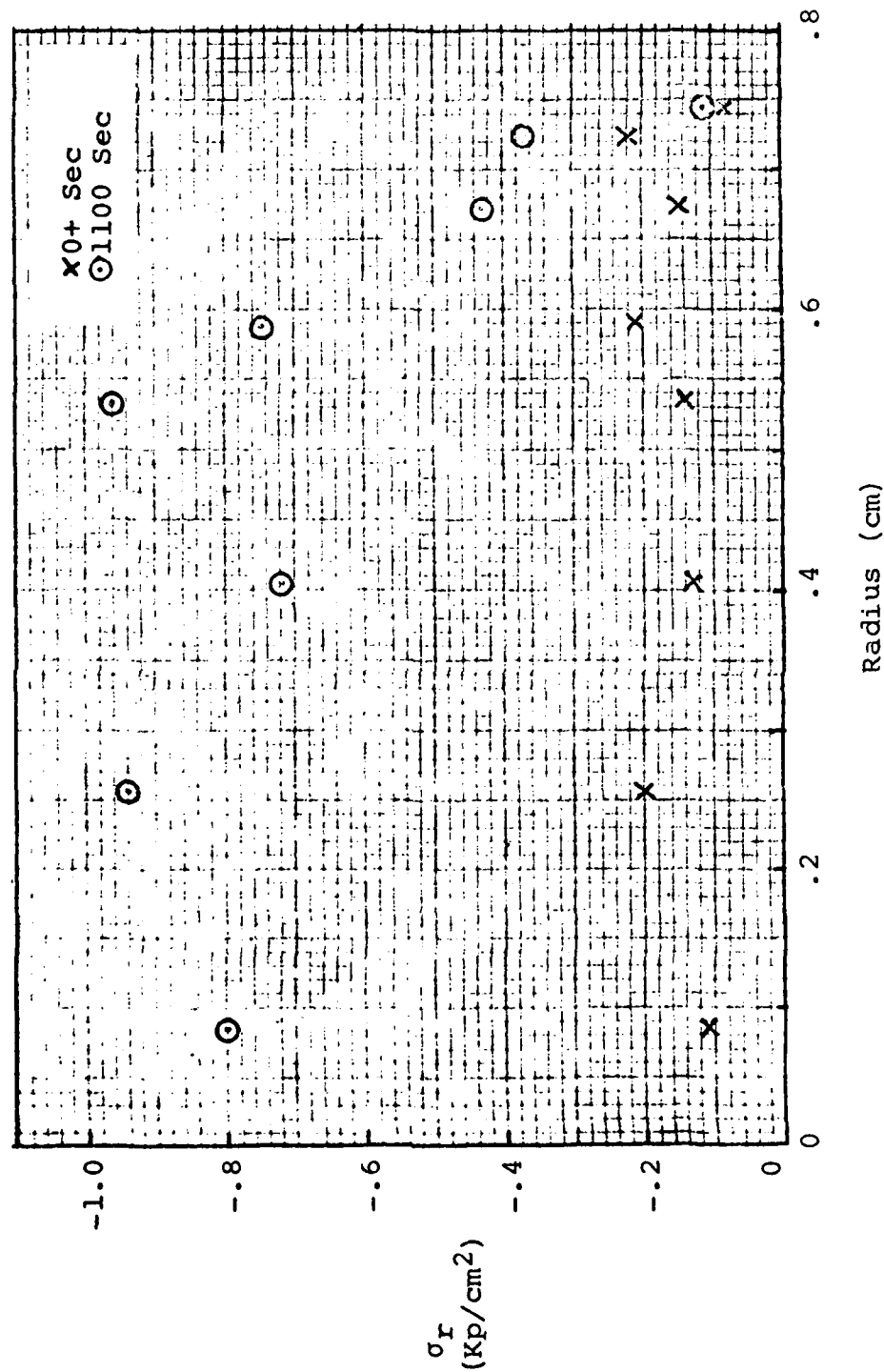


Fig. 3.3-AB. σ_r Distribution in Midplane, Homogeneous Case

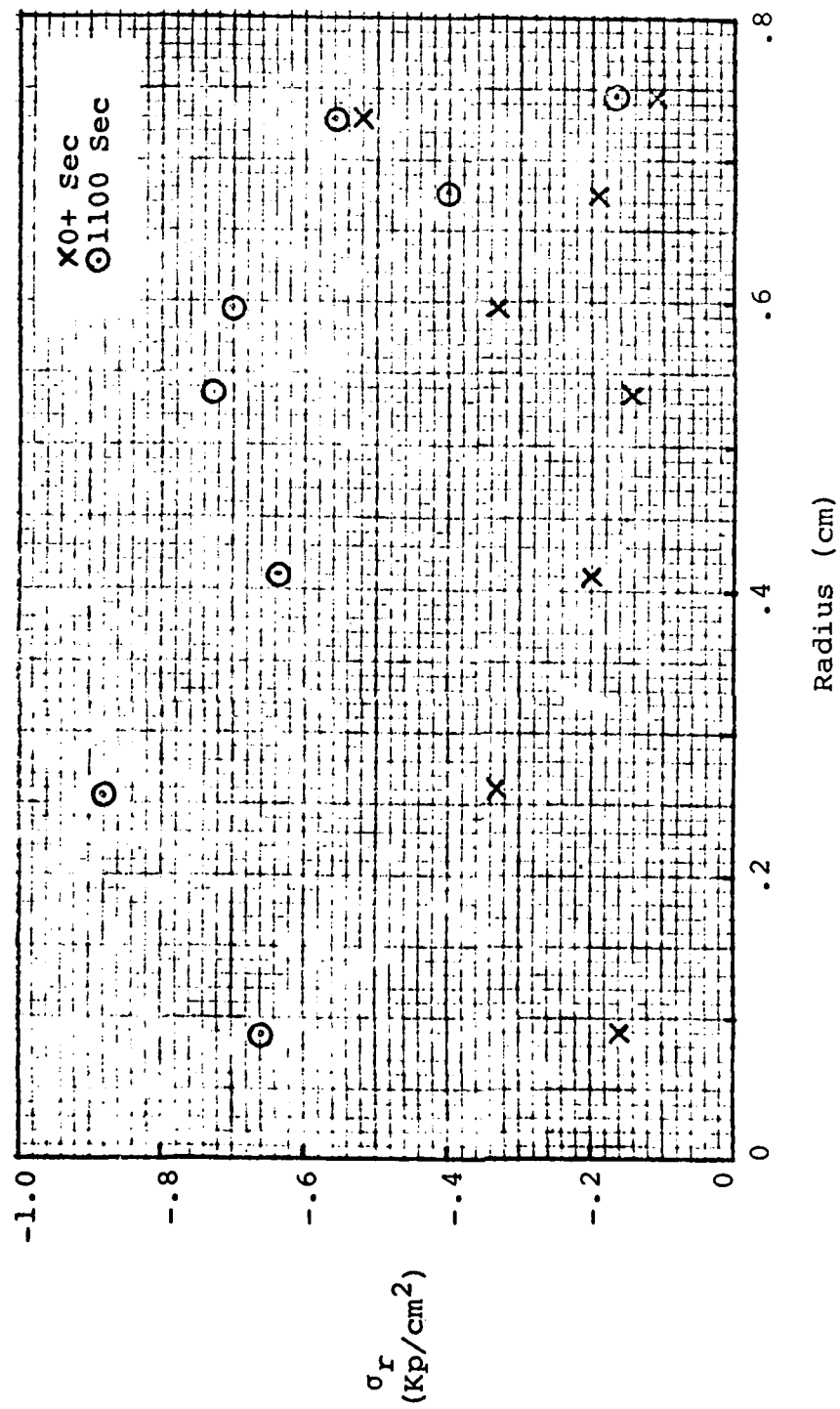


Fig. 3.3-AC. σ_r Distribution in Midplane, Higher Load Case

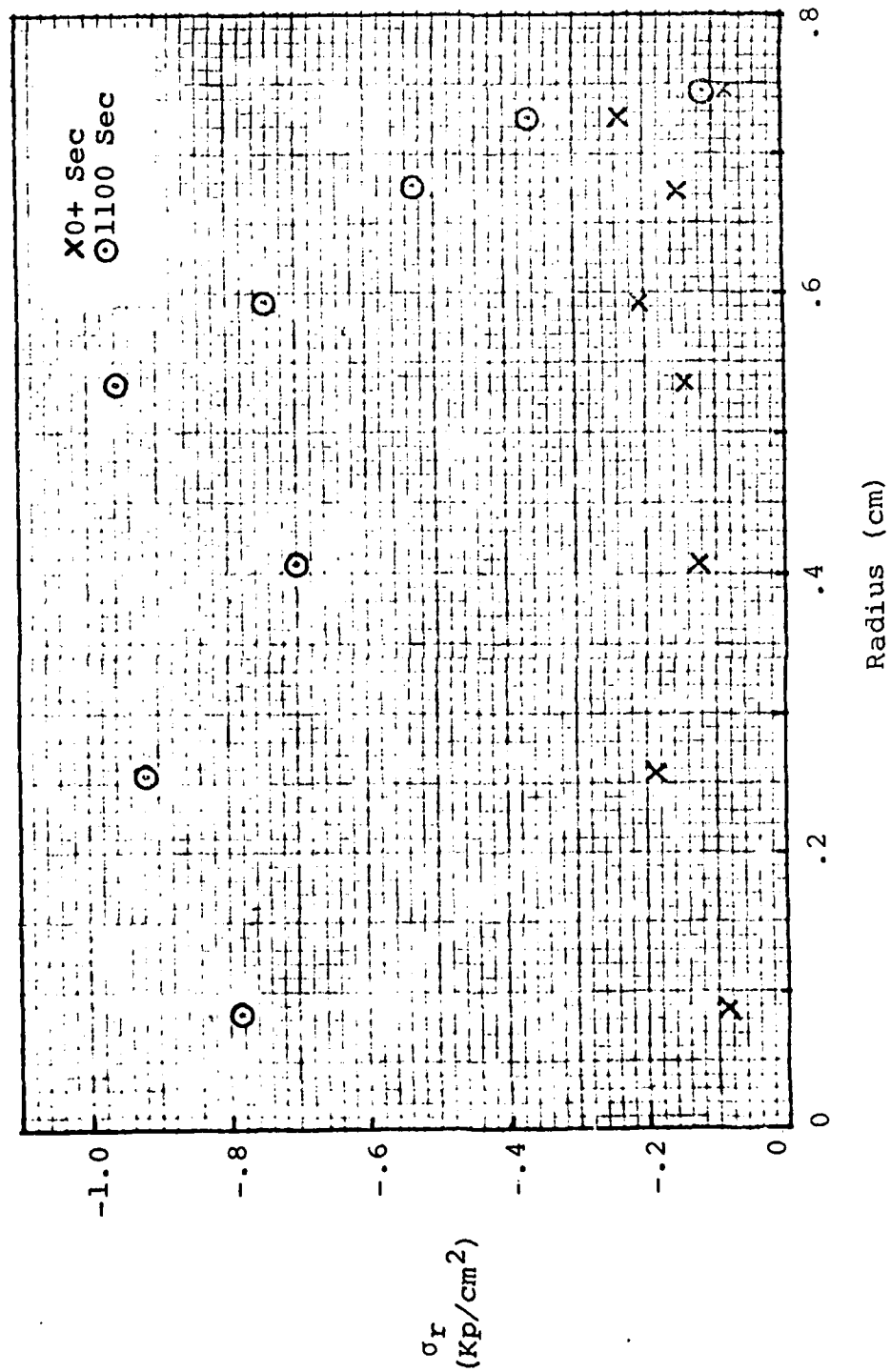


Fig. 3.3-AD. σ_r Distribution in Midplane, Inhomogeneous Case

Since the Cortex is relatively free to expand outwardly in this plane, radial stress applied by the Trabeculae could be relieved. This factor also explains why the Cortex experienced a greater proportion of hoop stress in this plane (Figs 3.3-AE through 3.3-AG), since radial displacement of the Cortex would tend to increase this stress. Finally shear stress (Figs 3.3-AH through 3.3-AJ) decreased with time in the Cortex and increased in the Trabeculae as a result of creep, again opposite to the trend in the boundary plane.

These differences in the stress variations in comparing the two planes suggest that the Bony end-plate has a dual role in helping to restrain the radial displacement of the Cortex, as well as transferring moment to it, as seen by the rise in local axial, radial, and shear stresses. This moment effect was even more pronounced when the Bony end-plate was made stiffer. For planes nearer the midplane of the Centrum, this restraining mechanism would not aid the Cortex allowing it to bulge outward (Fig. 3.3-AK) and hence experience greater hoop and radial stresses while relieving stress in the Trabeculae. If one compares the variation of stress in this plane, considering the higher load case with the homogeneous case, one notes that the hoop stress in the Cortex at 1100 seconds for the higher load (Fig. 3.3-AF) was about equal to the value at that location and time for the homogeneous case. Apparently, the hoop stresses within this plane, after enough creep deformation has taken place, are independent of

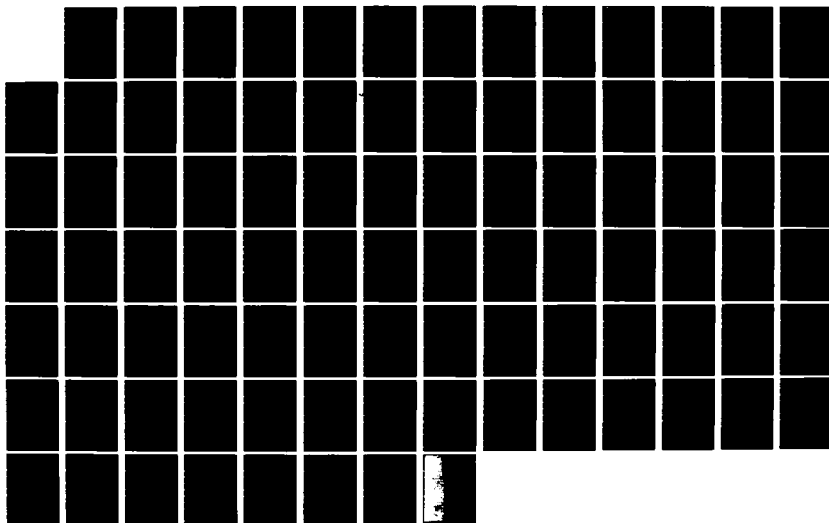
AD-A124 740

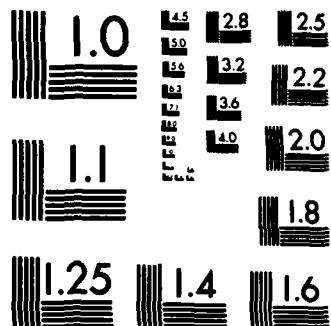
A FINITE ELEMENT ANALYSIS OF THE CREEP RESPONSE OF
LUMBAR INTERVERTEBRAL... (U) AIR FORCE INST OF TECH
WRIGHT-PATTERSON AFB OH SCHOOL OF ENGI... W J ROTHWELL
DEC 82 AFIT/GAE/AR/82D-24 F/G 6/19

2/2

UNCLASSIFIED

NL





MICROCOPY RESOLUTION TEST CHART
NATIONAL BUREAU OF STANDARDS-1963-A

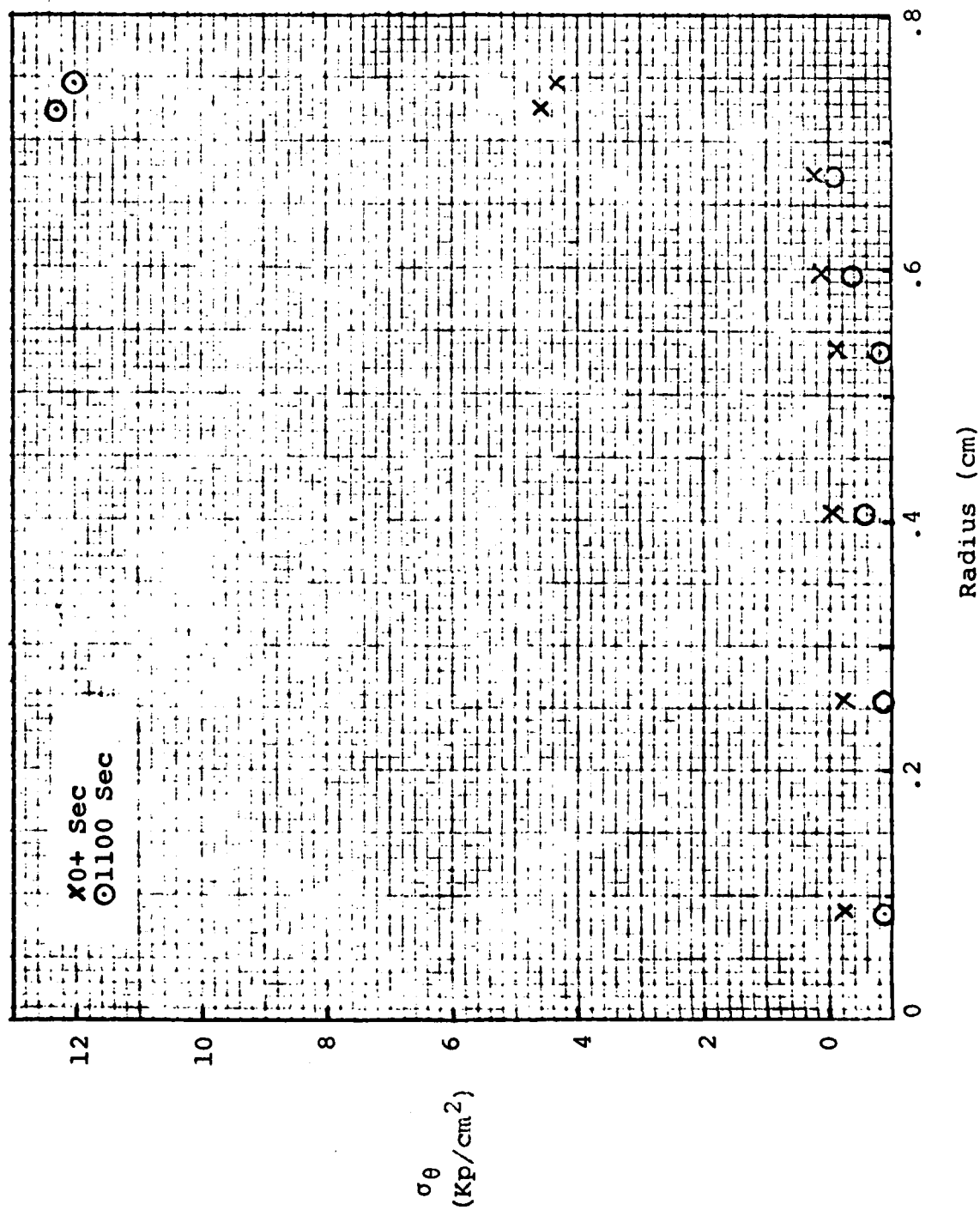


Fig. 3.3-AE. σ_θ Distribution in Midplane, Homogeneous Case

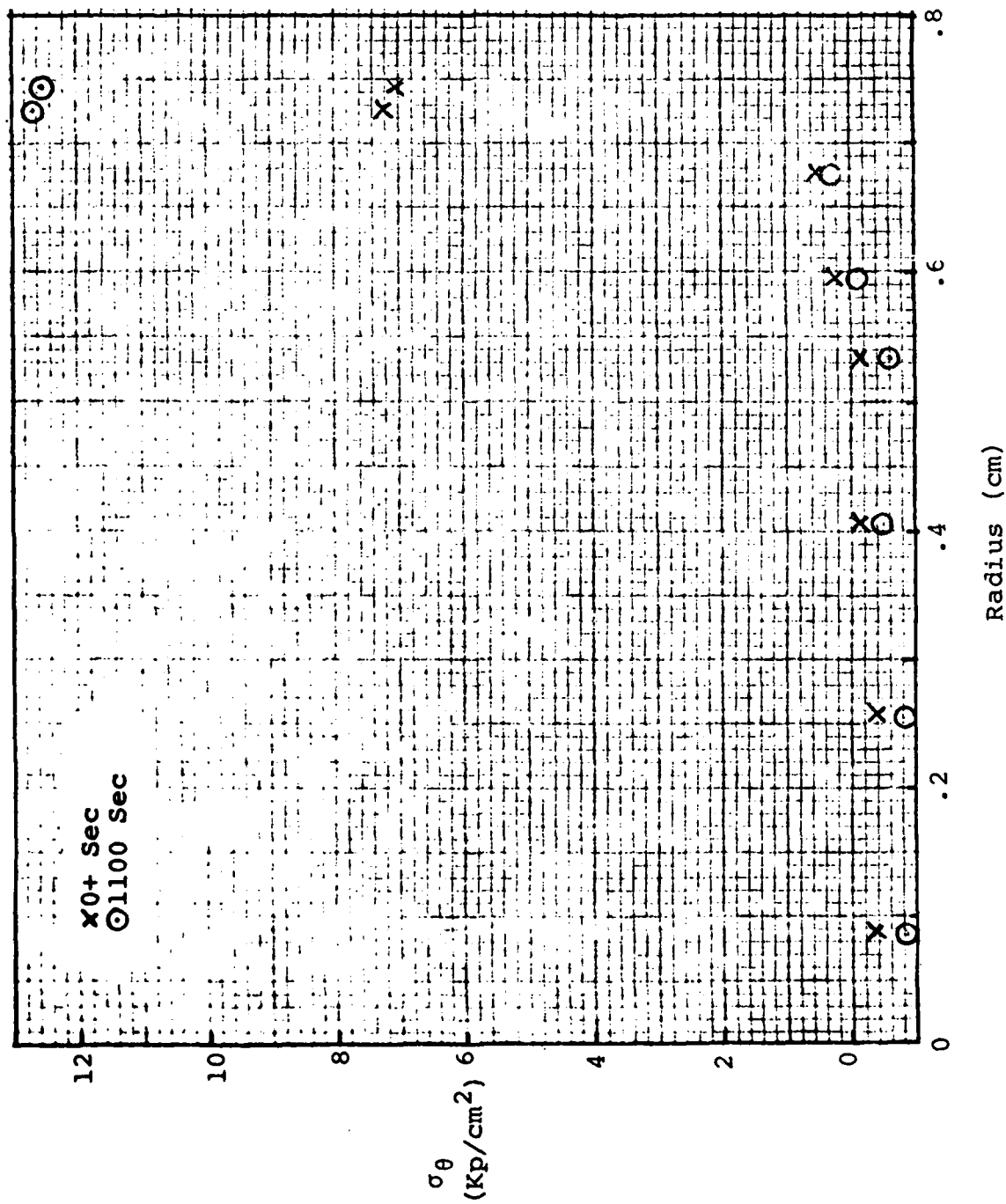
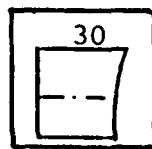


Fig. 3.3-AF. σ_θ Distribution in Midplane, Higher Load Case



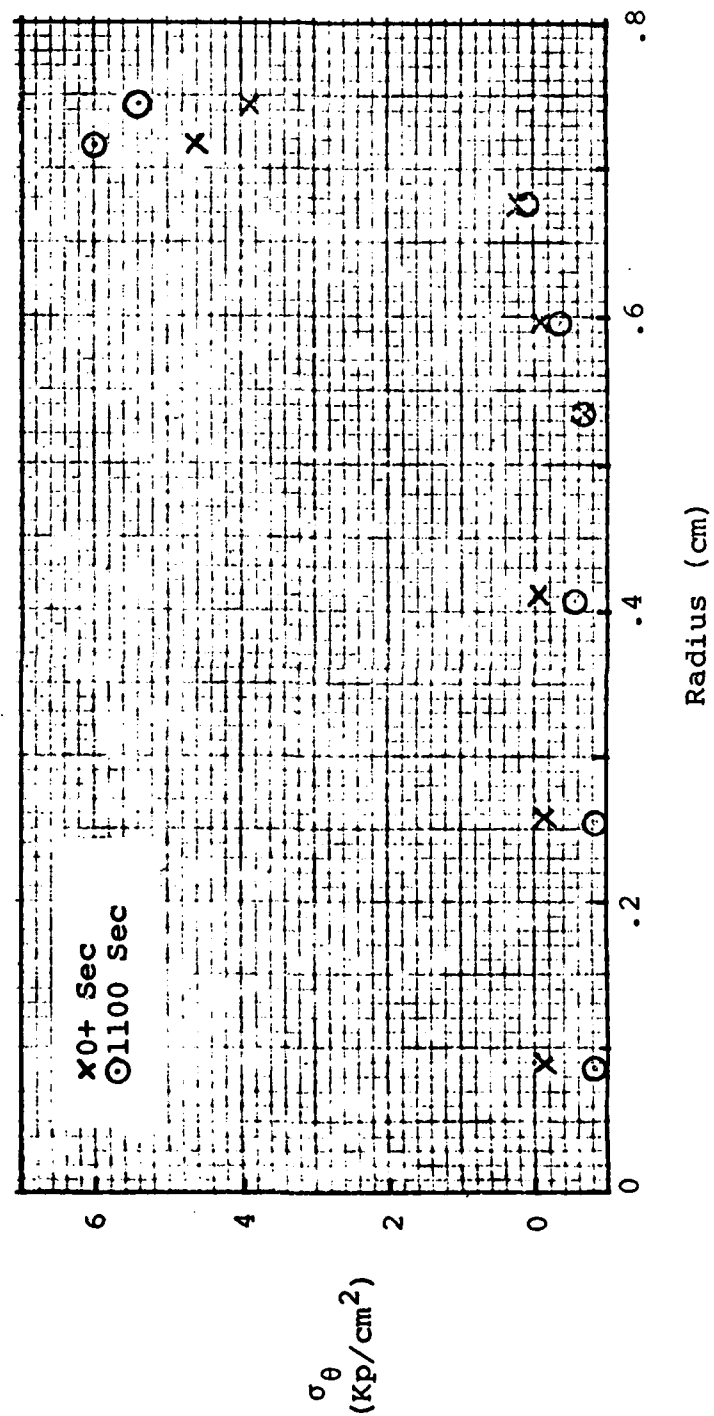
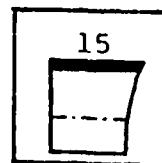


Fig. 3.3-AG. σ_θ Distribution in Midplane, Inhomogeneous Case



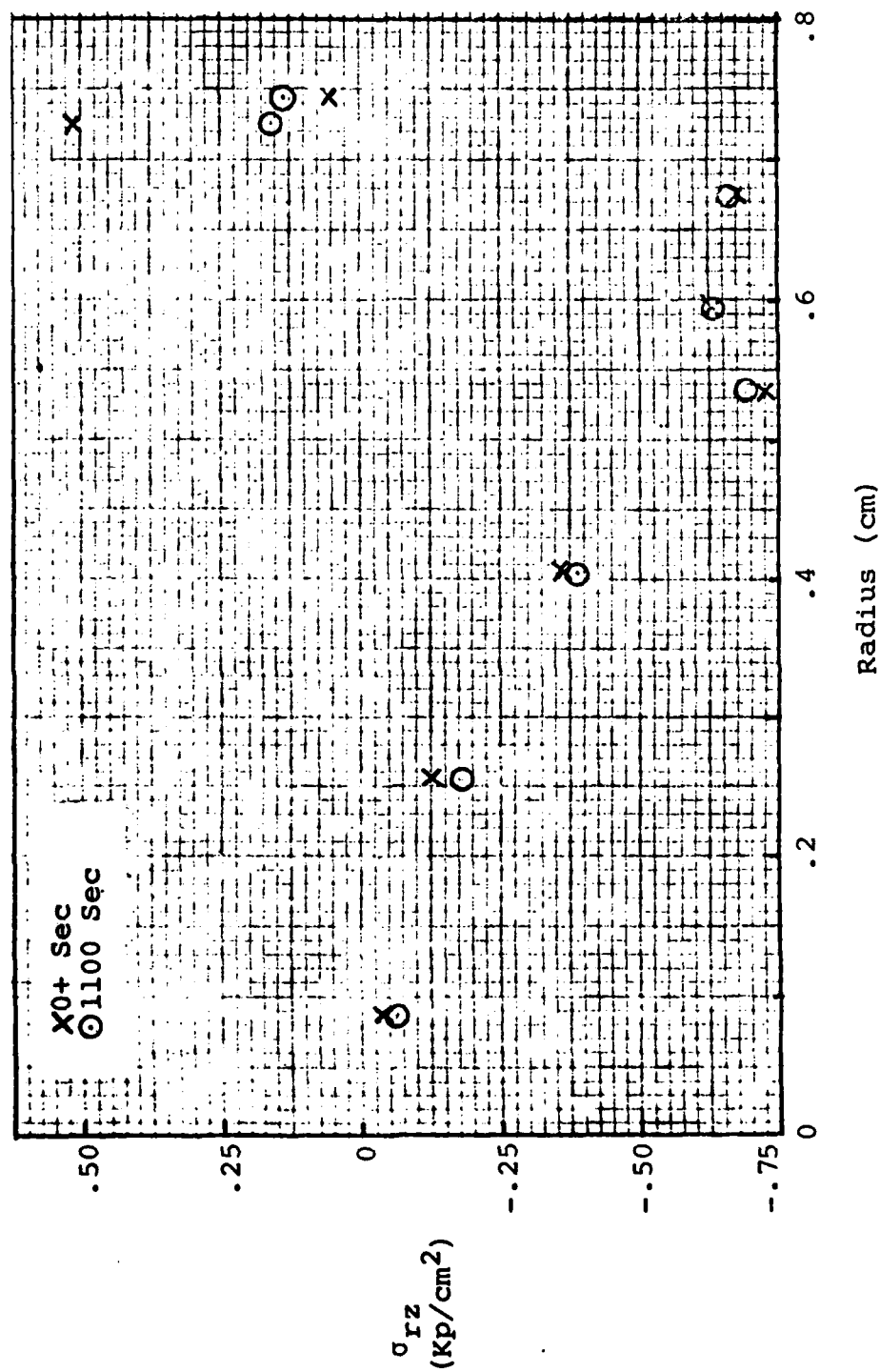
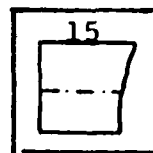


Fig. 3.3-AH. σ_{rz} Distribution in Midplane, Homogeneous Case



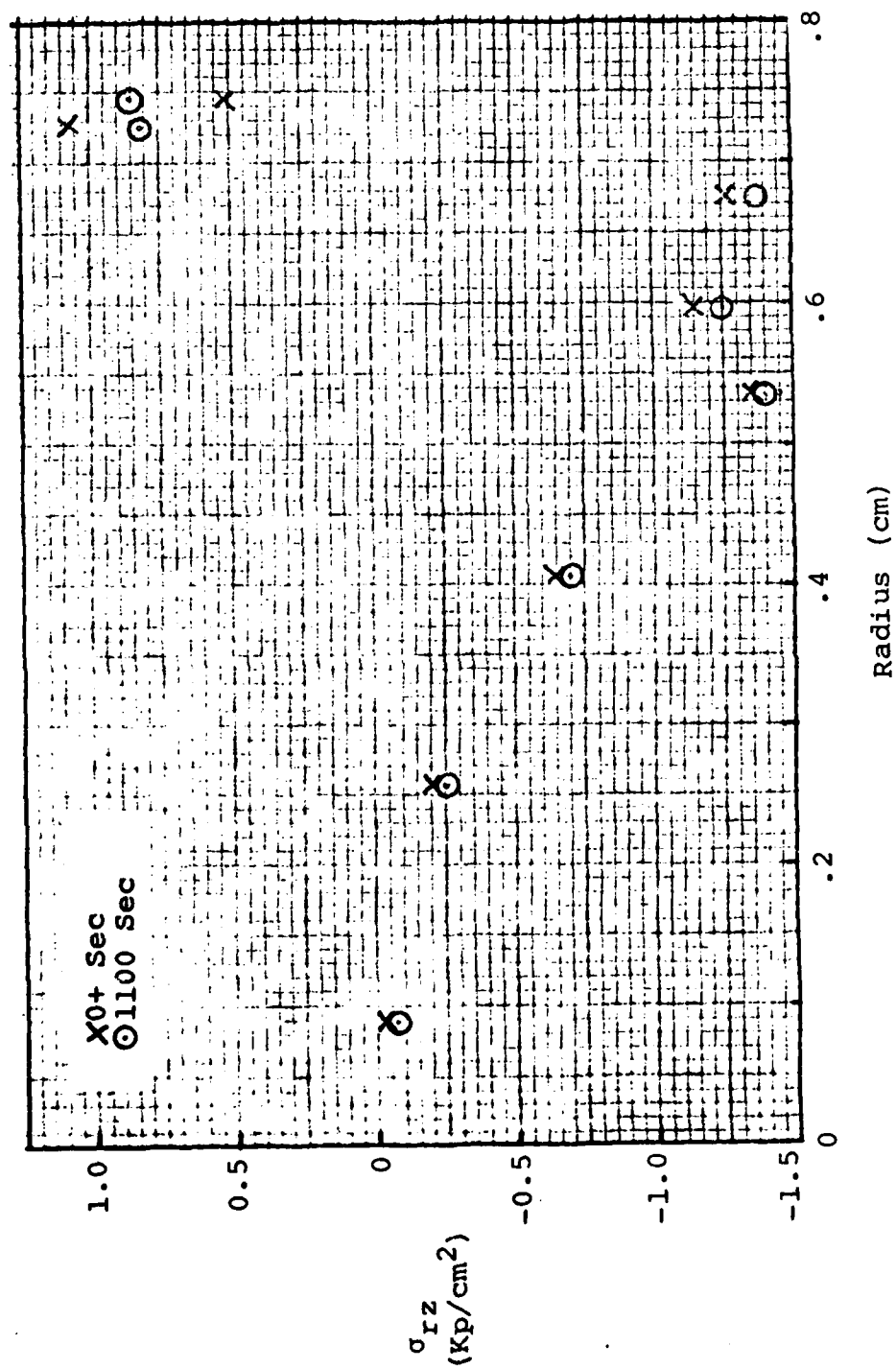
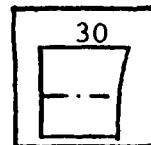


Fig. 3.3-AI. σ_{rz} Distribution in Midplane, Higher Load Case



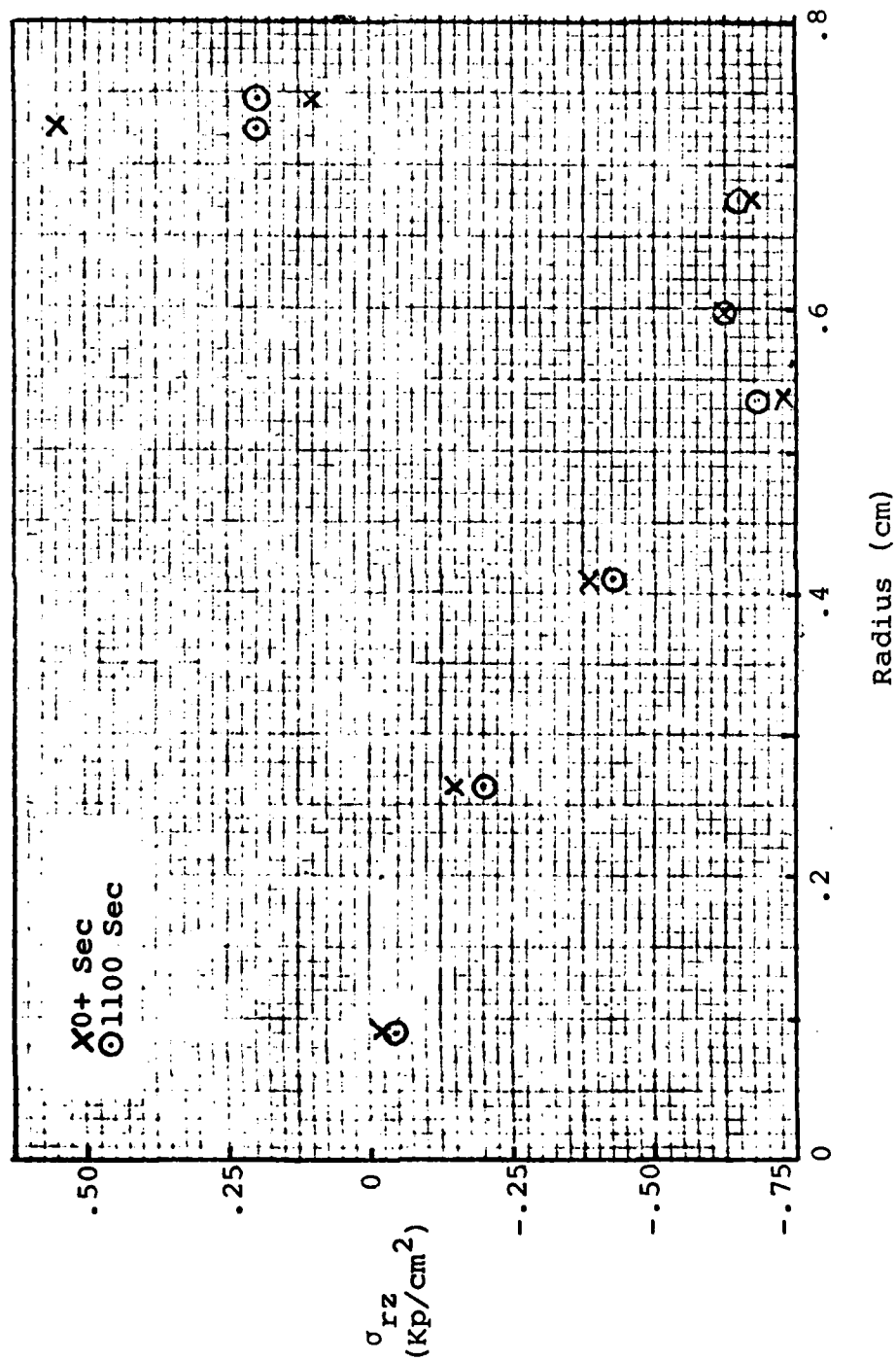


Fig. 3.3-AJ. σ_{rz} Distribution in Midplane, Inhomogeneous Case

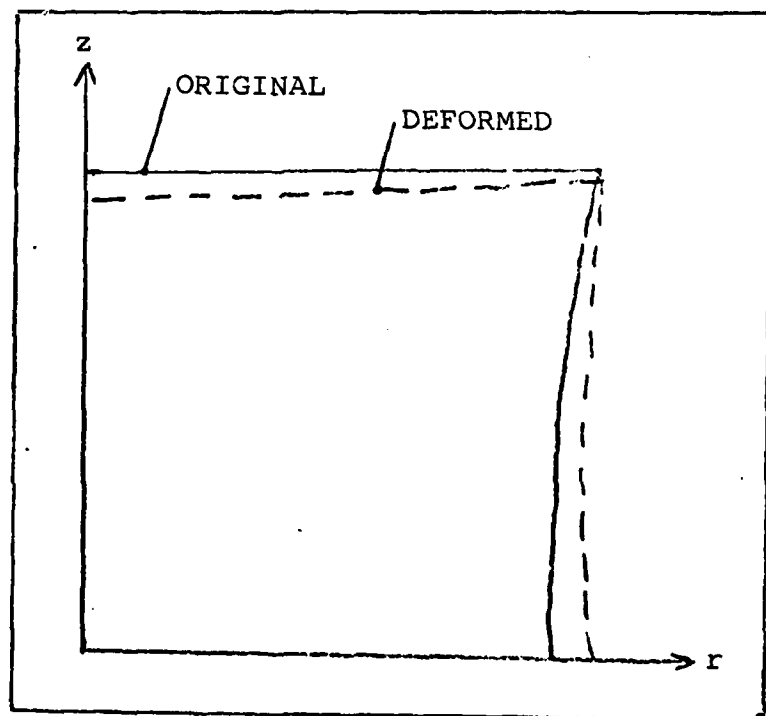


Fig. 3.3-AK. Comparison of Deformed to Undeformed Shape

the load.

Doubling the Bony end-plate stiffness affected the stresses more in the midplane than in the boundary plane. Most apparent was the relatively small amount of hoop stress redistributed in the Cortex (Fig. 3.3-AG) over the 1100 second period for the inhomogeneous case. This shows that the effect of a stiffer Bony end-plate has an effect on stresses in the far field as well as in the near field.

An analysis of the stresses versus time for the midplane element confirms this conclusion, as seen in Figs 3.3-AL through 3.3-AS, especially for the axial and shear components. Over time, for all three cases, the element experienced a reduction in axial and shear stresses, while the radial and tangential (hoop) components increased. Most interesting is the fact that the radial and tangential components were less in this element for the higher load case than for either 15 pound load cases. As before, this can be traced to the radial displacement, as the element lengthened radially nearly 10% more under the 30 pound load (Fig. 3.3-AT). In this manner, the higher axial load caused the element to be relieved of radial and hoop stress by these radial displacements, as the element achieved a state of equilibrium.

The overall results for the flexible analysis imply that the effect of load was to cause a greater radial displacement of the Centrum midplane. The assumption that the Bony end-plate and the Cortex are homogeneous is reasonable,

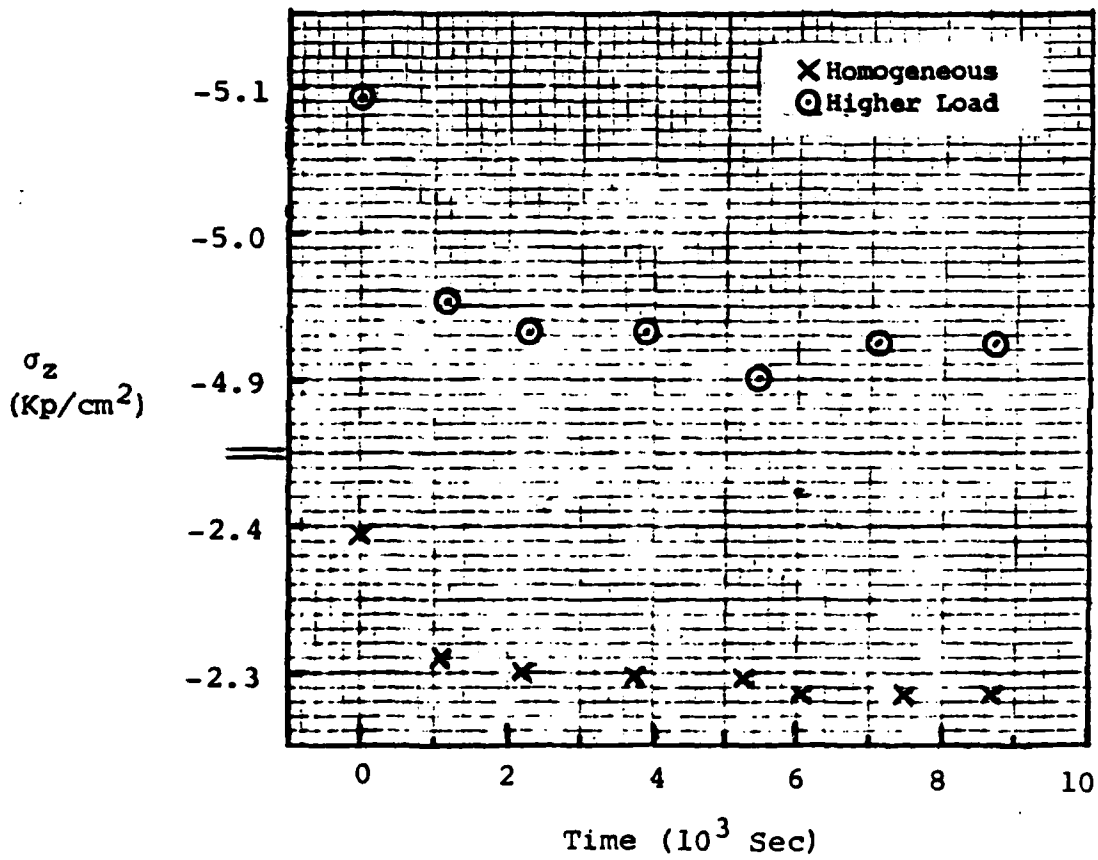
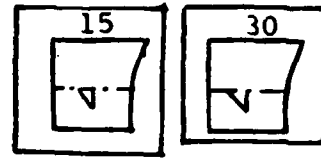


Fig. 3.3-AL. σ_z Versus Time in Midplane Element, Homogeneous and Higher Load Cases

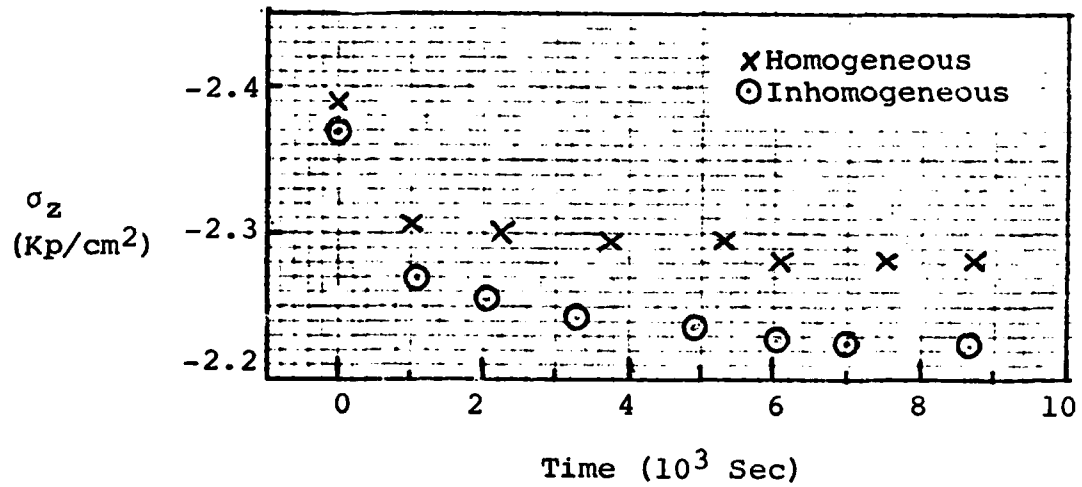
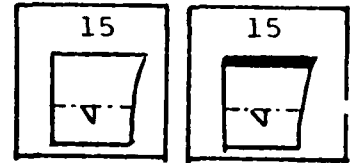


Fig. 3.3-AM. σ_z Versus Time in Midplane Element, Homogeneous and Inhomogeneous Cases

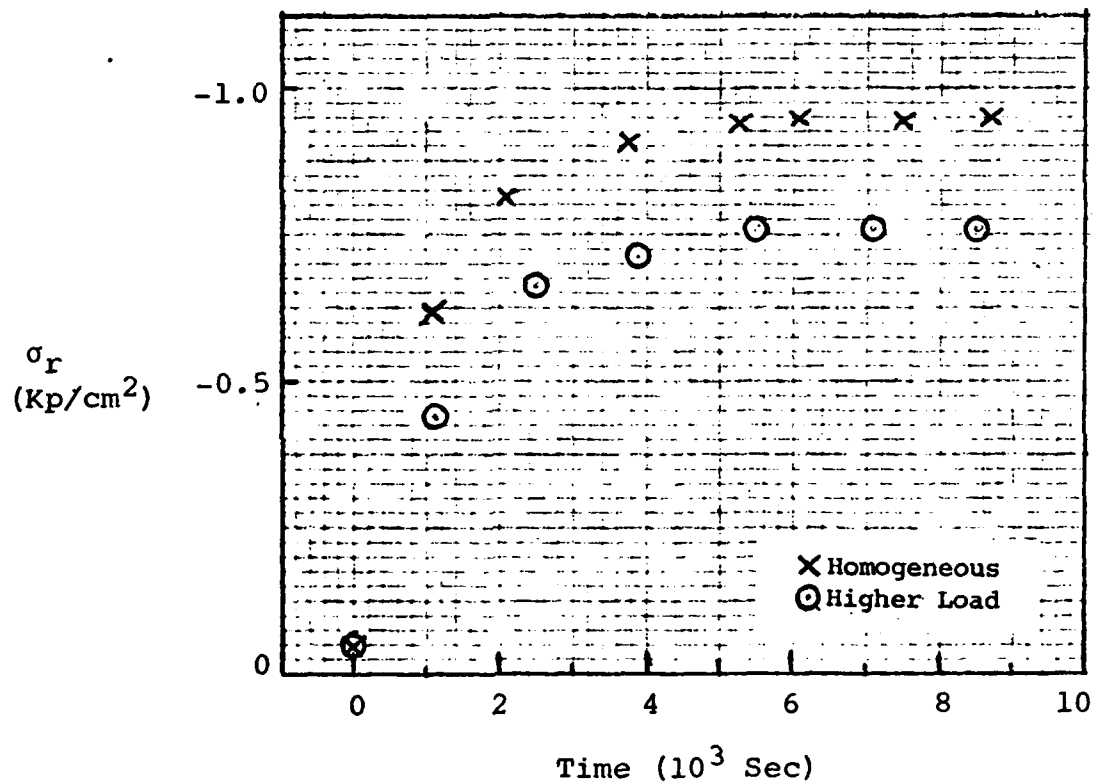
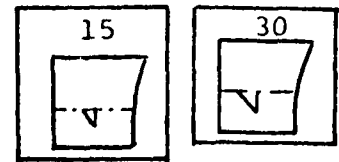


Fig. 3.3-AN. σ_r Versus Time in Midplane Element, Homogeneous and Higher Load Cases

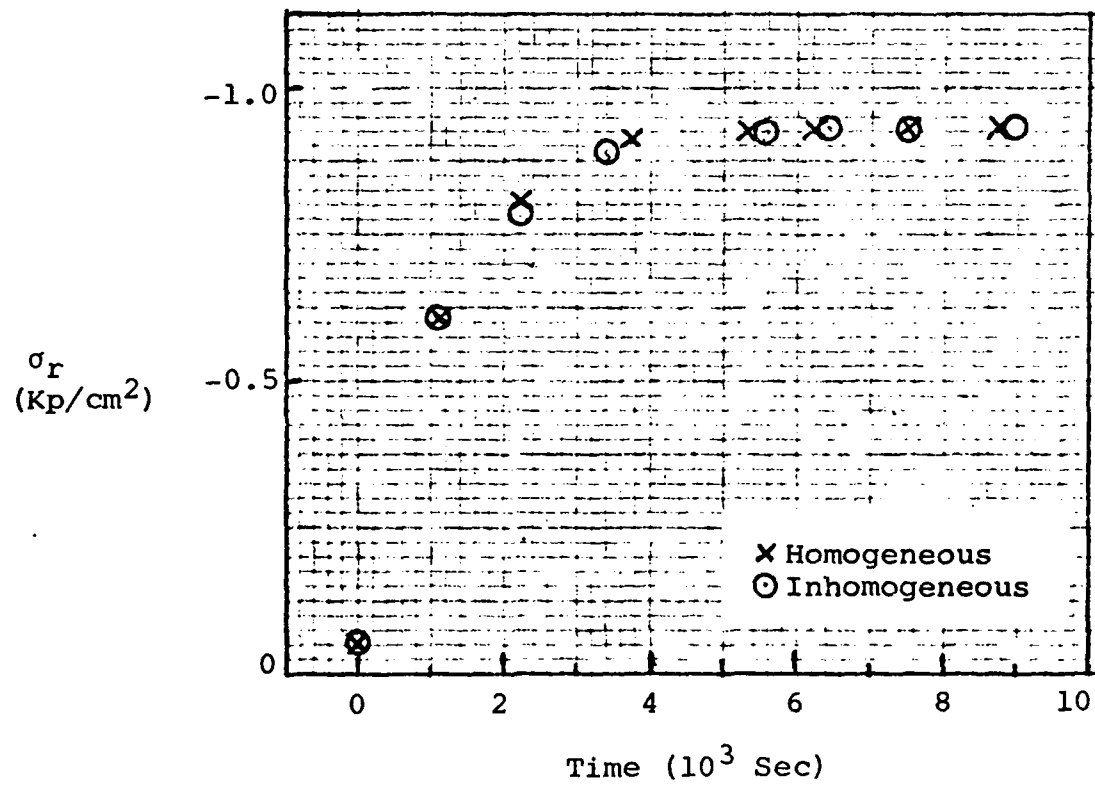
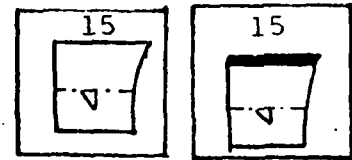


Fig. 3.3-A0. σ_r Versus Time in Midplane Element, Homogeneous and Inhomogeneous Cases

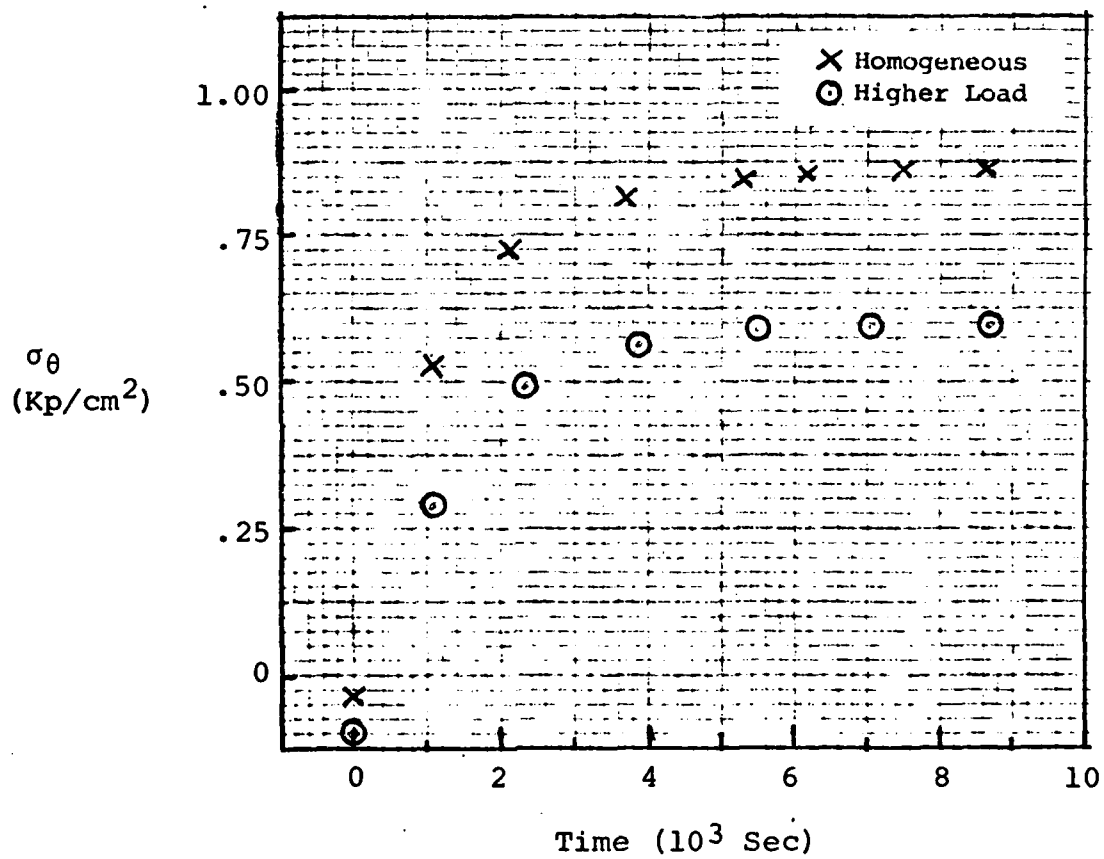
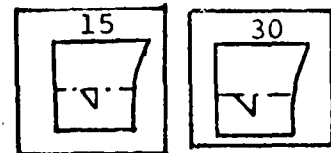


Fig. 3.3-AP. σ_{θ} Versus Time in Midplane Element, Homogeneous and Higher Load Cases

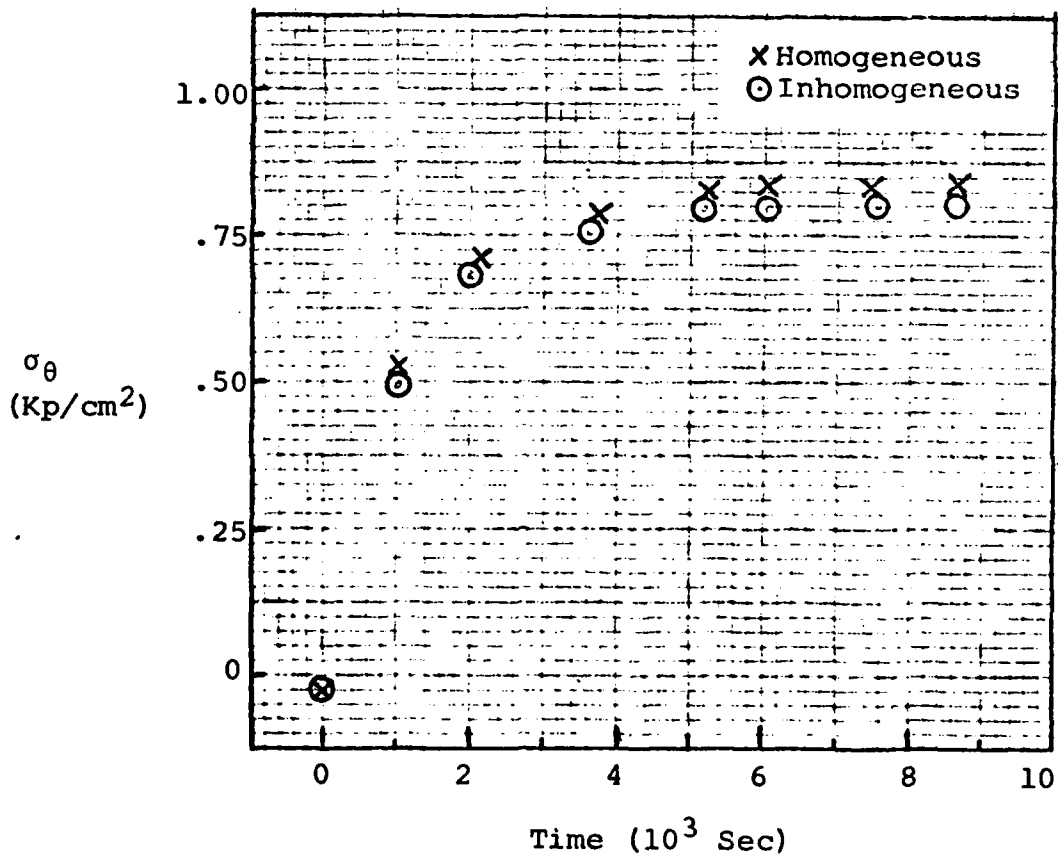
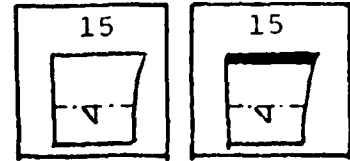


Fig. 3.3-AQ. σ_θ Versus Time in Midplane Element, Homogeneous and Inhomogeneous Cases

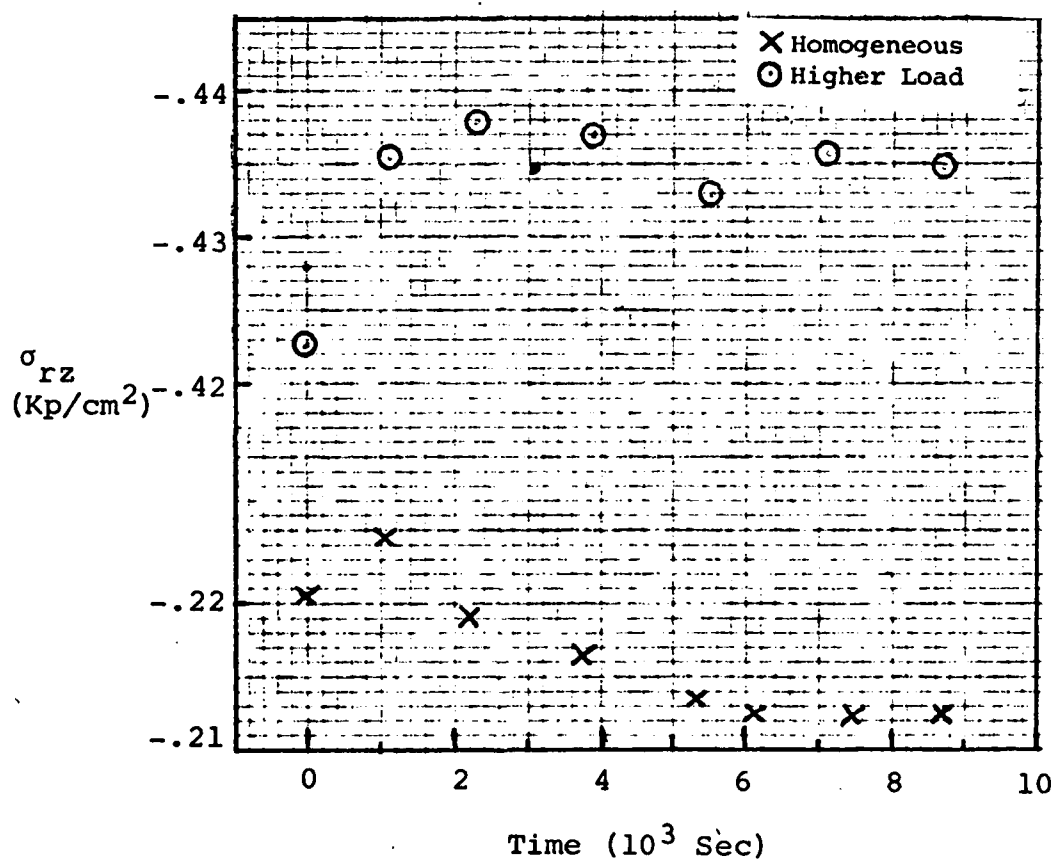
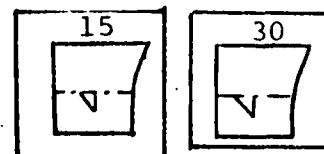


Fig. 3.3-AR. σ_{rz} Versus Time in Midplane Element, Homogeneous and Higher Load Cases

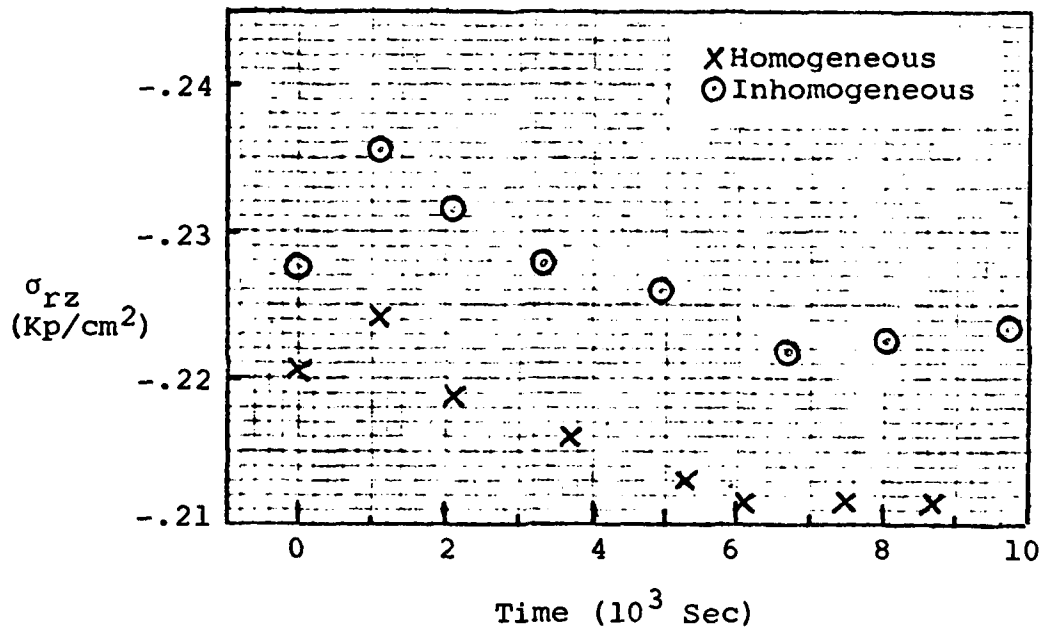
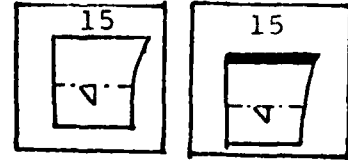


Fig. 3.3-AS. σ_{rz} Versus Time in Midplane Element, Homogeneous and Inhomogeneous Cases

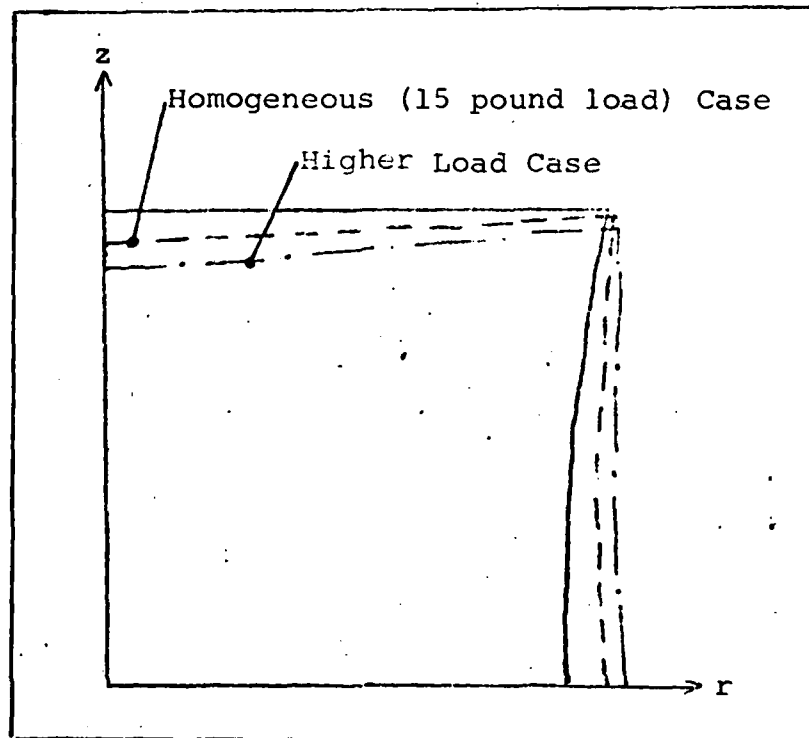


Fig. 3.3-AT. Comparison of Deformed Shapes for the Homogeneous and Higher Load Cases After 1100 Seconds

since doubling the stiffness of the former had little effect on the overall creep response of the Centrum. Unless the Bony end-plate is significantly stiffer than was assumed, the homogeneous assumption is adequate.

3.3.2 Stiff Case. To account for the upper bound on the range of values, the Cortex and Bony end-plate were next assigned an E value much greater than before, and a new set of viscoelastic parameters found for the Trabecular region. These new values were $E = 98.5 \text{ Kp/Sq cm}$, $q_0 = 14 \text{ Kp/Sq cm}$, and $q_1 = 28,140 \text{ Kp/Sq cm-sec}$. Each value was less than its respective counterpart determined using the flexible Bony end-plate and Cortex, again underscoring the influence of the two regions on the creep response of the Centrum.

To provide a check on the results, Eq (3-3) of section 3.2.1 was used to compare the known ratio of Human to Rhesus Monkey Centrum moduli of elasticity to the analytically determined ratio of Human to Rhesus Monkey Trabeculae moduli of elasticity. Using the information in that section as well as a Human Trabeculae E value obtained from Belytschko, et al (Ref 3), the two ratios were 6.2 for the Centra and 7.6 for the Trabecular regions. Hence, Eq (3-3) is a useful method to approximate Rhesus Monkey moduli of elasticity, in the absence of precise values.

Figure 3.3-AU shows the analytical solution for average top-surface displacement. To avoid repetition of the analyses of the flexible case, only the 15 pound load data was matched. Figures 3.3-AV through 3.3-BC show the stress distributions

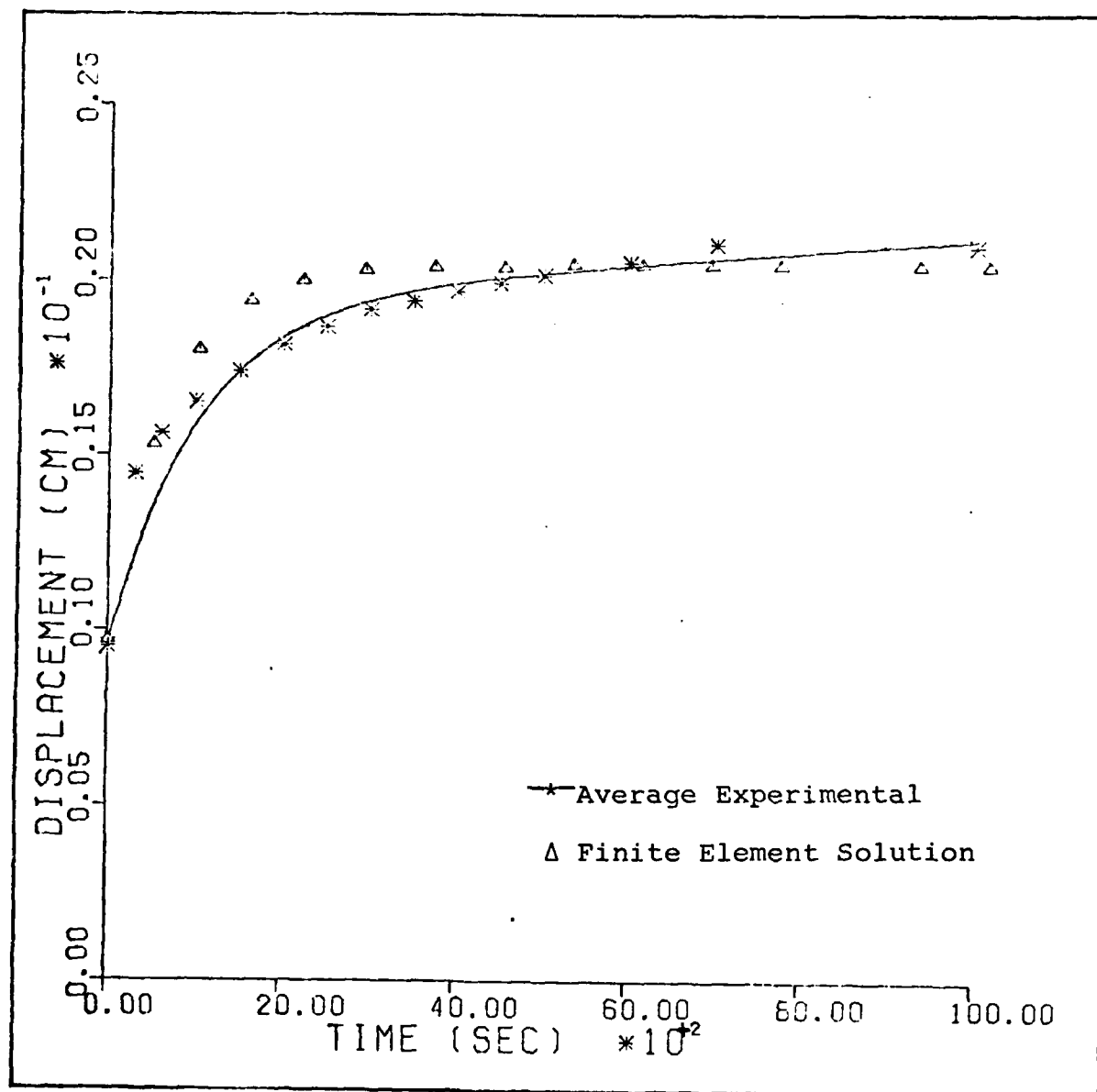


Fig. 3.3-AU. Finite Element Solution, Stiff Case

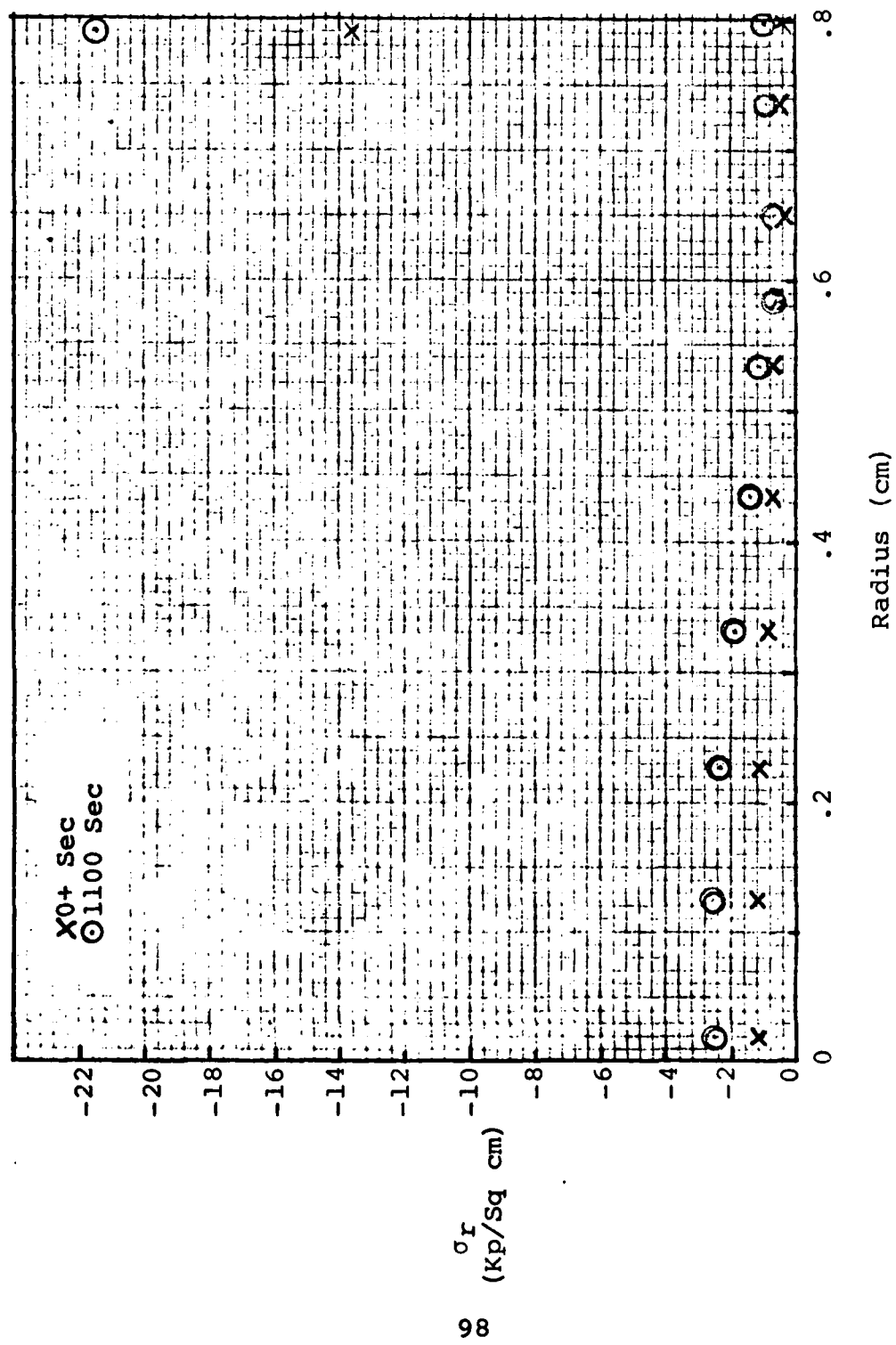
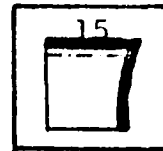


Fig. 3.3-AV. σ_r Distribution in Boundary Plane, Stiff Case



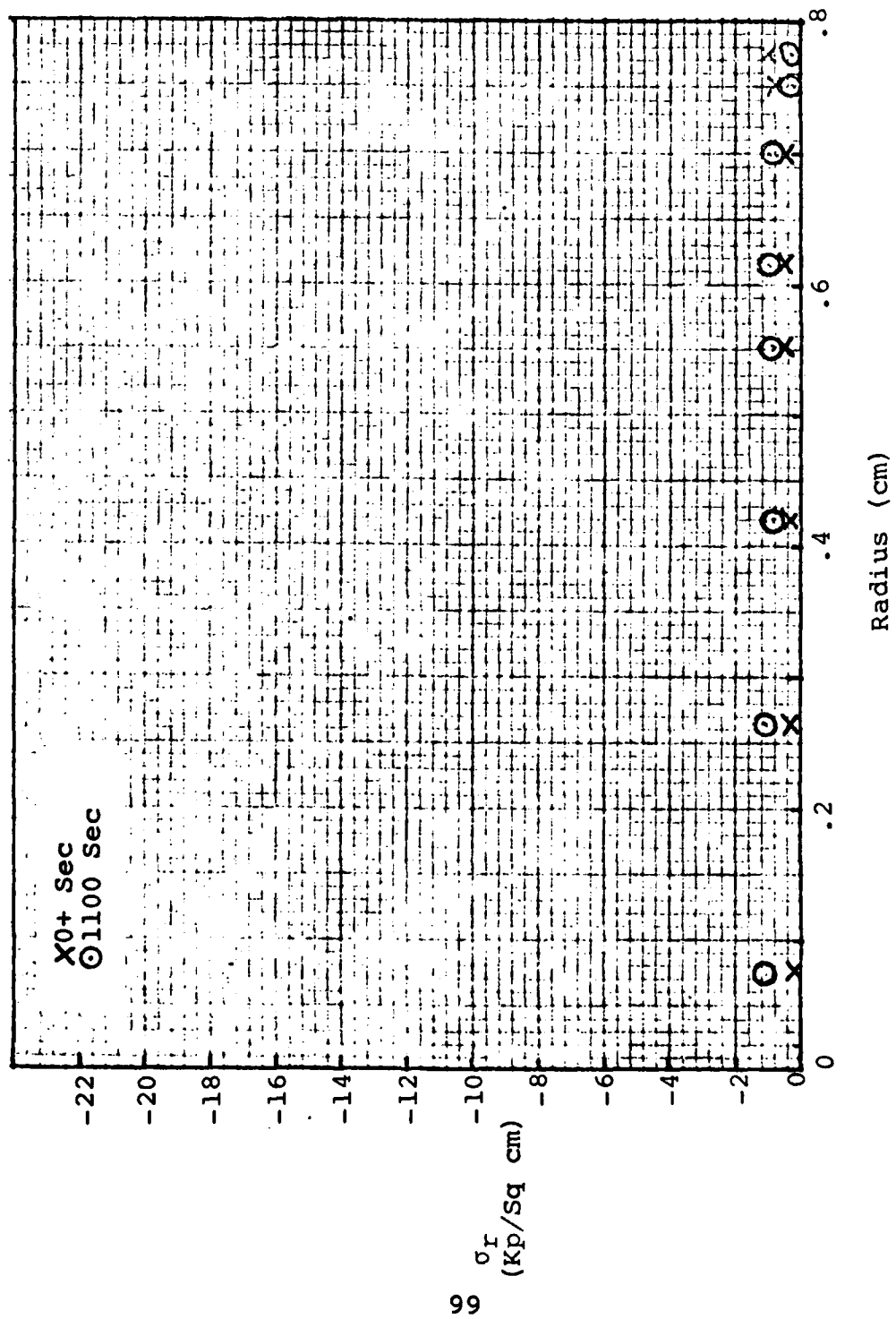


Fig. 3.3-AW. σ_r Distribution in Midplane, Stiff Case

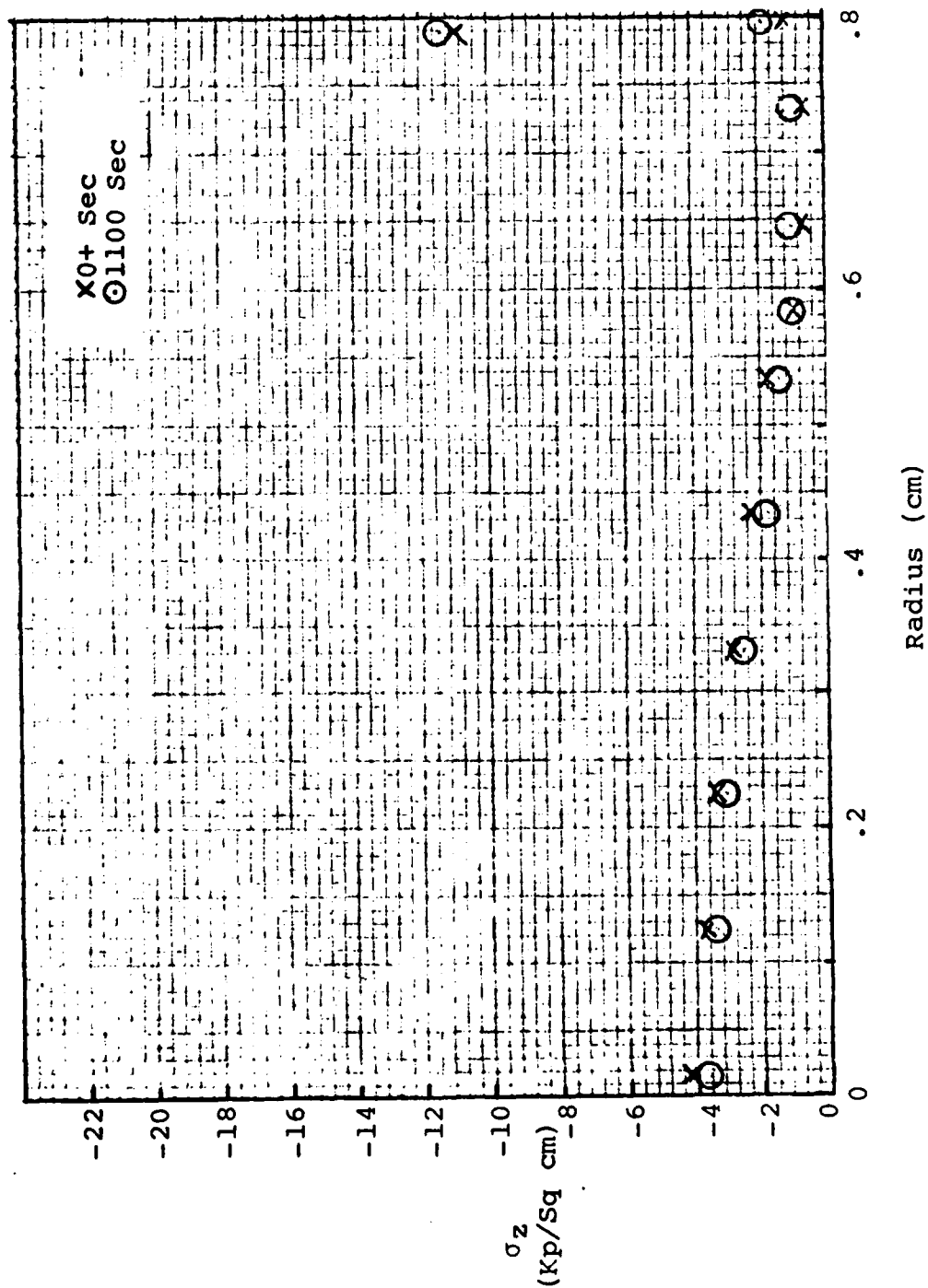


Fig. 3.3-AX. σ_z Distribution in Boundary Plane, Stiff Case

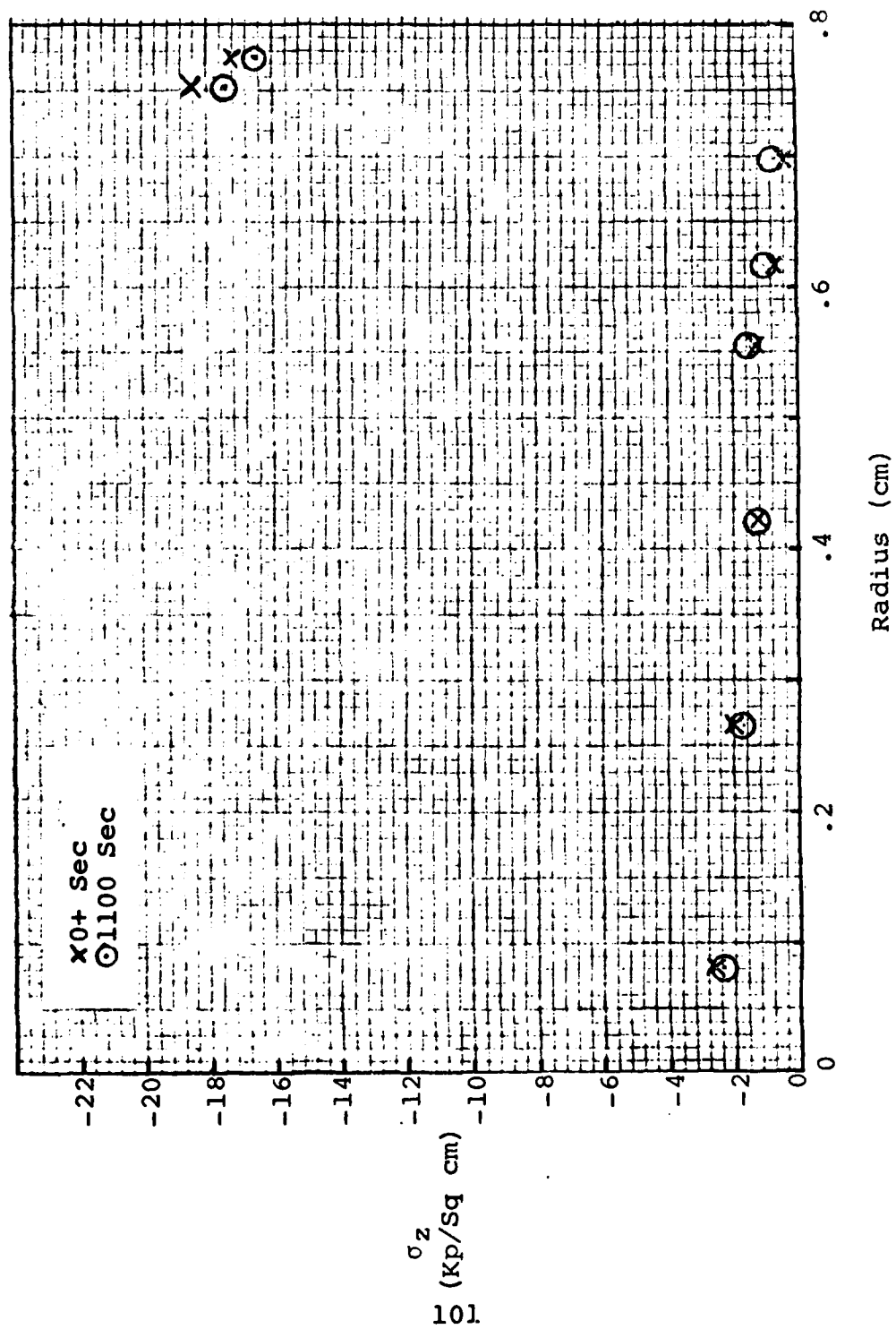


Fig. 3.3-AY. σ_z Distribution in Midplane, Stiff Case

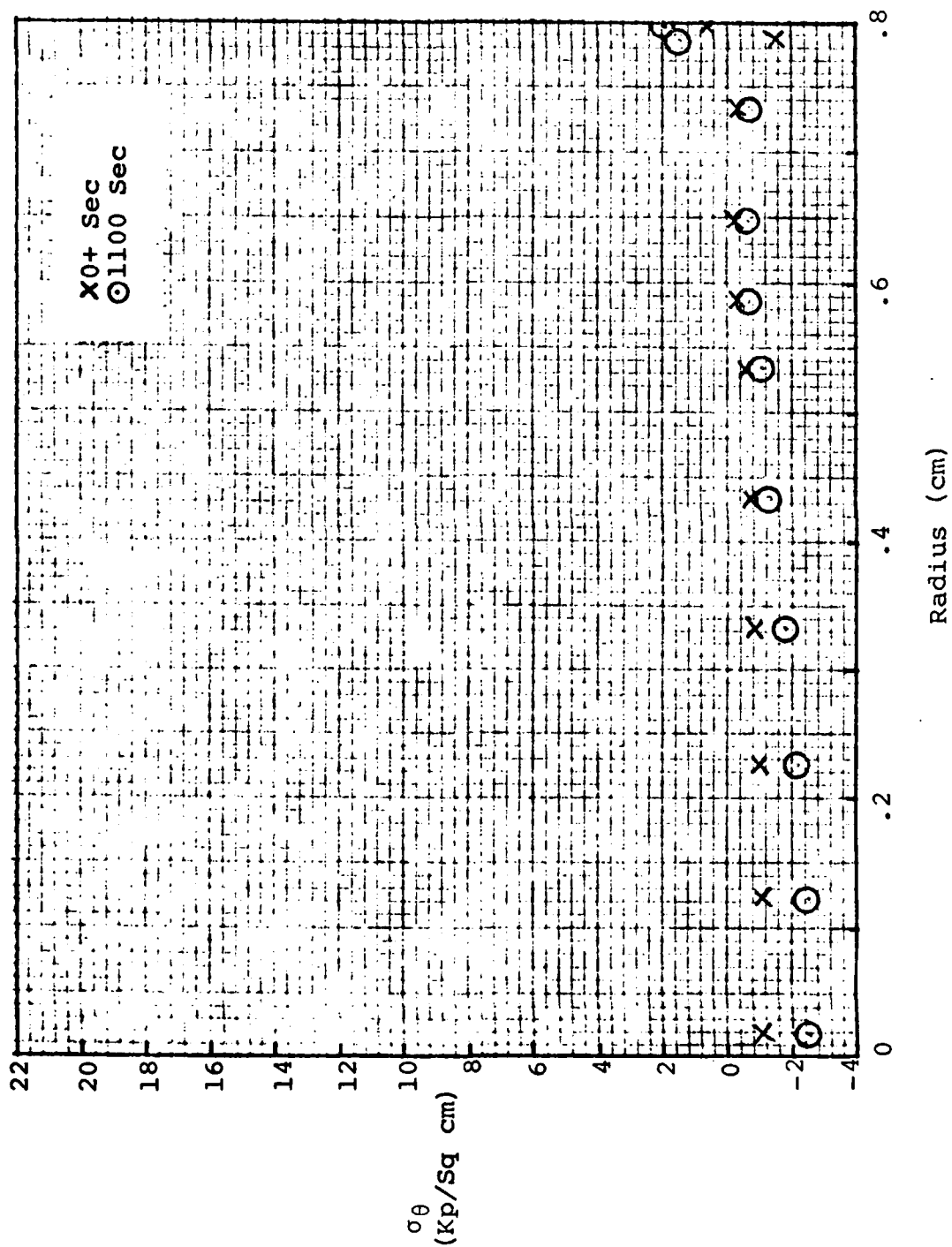
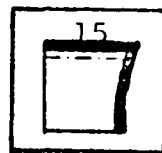


Fig. 3.3-AZ. σ_θ Distribution in Boundary Plane, Stiff Case



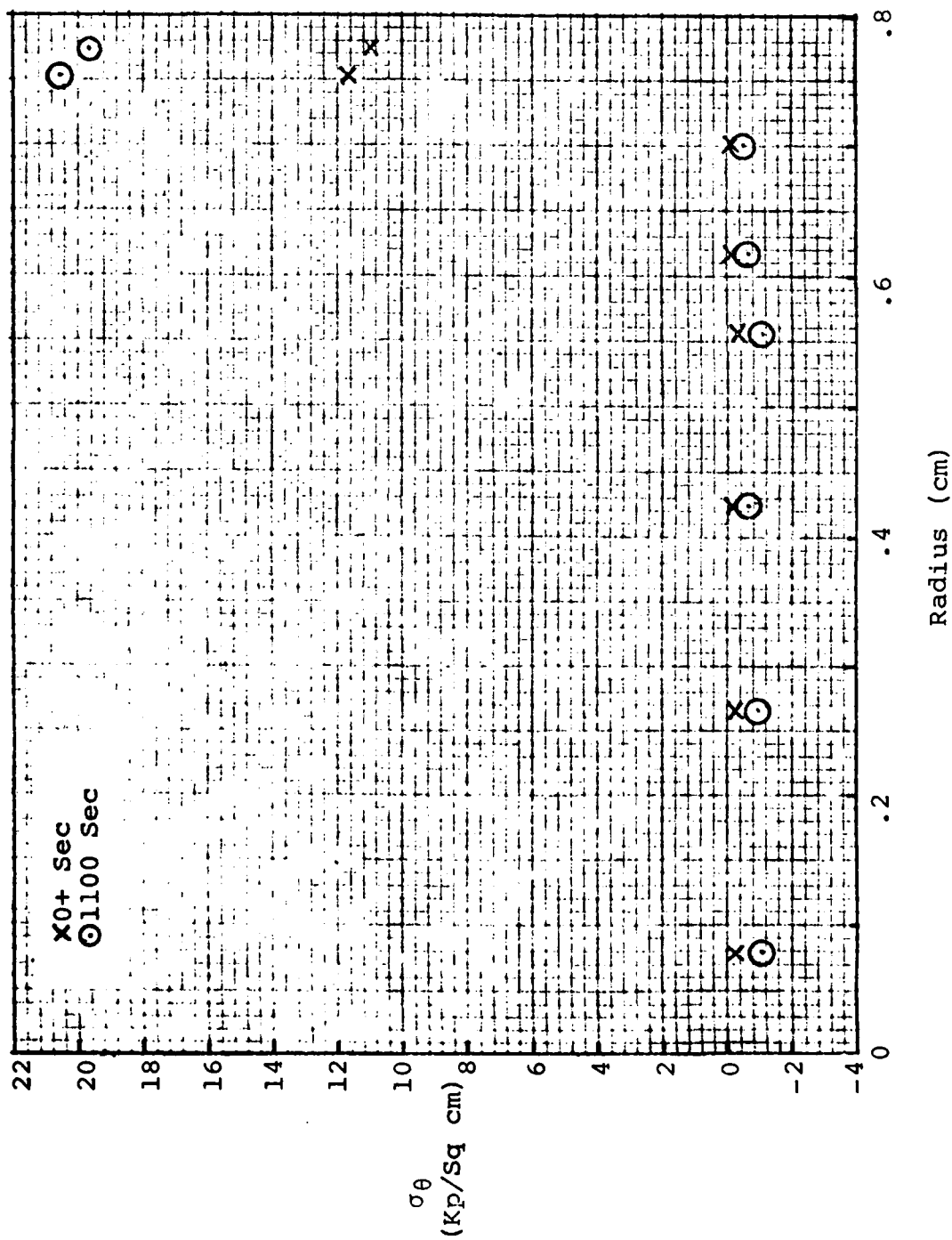


Fig. 3.3-BA. σ_θ Distribution in Midplane, Stiff Case

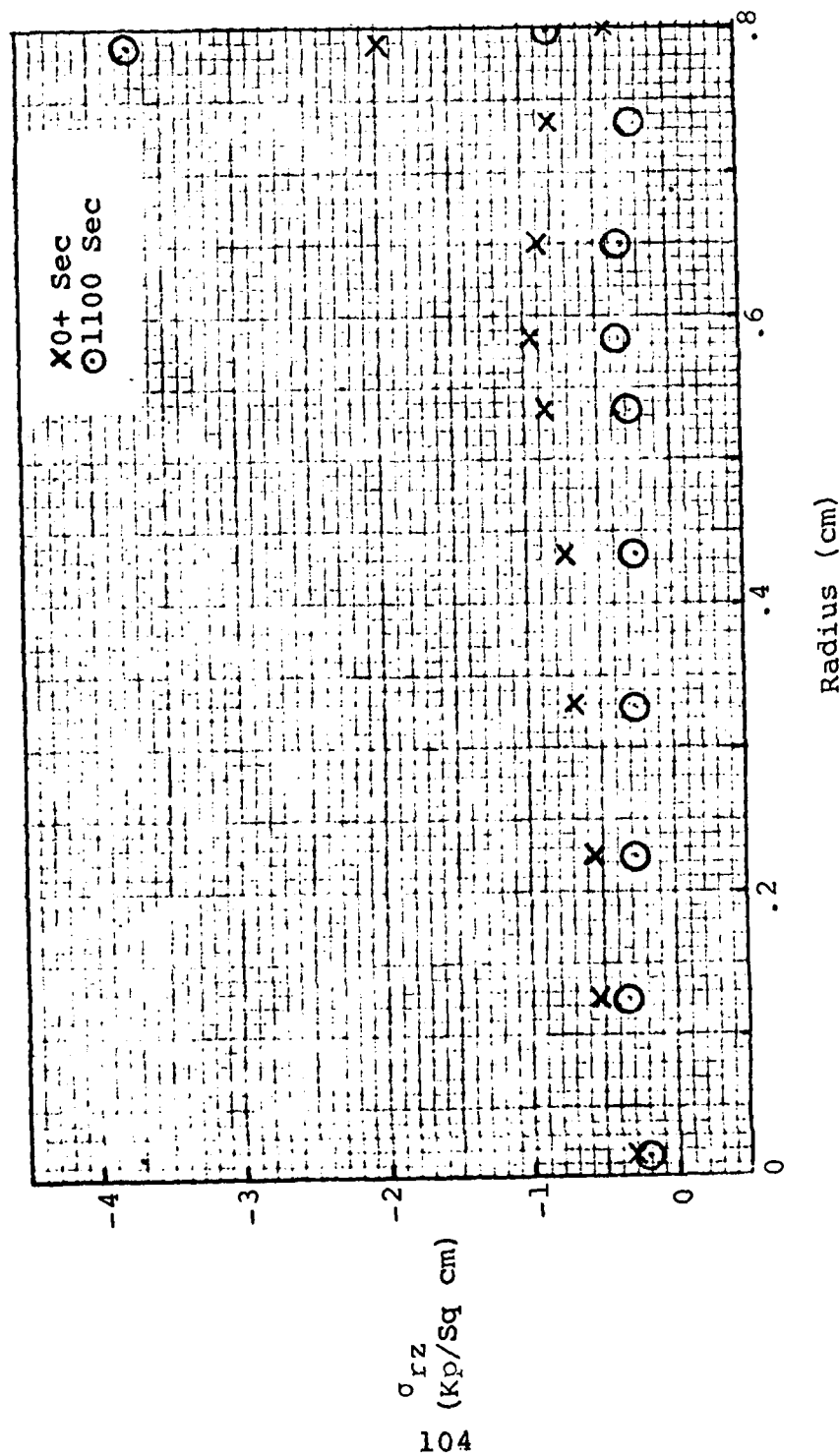


Fig. 3.3-BB. σ_{rz} Distribution in Boundary Plane, Stiff Case

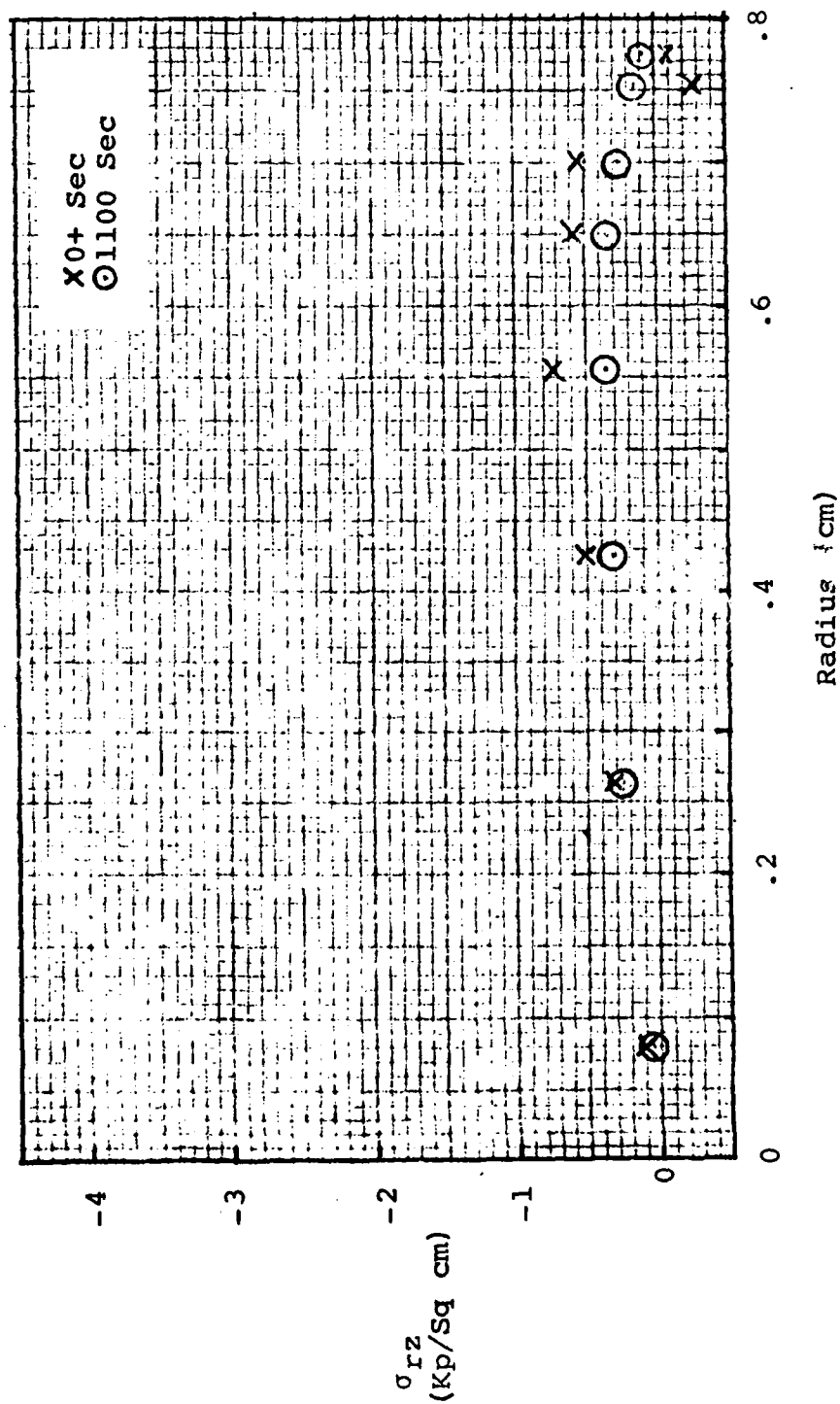


Fig. 3.3-BC. σ_{rz} Distribution in Midplane, Stiff Case

in the boundary plane and midplane, where the plots are again organized by stress component for comparison purposes. The same general trends existed in each plane regarding radial stress variation and stress redistribution, as existed in those planes for the homogeneous case (flexible Cortex) discussed in the previous section. Differences were in the relative contribution of Cortex and Trabeculae in carrying loads. In the stiff case, the Cortex carried a proportionately larger share of radial and tangential stresses in the boundary plane (Figs 3.3-AV and 3.3-AZ). Trabeculae stresses also tended to be more evenly distributed in both planes.

The midplane element experienced the same general stress-time response (Figs 3.3-PD through 3.3-BG), but the axial stress for the boundary element (Fig. 3.3-BE) decreased with time instead of increasing, as it did for the homogeneous case of the previous section. The stiffer Bony end-plate/Cortex combination allowed the axial stress to relax under creep deformation.

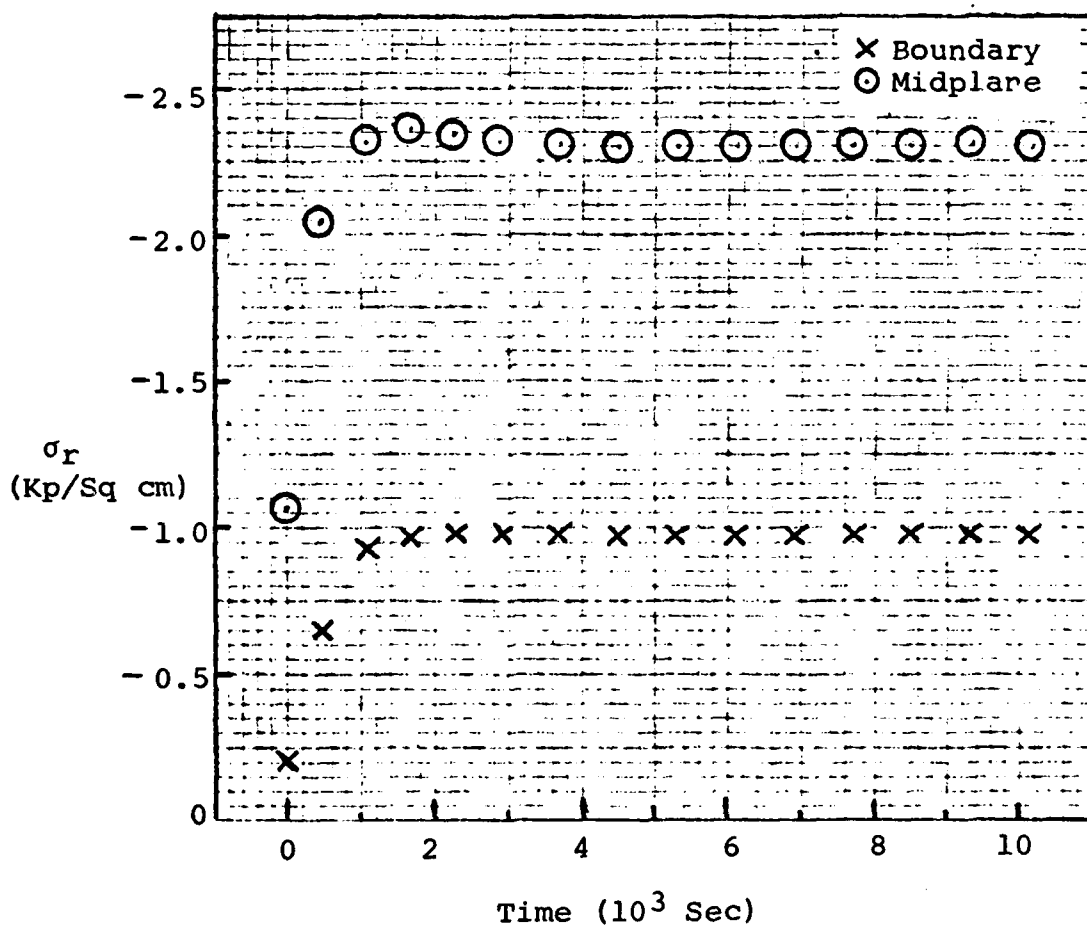
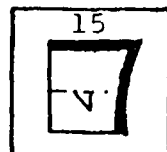
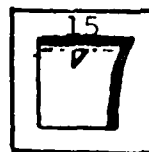


Fig. 3.3-BD. σ_r Versus Time in Boundary and Midplane Elements, Stiff Case

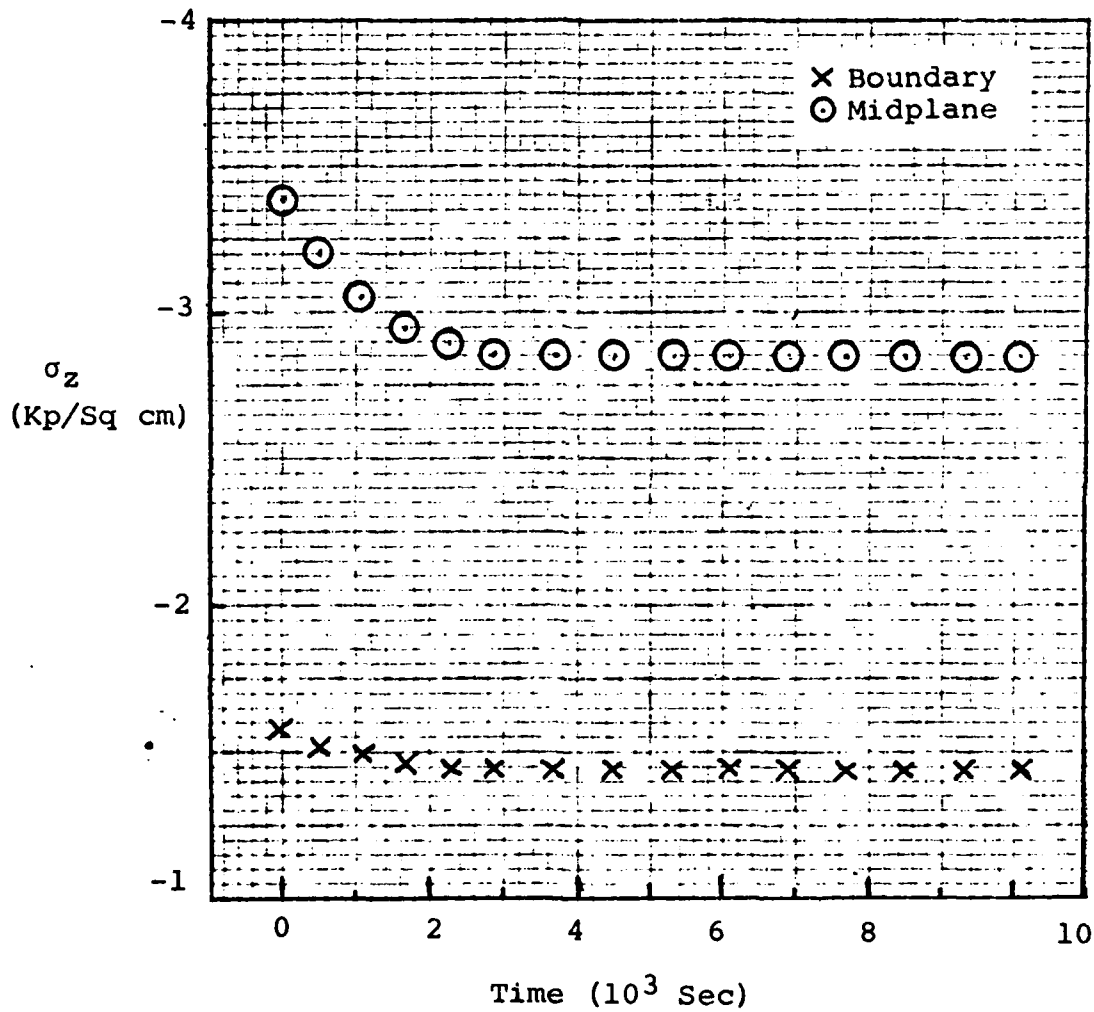
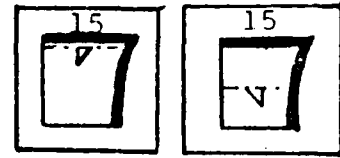


Fig. 3.3-BE. σ_z Versus Time in Boundary and Midplane Elements, Stiff Case

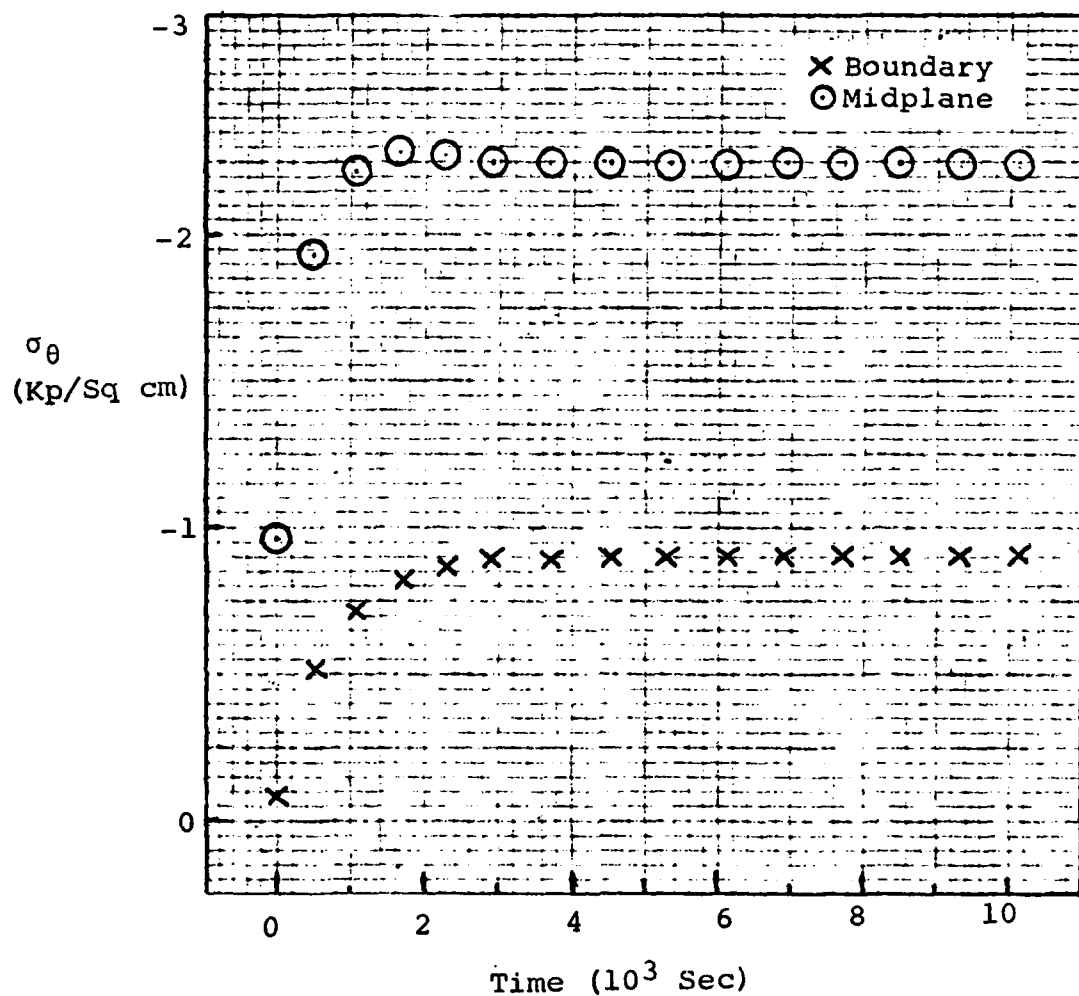
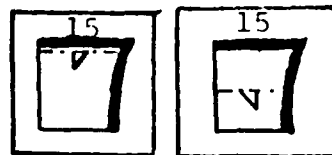


Fig. 3.3-BF. σ_θ Versus Time in Boundary and Midplane Elements, Stiff Case

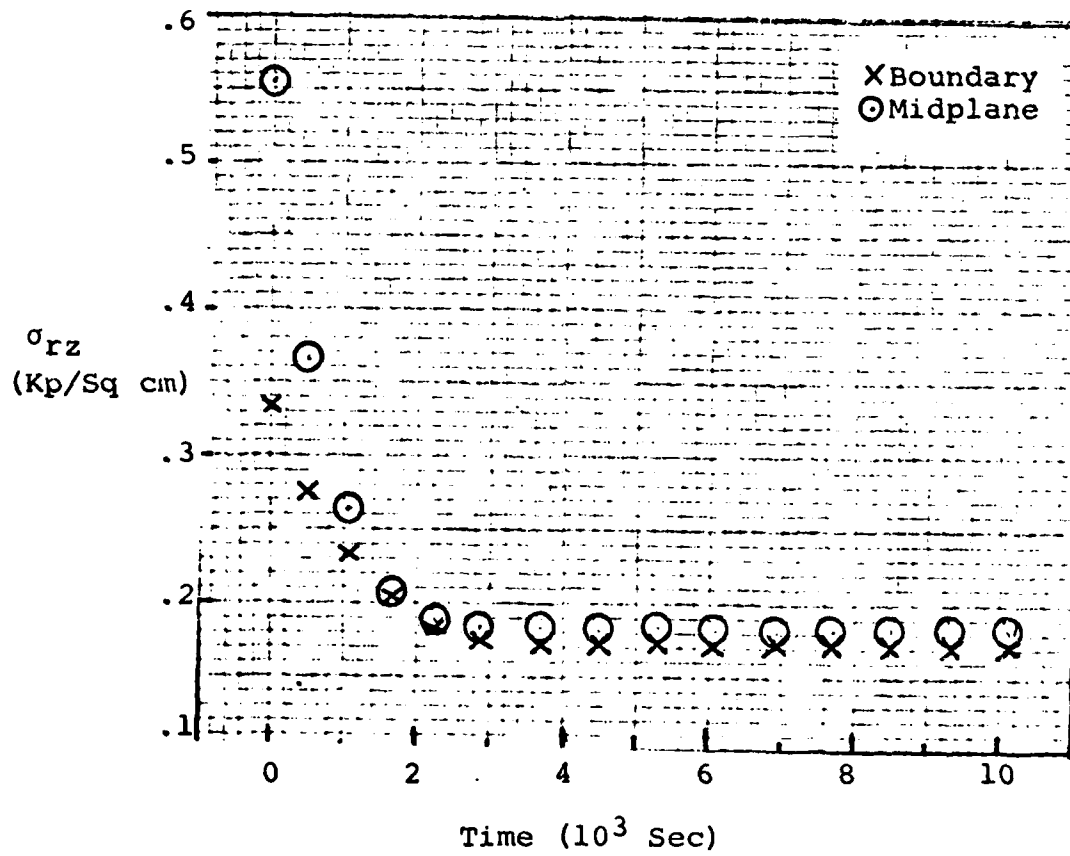
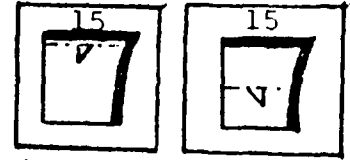


Fig. 3.3-BG. σ_{rz} Versus Time in Boundary and Midplane Elements, Stiff Case

IV. Joint Analysis

The second phase of analysis for this investigation involved obtaining viscoelastic constants for the disk modelled as a homogeneous region. These constants described the average creep response reported by Furlong (Ref 8), who obtained creep data on healthy intervertebral units from the L1-L2 level of the Rhesus Monkey spine. He conducted his tests by subjecting specimens to an axial compressive load of 15 pounds (67 Newtons) for 8 hours followed by a 16-hour relaxation period. Specimens were obtained by cutting the joints through the disk midplane and through adjacent Centrum midplanes (Fig. 4.1-A).

4.1 Finite Element Model

The finite element mesh used for this analysis was obtained from Furlong and is also shown in Fig. 4.1-A. The material properties (E and ν) used for the Trabeculae, Bony end-plate, and Cortex were identical to those used in the Centrum analysis previously discussed in this thesis. The Bony end-plate and Cortex were assumed homogeneous with $E = 3,400 \text{ Kp/Sq cm}$ and $\nu = 0.25$. The viscoelastic constants (E , q_0 , and q_1) for the Trabecular region were those found in the Centrum analysis for the flexible case at an applied load of 15 pounds. Poisson's ratio for the disk was 0.48. E , q_0 , and q_1 for the disk were initially set equal to the

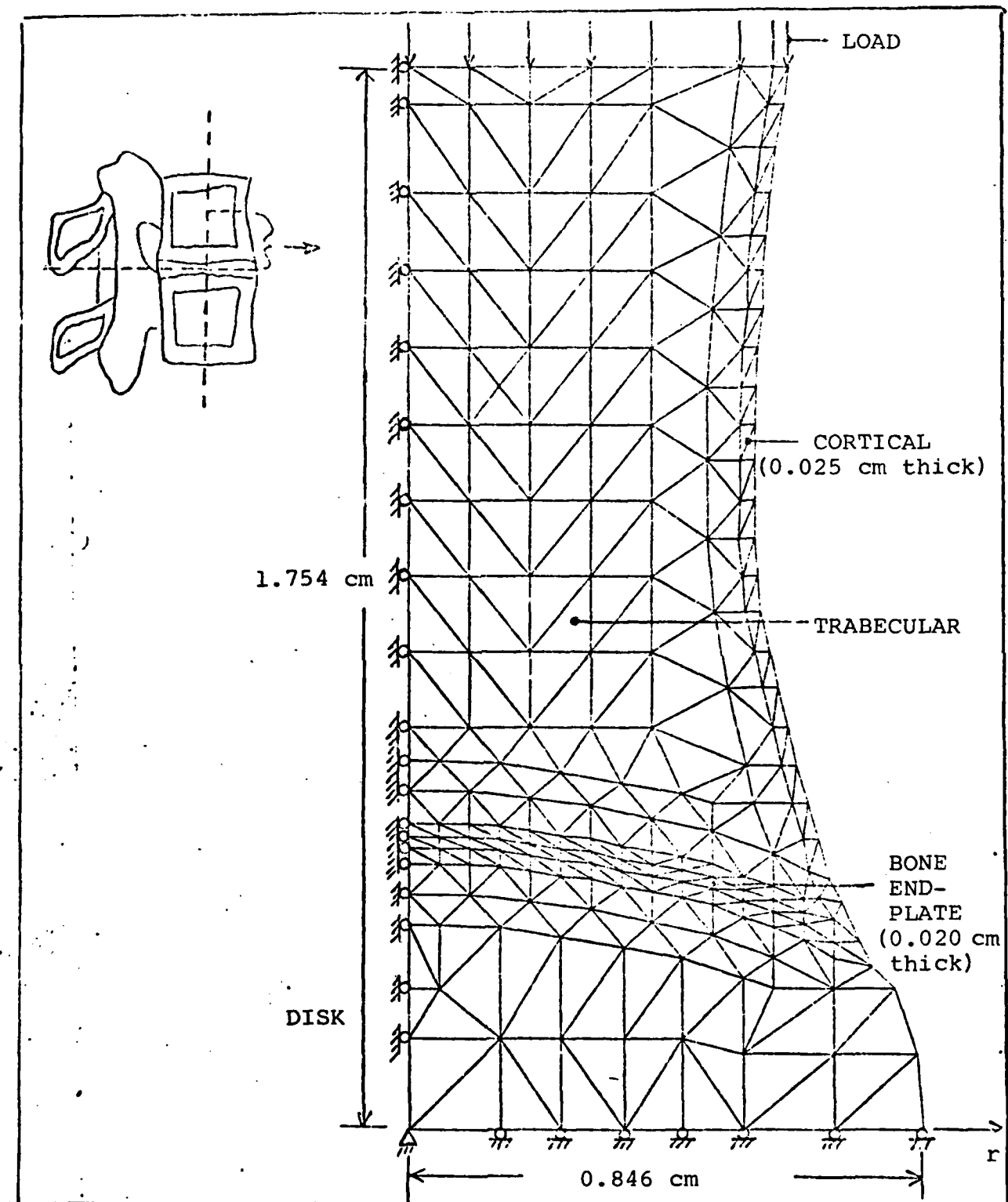


Fig. 4.1-A. Joint Mesh

values Furlong obtained for the disk as he modelled it.

4.2 Film Data

One major limitation of the method of analysis used in this study was that one-dimensional data (top surface displacement) was used to approximate properties describing a two-dimensional displacement phenomena. A means was required for confirming the validity of the analytical results obtained from this standpoint.

A series of time-lapse films was used to provide such a check. These films were taken by Furlong (Ref 8). The test cell was filmed during each test; each film included a clock to indicate elapsed time. The diameter of the disk midplane (mid-height of the specimen) was measured using a travelling microscope. Three tests were chosen (one test per film) and five frames were selected from each film to obtain these measurements.

Two major difficulties were encountered in taking these measurements. First, the amorphous nature of the biological material as well as a lack of contrast made measurement points hard to see at times. Secondly, the accuracy required to measure the very small displacements of the disks between successive frames very nearly approached the accuracy limits of the microscope. However, using a technique where each frame was measured several times, an average measurement was then obtained for that frame.

Only the first 2,000 seconds of each test film was used, since that was the limit of the experimental displacement time data modelled in this analysis. Measurements were taken at approximately 400 seconds into each test and at 400 second intervals thereafter. Since frames were exposed once every 25 seconds, these intervals could only be approximated.

Disk midplane radii were computed from each diameter measured by simply dividing by two. The difference in radii between chronologically successive frames thus represented an unscaled displacement over the interval. These values will hereafter be referred to as measured interval displacements, ΔU_{r_m} . Each film yielded four such values.

These measured interval displacements were adjusted to full-scale interval displacements, ΔU_r , using a scale factor obtained by dividing the measured disk radius for the 400-second (earliest) frame into the disk radius used in the finite element model (0.85 cm). Thus

$$\text{Scale Factor} = \frac{0.85}{\text{Disk radius at 400 Sec}} \quad (4-1)$$

The actual interval displacements were therefore expressed as

$$\Delta U_r = \Delta U_{r_m} \cdot (\text{Scale Factor}) \quad (4-2)$$

Interval median times were determined for each time interval. These times were based on the 400-second initial measurement as well as its corresponding time interval. Four

average median times, t_m , were then obtained from the four time intervals in each of the three films.

Finally, for each time interval, the four values of ΔU_r from the films were averaged to obtain an average interval displacement, $\overline{\Delta U_r}$. The results of this procedure are listed in Tables 4.2-A through 4.2-D. Good agreement existed between these values and the analytical displacements reported by Furlong (Ref 8).

4.3 Results

Experimental displacement-time values and the analytically generated data are shown in Fig. 4.3-A. The displacement function described in section 3.1.3 (Eq 3-2) was again used to provide a curve-fit to the experimental data. Constants defining this curve were $C_1 = 0.0312$, $C_2 = 9.333 \times 10^{-6}$, $C_3 = 0.0055$, and $\lambda = 0.0432$.

Viscoelastic constants obtained for the disk were $E = 1,000$ Kp/Sq cm, $q_0 = 1,000$ Kp/Sq cm, and $q_1 = 99,000$ Kp/Sq cm-sec. It is the author's opinion, based on previous experimental results reported by Furlong (Ref 8), Allen (Ref 2), and Hinnrichsen (Ref 13), that these constants are unrealistically high, indicating a disk which is stiffer and creeps at a slower rate than the Trabecular region in the Centrum. Efforts to match the experimental curve precisely resulted in viscoelastic constants at least three orders of magnitude larger than those determined. One possible reason for this

TABLE 4.2-A
Film Measurement Data, Test R/1

Time (Sec)	Measured Frame Time	Interval Median Time (Sec)	Measured Diameter (cm)	Measured Radius (cm)	ΔU_{rm} (cm)	ΔU_r (cm)
400	0816:48	621	0.2207	0.11035	0.00040	0.00308
800	0824:11	1043	0.2215	0.11075	0.00025	0.00193
1200	0830:50	1446	0.2220	0.11100	0.00025	0.00193
1600	0837:39	1848	0.2225	0.11125	0.00025	0.00193
2000	0844:12		0.2230	0.11150		

TABLE 4.2-B

Film Measurement Data, Test R/4

Time (Sec)	Measured Frame Time	Interval Median Time (Sec)	Measured Diameter (cm)	Measured Radius (cm)	ΔU_{r_m} (cm)	ΔU_r (cm)
400	0833:16		0.2075	0.10375		
		601			0.00025	0.00205
800	0839:58		0.2080	0.10400		
		1009			0.00025	0.00205
1200	0846:52		0.2085	0.10425		
		1406			0.00025	0.00205
1600	0853:12		0.2090	0.10450		
		1806			0.00015	0.00123
2000	0900:13		0.2093	0.10465		

TABLE 4.2-C
Film Measurement Data, Test R/9

Time (Sec)	Measured Frame Time	Interval Median Time (Sec)	Measured Diameter (cm)	Measured Radius (cm)	ΔU_{r_m} (cm)	ΔU_r (cm)
400	0817:39		0.2235	0.11175		
		608			0.00039	0.00297
800	0824:36		0.22428	0.11214		
		1004			0.00036	0.00274
1200	0830:50		0.2250	0.11250		
		1400			0.00025	0.00190
1600	0837:48		0.2255	0.11275		
		1809			0.00015	0.00114
2000	0844:29		0.2258	0.11290		

TABLE 4.2-D

Average Film Measurement Data

Time Interval (Sec)	Average Interval Median Time t_m (Sec)	Average Interval Displacement ΔU_r (cm)
400 - 800	610	0.00270
800 - 1200	1019	0.00224
1200 - 1600	1417	0.00196
1600 - 2000	1821	0.00143

discrepancy could be that the rheological model, consisting of two three-parameter Kelvin solids in series, used to represent the creep deformation of the overall joint will not permit determination of unique viscoelastic constants for the disk given similar constants for the Centrum. Perhaps a Three-parameter Kelvin Solid in series with a Kelvin Solid would yield better results. Further investigation is required to determine a viable model.

To provide a check on the creep deformation experienced by the model, the film data determined in the previous section for the radial displacement of the disk midplane was compared to the model deformation of a corresponding node located at the outer edge of the disk midplane. The results of this comparison are summarized in Table 4.3-A. One notes immediately that the model displaced several orders of magnitude less than the film measurements predicted, further implying that the disk has been modelled as being too stiff.

Despite the limitations of the analytical results, it was determined that an analysis of stress patterns would prove beneficial in describing the manner in which stresses are distributed and redistributed in the intervertebral joint. Two planes were selected for this analysis (Fig. 4.3-B). Figures 4.3-C through 4.3-E present these plots for the disk plane and Figures 4.3-G through 4.3-J present them for the centrum plane. In the disk plane, radial stress (Fig. 4.3-C)

TABLE 4.3-A

Comparison of Disk Radial Displacement
From Film Measurements and Analytical Results

Median Time (sec)	ΔU_r (cm)	
	Films	Analytical
610	0.00270	-
644	-	0.0000124
1019	0.00224	-
1065	-	0.0000225
1417	0.00196	-
1465	-	0.0000084
1821	0.00143	-
1840	-	-0.0000012

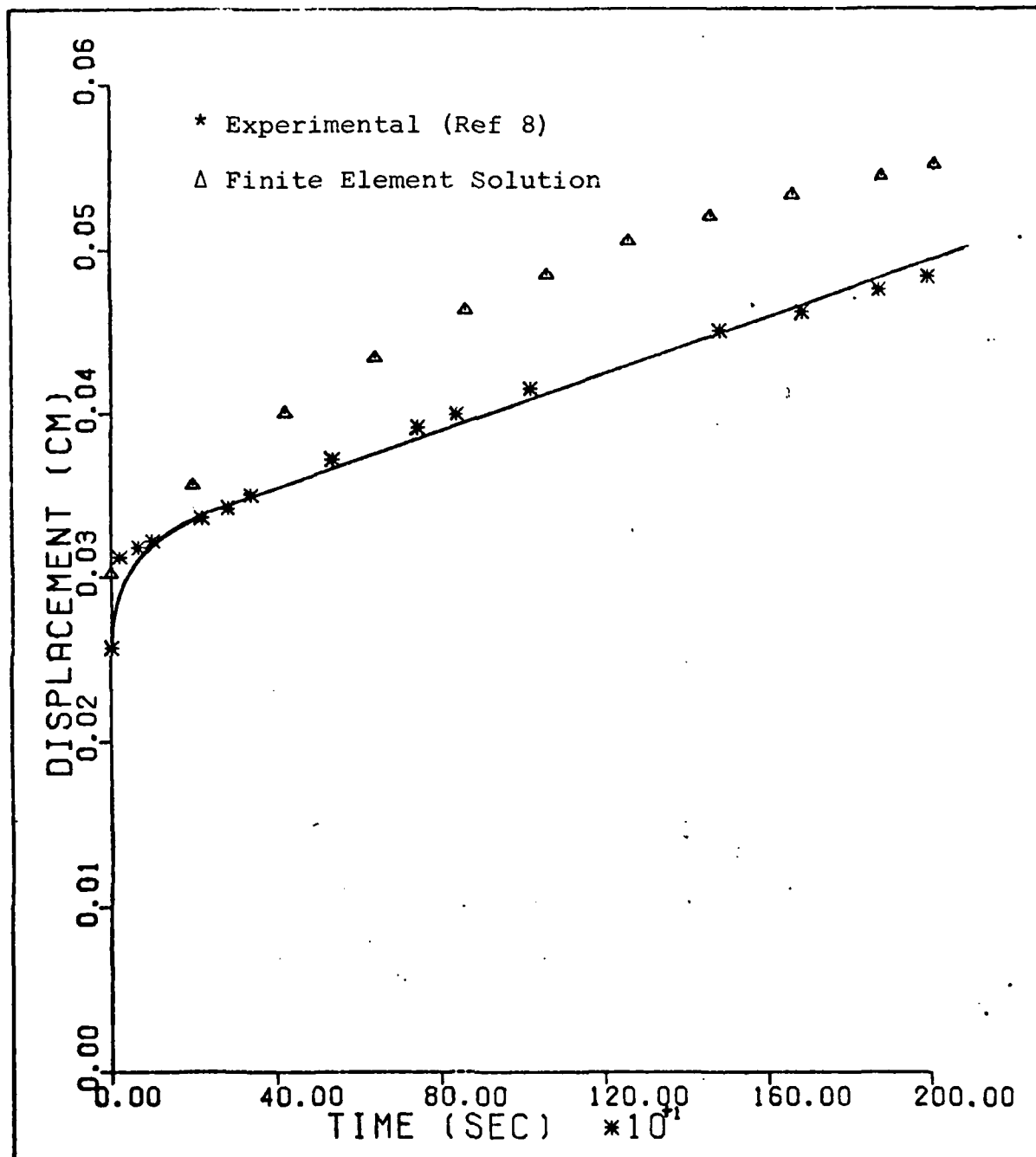


Fig. 4.3-A. Finite Element Solution,
Joint Analysis

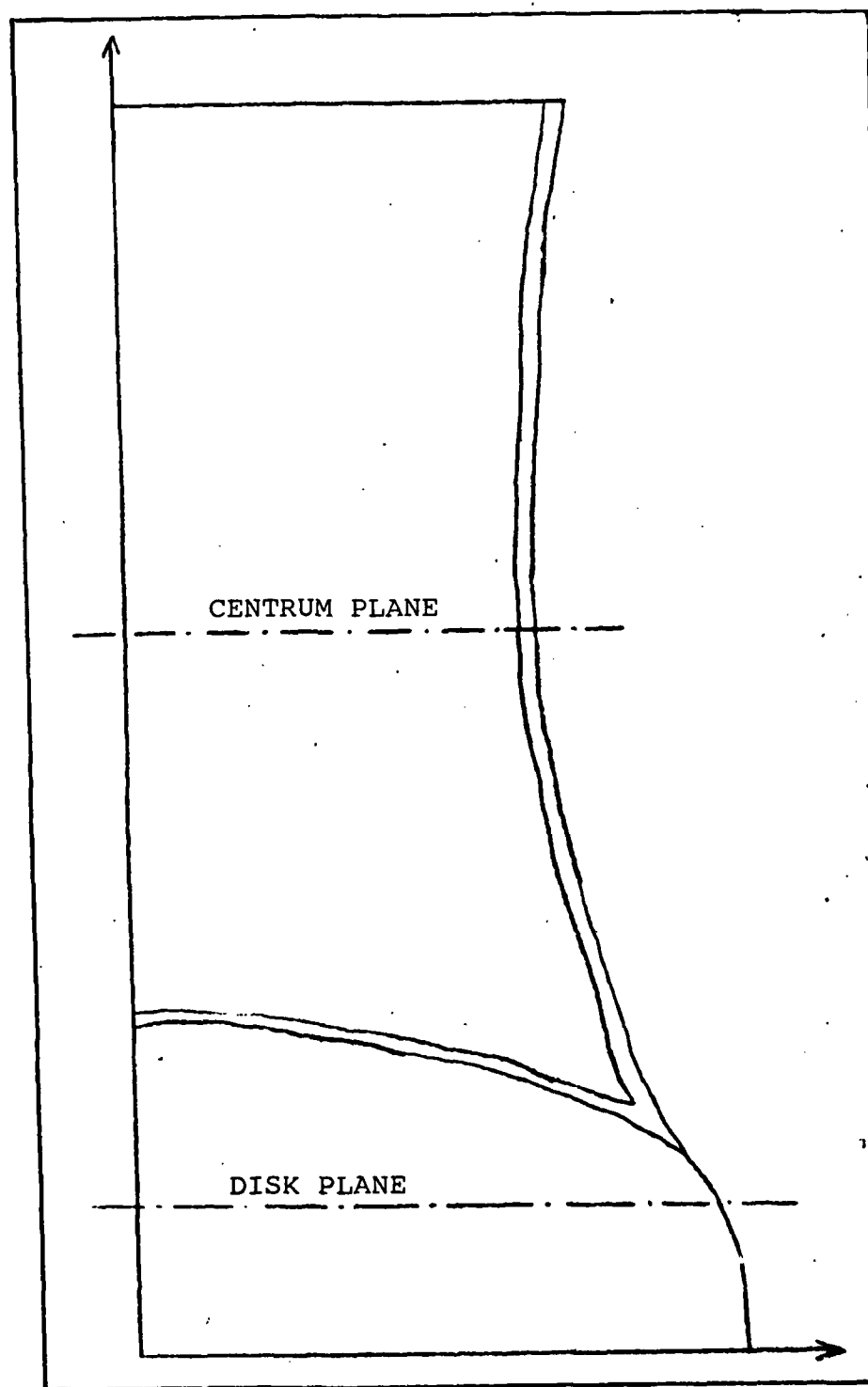


Fig. 4.3-B. Planes Chosen for Stress Profiles,
Joint Analysis

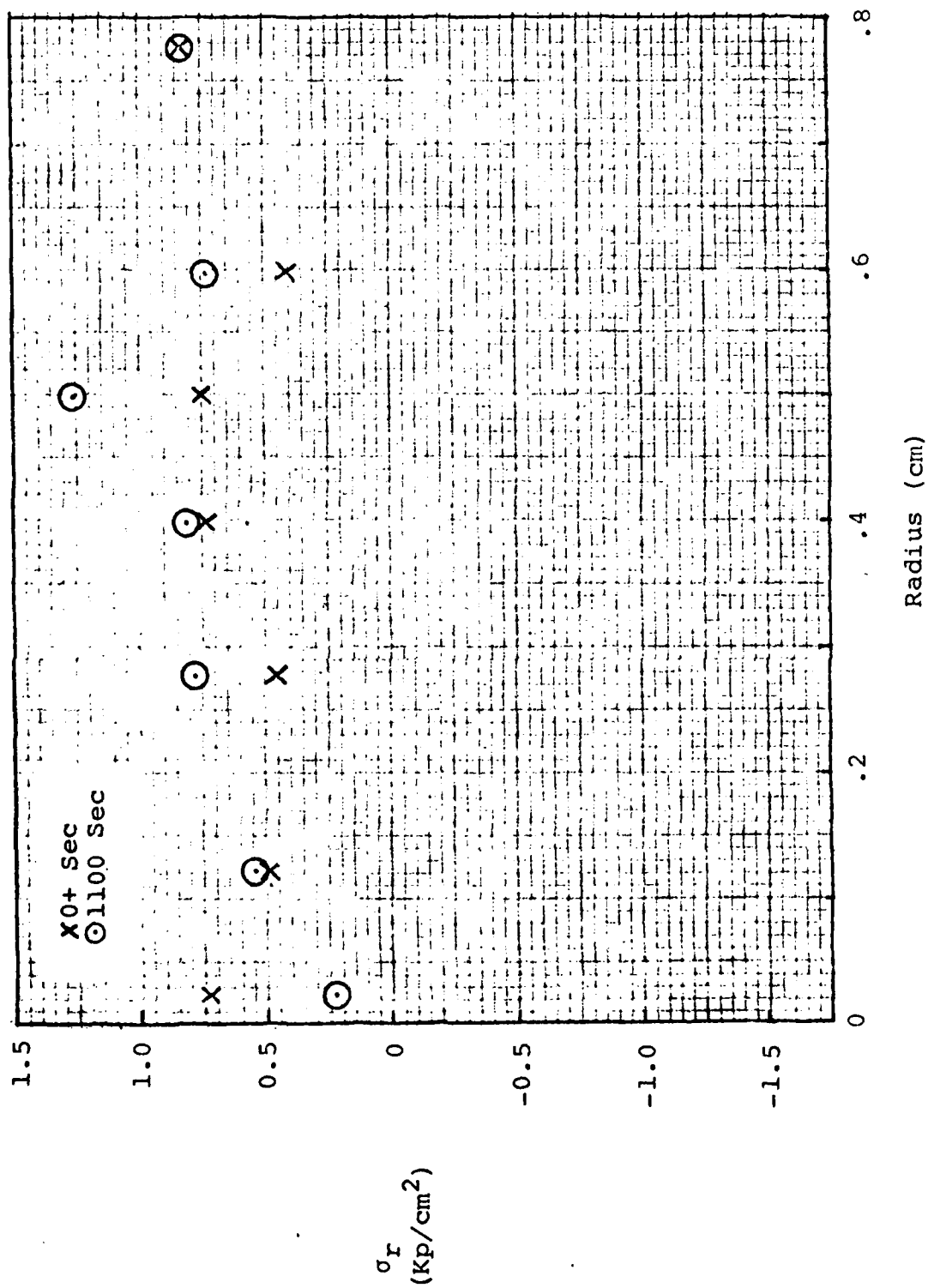


Fig. 4.3-C. σ_r Distribution in Disk Plane

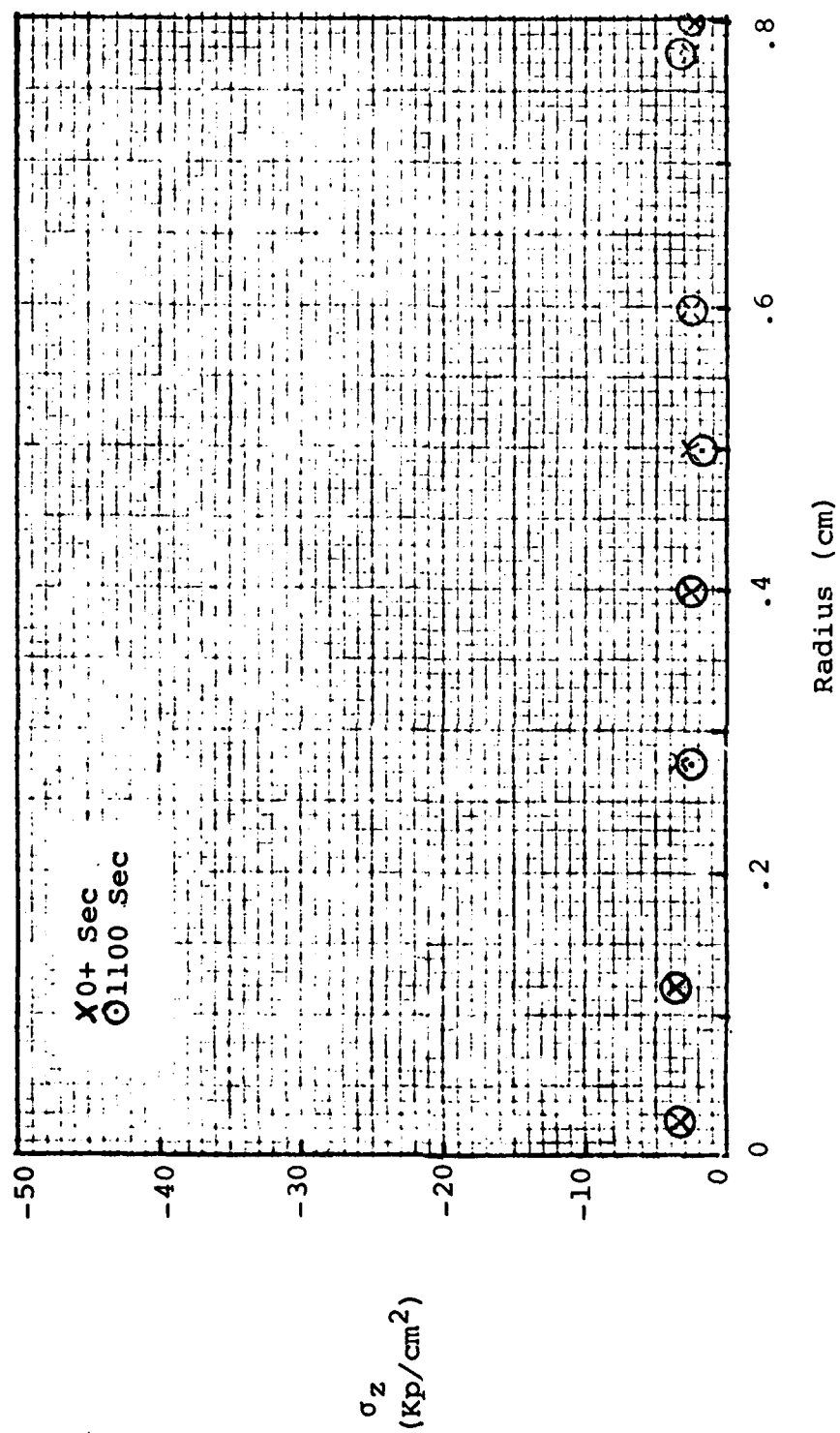


Fig. 4.3-D. σ_z Distribution in Disk Plane

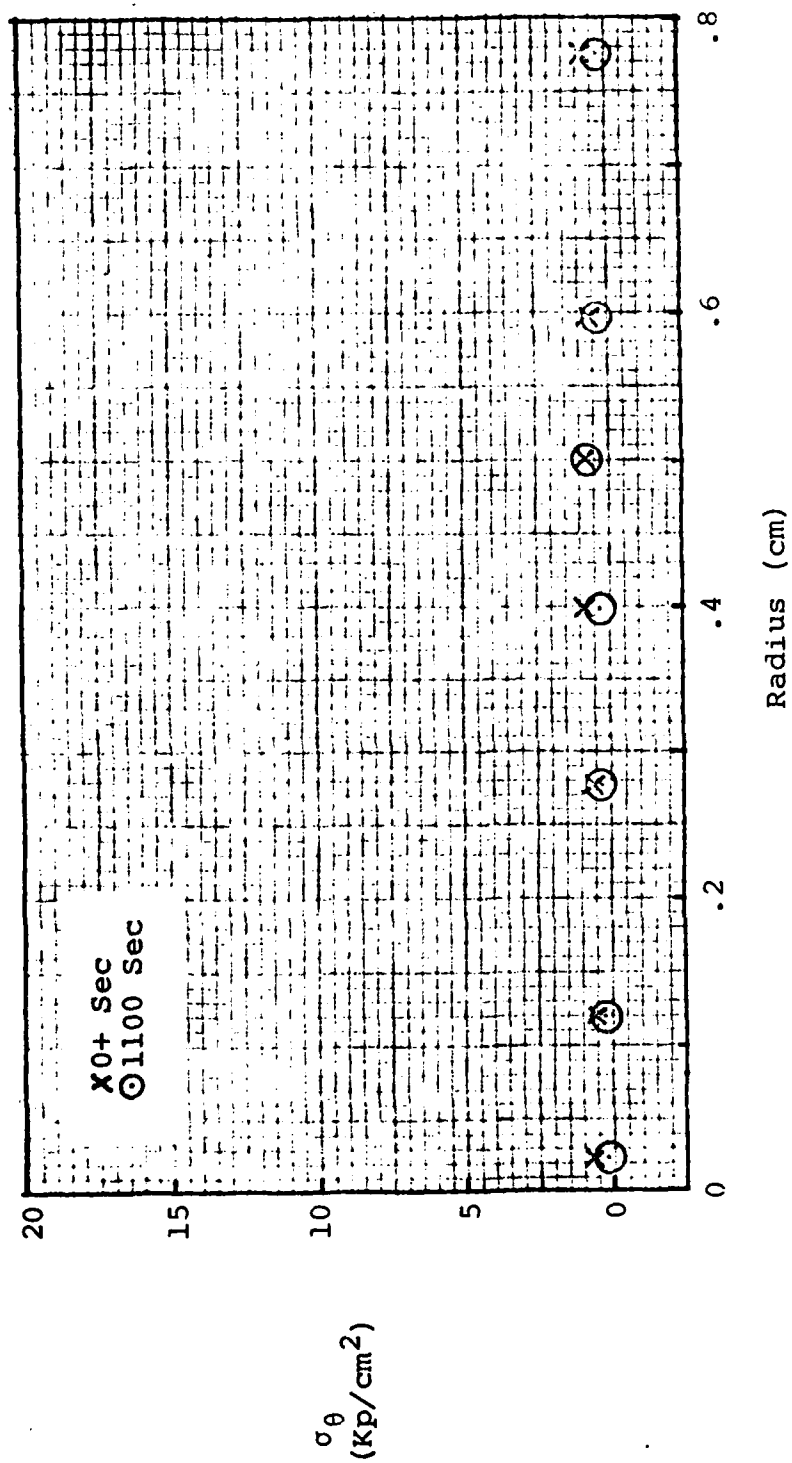


Fig. 4.3-E. σ_θ Distribution in Disk Plane

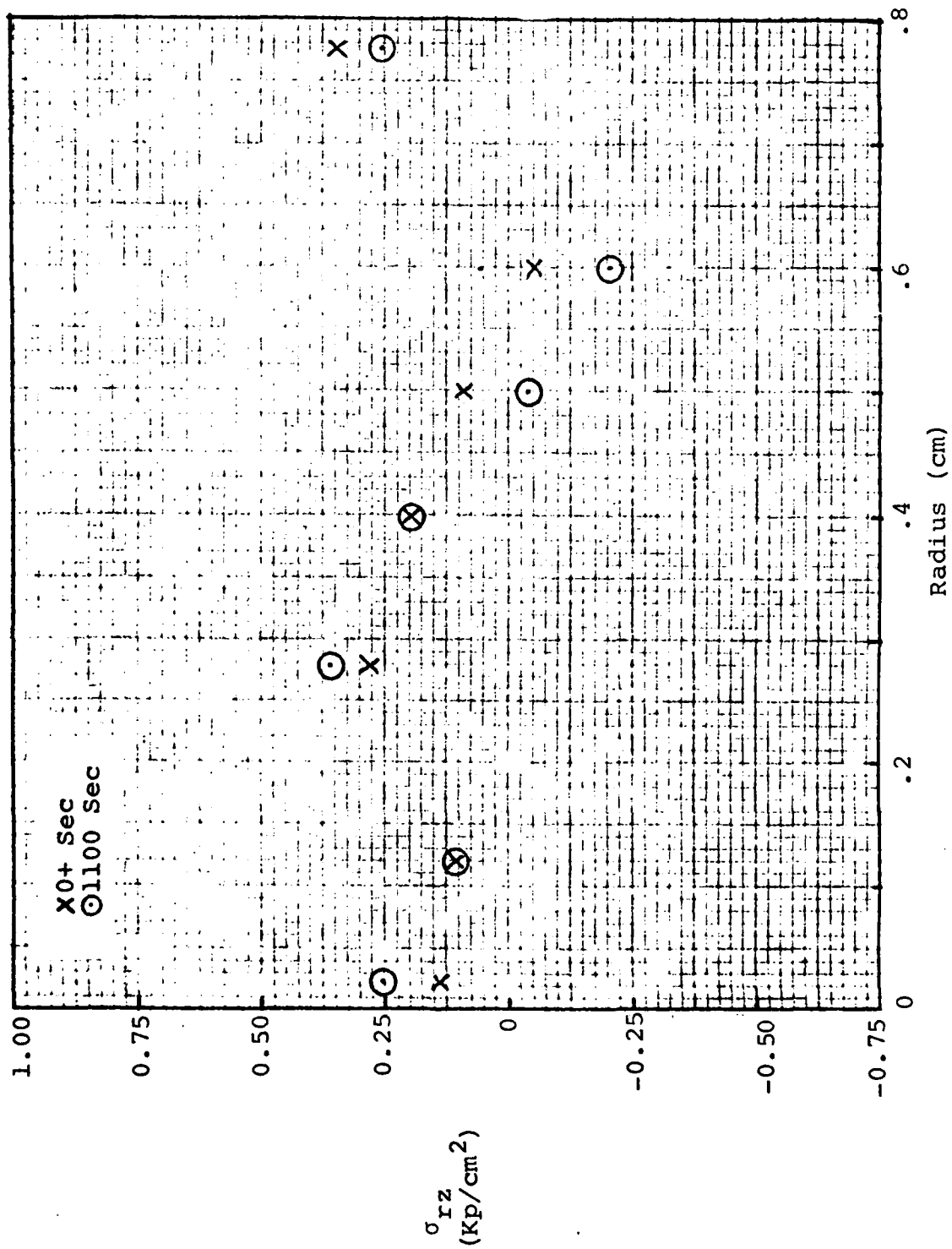


Fig. 4.3-F. σ_{rz} Distribution in Disk Plane

varied little with radius and generally increased in magnitude as creep occurred. Axial and tangential stresses (Figs 4.3-D and 4.3-E) also varied little. Hoop stress was tensile near the edge of the disk, indicating that the disk is acting like a shell. The greatest radial variation occurred in the shear stress component (Fig. 4.3-F) where, over time, stress magnitude generally increased for most radii. The fact that little stress redistributed in this plane can again be traced to the high q_1 value determined, indicating a relatively creep-resistant material. These patterns are thus in disagreement with prior studies (Refs 2, 8, and 13).

Stresses in the Centrum plane, however, are more realistic, parallelling the results for the midplane in the Centrum analysis of this thesis. Radial stress (Fig. 4.3-G) was compressive and increased in magnitude as creep occurred. Axial stress (Fig. 4.3-H) was highest in the Cortex (data point having the highest radius); stress was transferred to the Cortex as creep progressed. Tangential stress (Fig. 4.3-I) was compressive in the Trabeculae and tensile in the Cortex; stress magnitudes increased at all radii. Finally, shear stress (Fig. 4.3-J) varied considerably, especially at the interface between the Trabeculae and Cortex, and also increased in magnitude over time. These patterns reconfirm the results of the Centrum analysis and again describe a Centrum whose Cortex is behaving like a thin shell constraining the outward flow of the Trabeculae.

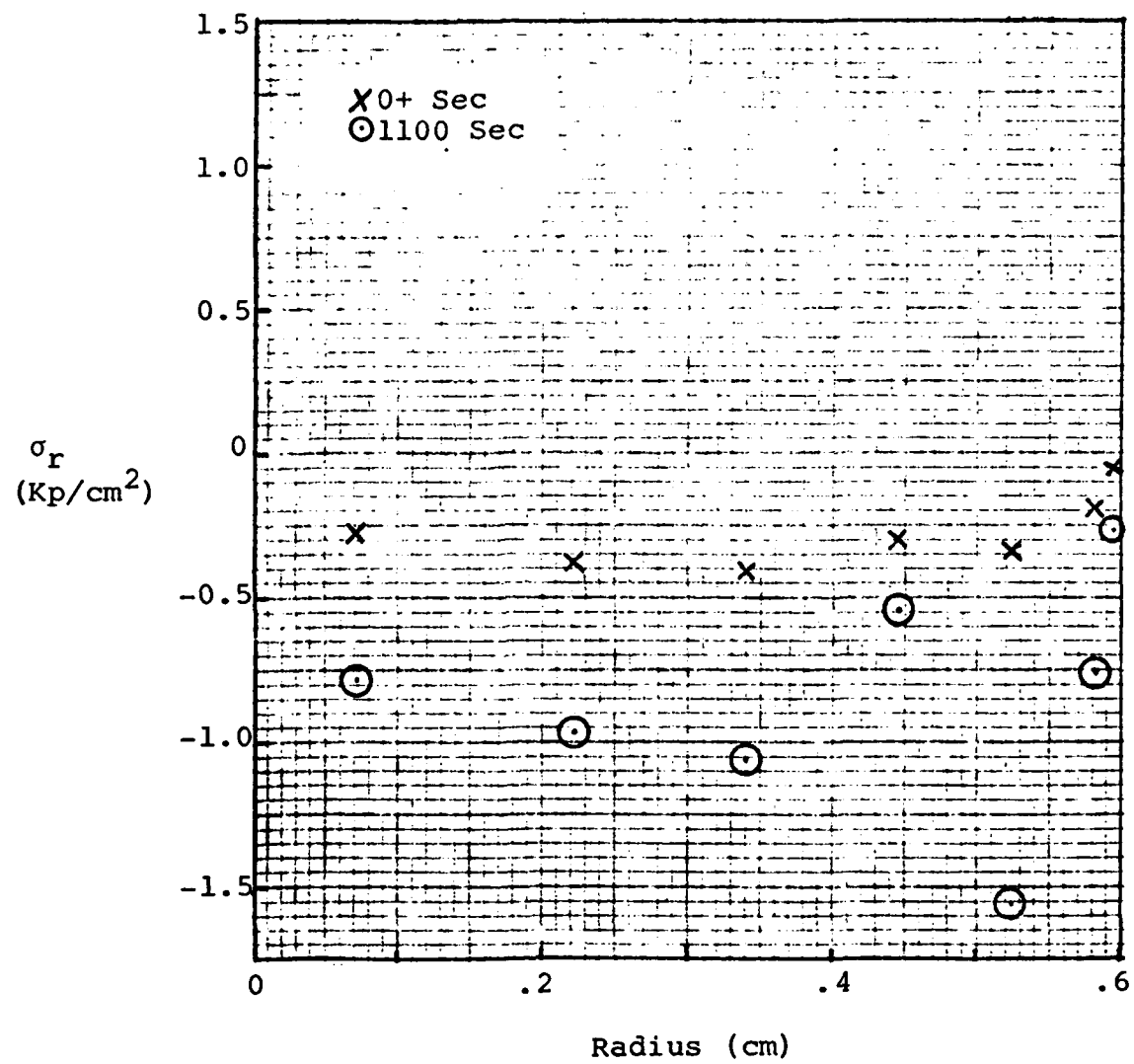


Fig. 4.3-G. σ_r Distribution in Centrum Plane

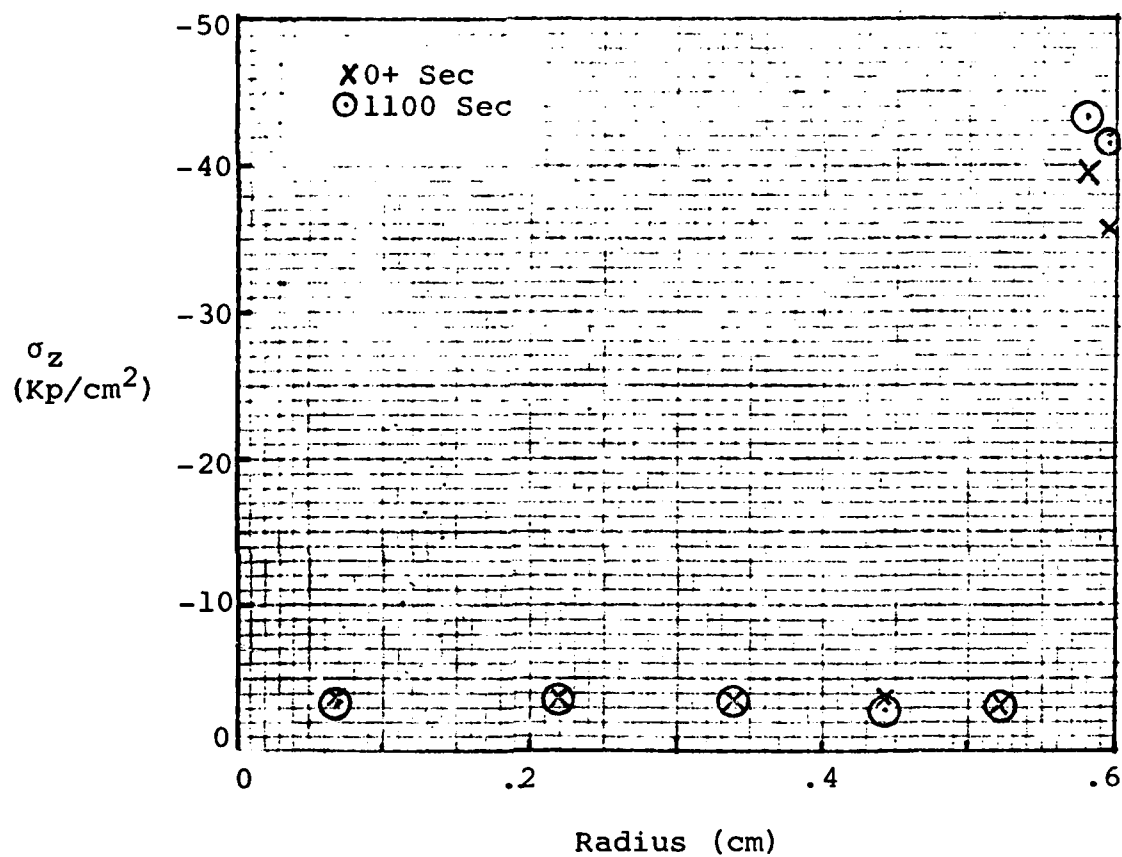


Fig. 4.3-H. σ_z Distribution in Centrum Plane

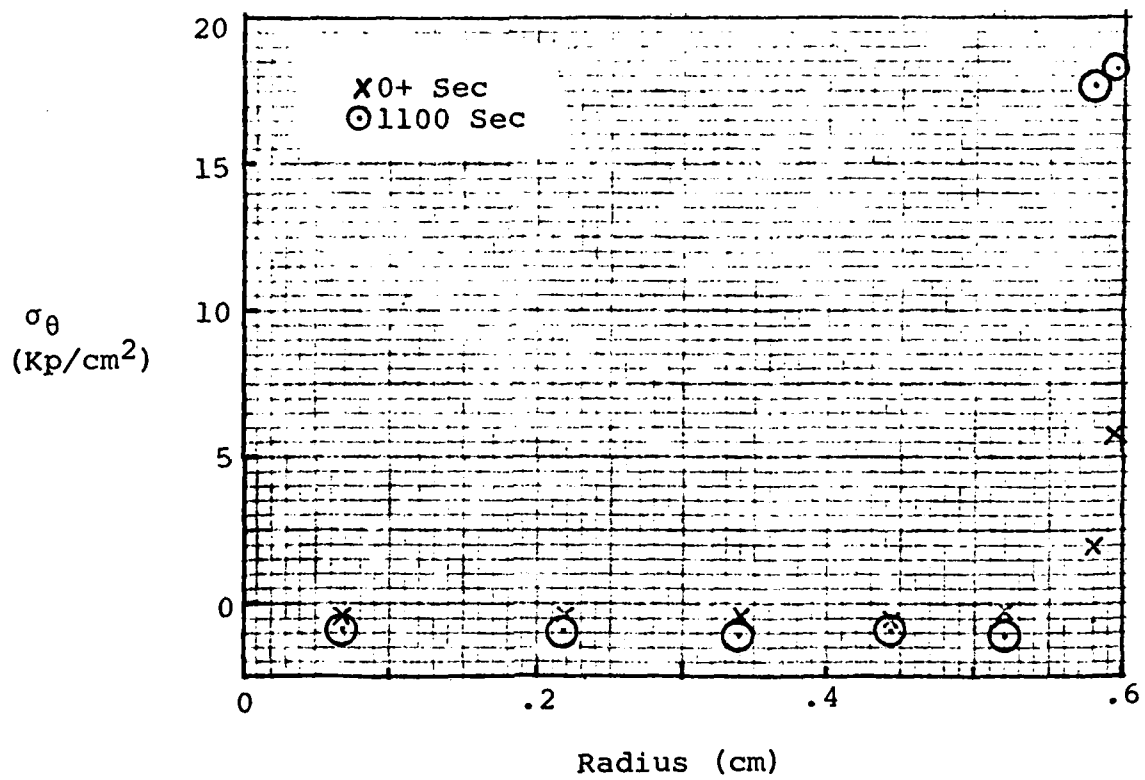


Fig. 4.3-I. σ_θ Distribution in Centrum Plane

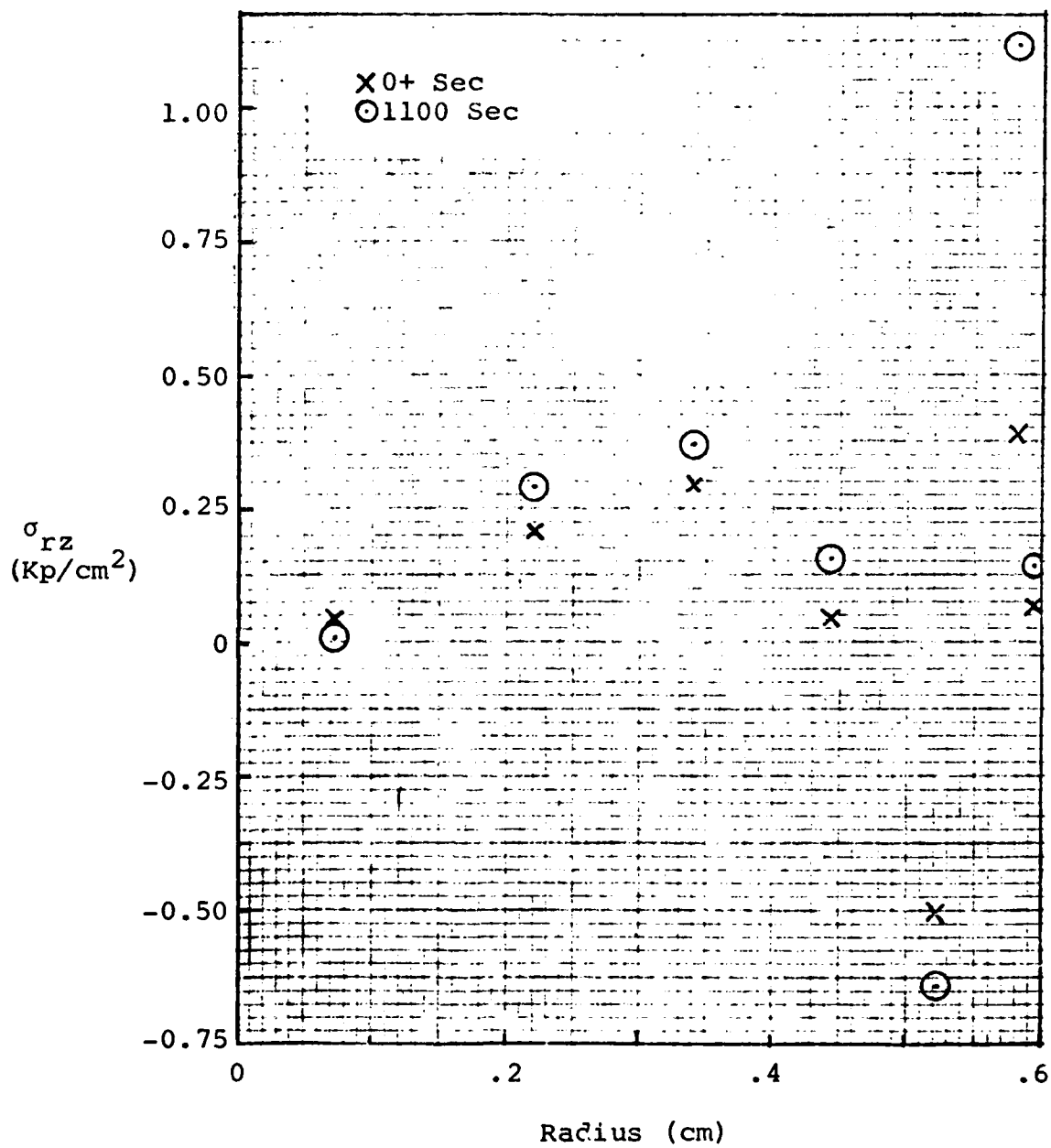


Fig. 4.3-J. σ_{rz} Distribution in Centrum Plane

V. Conclusions and Recommendations

Centra from Rhesus Monkey intervertebral joints were subjected to axial compressive loads for eight hours and observed to exhibit viscoelastic (creep) behavior. Using an axisymmetric finite element model of the Centrum which incorporated a viscoelastic Trabecular bone, material parameters quantifying this behavior were determined for applied loads of 15 and 30 pounds by matching one-dimensional experimental displacement data.

Significant stress redistributions occurred in the Centrum as a result of creep behavior. It was found that the Trabecular bone, as it creeps, transfers load to the Cortex. Thus, the Centrum can be characterized as having a Cortex which is acting like a thin shell constraining the outward flow of the Trabecular bone.

It was determined that it is reasonable to consider the Cortex and Bony end-plate as a homogeneous unit, in the absence of precise material properties for the latter region.

Load level had an effect on the material parameters found in the Centrum. In general, all three constants were so dependent, as the overall creep response was non-linear with load.

For the follow-on analysis, viscoelastic constants determined for the Trabecular bone were applied to an overall

model of the intervertebral joint (minus the articular facet joint and associated ligaments) with the object of determining similar constants for the disk region. Constants determined were unreasonably high, indicating an excessively stiff, creep-resistant disk. It was determined that the use of two Three-parameter Kelvin Solids in series may be an inadequate rheological model, since unique parameters for the disk were unobtainable by the analytical method utilized. It is recommended that other rheological models be considered to ascertain a more viable model of the overall joint creep response. Viscoelastic constants for the disk should then be determined.

A crude optical technique was used wherein time-lapse film images were measured to determine disk radial displacements, and provide a check on the two-dimensional creep response of the finite element model. It is recommended that such a technique be explored to ascertain ways of improving related photographic and measurement techniques.

The incorporation of a viscoelastic Trabecular bone region is necessary to precisely model the time dependent deformation of the intervertebral joint. As such, the disk cannot be considered the sole medium of creep behavior.

Bibliography

1. Adey, R. A. and Brebbia, C. A., "Efficient Method for Solution of Viscoelastic Problems," Journal of the Engineering Mechanics Division, ASCE, 99: 1119-1127 (1973).
2. Allen, Leslie J., Finite Element Analysis of the Viscoelastic Interaction of the Annulus Fibrosis and Nucleus Pulposus Within the Human Intervertebral Joint, M.S. Thesis. Wright-Patterson AFB, Ohio: School of Engineering, Air Force Institute of Technology, December 1981.
3. Belytschko, T., Kulak, R. K., Schultz, A. B., and Galante, J. O., "Finite Element Analysis of an Intervertebral Disk," Journal of Biomechanics, 7: 277-285 (1979).
4. Burns, M. L., Analytical Modelling of Load Deflection Behavior of Intervertebral Discs Subjected to Axial Compression. AFOSR-TR-79-0795. Air Force Office of Scientific Research, July 1979. (AD-A071019)
5. Christensen, R. M. Theory of Viscoelasticity, an Introduction. New York: Academic Press, Inc., 1971.
6. Fung, Y. C., "Biomechanics (Its Scope, History, and Some Problems of Continuum Mechanics in Physiology," Appl. Mech. Rev., 21: 1-20 (1960).
7. Flugge, W. Viscoelasticity. Waltham, Mass.: Blaisdell Publishing Company, 1967.
8. Furlong, David R., The Influence of Surgical Herniation on the Viscoelastic Properties of the Intervertebral Joint, M.S. Thesis. Wright-Patterson AFB, Ohio: School of Engineering, Air Force Institute of Technology, December 1981.
9. Galante, J., Rostaker, W., and Ray, R., "Physical Properties of Trabecular Bone," Calcified Tissue Res., 5: 236-246 (1970).
10. Galante, J. O., "Tensile Properties of the Human Lumbar Annulus Fibrosis," Acta Orthop. Scand., Supplement 100 (1967).
11. Hakim, N. S., and King, A. I., "A Three Dimensional Finite Element Dynamic Response Analysis of a Vertebra with Experimental Verification," Journal of Biomechanics, 12: 277-292 (1979).

12. Hinnericks, T., Viscoplastic and Creep Crack Growth Analysis by the Finite Element Method, Ph.D. dissertation. Wright-Patterson AFB, Ohio: Air Force Institute of Technology, June 1980.
13. Hinrichsen, R. L., A Viscoelastic Finite Element Model of the Human Intervertebral Joint, M.S. Thesis. Wright-Patterson AFB, Ohio: School of Engineering, Air Force Institute of Technology, December 1980.
14. Horton, W. G., "Further Observations on the Elastic Mechanism of the Intervertebral Disc," Journal of Bone and Joint Surgery, 40B: 552-557 (1958).
15. Kazarian, Leon E. and Graves, George. Compressive Strength Characteristics of the Primate (Macaca Mulatta) Vertebral Centrum. AMRL-TR-79-8. Wright-Patterson AFB, Ohio: Air Force Aerospace Medical Research Laboratory, May 1979. (AD-AO73373)
16. Kazarian, L. E. and Kaleps, I., Mechanical and Physical Properties of the Human Intervertebral Joint. AMRL-TR-79-3. Wright-Patterson AFB, Ohio: Air Force Aerospace Medical Research Laboratory, June 1979. (AD-AO75107)
17. Kazarian, Leon E. and von Gierke, Henning, The Validation of Biodynamic Models. AMRL-TR-78-105. Wright-Patterson AFB, Ohio: Air Force Aerospace Medical Research Laboratory, November, 1978. (AD-AO80340)
18. Kulak, R. F., Belytschko, T. B., Galante, J. O., and Schultz, A. B., "Nonlinear Behavior of the Human Intervertebral Disc Under Axial Load," Journal of Biomechanics, 9: 377-386 (1976).
19. Lin, H. S., Liu, Y. K., and Adams, K. H., "Mechanical Response of the Intervertebral Joint Under Physiological (Complex) Loading," Journal of Bone and Joint Surgery, 60A: 41-54 (1978).
20. Lin, H. S., Liu, Y. K., Ray, Gautom, and N. Kravesh, P., "System Identification for Material Properties of the Intervertebral Joint," Journal of Biomechanics, 11: 1-14 (1978).
21. Markolf, K. and Morris, J., "The Structural Components of the Intervertebral Disc," Journal of Bone and Joint Surgery, 56A: 675-687 (1974).

22. Nachemson, A. L., Schultz, A. B., and Berkson, M. H., "Mechanical Properties of Human Lumbar Spine Motion Segments, Influences of Age, Sex, Disc Level, and Degeneration," Spine, 4: 1-5 (1979).
23. Rockoff, S., Sweet, E., and Bluestein, J., "The Relative Contribution of Trabecular and Cortical Bone to the Strength of Human Lumbar Vertebra," Calc. Tissue Res., 3: 163-175 (1969).
24. Spilker, R. L., "A Simplified Finite Element Model of the Intervertebral Disc," International Conference Proceedings, Finite Elements in Biomechanics, Vol. II: 728-747 (1980).
25. Stark, Peter A. Introduction to Numerical Methods. New York: The Macmillan Company, 1970.
26. Swanson, S. A. V., "Biomedical Characteristics of Bone," Advances in Biomedical Engineering, Vol. I. New York: Academic Press, Inc., 1971.
27. Tencer, A. F., Ahmed, A. M., and Burke, D. L., "Some Static Mechanical Properties of the Lumbar Intervertebral Joint, Intact and Injured," Journal of Biomedical Engineering, Transactions of the ASME, 104: 193-201 (1982).
28. Virgin, W. J., "Experimental Investigation Into the Physical Properties of the Intervertebral Disc," Journal of Bone and Joint Surgery, 33B: 607-611 (1951).
29. White, Augustus A. and Panjabi, Manottar M. Clinical Biomechanics of the Spine. Philadelphia: T. P. Lippincott Company, 1978.
30. Zienkiewicz, O. C. The Finite Element Method (Third Edition). Maidenhead, Berkshire, England: McGraw-Hill Book Co., Ltd., 1977.
31. Zienkiewicz, O. C., Watson, M., and King, I. P., "A Numerical Method of Visco-Elastic Stress Analysis," International Journal of Mechanical Science, 10: 807-827 (1968).

APPENDIX A

Stiffness Matrix and Nodal Force Vector For Axisymmetric Problems

The derivation of the Stiffness Matrix and Nodal Force Vector proceeds as follows for an axisymmetric problem.

A.1 Stiffness Matrix (Ref 31)

The general equation for the stiffness matrix of an element is given by

$$[k] = \int_V [B]^T [D] [B] d(\text{volume}) \quad (\text{A-1})$$

For an axisymmetric problem, this integration must proceed over the entire ring. Hence,

$$[k] = 2\pi \int [B]^T [D] [B] r dr dz \quad (\text{A-2})$$

Summing the contributions from each of the elements, the structural stiffness matrix becomes, for N elements

$$[K] = \sum_{n=1}^N 2\pi \int [B]^T [D] [B] r dr dz \quad (\text{A-3})$$

Since $[B]$ contains terms dependent on the coordinates, straightforward integration may not be possible. An approximate solution can always be obtained by evaluating $[B]$ at a centroid defined by

$$\bar{r} = (r_1 + r_2 + r_3)/3 \quad (\text{A-4a})$$

$$\bar{z} = (z_1 + z_2 + z_3)/3 \quad (\text{A-4b})$$

If we then define $[\bar{B}]$ to be $[B]$ evaluated at the centroid, one can obtain the approximate expression

$$[K] = \sum_{n=1}^N 2\pi A_n [\bar{B}]^T [D] [\bar{B}] \bar{r} \quad (A-5)$$

where A_n is the area of element n .

A.2 Nodal Force Vector Due to a Surface Traction

Consider a triangular element subjected to a surface traction, $F(r, z)$ (Fig. A.2-A). The Nodal Force Vector representing this traction is

$$\{p\} = \int_A [N]^T \{F\} dA \quad (A-6)$$

For an axisymmetric problem, this becomes

$$\{p\} = 2\pi \int_s [N]^T \{F\} r ds \quad (A-7)$$

where

$$\{F\} = \begin{Bmatrix} F_r \\ F_z \end{Bmatrix} \quad (A-8)$$

and F_r and F_z are force intensities (force per unit area) in the indicated directions. On the surface subjected to the traction, the area coordinates and, hence, shape functions, N_i , are

$$L_1 = N_1 = 0 \quad (A-9a)$$

$$L_2 = N_2 = 1 - \frac{s}{L} \quad (A-9b)$$

$$L_3 = N_3 = \frac{s}{L} \quad (A-9c)$$

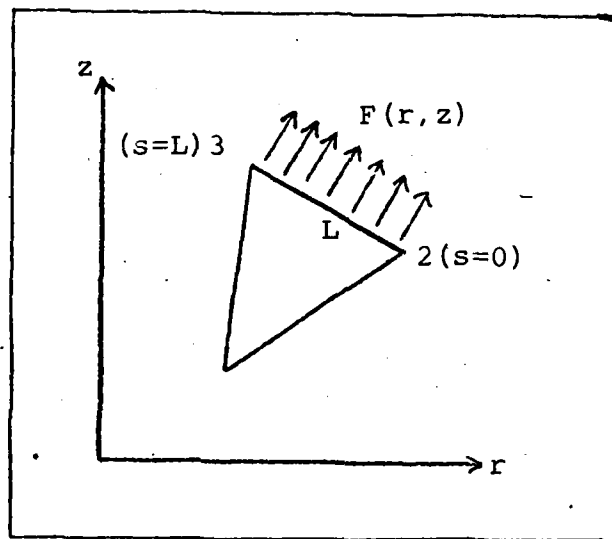


Fig. A.2-A. Triangular Element with Surface Traction

where L is the length of the side. Since the element shown is isoparametric, we may express the radius as a function of the nodal coordinates:

$$r = L_1 r_1 + L_2 r_2 + L_3 r_3 \quad (\text{A-10})$$

so that

$$r = (1 - \frac{S}{L}) r_2 + \frac{S}{L} r_3 \quad (\text{A-11})$$

Substituting Eqs A-8, A-9, and A-11 into Eq A-7, one obtains the following

$$\{p\} = \begin{Bmatrix} p_{1r} \\ p_{1z} \\ p_{2r} \\ p_{2z} \\ p_{3r} \\ p_{3z} \end{Bmatrix} = 2\pi L \begin{Bmatrix} 0 \\ 0 \\ F_r (r_2/3 + r_3/6) \\ F_z (r_2/3 + r_3/6) \\ F_r (r_2/6 + r_3/3) \\ F_z (r_2/6 + r_3/3) \end{Bmatrix} \quad (\text{A-12})$$

A structural nodal force vector $\{P\}$ can then be obtained by assembling element nodal force vectors.

APPENDIX B

Experimental Data

This section contains experimental data for the Centrum tests. It includes Calibration Data, Experimental Curves, Extracted Data, and Internal and External Measurements.

TABLE B-1
Calibration Data*

Specimen I.D.	Load (lb)	Calibration Factor (10^{-4} in/in)	Zero (in)
KAZ 7(L1)	15	0.9366	-8
KAZ 7(L2)	15	0.9198	+4
KAZ 10(L1)	15	0.9901	+7
KAZ 10(L2)	15	0.9671	-3
KAZ 30(L1)	15	0.9398	+10
KAZ 30(L2)	15	1.0024	+8
KAZ 3(L1)	30	1.0378	+7
KAZ 3(L2)	30	0.9634	+9
KAZ 6(L1)	30	0.9679	-4
KAZ 6(L2)	30	1.0229	0
RHES 17(L1)	30	0.9992	+14
RHES 17(L2)	30	0.9785	+32

* Displacement (in) = Calibration Factor x (Digitized Value - Zero)

TABLE B-2A

Extracted Data***
15 pound tests

Time (Sec)	Displacement (10^{-4} in)						Midplane Average (cm)**
	KAZ7(L1)	KAZ7(L2)	KAZ10(L1)	KAZ10(L2)	KAZ30(L1)	KAZ30(L2)	
0+	113	49	29	71	89	99	.00952
300	147	87	53	103	143	150	.01448
600	159	96	63	110	156	157	.01562
1000	163	104	68	115	168	165	.01651
1500	167	111	75*	123	175	171	.01740
2000	174	118	80*	126	182	177	.01816
2500	178	122	86*	130	185	181	.01867
3000	181	127	91*	132	188	184	.01918
3500	181	127	95	134	192	188	.01943
4000	185	130	98	134	195	190	.01969
4500	187	131	101	134	195	192	.01994
5000	187	133	106	135	200	192	.02019
6000	189	133	109	137	207	200	.02057
7000	191	136	110	138	208	206	.02110
10000	189	140	110	143	210	206	.02108

* Linearly interpolated

** Midplane displacement is half of specimen displacement.

*** Data from creep plots. Specimens are identified by primate name and location (in parentheses).

TABLE B-2B

Extracted Data***
30 pound tests

Time (Sec)	Displacement (10^{-4} in)						Midplane Average (cm)**	
	KAZ3(L1)	KAZ3(L2)	KAZ6(L1)	KAZ6(L2)	RHES17(L1)	RHES17(L2)	Average	Average
0+	253	188	100	122	10	23	116	.01473
300	274	238	133	134	28	37	141	.01791
600	282	248	140	137	32	39	146	.01854
1000	291	257	147	142*	36	40	152	.01930
1500	295	260	152	144*	37	41	155	.01969
2000	300	265	155	146*	40	42	158	.02007
2500	309	270	159	148*	40	42	161	.02045
3000	310	272	161	150*	43	44	163	.02070
3500	312	276	164	153*	43	45	165	.02096
4000	312	276	165	155*	43	46	166	.02108
4500	315	278	167	156*	43	47	168	.02134
5000	316	280	167	158*	44	47	169	.02146
6000	323	281	169	162	45	48	171	.02172
7000	326	285	169	167	46	49	174	.02210
10000	326	288	169	168	47	52	175	.02223

* Linearly interpolated

** Midplane displacement is half of specimen displacement.

*** Data from creep plots. Specimens are identified by primate name and location (in parentheses).

TABLE B-3

Specimen External Measurements*

Specimen I.D.	Caliper Measurements (10^{-2} in)								Photographed Areas (in^2 times 2)	
	1	2	3	4	5	6	7	8	Superior Upper	Inferior Lower
KAZ 3 (L1)	45	43	50	56	52.5	57	50	61	1.1589	1.1273
KAZ 3 (L2)	48	43	51	60	60	63	55	67	1.3037	1.2813
KAZ 6 (L1)	42	41	45	60	58	64	57	68	0.9134	1.0248
KAZ 6 (L2)	45	40	45	63	62	66	58	68	1.1070	1.0243
KAZ 7 (L1)	49	48	51	53	50	56	45	60	1.3672	1.4936
KAZ 7 (L2)	48	50	53	60	58	63	53	67	1.4866	1.6783
KAZ 10 (L1)	50	47.5	53	68	68	69	62	72.5	1.3205	1.3656
KAZ 10 (L2)	49	48	51	63	63	64	58	68	1.3309	1.3656
KAZ 30 (L1)	47.5	40	45	60	58	62.5	56	67.5	1.0306	1.0579
KAZ 30 (L2)	43	40	45	63	64.5	66	64	69	1.1356	1.1304
RHES 17 (L1)	48	46	52	62	58	63	51	67	1.3129	1.4368
RHES 17 (L2)	50	46	55	65	62	67	58	70	1.5068	1.5408
AVERAGE	47.04	44.38	49.67	61.08	59.50	63.38	55.83	67.08	1.2478	1.2939

Model Average Height (measurements 4 - 8) = 0.3069 in. = 0.7794 cm.

Computed midplane radius = 0.2918 in. = 0.7412 cm.

Average end surface radius = 0.3180 in. = 0.8077 cm.

* See Fig. B-1 for measurement designations.

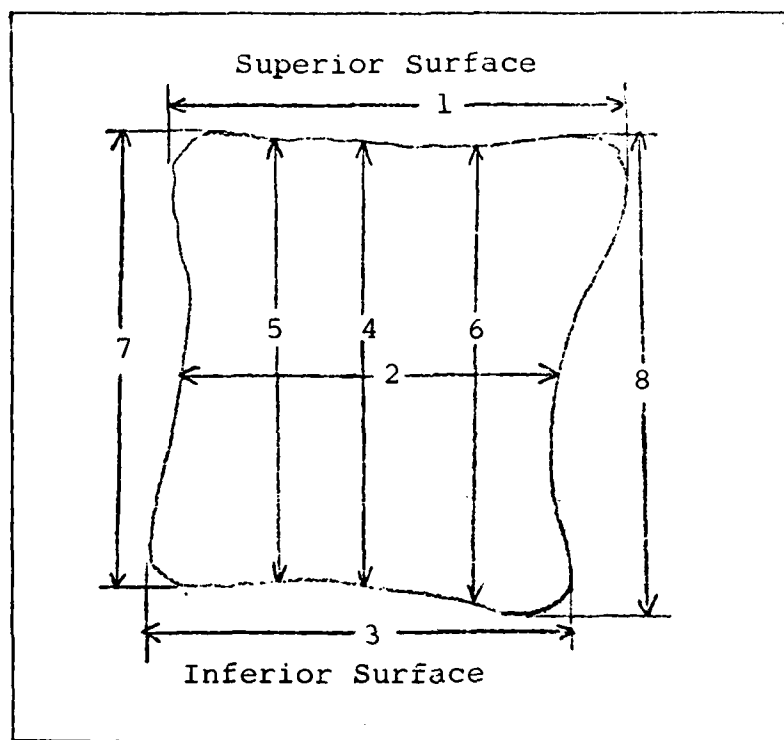


Fig. B-1. External Measurement Code, Centrum Tests.

TABLE B-4

Specimen Internal Measurements
(10^{-2} cm)

Specimen I.D.	Cortical		Center		Bony End-Plate		Center
	End		End		End		
KAZ 3 (L1)	5	4	4	5	3	2	3
KAZ 3 (L2)	7	4	5	6	5	4	3
KAZ 6 (L1)	6	6	6	6	3	4	3
KAZ 6 (L2)	4	5	5	6	4	3	3
KAZ 7 (L1)	9	11	12	10	4	4	3
KAZ 7 (L2)	6	5	5	4	4	3	3
KAZ 10 (L1)	4	4	5	3	2	2	2
KAZ 10 (L2)	8	7	9	10	2	2	2
KAZ 30 (L1)	10	9	11	10	3	3	3
KAZ 30 (L2)	11	10	11	12	4	4	4
RHES 17 (L1)	5	5	6	6	3	3	4
RHES 17 (L2)	8	8	7	9	4	4	3
Average	7.17		3.18				

* All measurements are thicknesses.

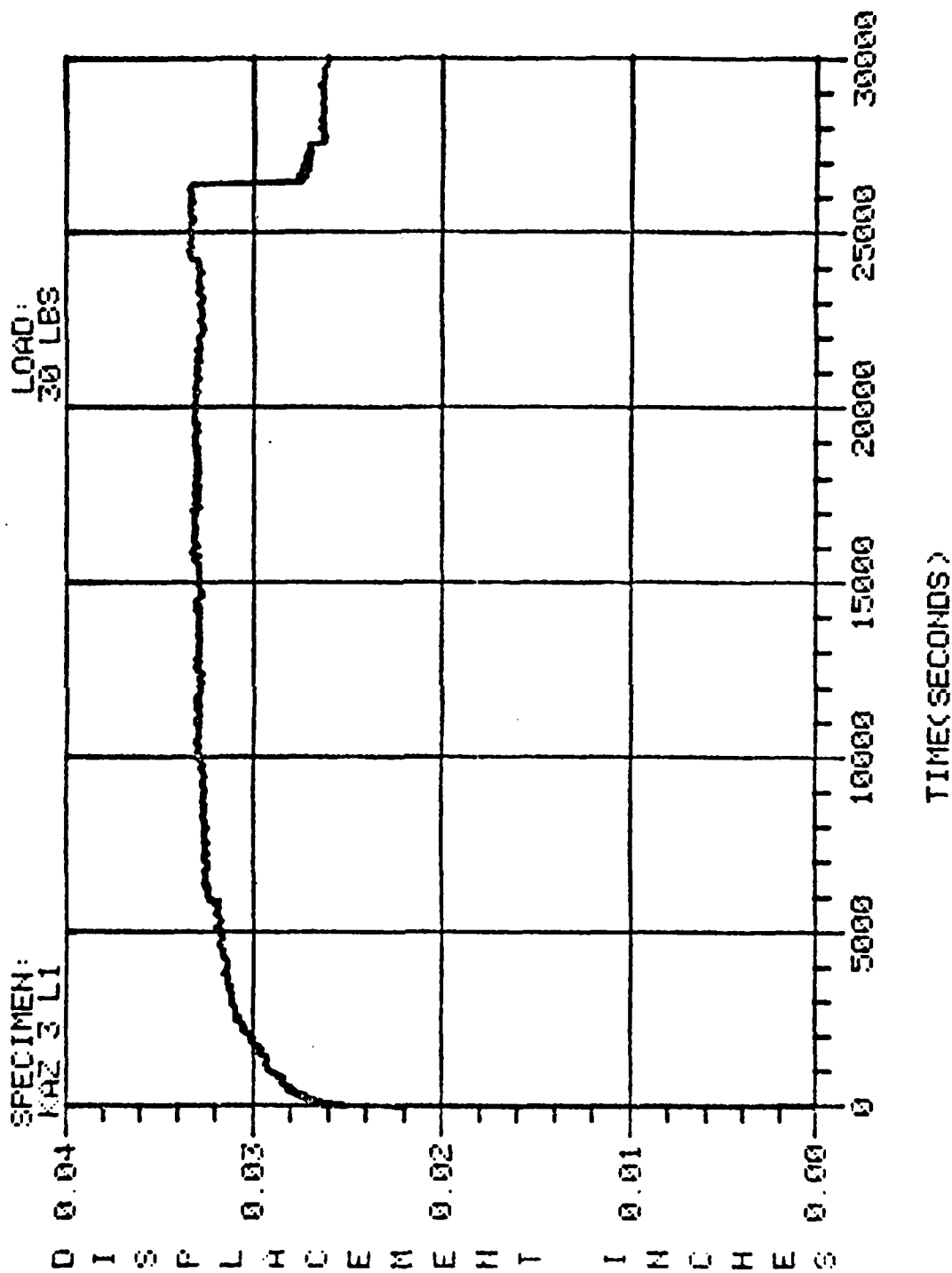


Fig. B-2. Test curve, specimen KAZ 3 (L1)

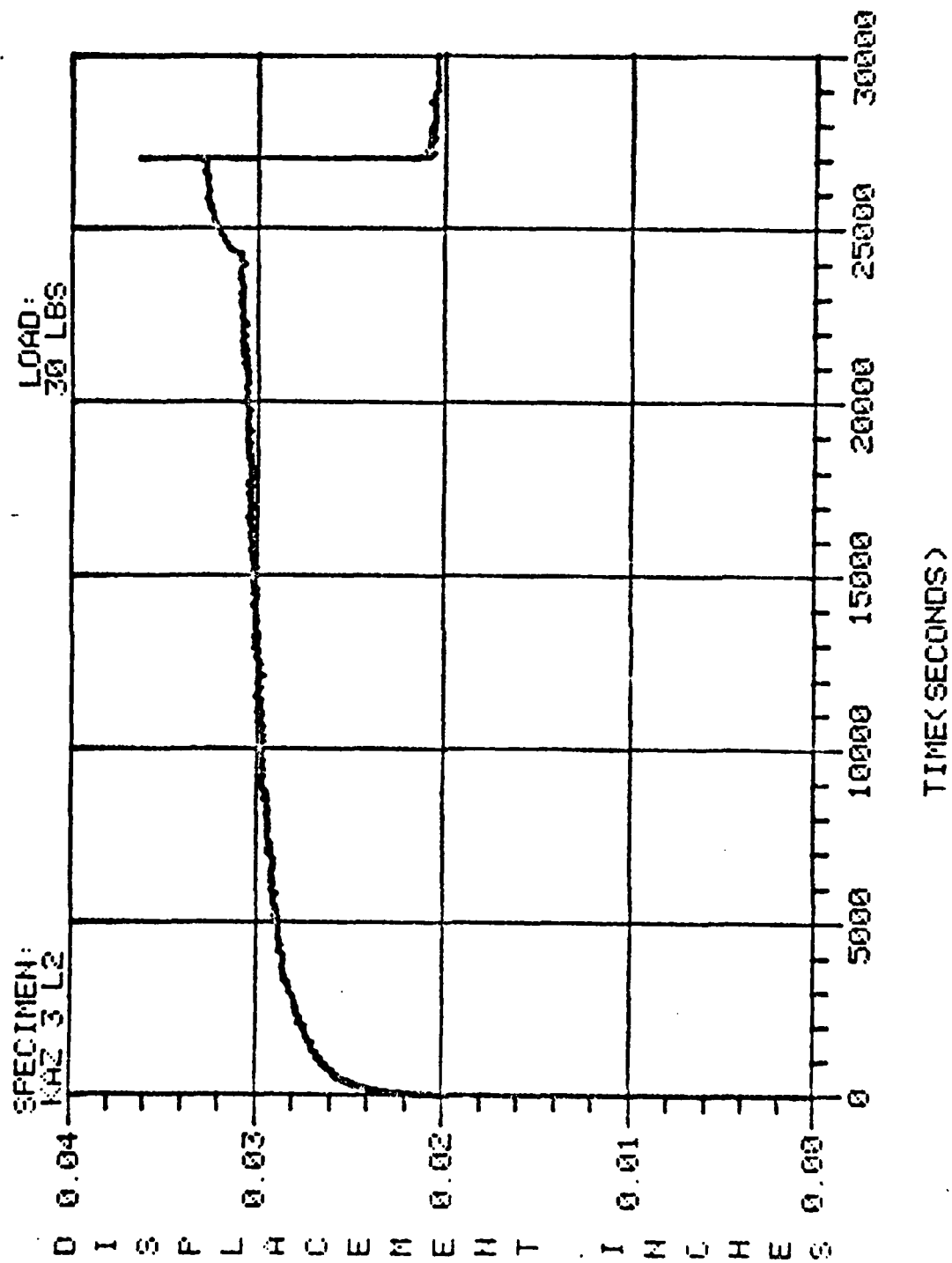


Fig. B-3. Test curve, specimen KAZ 3 (L2)

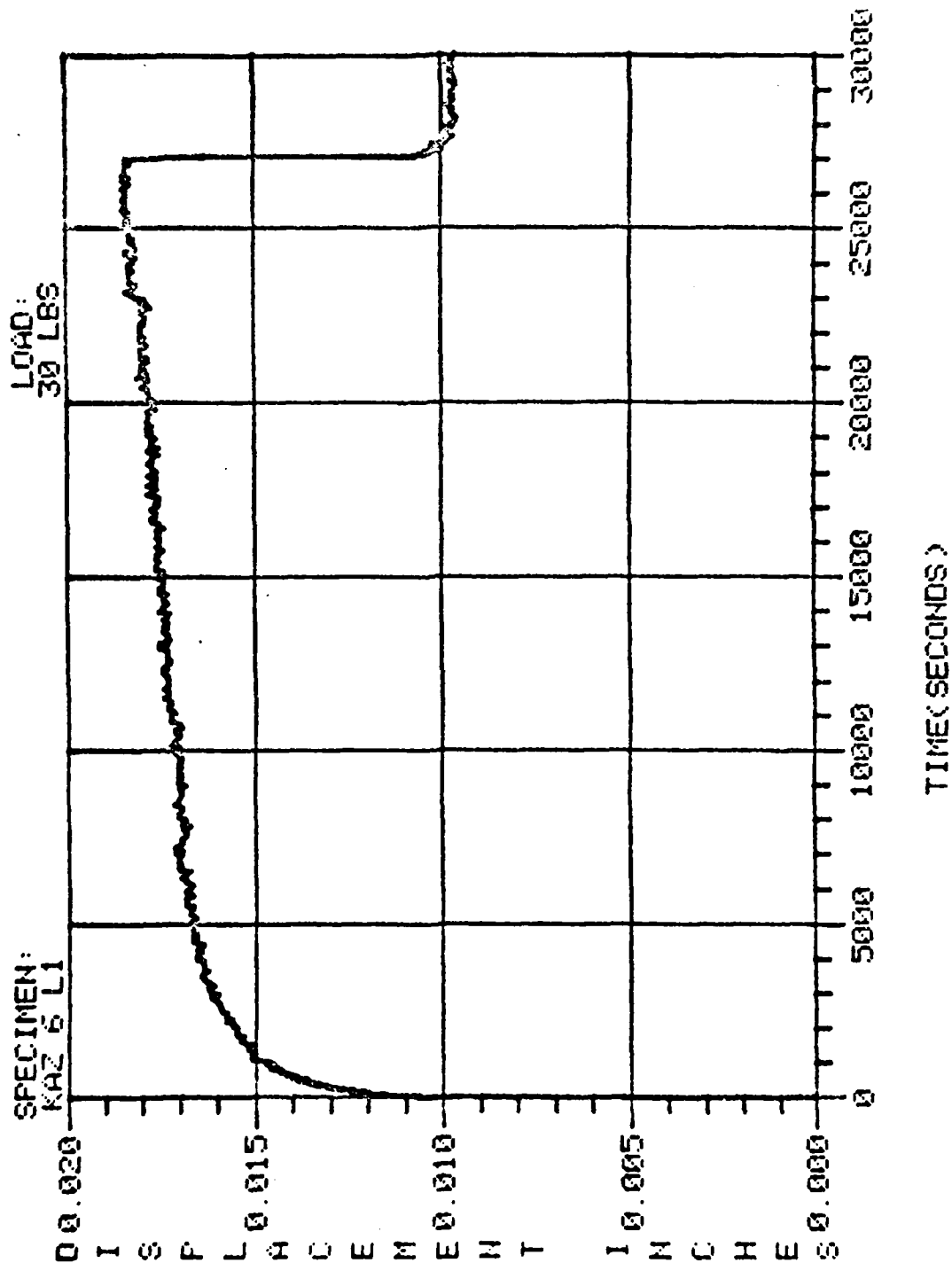


Fig. B-4. Test curve, specimen KAZ 6 (L1)

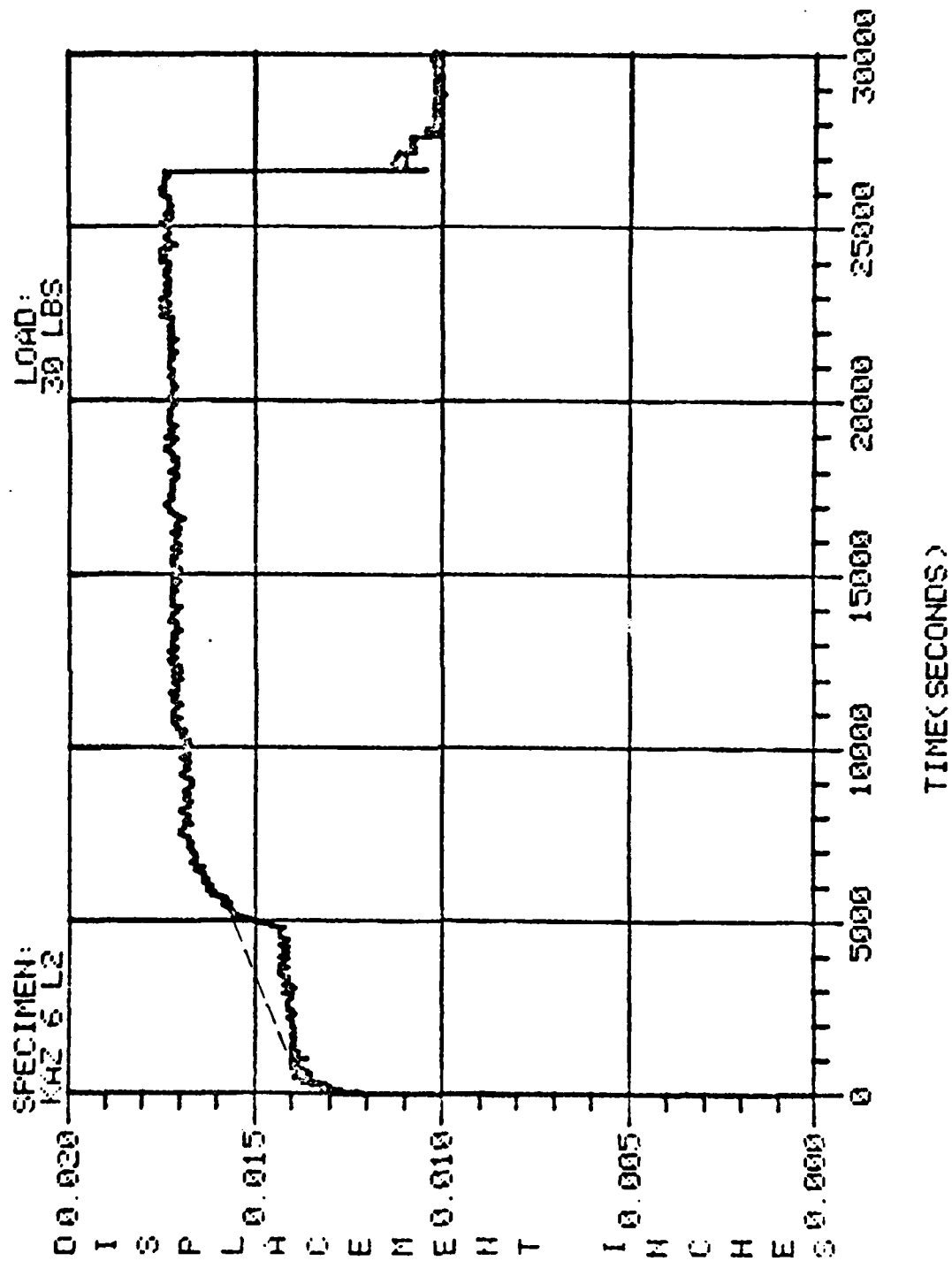


Fig. B-5. Test curve, specimen KAZ 6 (L2)

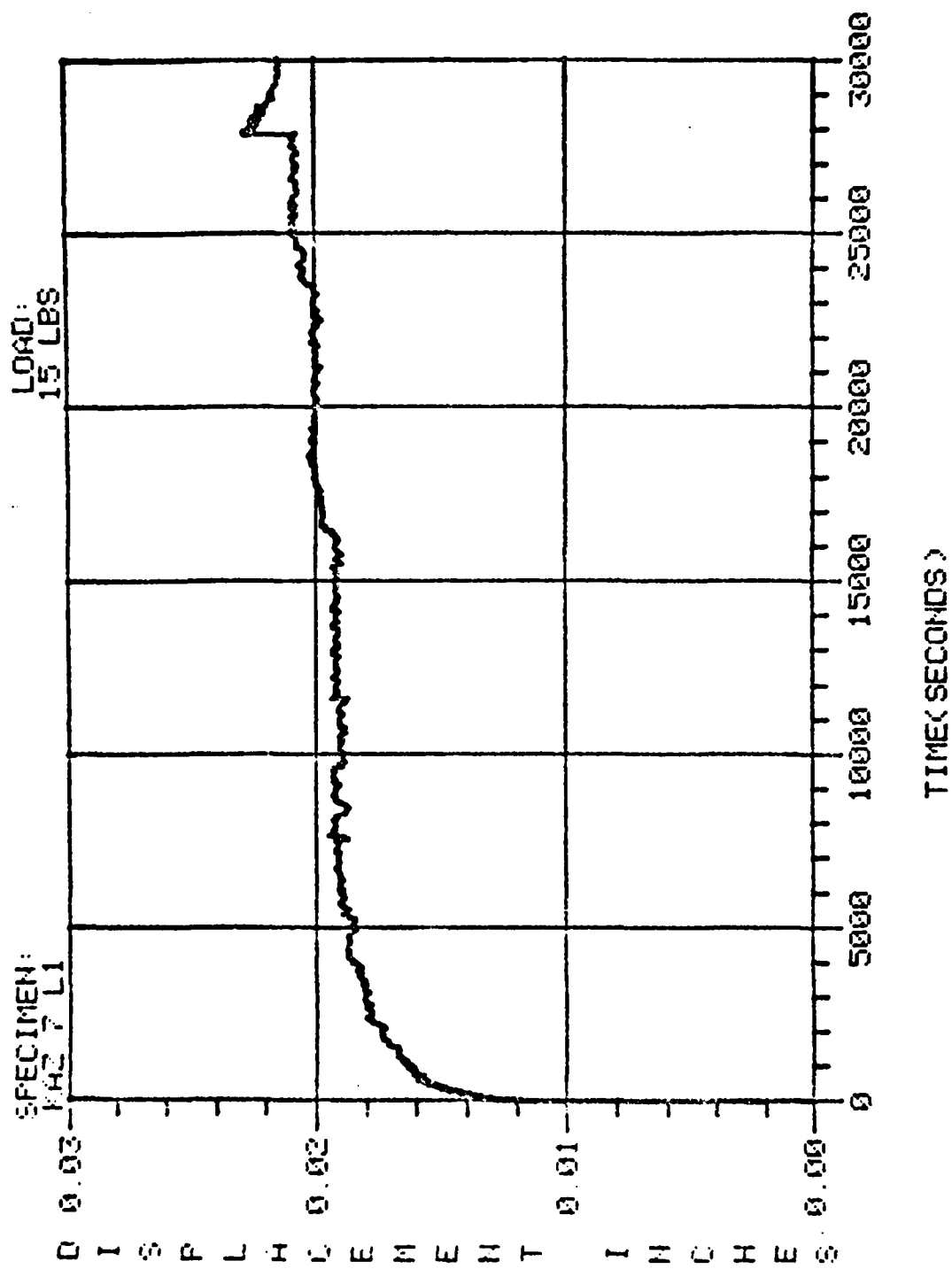


Fig. B-6. Test curve, specimen KAZ 7 (L1)

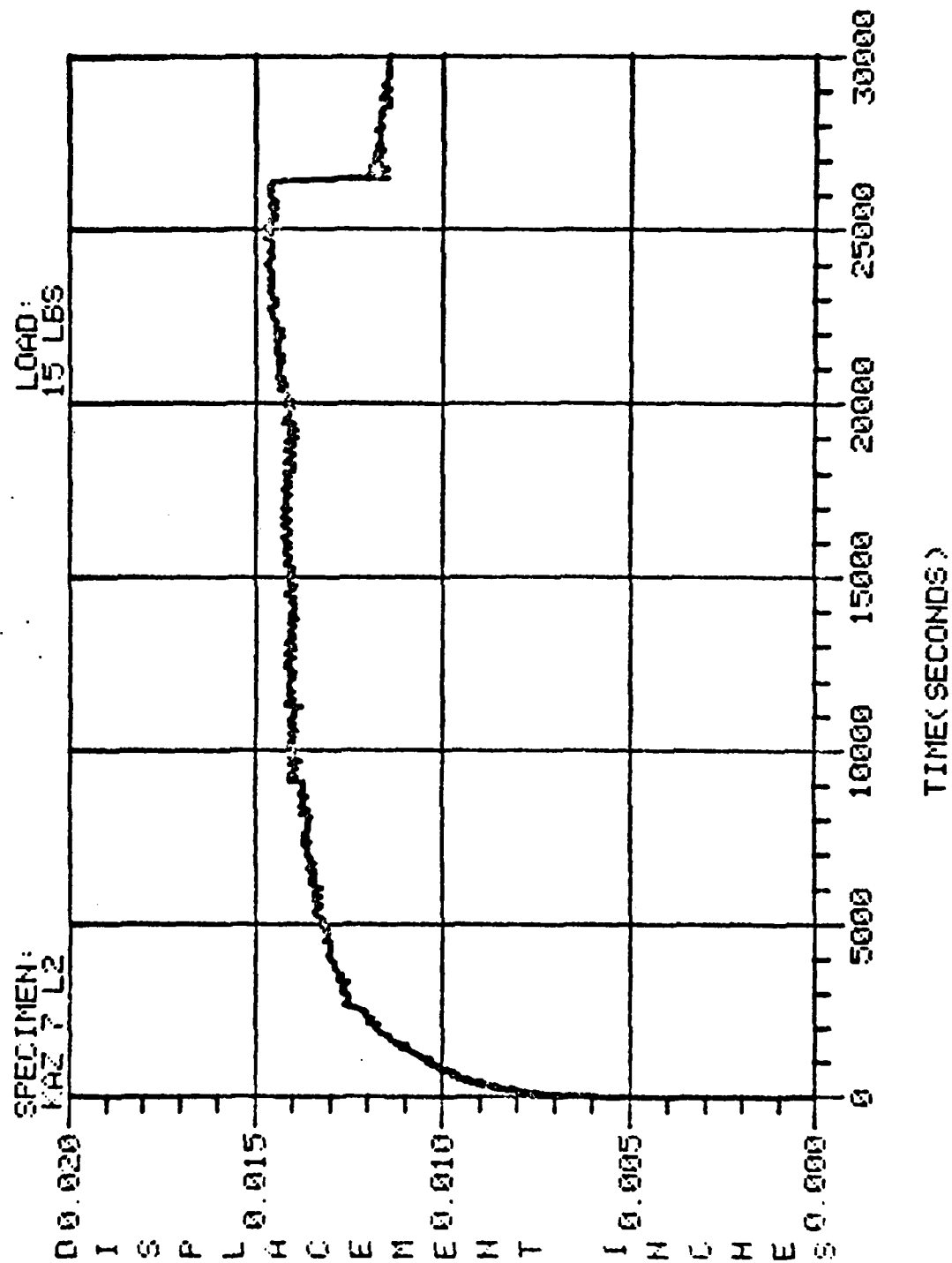


Fig. B-7. Test curve, specimen KAZ 7 (L2)

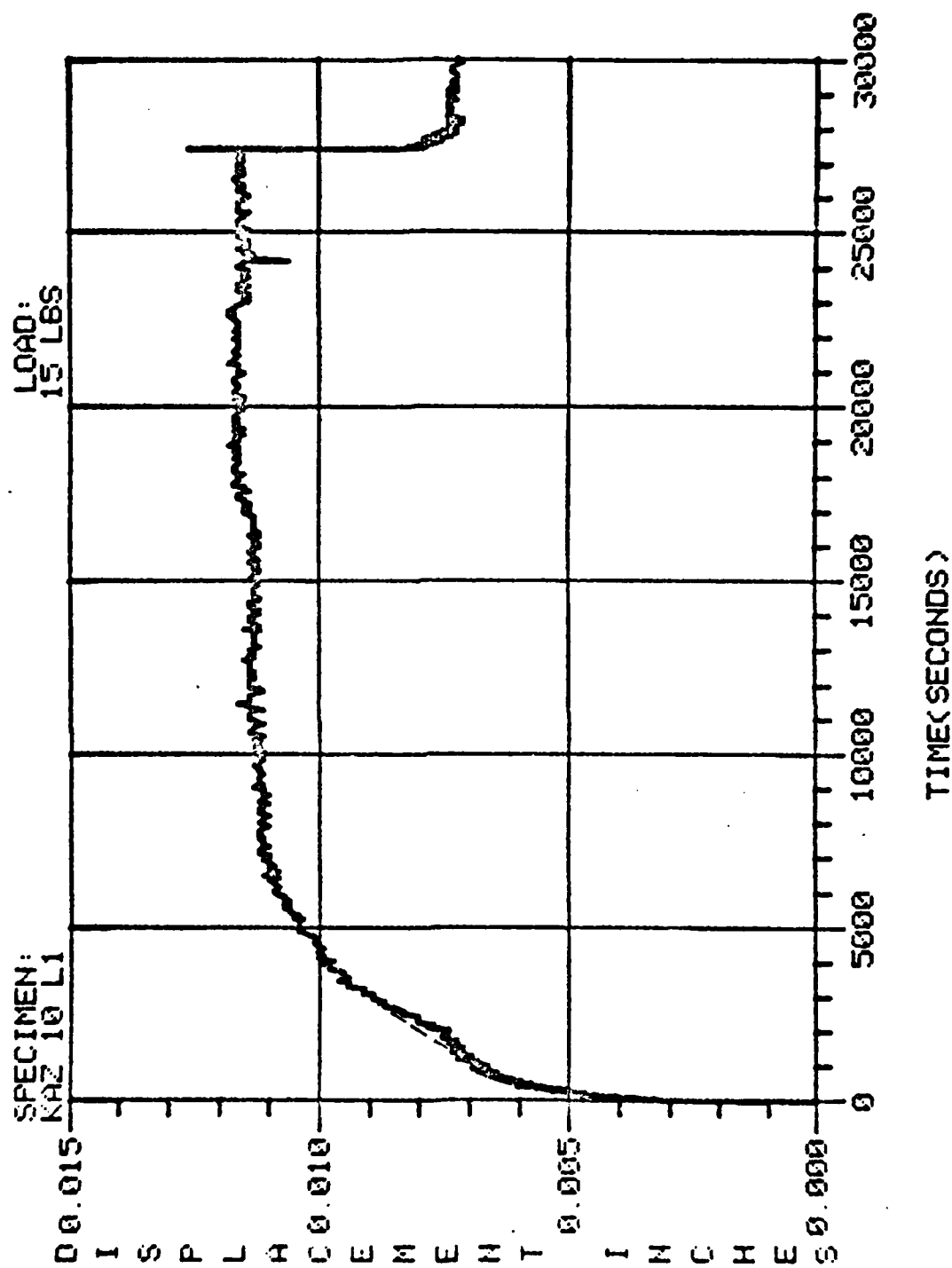


Fig. B-8. Test curve, specimen KAZ 10 (L1)

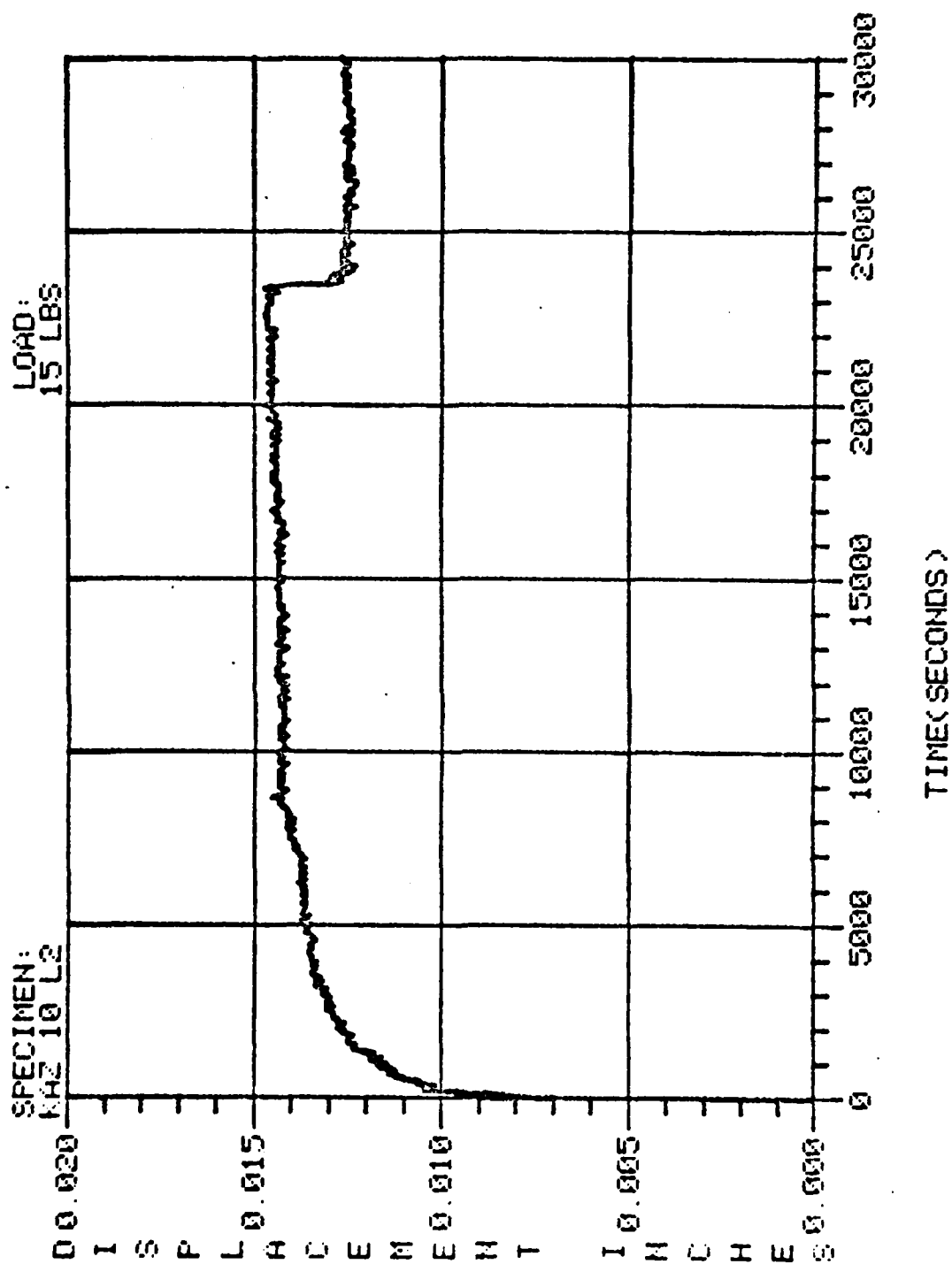


Fig. B-9. Test curve, specimen KAZ 10 (L2)

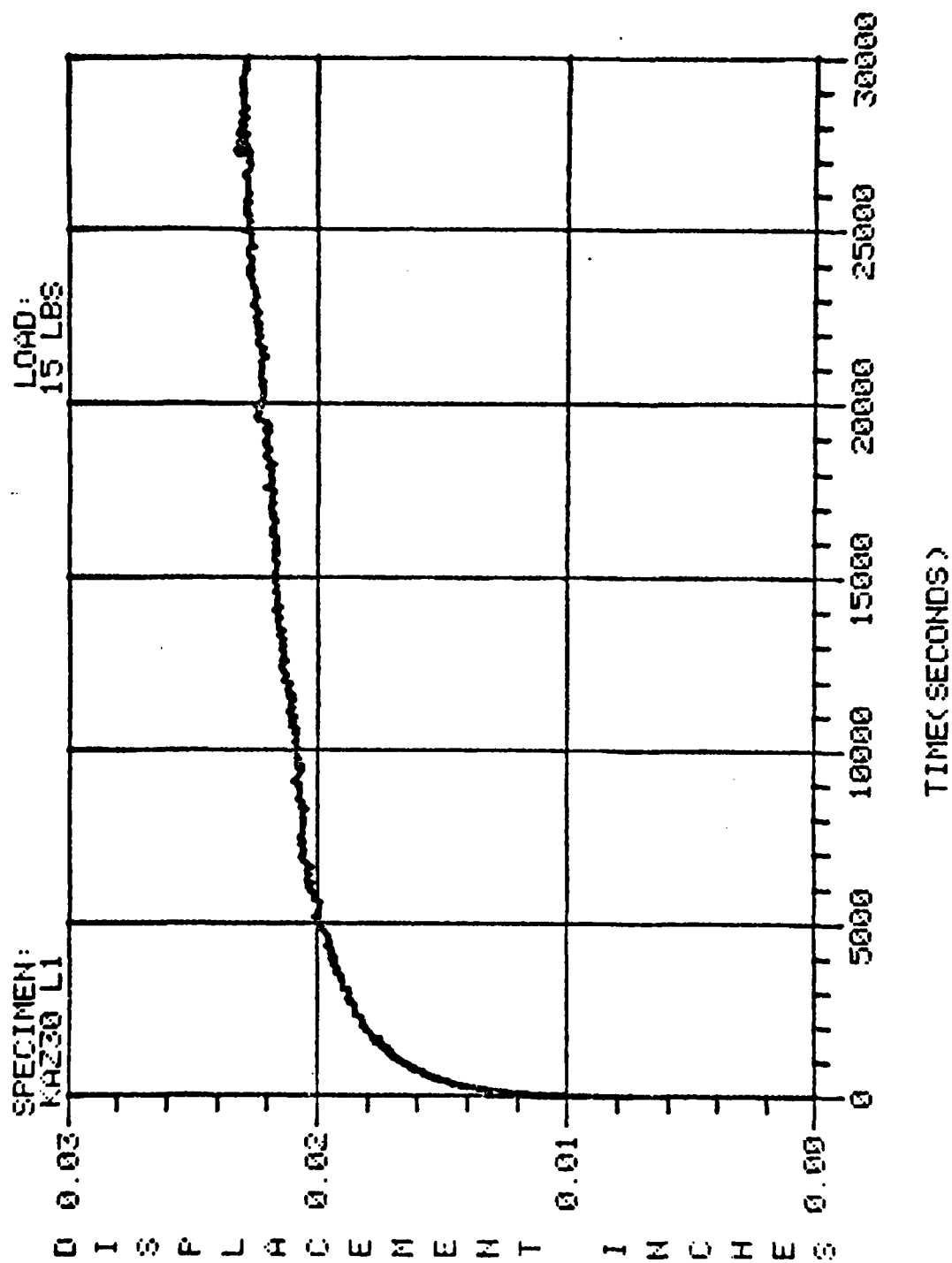


Fig. B-10. Test curve, specimen KAZ 30 (L1)

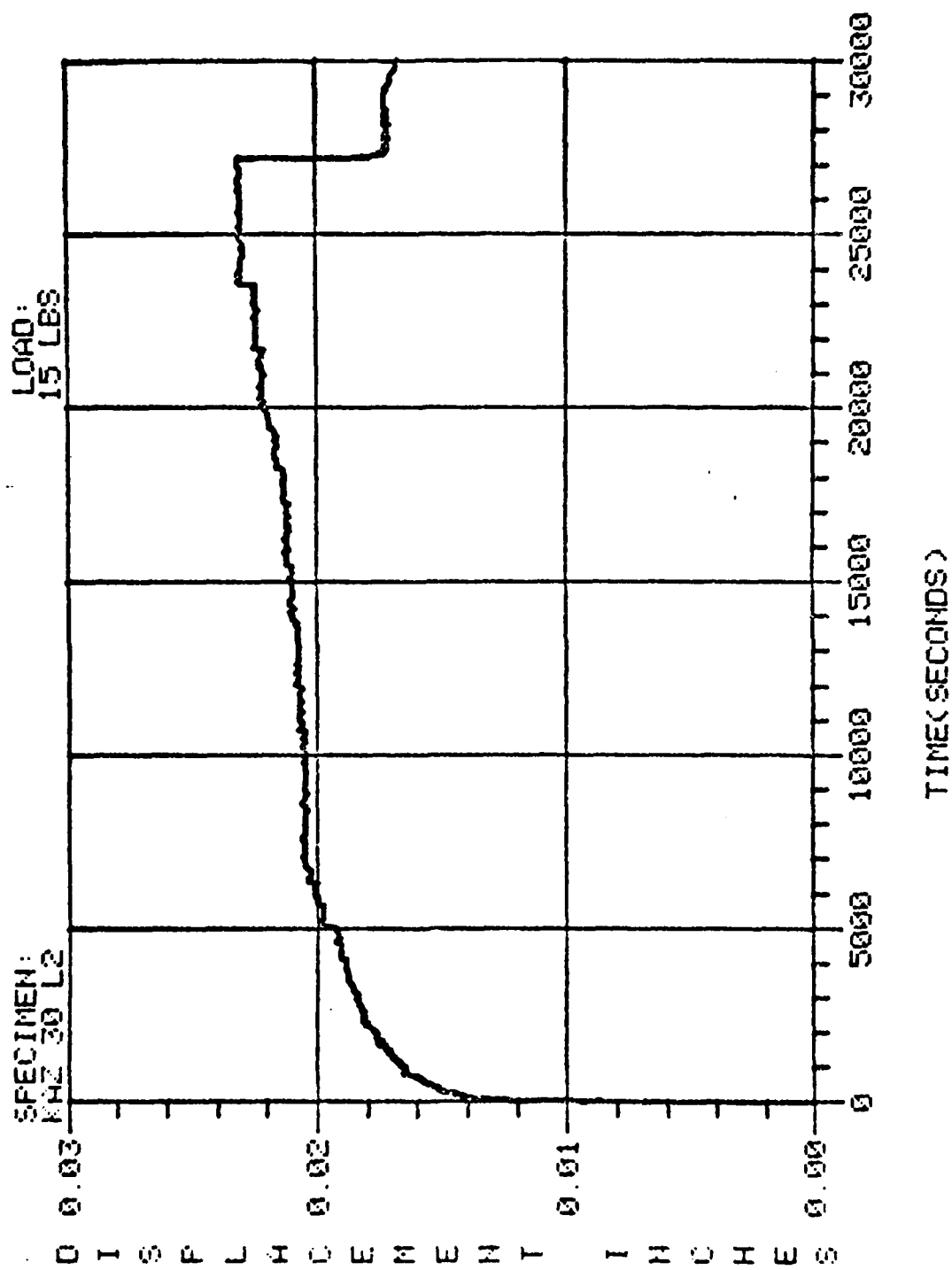


Fig B-11. Test curve, specimen KAZ 30 (L2)

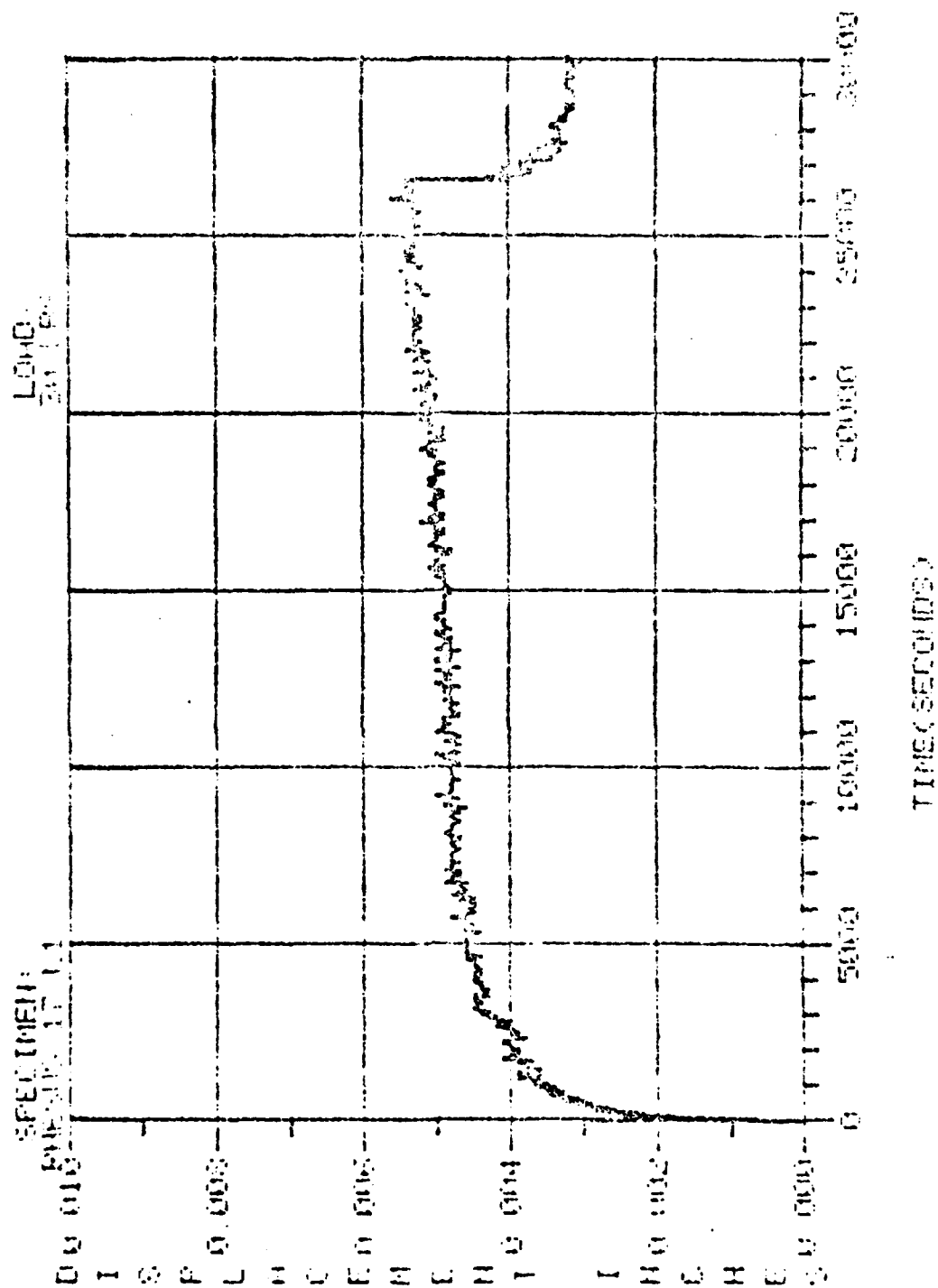


Fig B-12. Test curve, specimen Rhesus 17(L1)

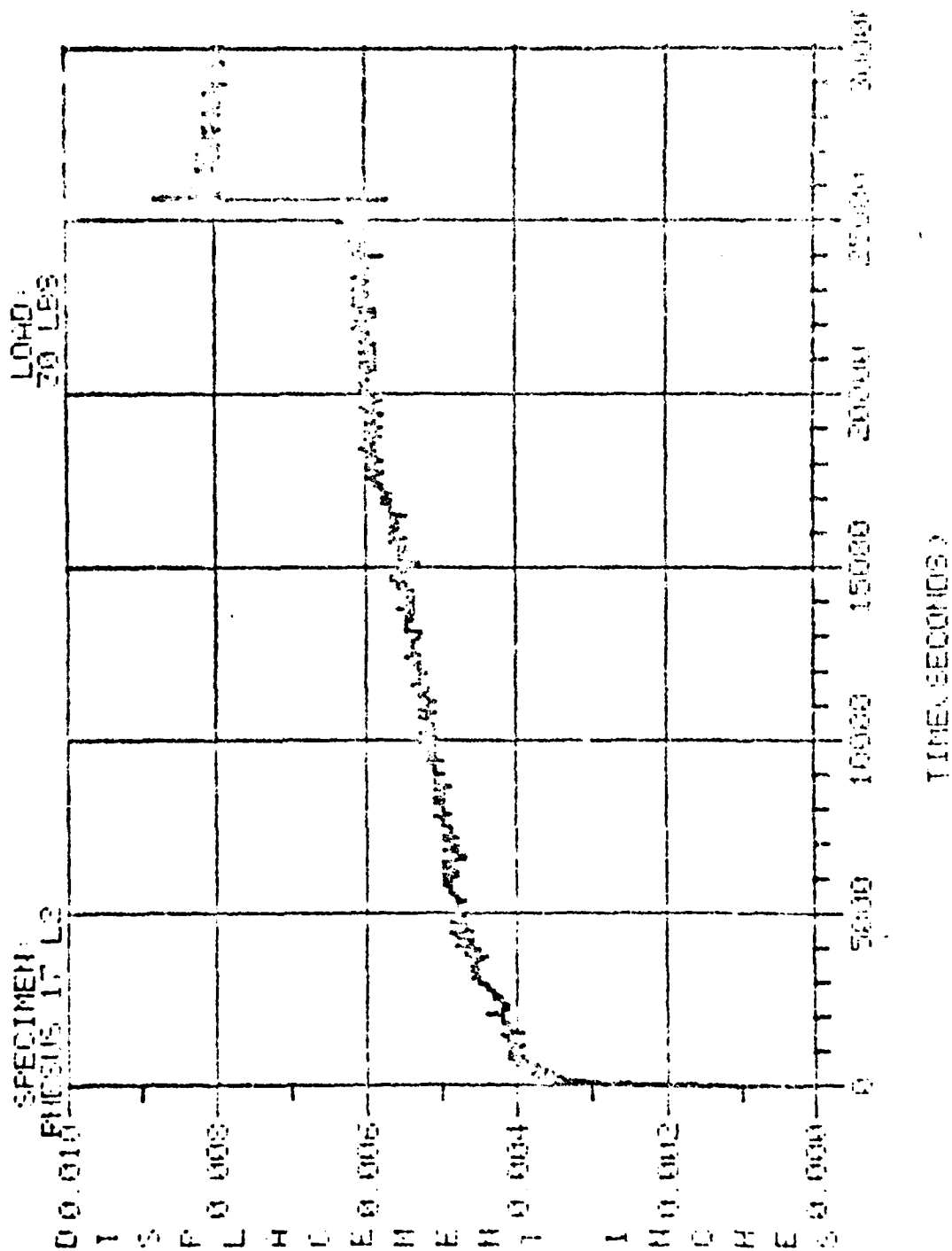


Fig. B-13. Test curve, specimen RHEBUS 17(L2)

APPENDIX C

Example of Calibration Procedure

This appendix presents an example of the procedure used to determine the calibration factor described in section 3.1.2 of the text.

Consider the following successive displacement readings taken at the data terminal for the indicated cylinders:

<u>Cylinder Used</u>	<u>Reading</u>
Long	-2712
Short	-1413
Long	-2699

The average reading using the long cylinder is -2705.5. The measured difference between this average reading and the reading from the short cylinder is therefore -1292.5. Finally, the calibration factor is

$$\begin{aligned}\text{Calibration Factor} &= \frac{0.1250}{|\text{Measured difference}| 10^{-4}} \quad (3-1) \\ &= \frac{0.1250}{|-1292.5| 10^{-4}}\end{aligned}$$

$$\text{Calibration Factor} = \underline{\underline{0.9671}}$$

APPENDIX D

Method for Predicting q_1

This appendix describes a method for graphically predicting an approximate value for the q_1 material parameter described in this thesis. It is based on a knowledge of the axial displacement - time behavior immediately after creep strain begins.

Consider the axial displacement - time curve illustrated in Fig. D-1, where u_{z0} represents the initial elastic displacement at $t = t_0$, and u_{z1} represents the displacement at $t = t_1$, a short time, Δt , later. An approximate expression for the initial displacement rate \dot{u}_0 is the slope, a , of a straight line between the two points, where

$$a = \frac{u_{z1} - u_{z0}}{t_1 - t_0} \quad (D-1)$$

An approximate expression for creep strain rate, $\dot{\epsilon}_c$, can thus be obtained as

$$\dot{\epsilon}_c = \frac{a}{L_0} \quad (D-2)$$

where L_0 is an average axial length immediately after elastic deformation has occurred and before any creep strain has accumulated. Using the fact that q_1 is related to the slope of the stress versus strain rate curve for $\epsilon_c = 0$ (see the main text for a discussion), and using an average axial stress,

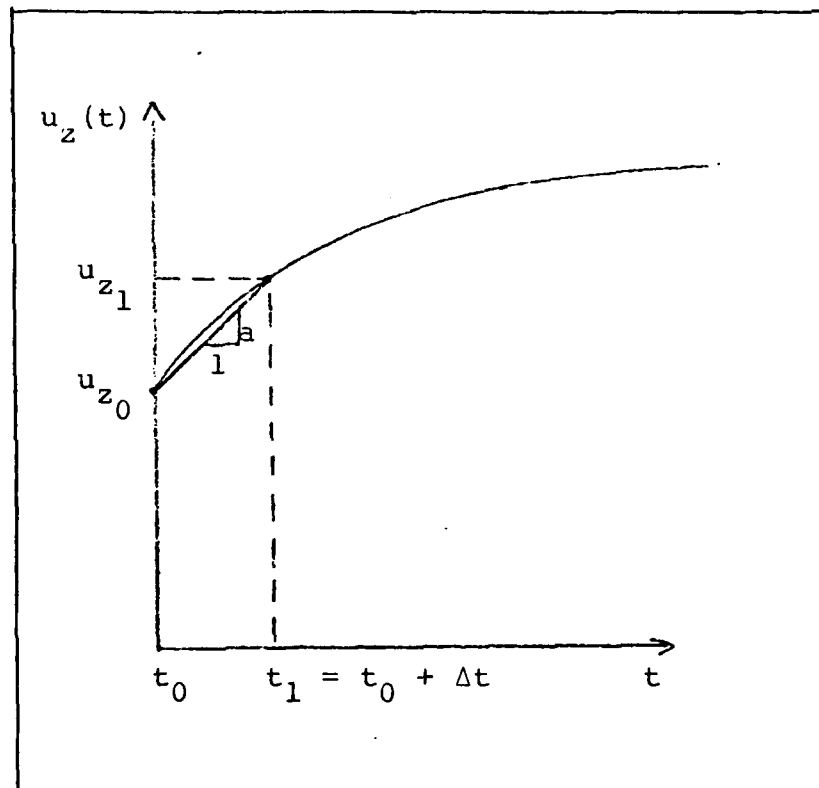


Fig. D-1. Approximate slope of the displacement-time curve after elastic deformation.

σ_{AVG} , over the loaded surface at $t = t_0$, we can approximate q_1 by

$$q_1 = \frac{\sigma_{AVG}}{\epsilon_c} \quad (D-3)$$

Estimation will improve as Δt is made smaller, since the true value of q_1 will then be approached in the limit as Δt approaches zero. This approximate value can then be used as a good first guess in which to begin the analytical technique described in this thesis. The author found it useful, permitting fewer computer runs to converge to a final value.

VITA

William John Rothwell, Jr. was born on 19 May 1951 in Anchorage, Alaska. He graduated from high school in Grants Pass, Oregon in 1969 and attended the U.S. Air Force Academy, receiving a commission and the degree of Bachelor of Science, Engineering Mechanics, in June 1973. He then attended Undergraduate Navigator Training and gained his wings in May 1974. Following upgrade training as an F-4D Weapons Systems Officer, he performed related duties in England, Korea, and at Holloman Air Force Base, New Mexico, after which he entered the School of Engineering, Air Force Institute of Technology in June 1981.

Permanent address: 2051 W. Jones Creek Rd.
Grants Pass, Oregon 97526

UNCLASSIFIED

SECURITY CLASSIFICATION OF THIS PAGE (When Data Entered)

REPORT DOCUMENTATION PAGE		READ INSTRUCTIONS BEFORE COMPLETING FORM
1. REPORT NUMBER AFIT/GAE/AA/82D-24	2. GOVT ACCESSION NO. AD A24 940	3. RECIPIENT'S CATALOG NUMBER
4. TITLE (and Subtitle) A FINITE ELEMENT ANALYSIS OF THE CREEP RESPONSE OF LUMBAR INTERVERTEBRAL JOINTS IN THE RHESUS MONKEY		5. TYPE OF REPORT & PERIOD COVERED MS Thesis
7. AUTHOR(s) Willaim J. Rothwell, Jr. Captain		6. PERFORMING ORG. REPORT NUMBER
9. PERFORMING ORGANIZATION NAME AND ADDRESS Air Force Institute of Technology (AFIT-EN) Wright-Patterson AFB, Ohio 45433		8. CONTRACT OR GRANT NUMBER(s)
11. CONTROLLING OFFICE NAME AND ADDRESS		10. PROGRAM ELEMENT, PROJECT, TASK AREA & WORK UNIT NUMBERS
14. MONITORING AGENCY NAME & ADDRESS (if different from Controlling Office)		12. REPORT DATE December 1982
		13. NUMBER OF PAGES 183
		15. SECURITY CLASS. (of this report) Unclassified
16. DISTRIBUTION STATEMENT (of this Report) Approved for Public Release; Distribution Unlimited.		15a. DECLASSIFICATION/DOWNGRADING SCHEDULE
17. DISTRIBUTION STATEMENT (of the abstract entered in Block 20, if different from Report)		
18. SUPPLEMENTARY NOTES Approved for public release; LAW AFR 190-17. LYNN E. WOLAVER Dean for Research and Professional Development Air Force Institute of Technology (ATC) Wright-Patterson AFB OH 45433 19 JAN 1993		
19. KEY WORDS (Continue on reverse side if necessary and identify by block number) Finite Element Creep Intervertebral Joint		
20. ABSTRACT (Continue on reverse side if necessary and identify by block number) This study consisted of two phases. During the first phase, Lumbar intervertebral centra from healthy, adolescent Rhesus Monkeys (Macaca Mulatta) were subjected to axial compression loads of 15 and 30 pounds for a period of eight hours and displacement-time data was gathered. An axisymmetric finite element model was used to analytically determine material parameters describing the observed creep for each applied load. A Three-parameter Kelvin		

DD FORM 1 JAN 73 1473

EDITION OF 1 NOV 65 IS OBSOLETE

UNCLASSIFIED
SECURITY CLASSIFICATION OF THIS PAGE (When Data Entered)

UNCLASSIFIED

SECURITY CLASSIFICATION OF THIS PAGE(When Data Entered)

20. ABSTRACT

Solid was used to represent the elastic and viscoelastic response. Parameters were found by adjusting them until the analytical displacement-time response matched the experimental response. The parameters determined characterized the initial elastic stiffness, initial creep rate, and creep stiffness.

Analytical stress profiles in two horizontal planes through the vertebral centrum indicated a predominance of stress in Cortical bone and the transition of stress from the Trabecular bone to the Cortical bone as creep proceeded. According to the model, the Centrum behaved as though the Cortex was acting like a thin shell constraining the outward flow of a viscoelastic Trabecular bone region.

During the second phase, viscoelastic constants determined for the Trabecular bone region were incorporated into an overall model of the intervertebral joint minus the Articular Facet Joint and associated spinous processes. Viscoelastic constants were then found for the disk. However, they proved to be unreasonably high, describing a very stiff, creep-resistant disk. It was determined that the rheological model used, two Three-Parameter Kelvin Solids in series, was inadequate to allow one to determine unique values of these parameters in the disk.

Final results indicate that an accurate model of the intervertebral joint must incorporate a viscoelastic Centrum. Creep behavior can no longer be attributed solely to the disk.

UNCLASSIFIED

SECURITY CLASSIFICATION OF THIS PAGE(When Data Entered)

END

FILMED

5-83

DTIC